2015-04-20

Computational Fluid Dynamics Simulations of Radial Dispersion in Low N Fixed Bed Reactors

Nicholas J. Medeiros

Computational Fluid Dynamics Simulations of Radial Dispersion in Low N Fixed Bed Reactors

Nicholas J. Medeiros

A Thesis

Submitted to the Faculty

of the

WORCESTER POLYTECHNIC INSTITUTE

In partial fulfillment of the degree requirements for the

Master of Science

in

Chemical Engineering

April 30th, 2015

Approved:

_____

Anthony G. Dixon, Advisor

_____

David DiBiasio, Department Head

Abstract

Fixed bed reactors are widely applicable in a range of chemical process industries. Their ease of use and simplified operation make them an attractive and preferred option in reactor selection, however the geometric complexities within the bed as a result of the unstructured packing has made the design of such beds historically based on pseudo-homogenous models together with correlation-based transport parameters. Low tube-to-particle diameter ratio (N) beds, in particular, are selected for highly exothermic or endothermic reactions, such as in methane steam reforming or alkane dehydrogenation. Due to the large fraction of tube to catalyst particle contact in these low N beds, wall effects induce a mass transfer boundary layer at the wall, and in the case of thermal beds, a simultaneous resistance to heat transfer. Computational Fluid Dynamics (CFD) has been shown to be an accurate tool for experimental validation and predictive analysis of packed beds, and may be used to derive more accurate design parameters for fixed bed reactors. More specifically, the elucidation of dispersion, or the transport of reactant and product within the bed due to molecular diffusion and convective flow is of fundamental interest to the design of fixed beds.

Computational Fluid Dynamics was used in this research to study solute dispersion in eight beds of varying N at a range of particle Reynolds numbers in the laminar flow regime. In the first stage of research, flow development was simulated in three-dimensional packed beds of spheres. Then, the reactor wall was sectioned to include a boundary condition of pure methane, from which the solute could laterally disperse into the bed.

In the second stage, a two-dimensional representation of the bed was created using the commercial Finite Element Analysis software COMSOL Multiphysics. In these models, axial velocity profiles and radial methane concentration profiles taken from the 3-D models were supplied, and a fitting procedure by use of the Levenberg-Marquardt Least-Squares optimization algorithm was completed to fit radial dispersion coefficients and near-wall mass transfer coefficients to the CFD data. These optimization runs were conducted for all N at a number of bed depths in each case. Two sub-studies were conducted in which a constant velocity profile and a local velocity profile were supplied to the 2-D model, and the optimization re-run. It was found that this two parameter model did not fully account for various mechanisms of dispersion in the bed, namely the increasing rate of dispersion from the tube wall boundary layer up to the bed center, but only accounted for a diffusive-dispersion at the wall and a constant-rate, convective-dispersion everywhere else in the bed. Length dependency of dispersion coefficients were also noted, particularly in the developing sections of the bed. Nevertheless, the combined CFD and optimization

procedure proved to be an accurate and time-efficient procedure for the derivation of dispersion coefficients, which may then lend themselves to the standard design of packed bed reactors.

Acknowledgements

This work is the result of the support of several individuals whom I must graciously thank. The last full year of my graduate studies was spent working full-time as an engineer and full-time as a graduate student – an atypical schedule for grad school. In August 2014, I decided to commit my time to both obligations, work and school, not knowing exactly the kind of toll it would take mentally or emotionally. Long commutes, longer work hours, many skipped meals, and several late nights later, we have this paper. This last year has been, unequivocally, the most stressful and, at times, unbearable. I was pushed beyond my limits, and it was only because of a combined effort among many caring individuals did I succeed.

I first wish to thank my research and academic advisor, Professor of Chemical Engineering, Anthony G. Dixon. Professor Dixon graciously supported me through a tough year, even offering to meet with me on Saturday mornings, given that I was working during the weekday. Both his scientific guidance and demanding, but supportive advising style were crucial to the completion of this project.

I must also thank several others in our wonderful department, namely Felicia Vidito, Tiffany Royal, Stephen Kmiotek, William "Don" Clark, David DiBiasio, and Behnam Partopour. You have all been fantastic and wonderful colleagues, and I am proud and thankful to consider you all my good friends.

I wish to thank those with whom I worked at LiquidPiston in Bloomfield, CT, the company at which I spent the first semester of this past year working. Each day I was surrounded by a talented group of brilliant engineers who challenged me every day and inspired me to reach my potential. It was there that I experienced tangible growth as an engineer and as a learner, more so than in any other setting.

I would also like to acknowledge my co-workers at Exa Corporation, the company at which I started in January 2015. Both welcoming and supportive, the company has given me a taste of what real-world engineers do, and the position there has proved that I am doing what I was always meant to do.

Most importantly, I wish to thank my close friends, without whom, I am sure I would have given up on working toward this degree. Thank you for listening to me during late night phone calls, and taking care of me on nights when I'd run away from school. You all have been there for me through this past year in immeasurable ways.

I wish to thank, specifically, brothers Donal and Michael Boyd, my two best friends, the two brothers I never had, who have helped me navigate not just through this thesis, but through the past five years of life. You two provided me with the encouragement to succeed when I was certain I could not. Your friendship

has given my life both a meaning and a depth, and I look forward to continuing our lives together. I love you both.

This work is dedicated to my mother, my love for whom, I've found, is immeasurable by any sort of mathematics.

Even when I was lost in the darkest of places,

I could always find you somewhere **in my middle.**

Table of Contents

List of Figures

List of Tables

1. Introduction

Fixed bed reactors are generally hollow tubes filled with catalytic packing material, on which a chemical reaction may occur. The packing material may be spherical, cylindrical, or of another topology, and made from ceramics or metals, among other materials. Fixed, or packed, bed reactors are preferred for their simplified technology and operation, however the geometric complexities within the bed as a result of the unstructured packing has made the design of such beds historically based on pseudo-homogenous models coupled with correlation-based transport parameters. It is for this reason that fixed beds are a current focus of computational and experimental research.

Low tube-to-particle diameter ratio (N) beds are typically selected for highly exothermic or endothermic reactions, such as in methane steam reforming or ammonia synthesis. The large contact area between the typically heated or cooled reactor wall to the catalyst particles offers better heat transfer rates and kinetic favorability. Additionally, the use of larger particles within a tube of relatively small diameter results in a reduced pressure drop across the bed, and thus a more economically favorable operation. However, this high void fraction near the wall of the bed induces significant flow and heat transport effects that are generally not accounted for in conventional packed bed models. In this near wall area, a boundary layer develops in which mass transfer is dominated by diffusion owing to no-slip velocity conditions, and a high resistance to heat transfer is present, causing a temperature jump near the wall. The figure below depicts benchscale fixed beds in the low N range:

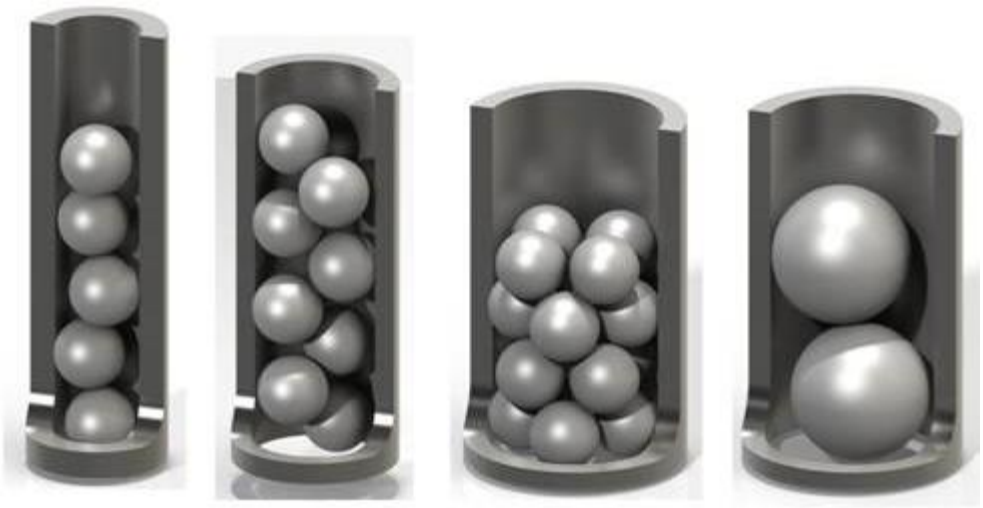

Figure 1.1. Collection of bench scale fixed beds in the low N range. Bed porosity near the wall appears higher in low N beds (Langsch, Mueller, Haase, & Lange, 2013).

Dispersion is the phenomenon responsible for the transport of a fluid in a packed bed as a result of the combined effects of molecular diffusion and convection in the bed interstices, or the space available for fluid flow between particles. Dispersion is analogous to Fickian diffusion by replacing the diffusion coefficients with dispersion coefficients as seen in the following partial differential equation:

$$D_L \frac{\partial^2 C}{\partial z^2} + \frac{1}{r}\frac{\partial}{\partial r} * \left(D_R r \frac{\partial C}{\partial r}\right) - u\frac{\partial C}{\partial r} = \frac{\partial C}{\partial t} \tag{1.1}$$

In equation 1.1., D_L is the axial, or longitudinal dispersion coefficient, and D_R is the radial, or transverse dispersion coefficient, related to flow in the freestream and cross-stream directions, respectively.

The study of dispersion in packed bed reactors is fundamental to their design in that dispersive phenomena characterize reactant and product transport within the bed. Flow within the geometrically complex interstitial area as a result of the random packing structure controls local mixing and transport processes in the bed, and these processes are globally described by convective-dispersive equations. Thus, it is necessary and useful to the design of fixed bed reactors to derive dispersion coefficients to model the flow behavior for predictive analysis of packed beds.

Computational Fluid Dynamics (CFD) is a numerical method-based computing approach for simulating fluid flow, mass and heat transport, and reaction kinetics, among other physical phenomena. In general, the

use of CFD requires converting the geometry of interest, here a fixed bed of spheres, into a number of small control volumes, collectively called the computational mesh, or grid. After supplying the appropriate boundary conditions related to flow and species transport, and an initial, estimated solution for the system of interest, a complete numerical solution can then be obtained by iterative, convergence-guided, numerical techniques. With the recent introduction of high performance computing capabilities and the continued growth of such computing resources, CFD is now used as an important tool for the design and simulation of fixed bed reactors. The use of CFD allows the elucidation of certain flow and heat characteristics that cannot be obtained from experimental methods, such as the velocity distribution around and between particles, or the temperature at any point within the bed. The images below show a contour plot of velocity taken from a center cutplane of a bed (left) and a concentration distribution of methane on the same plane, results that may not be as exactly obtained in an experimental environment.

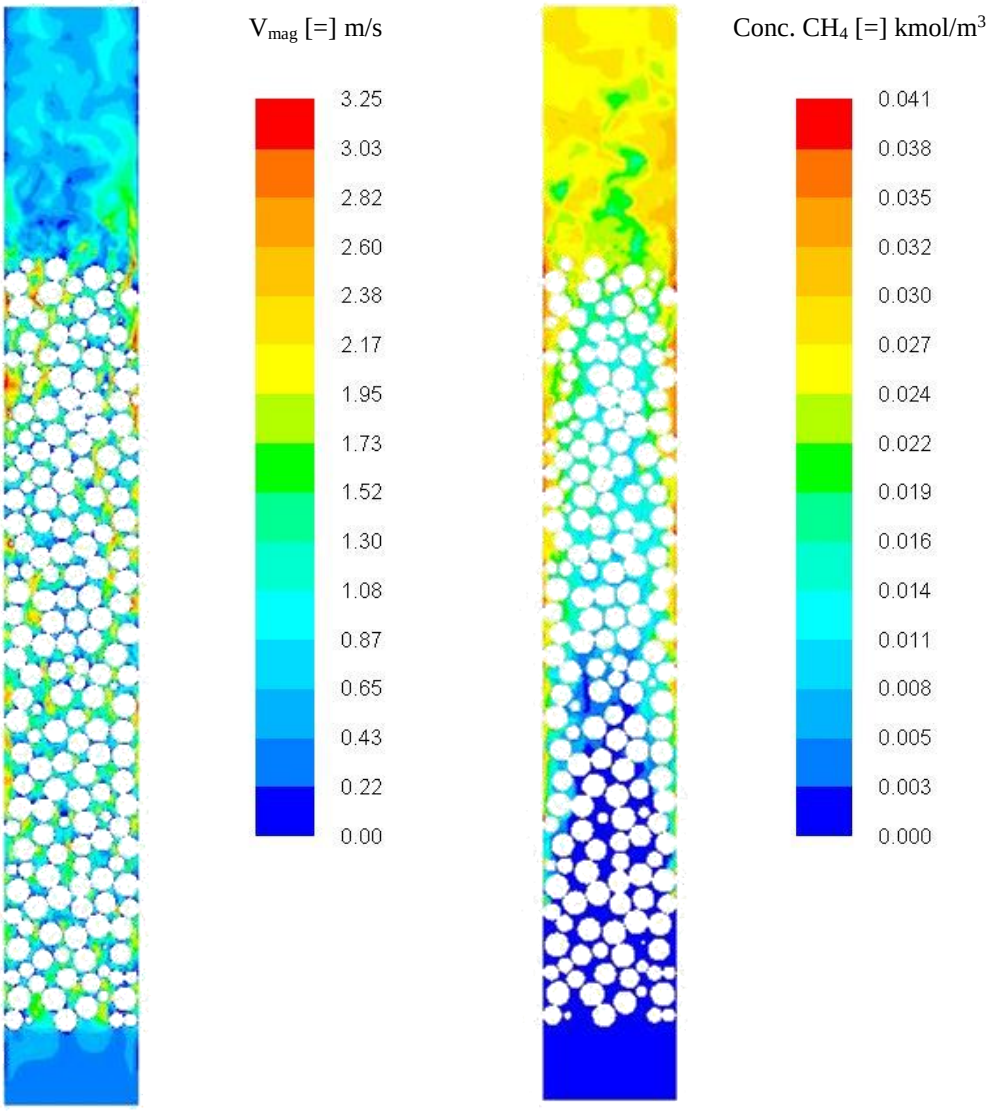

Figure 1.2. Contour plots of velocity magnitude (left) and methane concentration (right) on center cutplane of N = 6.40 at Re = 696.

This research aims to provide more accurate design parameters for fixed bed reactors, in terms of fitted radial dispersion coefficients for a range of bed diameters and particle Reynolds numbers, using a CFD-based approach. The commercial finite-volume method code FLUENT is used to simulate fluid flow and dispersion in beds of various low N in the laminar flow regime of $87 \leq Re \leq 870$. Using the three-dimensional radial concentration profiles produced in FLUENT, the optimization solver offered by

COMSOL Multiphysics is used to fit radial dispersion coefficients for each bed in the presence of the near-wall diffusion boundary layer. The goal is to arrive at a set of dispersion coefficients that are a result of the velocity distribution and radial concentration profiles in the bed due to the geometrically complex, unstructured spherical packing arrangement.

2. Literature

Fixed bed reactors share a wide range of applications in chemical process industries. Low tube-to-particle diameter ratio (N) beds, in particular, are often selected for highly exothermic or endothermic reactions. The design of fixed bed reactors have historically been based on pseudo-homogenous models together with correlation-based transport parameters that effectively ignore local flow phenomena and reduce the geometric complexity of the bed. In these beds of low diameter, tube wall effects are significant across the length of the bed, owing to the larger fraction of particle-wall contact. Recently, Computational Fluid Dynamics (CFD) has proved to be an accurate tool for experimental validation and predictive analysis of fixed bed reactors. Using CFD, transport phenomena, and more fundamentally mass dispersion, may be elucidated to provide more accurate design parameters for fixed bed reactors.

2.1 CFD modeling of fixed bed reactors

The application of Computational Fluid Dynamics in packed bed modeling began in the late 1990s as advances in computing power became suitable for simulative experiments. With the continued growth and development of computational resources, CFD has become an important tool for predictive analysis in various fields of scientific research, including automotive engineering, chemical reaction engineering, pharmaceutical applications, and in the oil and gas industries, among others.

In an early study, researchers used CFD to model a bed comprising 10 spheres of N=2.43, which included wall-particle and particle-particle contact points (Logtenberg et al., 1999). This work was able to show eddy formation near wall-particle contact points, thus showing local, near-wall heat transfer, and correctly modeled back-flow regions which were in agreement to experimental studies of packed beds.

Nijemisland and Dixon successfully modeled a 44-sphere bed of N = 2 using Computational Fluid Dynamics (2001). After reconciling CFD modeling and experimental deficiencies, both excellent qualitative and quantitative agreement was reached between simulative and experimental results. The two were also able to model turbulent flow through the bed by reducing the particle size to 99% of its original size, thus preventing meshing issues in the particle-particle contact points, while maintaining a consistent velocity profile around the contact points.

Freund et al. studied transport in packed beds of spheres by means of Lattice-Boltzmann direct simulation techniques, stepping away from the conventional Navier-Stokes equation-based CFD codes (2003). Their numerical experiments proved that local effects due to packing structure and channeling (i.e., wall effects)

were present and responsible for variations in pressure drop and mean porosity from experimental studies of the same beds, in the range $1 < Re < 100$. Their focus on local flow effects showed that pseudo-homogenous equations with semi-empirical parameters for fixed bed modeling ignore important flow behaviors present in the beds as a result of local packing structure.

More recently, Augier et al. simulated laminar flow and heat transfer through beds of 620 spheres of $N \approx 24$ (Augier, Idoux & Delenne 2010). Spheres comprising the bed packing were contracted, again, to prevent the problematic meshing in contact point areas. While global flow and heat transport CFD results were validated by experimental studies, the researchers state the contraction of the spheres resulted in an underestimation of radial dispersion.

Given the problematic meshing that arises due to particle-particle contact points in fixed bed modeling, correcting these geometric issues has been a focus of research in the realm of computational fluid dynamics.

In a 2013 study of mesh development for treating the contact point problem, Dixon et al. (2013) noted the issue in contracting the particle diameter, as done in the previously reviewed studies, results in a bed with too large a voidage and high errors in drag coefficient and particle-particle heat transfer rates. Another method to modify contact points, as studied by Guardo et al. (2004), is to expand the particles to allow for a 1% overlap. However, this global increase in particle diameter increases the number of contact points than were previously present. In a third method, deemed the "bridges" method, a small cylinder is placed between the spheres at an existing contact point, aligned with the center-center line of the two spheres. An advantage to this method is that its effect on bed void fraction is not as significant as globally contracting or expanded the particle diameter as in the "gaps" or "overlap" methods discussed previously (Ookawara, Kuroki, Street & Ogawa, 2007). A fourth contact point modification, described by Eppinger et al. (2011), includes removing the local spherical caps of the spheres that are in contact with another sphere, denoted as the "caps" method. Again in this method, a change in void fraction is not as extreme because the capping of the particles happens only locally at a contact point, as compared to a global reduction in particle size. The four contact point methods are illustrated below, with an exaggeration in the modification for easier viewing:

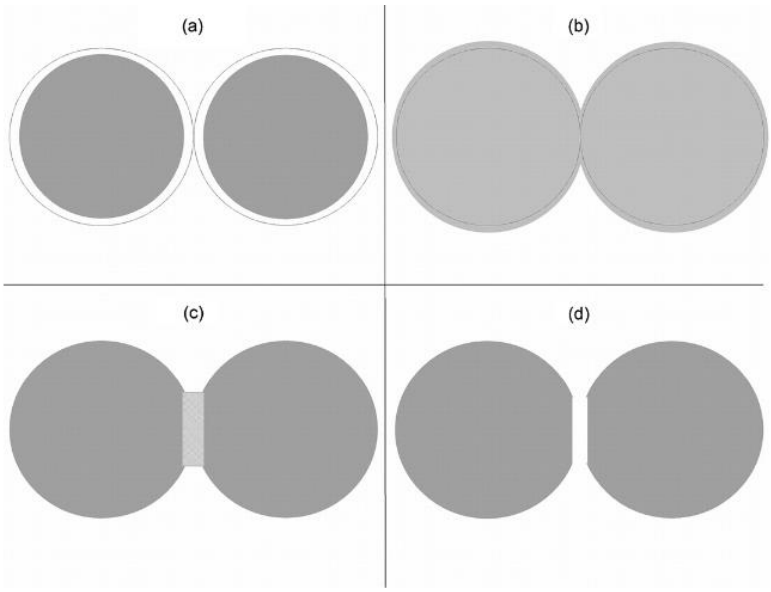

Figure 2.1.1. Schematics of the four contact point modifications: (a) Gaps; (b) Overlaps; (c) Bridges and (d) Caps (Dixon, Nijemeisland & Stitt, 2013).

Their study detailed a mesh development scheme depending on the type of contact point modification. In general, each scheme included a method of fine meshing around the contact point. Then, by making use of size functions, the mesh size grew as it transitioned from the contact point area to a larger, unstructured mesh in the so-called "non-critical" region of the domain.

Based on their results of flow and heat transfer studies, the authors offer a set of recommendations on caps and bridge sizing depending on the Reynolds number and type of study to be done. For research on pressure drop and dispersion only, the shell-type domain may be used, by which only the fluid domain (not catalyst particles) is meshed. In addition, the "caps" approach to contact points is used as particle-particle heat transfer is not modeled. For heat transfer, intraparticle diffusion, and reaction studies, particle-type domain should be used, in which both the fluid and solid catalyst particles are meshed, together with the "bridges" approach.

2.2 Dispersion in fixed bed reactors

Dispersion is the phenomenon responsible for the transport of a fluid in a bed of solid particles as a result of the combined effects of molecular diffusion and convection in the bed interstices. The study of dispersion lends itself to several applications, for example in quantifying contaminant transport in soils or in modeling

solute transport in fixed bed reactors. Quantitatively, dispersion is analogous to Fickian diffusion, exchanging the diffusion coefficients for dispersion coefficients as in the following partial differential equation:

$$D_L \frac{\partial^2 C}{\partial z^2} + \frac{1}{r}\frac{\partial}{\partial r} * \left(D_T r \frac{\partial C}{\partial r}\right) - u\frac{\partial C}{\partial r} = \frac{\partial C}{\partial t} \tag{2.1}$$

The previous is a mass balance taken on the solute in a small control without reaction. The coefficient D_L is the longitudinal dispersion coefficient (also referred to as the axial dispersion coefficient) related to flow in the freestream direction. Similarly, D_T is the transverse dispersion coefficient (also referred to as the lateral, or radial, dispersion coefficient) related to flow in the cross-stream direction. When dealing with dispersion, it is often useful to define the dimensionless Peclet number, the ratio of advective to dispersive transport:

$$Pe_r = \frac{v_0\, d_p}{D_r} \tag{2.2}$$

$$Pe_a = \frac{v_0\, d_p}{D_L} \tag{2.3}$$

Where v_0 is the interstitial velocity in the bed, d_p is the particle diameter, and D_r and D_a are the radial and axial dispersion coefficients, respectively.

In an early study, Gunn (1969) described axial and radial dispersion in terms of probability theory, accounting for dispersion in the fast stream (convective-dominated), and the slow stream near the tube wall (diffusion-dominated). His research estimates the probability of a particle existing in the diffusion boundary layer or moving into the fast stream area of the bed. He states that diffusion in the bed has little effect on convective radial dispersion, and introduces a fluid-mechanical Peclet number based on convective-dispersion alone:

$$\frac{1}{Pe} = \frac{1}{Pe_f} + \frac{1}{ReSc\tau_R} \tag{2.3}$$

Where τ_R is the tortuousity in the bed. His theoretical evaluation of dispersion is compared to liquid-phase experimental studies of dispersion in fixed beds, so that any dispersion due to molecular diffusion is negligible. His results show that in the limit of high Reynolds number, Pe tends to 11.

In a later experimental and modeling study, Coelho and Guedes de Carvalho (1988) studied transverse dispersion in granular beds. This study focused on a dual-parameter method to study transverse dispersion in the bed, as a result of combined diffusion and dispersion phenomena occurring. Near the wall, the velocity approaches zero and eventually is zero at the wall, owing to the no-slip condition. This near-wall area may be thought of as a laminar sub-layer in which diffusion is the dominant flow regime. Outside of this layer, the transport in the bed is due solely to dispersion.

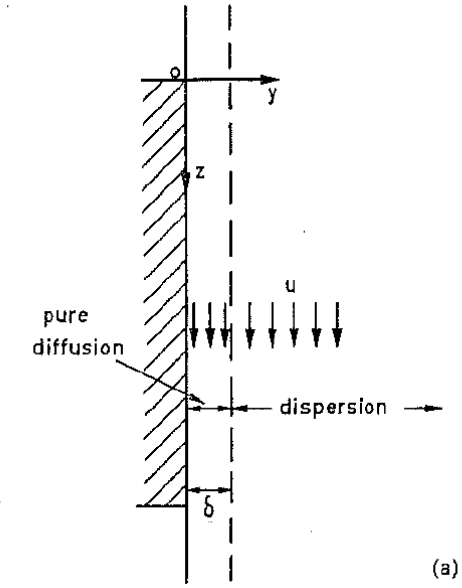

Figure 2.2.1. Model illustration showing the two regions of mass transfer (Coelho & Guedes de Carvalho, 1988).

The researchers then offer a two parameter model that may predict transverse dispersion by the use of a wall mass transfer coefficient and a dispersion coefficient. In the cases for which bed depth was varied, and a dependence of the transverse dispersion coefficient on bed length was found, the institution of the wall mass transfer coefficient was employed, as this parameter is a function of near wall velocity and particle diameter only. Results from the studies shown below concluded that for a given Re, Peclet numbers were nearly constant and independent of bed depth, using the two parameter model.

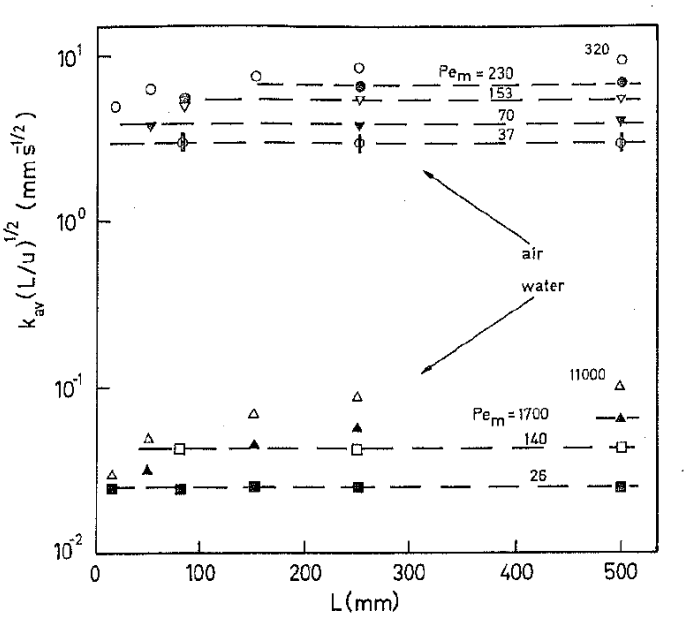

Figure 2.2.2. Effects of Bed Length on Mass Transfer Coefficients (Coelho & Guedes de Carvalho, 1988).

In an experimental study, Guedes de Carvalho and Delgado (2000) studied lateral dispersion in fixed beds of spheres by including in the bed a soluble cylinder of benzoic acid aligned with the flow of water entering the tube. The experimental setup is shown in Figure 2.2.3:

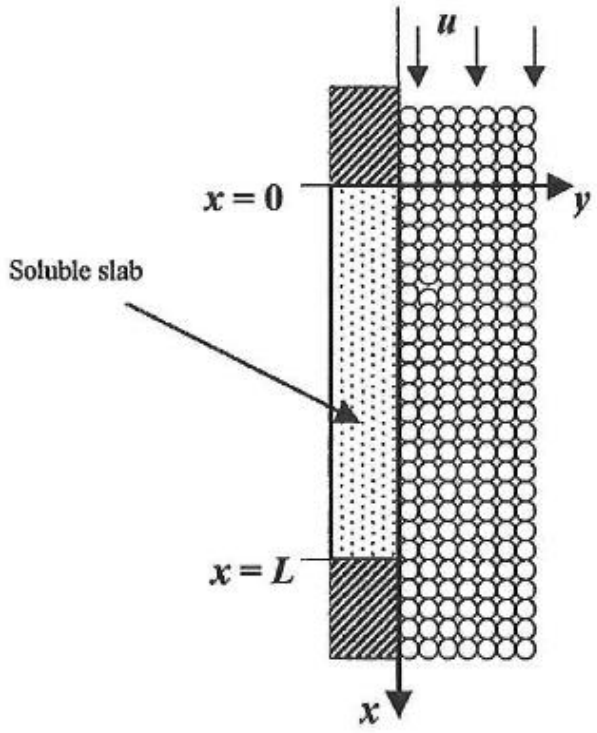

Figure 2.2.3. Flow through packed bed near soluble surface (Guedes de Carvalho & Delgado, 2000).

The two researchers neglect any near-wall effects on dispersion, stating that the section of packing contacting the soluble slab actually indents onto this soluble section, removing the near-wall, high-voidage section that is typical in a fixed bed. Solute concentration in the outlet section of the bed is measured as a means to determine the rate of dissolution of the cylinder. Diffusion is treated as occurring in one dimension, given that the bed follows the criterion $L/d > 20$, where d is particle diameter. Because the mass transfer boundary layer is thin compared to the thickness of the soluble cylinder, the solute material balance reduces from equation 2.4 to equation 2.5:

$$u\frac{\partial C}{\partial x} = D_T\frac{\partial^2 C}{\partial y^2} + D_L\frac{\partial^2 C}{\partial x^2} \tag{2.4}$$

$$u\frac{\partial C}{\partial x} = D_T\frac{\partial^2 C}{\partial y^2} \tag{2.5}$$

Where D_T and D_L are the transverse and longitudinal dispersion coefficients.

The authors offer two equations for the ratio of transverse dispersion coefficient to the molecular diffusion coefficient, D_m, for gas-phase fluids:

$$\frac{D_T}{D_m} = \frac{1}{\tau} + \frac{1}{12}\frac{ud}{D_m} \quad \text{for } Pe_m < 80 \tag{2.6}$$

and

$$\frac{D_T}{D_m} = \frac{1}{\tau} + 0.50 Pe_m^{0.57} \quad \text{for } 80 < Pe_m \tag{2.7}$$

Where τ is the tortuosity of the packed bed.

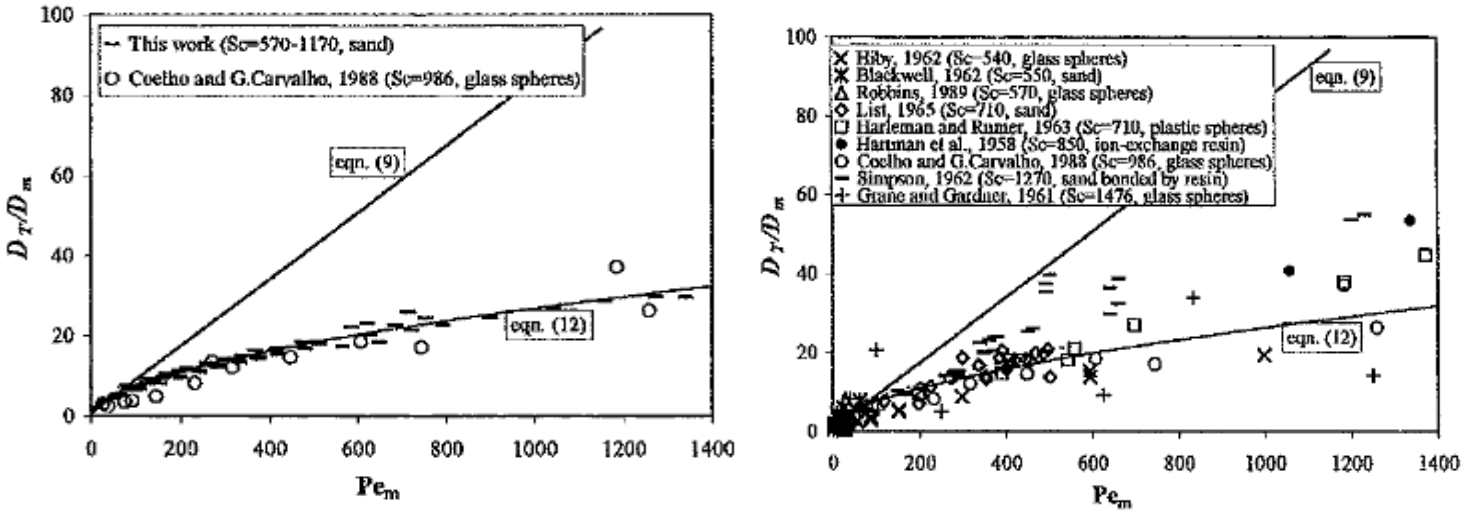

Figure 2.2.4. Comparison data for Sc > 500 (Guedes de Carvalho & Delgado, 2000).

The authors note the strong dependence of D_T/D_m on Sc in the range 140 < Sc < 500, and show that dispersion behavior is generally independent of particle size. While the correlations listed above show reasonably good agreement with prior experimental data, this work neglects the near-wall effect that is critical in low N fixed beds.

In a later work by Delgado (2007), both longitudinal and transverse dispersion in porous media was studied over a wide range of the Schmidt and Peclet numbers, giving rise to newer correlations for both axial and radial dispersion coefficients with improved accuracy.

After an exhaustive compilation of experimental data for flow in porous media, the author supplies a set of equations each for the longitudinal and transverse dispersion coefficients, subdivided by different regimes of dispersion based on the Peclet number: (1) diffusion regime ($Pe_m < 0.1$), (2) predominant diffusional regime ($0.1 < Pe_m < 4$), (3) predominant mechanical dispersion ($4 < Pe_m$ and $Re < 10$), (4) pure mechanical dispersion ($10 < Re$, $Pe_m < 10^6$), and (5) dispersion beyond the validity of Darcy's law ($Pe_m > 10^6$). The table below, adapted from the article, summarizes the equations for liquid flow through porous media:

Table 2.2.1. Correlative equations for longitudinal and transverse dispersion coefficients (Delgado, 2007).

Regime of Dispersion	Longitudinal Dispersion	Transverse Dispersion
Diffusion	$\frac{D_L}{D'_m} = 1$	$\frac{D_T}{D'_m} = 1$
Predominant diffusion	$\frac{D_L}{D'_m} = \frac{Pe'_m}{\frac{0.8}{Pe'_m} + 0.4}$	
Predominant mechanical dispersion, Sc < 550	$\frac{D_L}{D'_m} = \frac{Pe'_m}{\sqrt{18{Pe'_m}^{-1.2} + 2.35Sc^{-0.38}}}$	$\frac{D_T}{D'_m} = 1 + \frac{1}{2.7 * 10^{-5}Sc + \frac{12}{Pe'_m}}$
Predominant mechanical dispersion, Sc ≥ 550		$\frac{D_T}{D'_m} = 1 + \frac{1}{0.017 + 14/Pe'_m}$
Pure mechanical dispersion, Sc < 550	$\frac{D_L}{D'_m} = \frac{Pe'_m}{\frac{25Sc^{1.14}}{Pe'_m} + 0.5}$	$\frac{D_T}{D'_m} = \frac{Pe'_m}{(0.058Sc + 14) - (0.058Sc + 2)\exp\left(-\frac{500Sc^{0.5}}{Pe'_m}\right)}$
Pure mechanical dispersion, Sc ≥ 550		$\frac{D_T}{D'_m} = \frac{Pe'_m}{45.9 - 33.9\exp\left(-\frac{21Sc}{Pe'_m}\right)}$
Beyond Darcy's law	$\frac{D_L}{D'_m} = \frac{Pe'_m}{2}$	$\frac{D_T}{D'_m} = \frac{Pe'_m}{12}$

The figures below show a comparison between experimental data for longitudinal dispersion coefficients (Figure 2.2.3) and transverse dispersion coefficients (Figure 2.2.4):

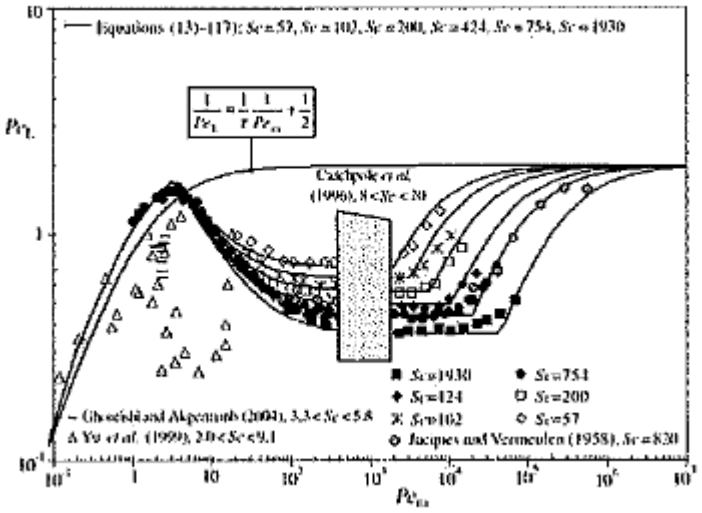

Figure 2.2.5. Comparison between experimental data and correlations, for longitudinal dispersion (Delgado, 2007).

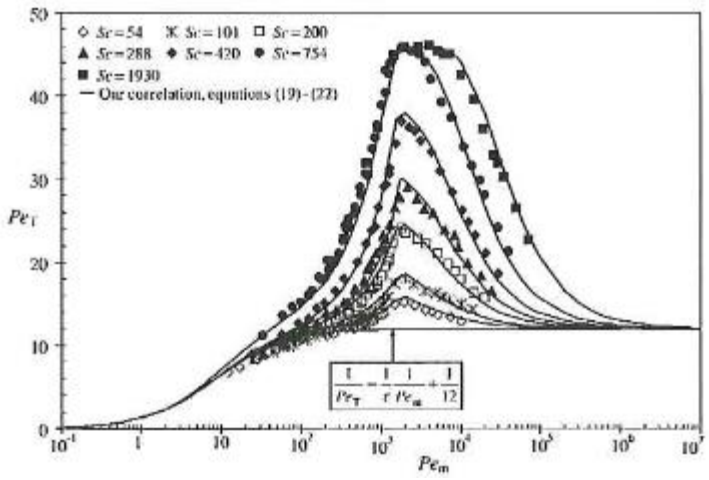

Figure 2.2.6. Comparison between experimental data and correlations, for transverse dispersion (Delgado, 2007).

While this paper presents important correlative equations for dispersion, data was compiled largely from experimental data with beds above the low N range ($2 < N < 8$).

A modeling study by Schnitzlein (2001) evaluated radial dispersion in packed beds by a transverse tracer injection at a specific axial position in the bed. In these simulative experiments, a reactor with an aspect ratio of $d_t/d_p = 10$ was used, modeled as a two dimensional, radially symmetric, pseudo-homogenous

medium. Schnitzlein accounts for wall effects of the cylindrical bed according to the correction term given by Fahien and Smith (1955):

$$Pe_r = \frac{u_0 d_p}{D_r} \frac{1}{1+19.4\left(\frac{d_p}{d_t}\right)^2} \tag{2.8}$$

In the paper, Schnitzlein defines fluid-mechanical dispersion as convective diffusion resulting from packing structure: eddy diffusion (local voids act as mixing cells), branching in the packing, and channeling due to the placement of particles and the wall effect. This work showed an increase in fluid-mechanical radial Peclet numbers for the range: 1 < Re < 1000, approaching an asymptotic value after Re = 75, as shown in the figure below:

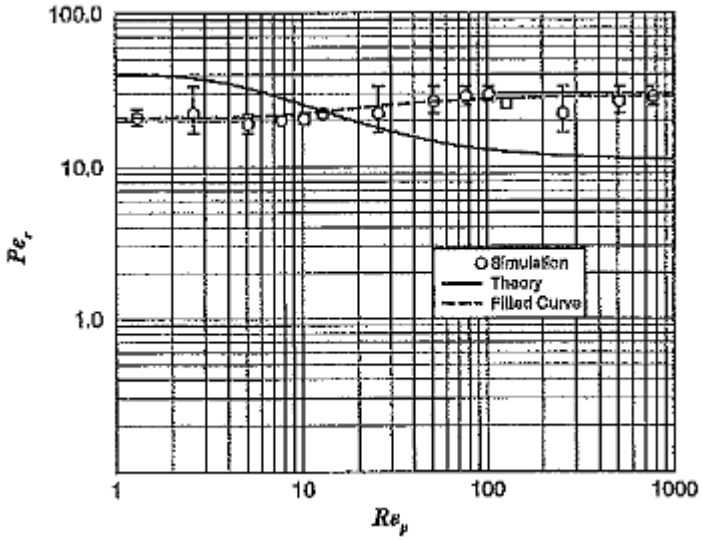

Figure 2.2.7. Fluid-mechanical Peclet numbers (Schnitzlein, 2001).

Schnitzlein reports this increase is due to branching and channeling effects in the bed, and it is also noted that the asymptotic value for radial Peclet number is more than twice that of experimentally obtained values. He concludes that previous experimental studies modeled radial dispersion via Fickian diffusion with effective dispersion coefficients that are dependent on the Reynolds number, where his model here accounts for fluid-mechanical dispersion that is dependent solely on packing structure and not a concentration gradient.

Magnico (2003) simulated beds of N = 5.96 and 7.8 consisting of 326 and 620 spheres, respectively, with a focus on near-wall effects on radial dispersion. The author used particle tracing to study near-wall phenomena via radial dispersion by removing flow effects due to molecular diffusion. The author states that a boundary layer exists near the wall, with a thickness of $d_p/4$, at low Re (Re = 7). At higher flows, namely Re = 200, the author admits that mesh resolution used in the study was too coarse to obtain dispersion profiles. However, at high Reynolds numbers, traced particles were not easily transported through the present boundary layer formed along the wall, signifying a molecular diffusion-dominated mechanism of mass transfer in this area.

Allain (2011), completed a study of dispersion using CFD models of fixed beds (N = 5.96, 7.99) of spheres. To quantify both axial and radial dispersion coefficients, a small cylinder of methane, acting as a tracer, was implemented at the inlet of the bed. Concentration profiles of methane at various axial positions in the bed, in addition to Peclet numbers, were gathered and compared to those given by proposed correlations in the literature. An analysis of the results showed that a tracer positioned at the point of axial symmetry in the bed (i.e., the centerline) did not allow for a complete analysis of near-wall dispersion phenomena, given that the rate of methane dispersion in the radial direction was much smaller relative to axial dispersion, due to the entrance velocity. However, Allain showed for beds of N = 5.96 and 7.99 that inclusion of velocity profiles as functions of radial position, rather than as a constant, resulted in a model that predicted higher axial dispersion.

In a very recent study by Jourak et al. (2014), radial dispersion coefficients were derived by supplying 3-D concentration profiles to a 2-D effective porous medium model, and fitting the coefficients to the data. Their simulative experiments used a bed of regular and randomly packed particles, with a fixed concentration boundary condition at the tube wall, to mimic earlier tracer injection experiments. Results were presented for laminar flow with $0.1 < Re < 100$. The researchers recommended using beds of large width and length, noting that radial dispersion coefficients showed some length dependency. That is, the radial dispersion coefficient was found to decrease as the length of the bed increased. They also note that a 2-D effective medium approach typically predicts dispersion coefficients higher in magnitude than the 3-D counterpart. This is due to higher intercellular fluid motion in the lateral direction, and therefore a higher radial dispersion coefficient.

Dispersion in packed beds of low N is an area of research that demands attention. Previous studies of radial dispersion typically neglect the presence of the tube wall, and these studies are generally conducted in beds of large N. The development of the diffusion-dominated boundary layer induces significant flow effects in

the bed, and research that includes this additional dispersion mechanism is important. In a review of previous studies, liquid phase flows were typically the fluid of interest in experimental situations. It is therefore important to study dispersion in a gas-phase system, and one in which the flow is laminar, but outside of the low Re (< 100) flow regime. Experimental tracer injections are highly erroneous when deriving dispersion coefficients: concentration data points are selected from few radial positions, and beds of long length are studied which yield concentration profiles with small gradients. It is therefore important to study dispersion in beds of developing flow also, in which a clear and total picture of the radial concentration profile is included.

3. Computational Methodology

3.1 Introduction

Computational Fluid Dynamics (CFD) is a computer modeling technique that uses numerical methods to simulate fluid flow, mass and heat transport, reaction kinetics, and structural mechanics, among other physical phenomena. With the continued growth of computational resources and available computer power, CFD is now used as an important tool for experimental validation and predictive analysis in fields such as automotive design, reaction engineering, microfluidic analysis, and oil and gas industries, among others.

The following chapter provides a review on the numerical methods offered by FLUENT 14.5, the commercial CFD code used in this study. In subsequent sections, a detailed methodology of the computational approach used to simulate dispersion in packed beds is given. A section describing the optimization studies using the finite element method commercial solver COMSOL Multiphysics is also included.

3.2 Theory

FLUENT utilizes finite volume analysis for simulation of various physics. In finite volume methods, numerical solutions to various generalized balances for fluid flow and species transport are obtained over a number of small control volumes. The collection of all control volumes, referred to as the mesh or computational grid, represents the real-scale geometry being simulated. By supplying necessary boundary conditions and an initial, estimated solution for the system under investigation, a complete numerical solution can then be obtained. The following sections are taken from the FLUENT user manual produced by ANSYS, Inc. (2011).

3.3 Fluid Mechanics

To describe fluid transport, FLUENT solves the continuity (mass conservation) and Navier-Stokes (momentum conservation) equations iteratively for each control volume in the geometry.

The general equation for continuity of mass is given by the following partial differential equation:

$$\frac{\partial \rho}{\partial t} + \nabla \cdot (\rho \vec{u}) = S_m \tag{3.1}$$

The source term S_m is mass added to the continuous phase through user-defined sources or through phase changes. For simulations completed in this study, this term was zero. The time-dependent term on the left describes transient flows and was also zero in this study, given that each simulation was at steady-state.

A momentum balance for a fluid in a non-accelerating reference frame in three dimensions is given by the generalized Navier-Stokes equation:

$$\frac{\partial}{\partial t}(\rho \vec{u}) + \nabla \cdot (\rho \vec{u}\vec{u}) = -\nabla \mathrm{p} + \nabla \cdot (\bar{\bar{\tau}}) + \rho \vec{g} + \vec{F} \tag{3.2}$$

In the above equation, p is the static pressure, and the term $\rho \vec{g}$ represents the gravitational body force. The last term $\vec{F}$ is used for external body forces acting on the fluid, and in this study was zero.

The stress tensor $\bar{\bar{\tau}}$ is defined as:

$$\bar{\bar{\tau}} = \mu \left[(\nabla \vec{u} + \nabla \vec{u}^T) - \frac{2}{3} \nabla \cdot \vec{u} \bar{\bar{I}} \right] \tag{3.3}$$

Where μ is the molecular viscosity, $\bar{\bar{I}}$ is the identity tensor, and the second term on the right gives the effect of volume dilation due to fluid motion.

3.4 Chemical Species Transport

FLUENT computes the chemical species mass fraction Y by solving the general form of the convection-diffusion equation for the i^{th} species:

$$\frac{\partial}{\partial t}(\rho Y_i) + \nabla \cdot (\rho \vec{u} Y_i) = -\nabla \cdot \vec{J}_i + R_i + S_i \tag{3.4}$$

The last two terms on the right R_i and S_i denote the rate of generation of species *i* by chemical reaction, and the rate of addition of species *i* through user-defined sources, respectively. Both were zero in this study.

The term $\vec{J}_i$ accounts for species diffusion flux that occurs from a concentration gradient and is as follows:

$$\vec{J}_i = -\rho D_{i,m} \nabla Y_i \tag{3.5}$$

Where $D_{i,m}$ is the diffusion of species *i* in the mixture *m*. To obtain the diffusion coefficient, FLUENT by default assumes Fickian diffusion under the dilute approximation method.

3.5 Energy Balance

FLUENT enables the solution of the energy equation whenever species transport is modeled. The general form of the energy balance is as follows:

$$\frac{\partial}{\partial t}(\rho E) + \nabla \cdot \left(\vec{u}(\rho E + p)\right) = \nabla \cdot \left(k_{eff} \nabla T - \sum_j h_j \vec{J_j} + \left(\bar{\bar{\tau}}_{eff} \cdot \vec{u}\right)\right) + S_h \tag{3.6}$$

Here, k_{eff} is the effective conductivity. The four terms on the right describe heat transfer due to conduction, via species diffusion, by viscous dissipation, and through user-defined sources or by heat of reaction. In these studies, however, only isothermal flow was modeled, and the energy equation was decoupled from the solution of the species and fluid transport equations.

3.6 Numerics

FLUENT solves the relevant conservation equations of momentum, mass, and chemical species by the finite volume method which consists of first discretizing the geometry into control volumes that make up the computational grid (mesh). The governing equations listed above are then integrated over the control volumes to produce algebraic equations of the dependent variables of interest (i.e., pressure, velocity). Finally, these equations are discretized and solved to yield values of these dependent variables. This solution method is repeated iteratively until specified convergence criteria have been met and a complete solution is reached.

In a pressure-based segregated algorithm, which is the solver approach employed in this study, governing equations are solved one after another in the solution scheme illustrated below (adapted from the FLUENT user manual):

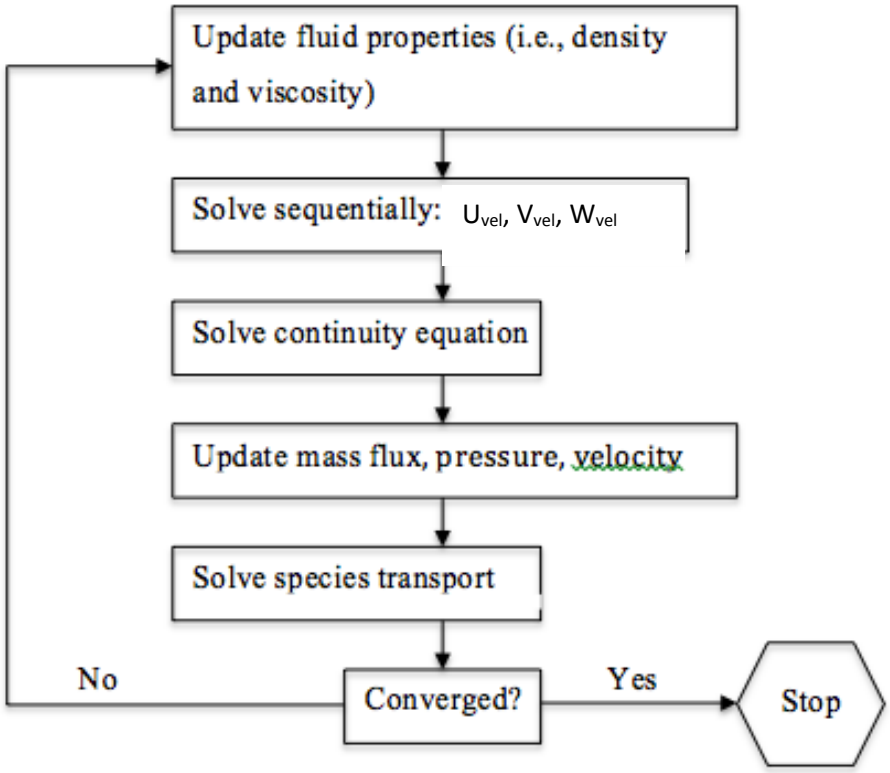

Figure 3.6.1. Solution scheme of pressure-based segregated algorithm (Fluent, 2011).

In this procedure, fluid properties are updated, after which each momentum equation is solved sequentially to obtain the velocity field. The continuity (pressure correction equation) is then solved. In the fourth step, face mass fluxes, pressure, and the velocity field are corrected. Finally, the species transport equations are then computed. This process is repeated until convergence criteria are met.

Discretization

In finite volume analysis, transport equations are transformed to algebraic equations that are solved numerically for a given control volume in the domain. This technique of dividing the geometric domain

into a computational grid is *discretization*. As adapted from the FLUENT user manual, the following is a general transport equation for a scalar:

$$\int_V \frac{\partial \rho \phi}{\partial t} dV + \oint \rho \phi \vec{v} \cdot d\vec{A} = \oint \Gamma_\phi \nabla \phi \cdot d\vec{A} + \int_V S_\phi dV \tag{3.7}$$

Where, ρ is the density, $\vec{v}$ is the velocity vector, $\vec{A}$ the surface area vector, Γ_ϕ the diffusion coefficient, and S_ϕ the source term per unit volume.

Discretization of this general equation gives:

$$\frac{\partial \rho \phi}{\partial t} V + \sum_f^{N_{faces}} \rho_f \vec{v}_f \phi_f \cdot \vec{A}_f = \sum_f^{N_{faces}} \Gamma_\phi \nabla \phi_f \cdot \vec{A}_f + S_\phi V \tag{3.8}$$

Where N_{faces} is the number of faces comprising the control volume, $\vec{A}_f$ is the area of the control volume face, and V is the cell volume.

The discretized equations are solved in each control volume, an example of which is pictorially shown below in two dimensions:

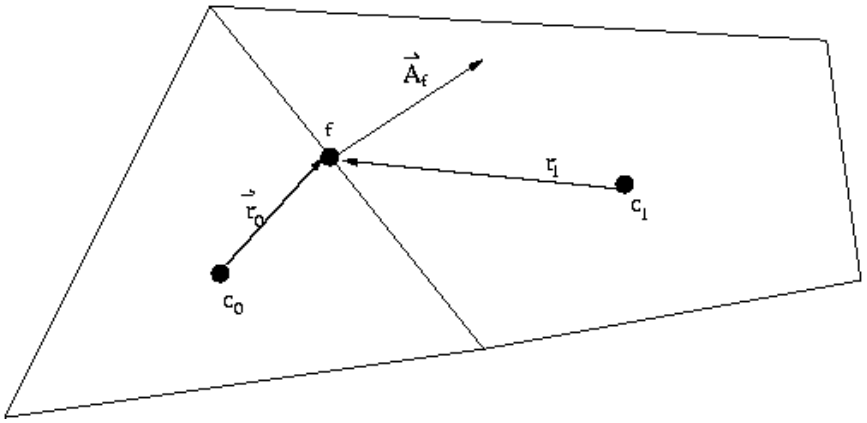

Figure 3.6.2. Two dimensional control volume showing discretization of the general scalar transport equation (Fluent, 2011).

Pressure-Velocity Coupling

Employing the segregated solver approach, the **S**emi-**I**mplicit **M**ethod for **P**ressure-**L**inked **E**quations (SIMPLE) algorithm was used for pressure-velocity coupling. In this algorithm, the momentum balances are solved with a guessed pressure field p*, and the resulting face flux, J^*_f is calculated from the following equation:

$$J_f^* = \hat{J}_f^* + d_f(p_{c0}^* - p_{c1}^*) \tag{3.9}$$

A correction term J_f' is added to the face flux to force it to satisfy continuity. According to the SIMPLE algorithm, the correction term is written as:

$$J_f = J_f^* + J_f' \tag{3.10}$$

$$J_f' = d_f(p_{c0}' - p_{c1}') \tag{3.11}$$

Where p' is the control volume pressure correction.

With these terms, the cell pressure and flux are corrected with the following equation to satisfy continuity:

$$p = p^* + \alpha_p p' \tag{3.12}$$

$$J_f = J_f^* + d_f(p_{c0}' - p_{c1}') \tag{3.13}$$

Here, α_p is the under-relaxation factor for pressure.

Under-Relaxation of Variables

Given the nonlinearity of the governing equations in these models, explicit relaxation by means of under-relaxation factors is used to control the value of a scalar that is passed to subsequent iterations:

$$\phi = \phi_{old} + \alpha\Delta\phi \tag{3.14}$$

Here, α represents the under-relexation factor, and ϕ_{old} is the cell value at the previous iteration. Under-relaxation factors were set such that stabilization of the solution, or plateauing of the residuals, occurred. Typically, default values for under-relaxation factors given by FLUENT were adequate for these simulations.

3.7 Meshing

Eight beds of varying N were studied, each with spherical particles, of uniform one inch size, using the "caps" contact point modification. Simulating only fluid transport mechanisms, the shells method (i.e., meshing of only the fluid domain) was employed. In this method, a cylinder of height 0.0202 inches formed the capped area subtracted from a particle-particle contact point. At the wall, this cylinder was 0.0242 inches. Boundary layers extended from the particle surface were 2 x 0.001 inch thick. Tetrahedral cells characterized the fluid domain, meshed at 0.05 inches.

The table below summarizes the bed geometries:

Table 3.7.1. Summarized reactor geometry.

N	L/d_p	No. spheres
5.04	50.13	1000
5.45	40.12	1000
5.96	36.36	1080
6.40	31.97	1113
7.04	29.18	1200
7.44	26.63	1250
7.99	23.15	1250
9.30	17.01	1250

Each bed consisted of three sections. The first is an empty section spanning 0.0762 m from the entrance of the bed, denoted as the "calming section." The following is the packed section, whose length is specified in Table 3.7.1. The final section is another empty section, 0.254 m in length, used to mitigate backflow effects near the exit of the bed. The following image is of the N = 5.04 bed:

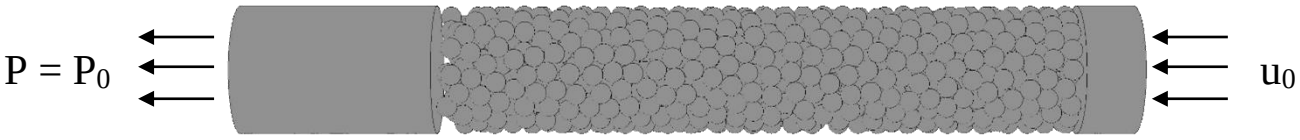

Figure 3.7.2. Geometry of the N = 5.04 packed bed.

3.8 Boundary Conditions

Flow Field Development

To obtain velocity profiles in the bed, a velocity-inlet boundary condition was set normal to the inlet of the bed, corresponding to four particle Reynolds numbers used in this study, namely 87, 348, 696, and 870. Air was specified as the fluid in the bed, with constant properties for isothermal conditions (i.e., $\mu = 1.7894e\text{-}5$ *kg/m/s,* $\rho = 1.225 kg/m^3$). A pressure-outlet condition was specified at the exit of the bed as atmospheric pressure. No-slip boundary conditions were assigned to the tube walls.

Species Transport Modeling

In an effort to model dispersion, and more specifically near-wall effects in low N beds, a methane species mass fraction condition was set as unity at the reactor walls, five particle diameters from the start of packing (axially) to the end of the packed section. This was done simply in FLUENT by adapting the mesh axially between these two bounds and specifying a methane mass fraction on the column wall. The velocity and pressure boundary conditions from velocity field development simulations remained unchanged in these studies.

3.9 Solvers

In each simulation, the SIMPLE method for pressure-velocity coupling was chosen. The Least Squares cells approach was selected for the gradient method. For spatial discretization, the first-order upwinding scheme was chosen for pressure, momentum, and species for the first 200 – 300 solution iterations. From there, it was switched to second-order upwinding for the remainder of the solution.

3.10 Convergence

Solution convergence was attained by ensuring that column pressure drop remained constant over at least 1000 iterations. For species transport, a monitor was added to a 2 mm isosurface at the end of the packed section to track methane concentration per iteration step. Once the concentration was no longer monotonically increasing (i.e., plateaued), the solution was deemed converged. A complete solution for a single case required approximately 15, 000 to 20, 000 iterations, with solution times averaging 1000 iteration steps per 12 hours. All simulations were completed on a Dell R620 PowerEdge Server running a Windows server 2008 R2 operating system. The server contained 2 Intel Xeon E5-2680 CPUs, each with 8 cores, and 128 GB of RAM.

3.11 Post-processing

To obtain velocity and methane concentration profiles, isosurfaces of constant mesh were generated in FLUENT at radial positions spanning the column diameter. Isosurfaces for velocity were aligned axially with the bed, and clipped five particle diameters from the start of bed packing and three particle diameters before the end of packing, to prevent any flow-development effects on velocity calculations. Isosurfaces for methane concentrations were created similarly, with those surfaces clipped to 2 mm giving methane

concentration profiles across the diameter of the bed. Area-weighted averages were performed within FLUENT to collect both data sets for all runs.

3.12 Optimization

To obtain dispersion coefficients based on 3D simulation results from FLUENT, the finite element commercial code produced by COMSOL Multiphysics was used.

This model was set up as a two-dimensional, axisymmetric geometry, of the same diameter and length of beds used in the FLUENT runs. Within COMSOL, in the physics model tree, Transport of Diluted Species and the Optimization modules were added.

Geometry

A snapshot of the geometry is pictured below:

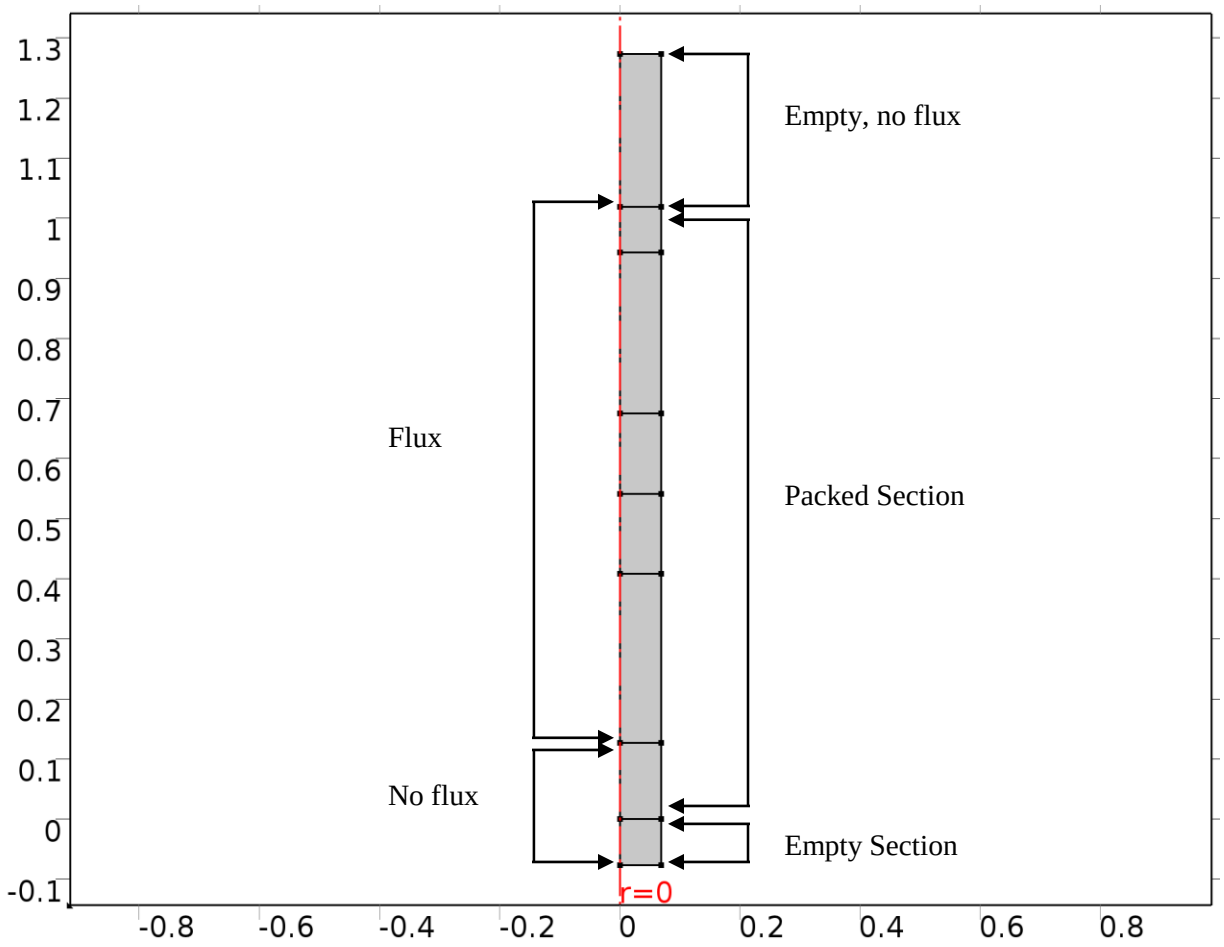

Figure 3.10.1. Two dimensional representation of packed bed in COMSOL Multiphysics.

The radius of the beds simulated in COMSOL was equivalent to those in FLUENT. The bed was sectionalized according to boundary conditions and the assignment of objective functions. In the image above, the first two and very last sections of the bed represent those areas that were not assigned a species wall boundary condition. These correlate to the empty sections at the beginning and end of the bed. The "flux" section represents the portion of the three-dimensional model that was assigned as a mass fraction of methane. In the two-dimensional model, a flux condition is instead assigned, as explained in the following section. The horizontal internal boundaries are not assigned boundary conditions, rather they are positioned at heights for assigning objective values for optimization, to be discussed shortly. In these locations, pictured above as *z = 0.407995, 0.541705, 0.675415, and 0.942834*, concentration data from FLUENT was extracted and used as the data set for fitting of radial dispersion coefficients. These bed depths varied for each N, and are specified fully in Appendix A, Reactor Data Sheets.

Boundary Conditions

The following model was solved:

$$-v_0(r)\frac{\partial c_i}{\partial z} + D_r\left(\frac{\partial^2 c_i}{\partial r^2} + \frac{1}{r}\frac{\partial c_i}{\partial r}\right) + D_a\frac{\partial^2 c_i}{\partial z^2} = 0 \qquad (3.15)$$

With v_0 being the interstitial velocity.

Subject to the following boundary conditions:

$z = 0,$ $\quad c_i = 0$

$r = R,\ z = [0.126845, L_p]$ $\quad -\vec{n}\cdot\ \vec{N} = \frac{Bi_m D_r}{R} * (c - c|_{r=R})$

$z = L,$ $\quad -\vec{n}\cdot\ D_i\nabla c_i = 0$

$r = R,\ z = [-0.0762, 0.126845], [L_p, L]$ $\quad -\vec{n}\cdot\ \vec{N} = 0$

The first condition represents the inflow of pure air, with a zero concentration of methane. The second condition represents the methane flux assigned at the wall for the length of the packed section, where L_p is the height at which the bed packing ends. Note the inclusion of the Biot mass transfer number, used in predicting the development of a diffusion boundary layer along the wall. The following condition is outflow (no diffusive flux). The final condition imposes a no flux condition at the wall for the empty sections at the beginning and end of the bed, and for the small length of the packed section that was free from a species wall boundary condition in the three-dimensional model.

Under the convective-diffusion model node, the diffusion coefficients were specified as $v_0 d_p/D_r$ and $v_0 d_p/D_a$. In this way, transport of the solute in the bed would be controlled by the dispersion coefficients.

Interstitial velocity as a function of radial position was supplied to the model directly from FLUENT, interpolated by COMSOL for those isosurfaces not processed by the 3D models. Radial symmetry was imposed at r = 0 for all z.

Computational Mesh

A global triangular mesh was assigned to the rectangular geometry. A boundary layer mesh was then added along the wall of the bed, to aid in resolving the no-slip boundary condition imposed on the FLUENT models. This prismatic boundary layer mesh extended typically 32 layers inward.

Mesh independence was assumed met when a global refinement of the grid produced a change in methane concentration profiles smaller than 2.0 %.

Optimization Solver

An optimization study was added to the model, coupled to the transport model. The Levenberg-Marquardt least-squares method was employed, which is used exclusively for parametric optimization. Under the optimization node, a single Least-Squares Objective was selected. A variable was assigned at the internal boundaries listed above for the use of objective functions. This variable represented the concentration of methane in the bed, along a constant bed height. A radial concentration of methane, extracted from the FLUENT models at the same bed height, was supplied as the data to which the dispersion coefficient would be fitted. Data from FLUENT was supplied to the model by file, and included a coordinate column for radial position, another for axial position, and the value of methane concentration at the specified coordinates. For a single optimization study, one bed depth was studied per Re and N. For each bed radius, four bed heights were studied at each Re. Two optimization control variables were selected, namely the radial Peclet number, and the Biot mass transfer number. Because the Biot number is called in a boundary condition, and the Peclet number in the calculation of the dispersion coefficient (i.e., $v_0 d_p / D_r$), the solver updates these two values continuously with each iteration, and passes the updated values to the input fields. The axial Peclet number remained constant at $Pe_a = 2$ in all runs. The study was complete when a minimization of the least-squares value of methane radial concentration was achieved and optimality tolerance (1e-6) was met

4. Results and Discussion

4.1 Flow Development

Establishing proper fluid flow and pressure drop in the bed was the first simulation step in FLUENT. The following results display the velocity profiles of the eight beds at the studied particle Reynolds number. Each plot contains axial interstitial velocity normalized by the superficial velocity assigned as a boundary condition at the bed entrance. Below each plot is the associated void fraction profile in the bed.

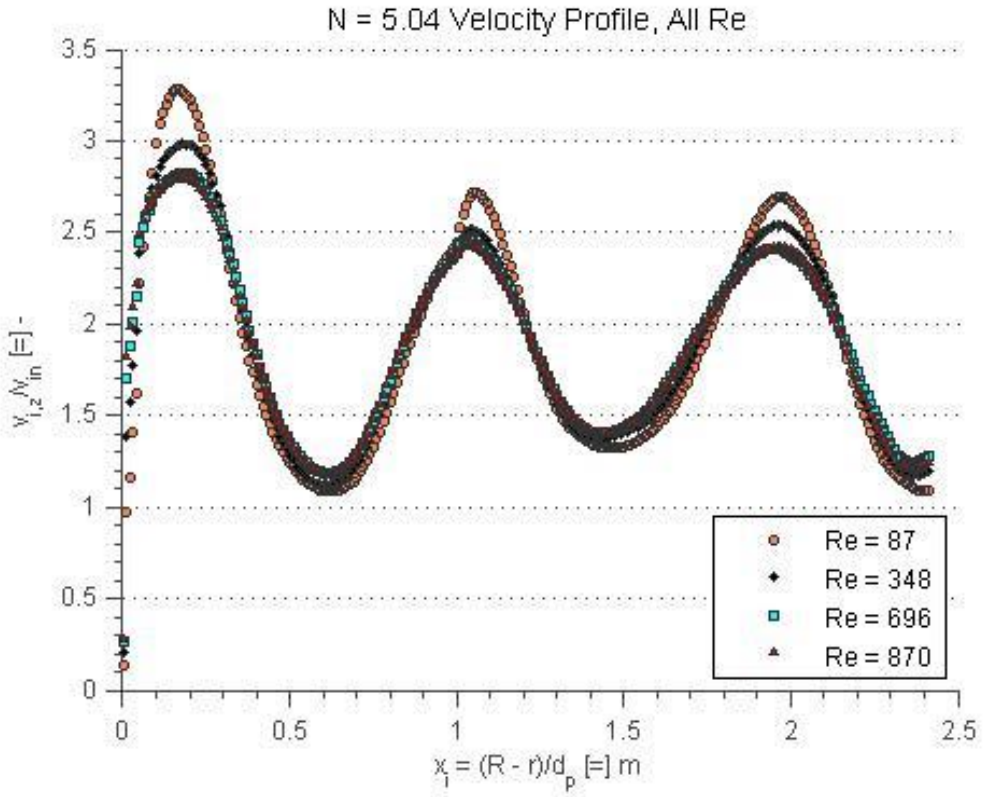

Figure 4.1.1. Velocity vs. Radial Coordinate, N = 5.04.

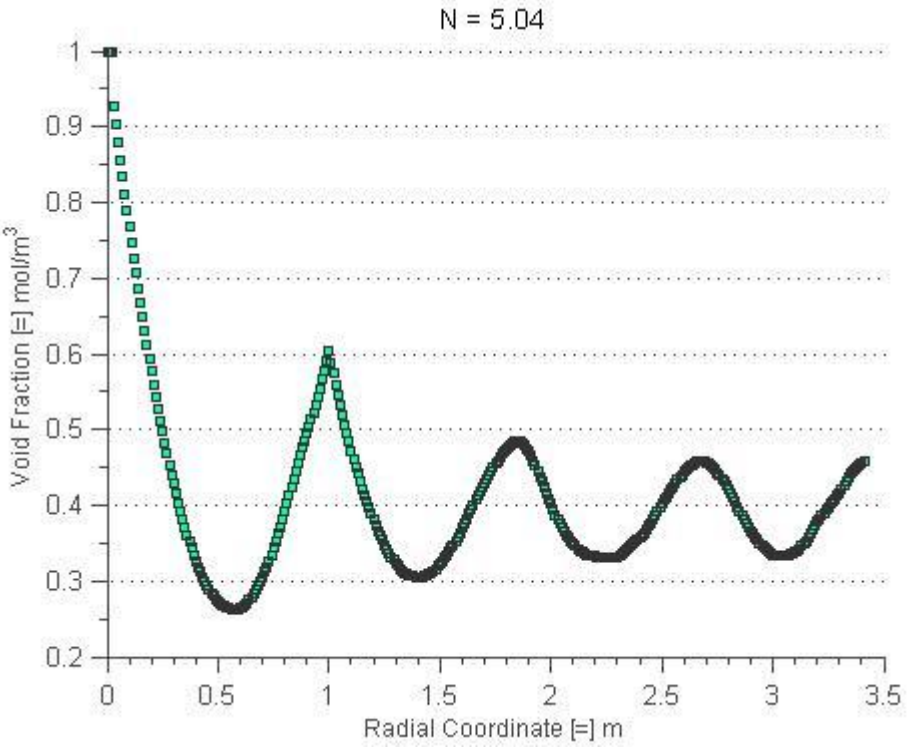

Figure 4.1.2. Void Fraction vs. Radial Coordinate, N = 5.04.

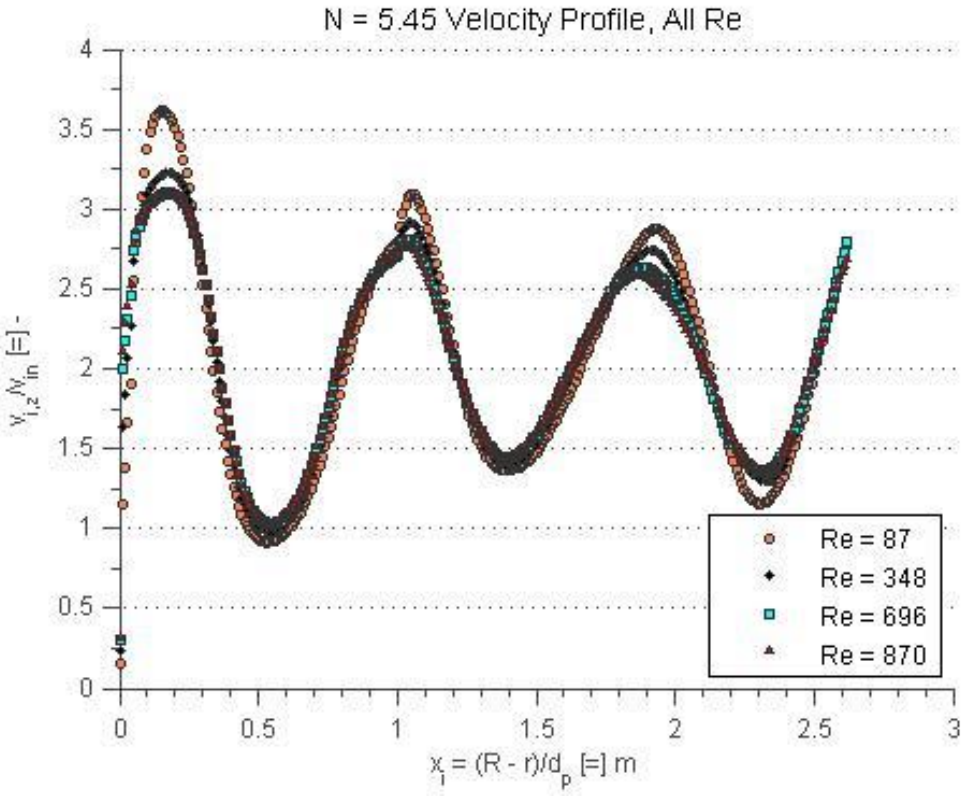

Figure 4.1.3. Velocity vs. Radial Coordinate, N = 5.45.

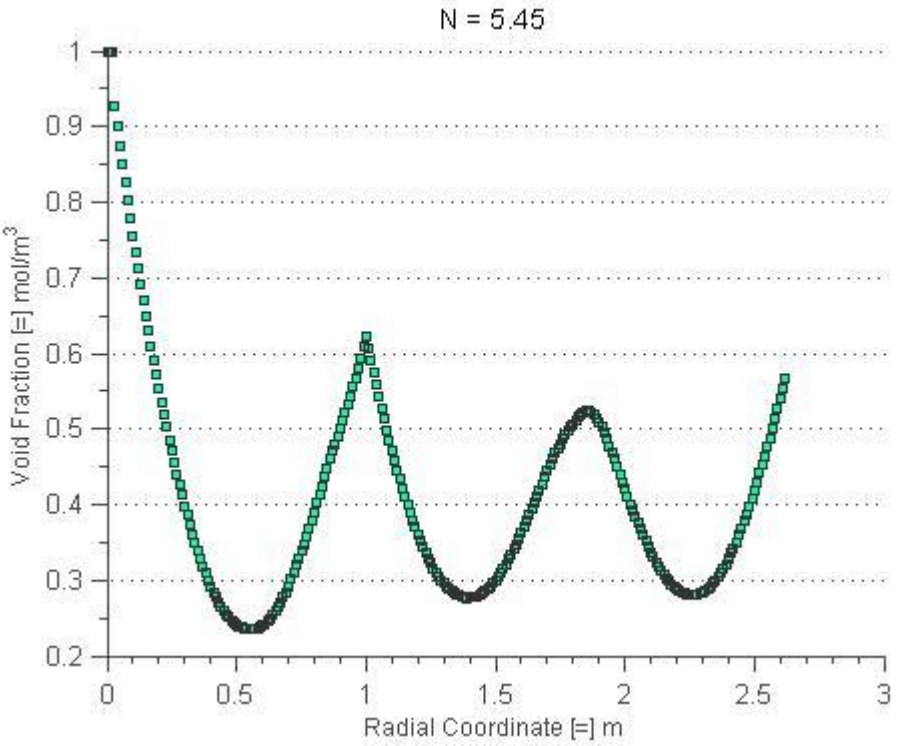

Figure 4.1.4. Void Fraction vs. Radial Coordinate, N = 5.45.

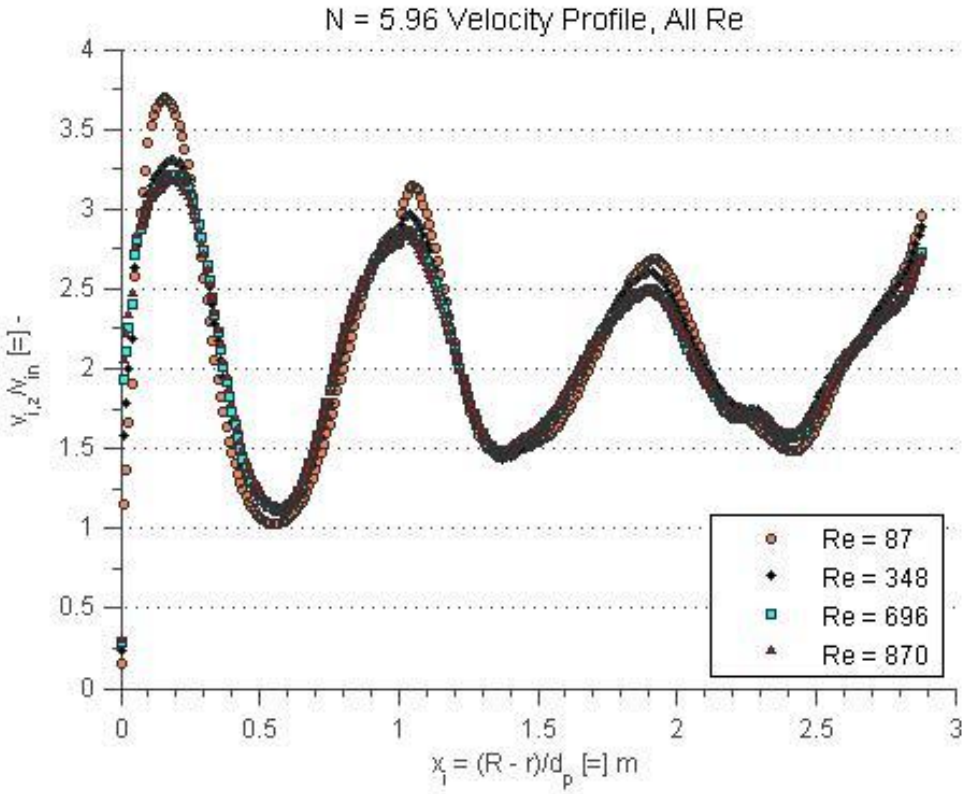

Figure 4.1.5. Velocity vs. Radial Coordinate, N = 5.96.

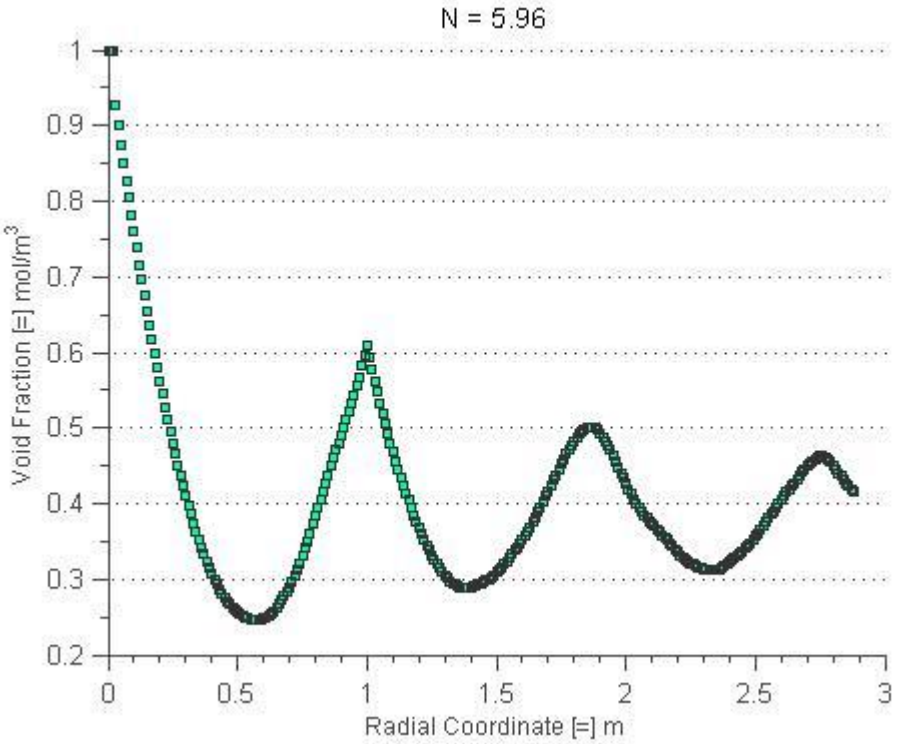

Figure 4.1.6. Void Fraction vs. Radial Coordinate, N = 5.96.

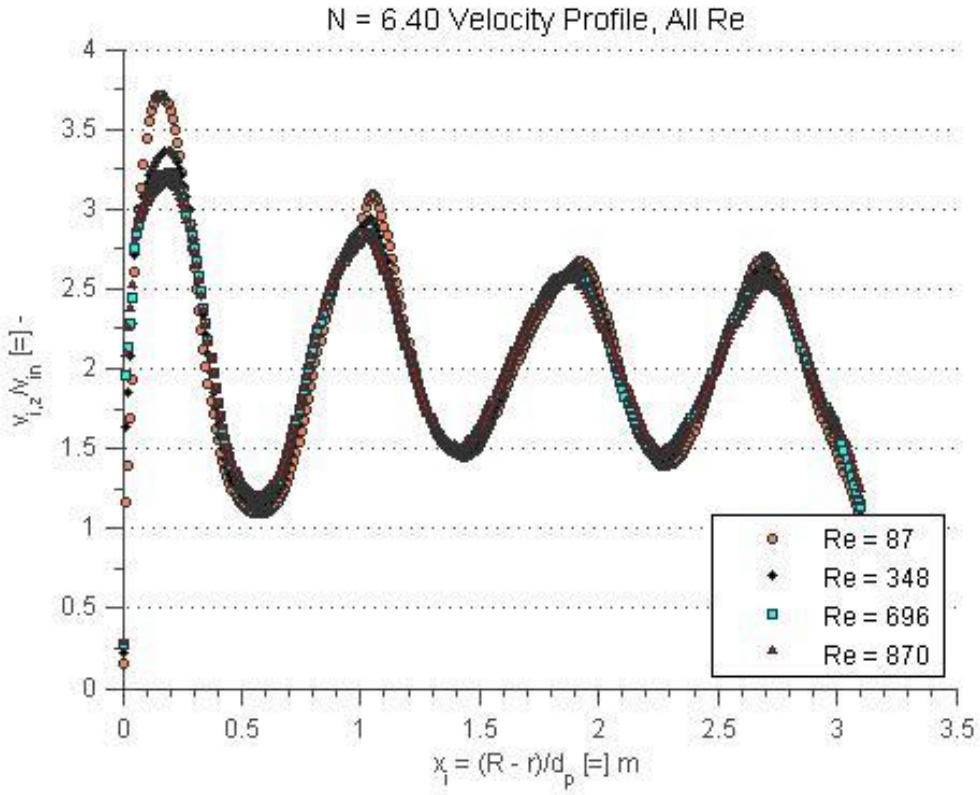

Figure 4.1.7. Velocity vs. Radial Coordinate, N = 6.40.

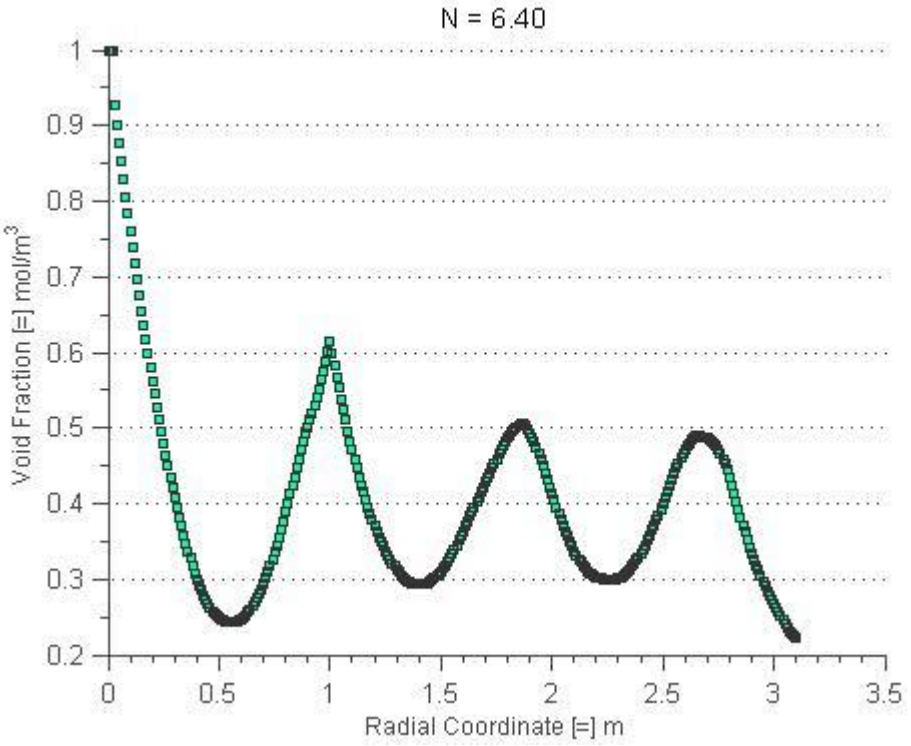

Figure 4.1.8. Void Fraction vs. Radial Coordinate, N = 6.40.

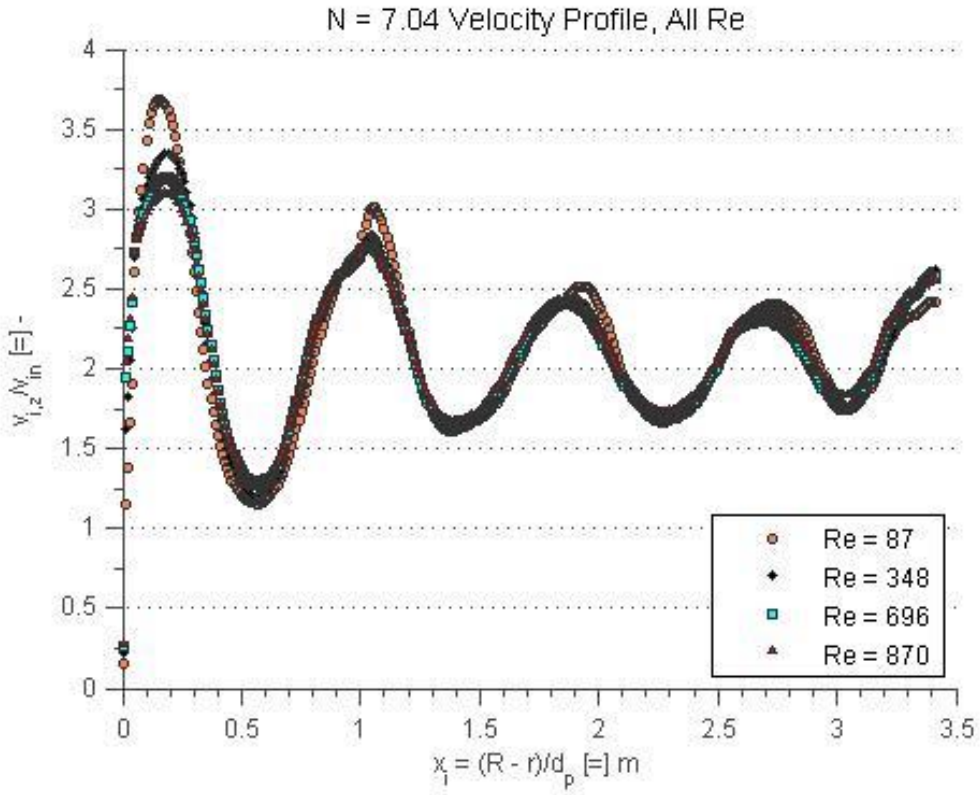

Figure 4.1.9. Velocity vs. Radial Coordinate, N = 7.04.

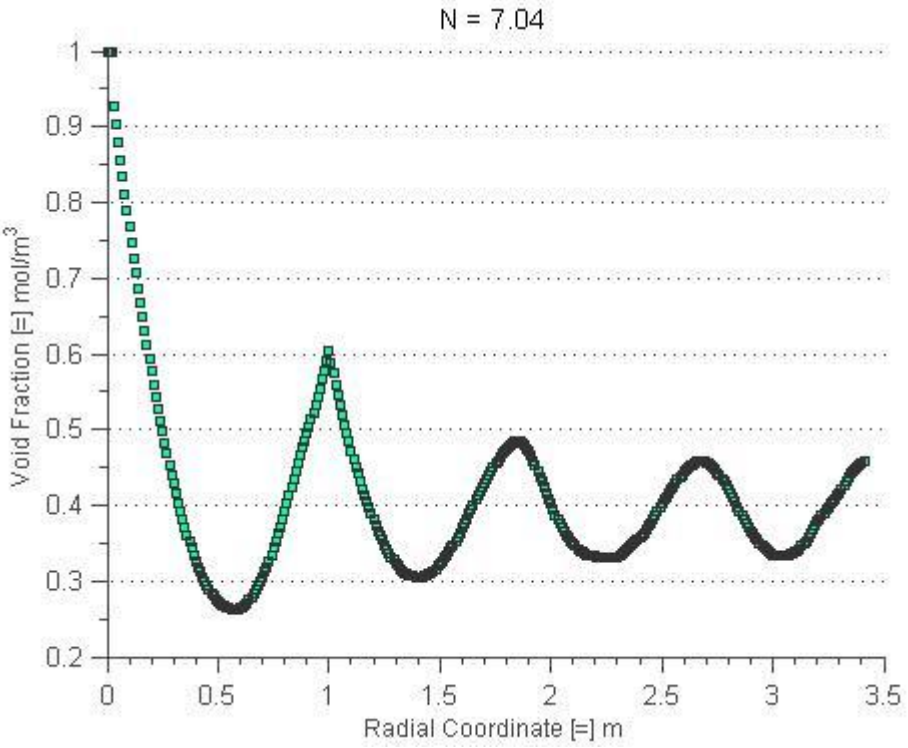

Figure 4.1.10. Void Fraction vs. Radial Coordinate, N = 7.04.

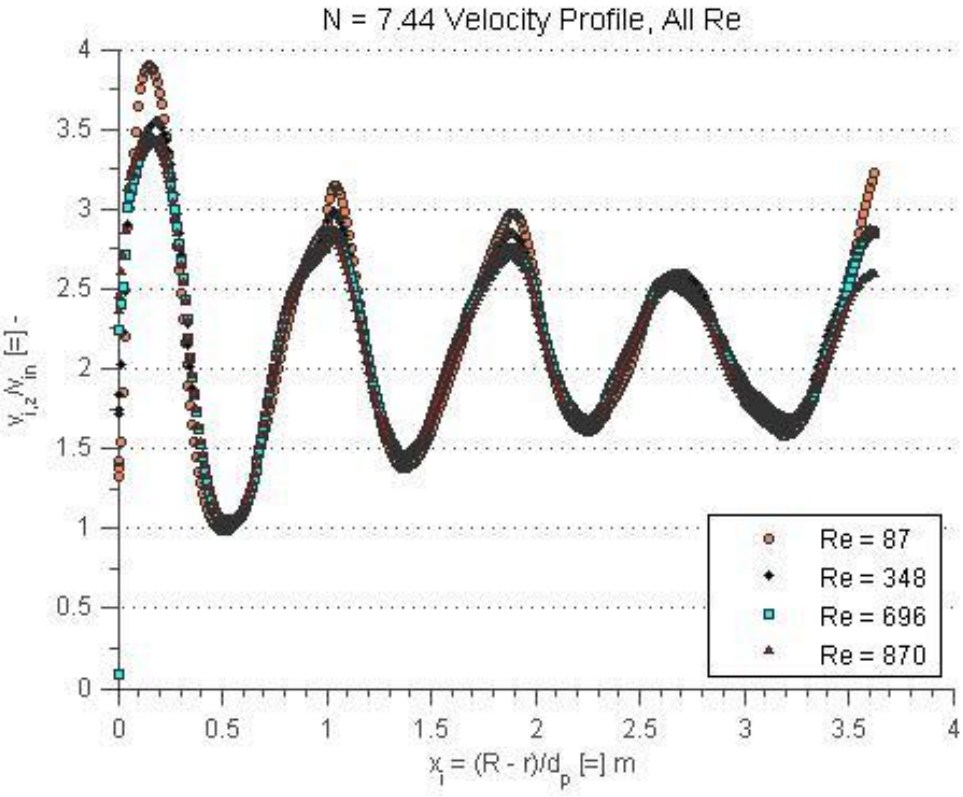

Figure 4.1.11. Velocity vs. Radial Coordinate, N = 7.44.

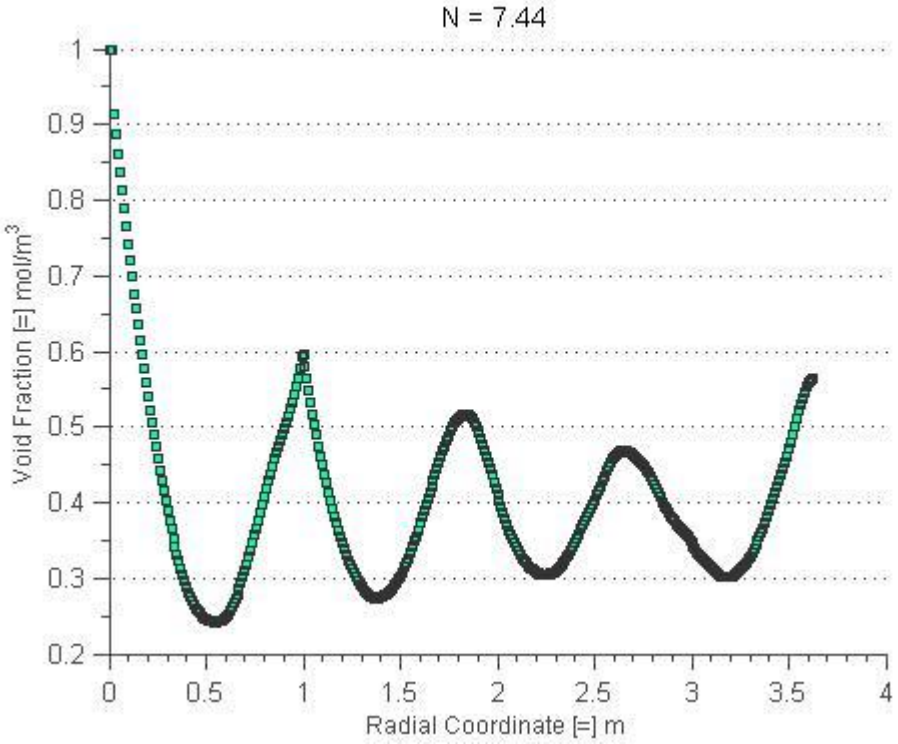

Figure 4.1.12. Void Fraction vs. Radial Coordinate, N = 7.44.

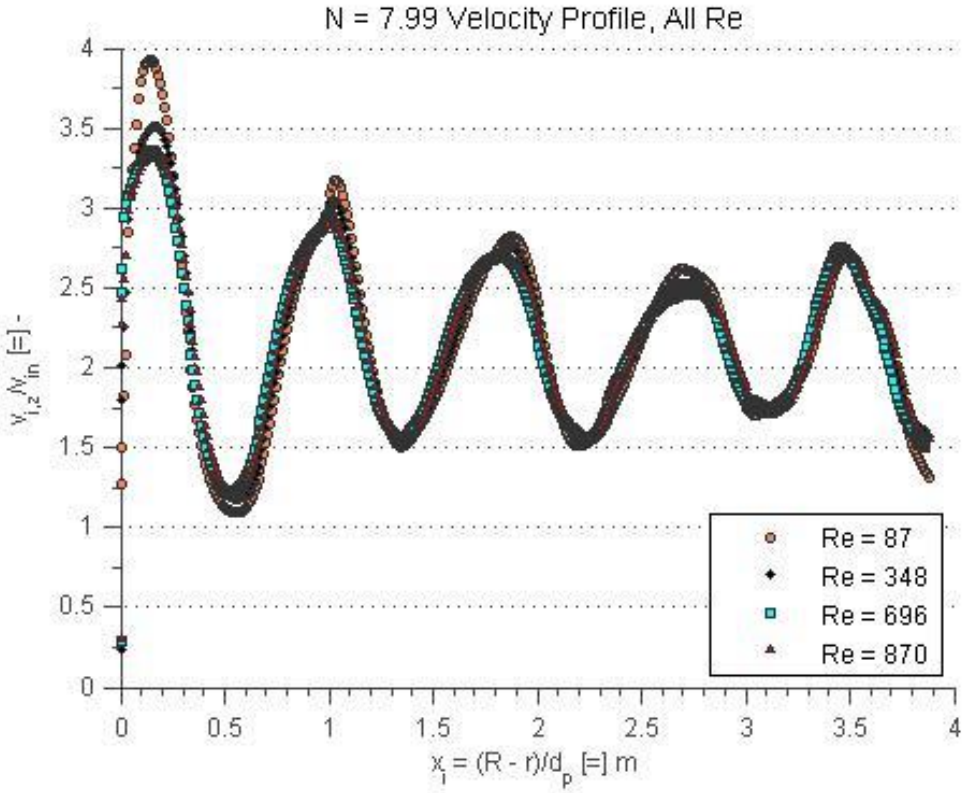

Figure 4.1.13. Velocity vs. Radial Coordinate, N = 7.99.

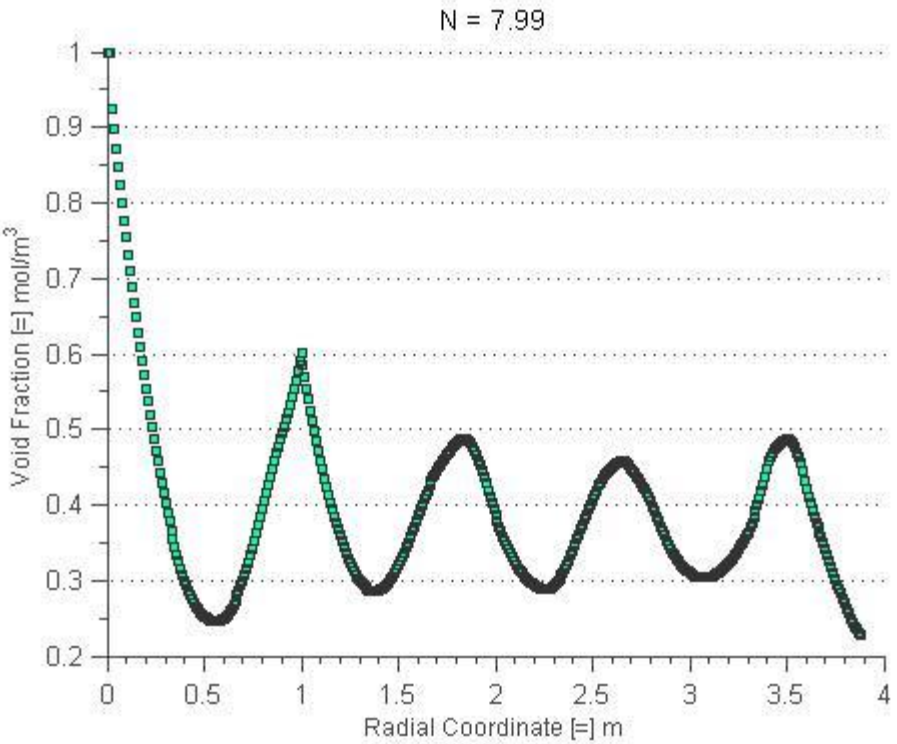

Figure 4.1.14. Void Fraction vs. Radial Coordinate, N = 7.99.

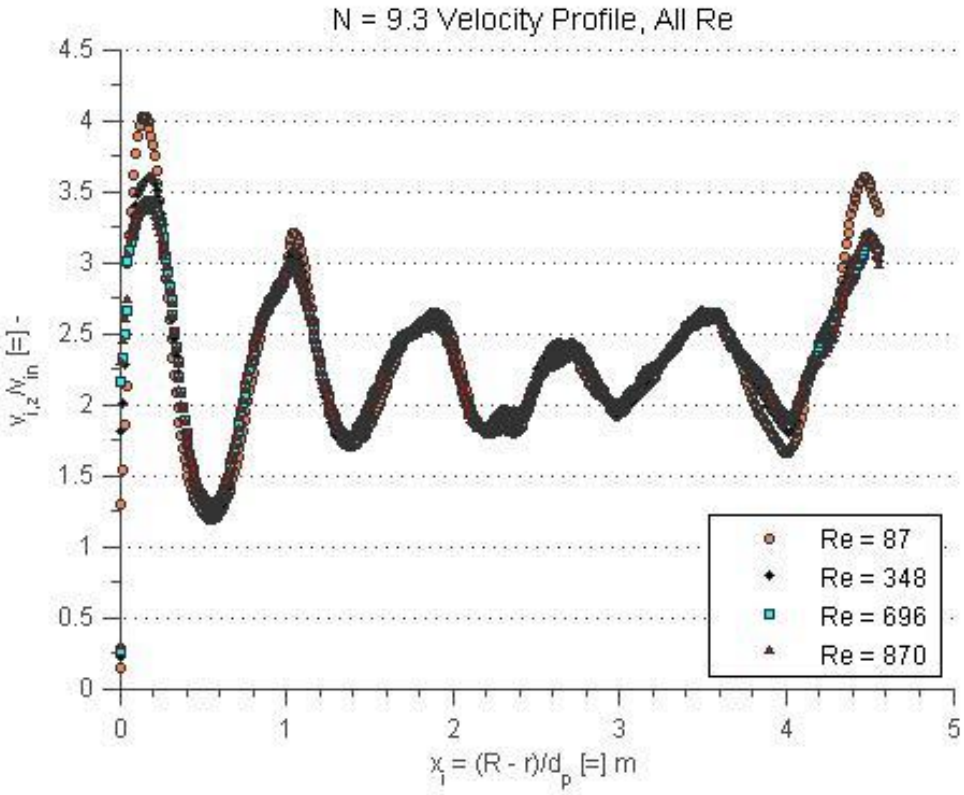

Figure 4.1.15. Velocity vs. Radial Coordinate, N = 9.30.

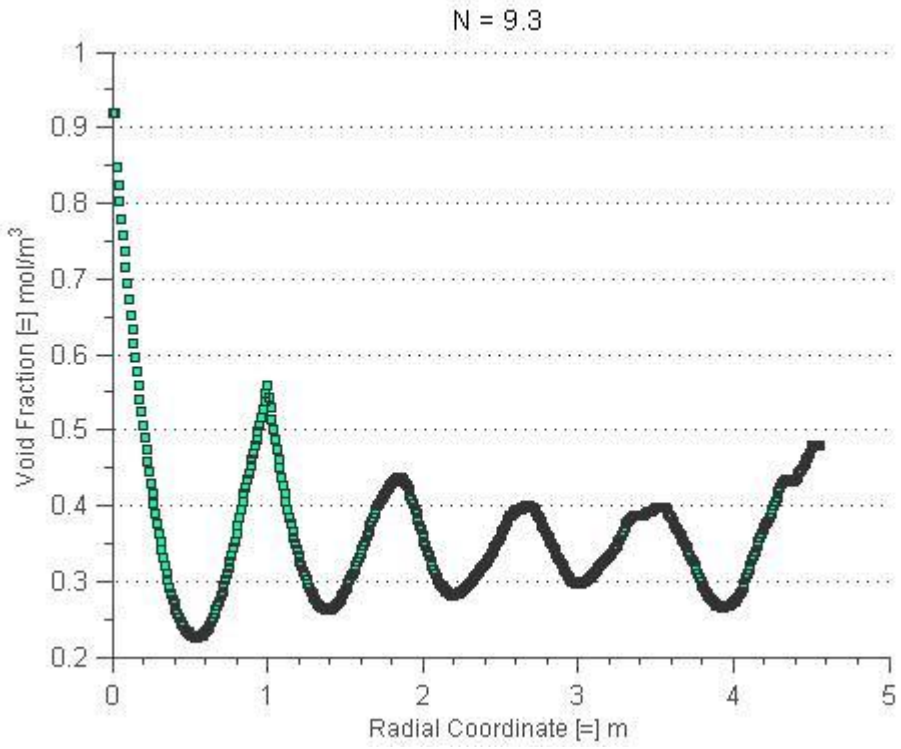

Figure 4.1.16. Void Fraction vs. Radial Coordinate, N = 9.30.

Consistently with each bed diameter, velocity at the lower limit Reynolds number (*Re = 87*) peaks higher than the remaining three velocity profiles, which are essentially coincident. This is likely due to viscous forces in the flow becoming more significant to inertial forces as the low Re flow regime is approached. It is also noted that velocities approach zero as the radial coordinate reaches the bed wall, owing to the no-slip boundary condition to which the tube wall was subjected. This zero-velocity region is the basis for the separation of the diffusion dominated boundary layer near the wall from the dispersion dominated flow in the rest of the bed. From a comparison of the void fraction profiles, higher axial velocities appear in areas of highest radial void fraction (i.e., low velocities in areas of low bed porosity, except in the near-wall vicinity). Near the wall, when the void fraction is close to unity, a channeling effect occurs, in which flow becomes uni-directionally parallel with a zero radial component of velocity. In this boundary layer area, resistance to mixing is strong, and, in the case of thermal beds, a resistance to heat transfer will simultaneously occur.

A validation for these porosity profiles was made by comparing some void fractions obtained by the CFD studies here to experimental studies of the same beds. The plot below is an example comparing void fraction as a function of radial coordinate from Giese et al. (1998). The succeeding table lists the void fractions

obtained for all beds used in this study, computed as the ratio of the void space divided by the empty tube volume, considering only the packed length.

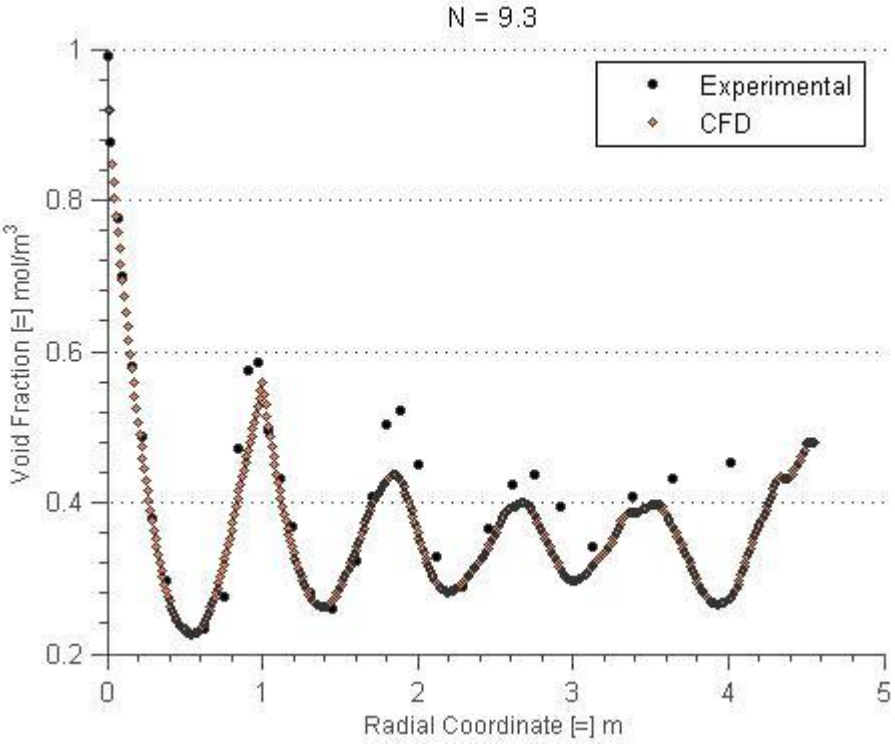

Figure 4.1.17. Void Fraction vs. Radial Coordinate, N = 9.30.

Table 4.1. Void Fraction of 3D Model Beds.

N	Global Void Fraction
5.04	0.484044
5.45	0.448155
5.96	0.451829
6.40	0.443431
7.04	0.457302
7.44	0.448329
7.99	0.448327
9.30	0.449104

4.2. Optimization

The following plots display the CFD results of radial concentration along with their fitted counterpart. Results are shown for a selected few N at various Reynolds numbers and bed depths. The optimization studies were conducted using the axial velocity profiles shown in Figures 4.1.1 – 4.1.15. The remaining profiles are given in Appendix C.

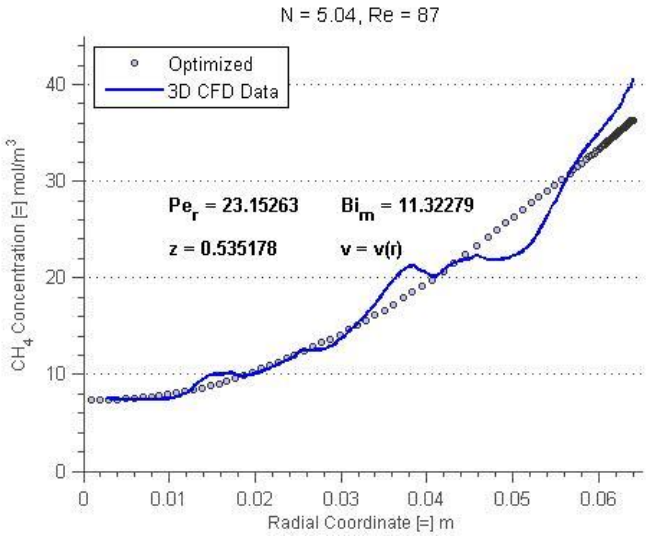

Figure 4.2.1. Fitted radial concentration profile for N = 5.04, Re = 87, bed depth 01.

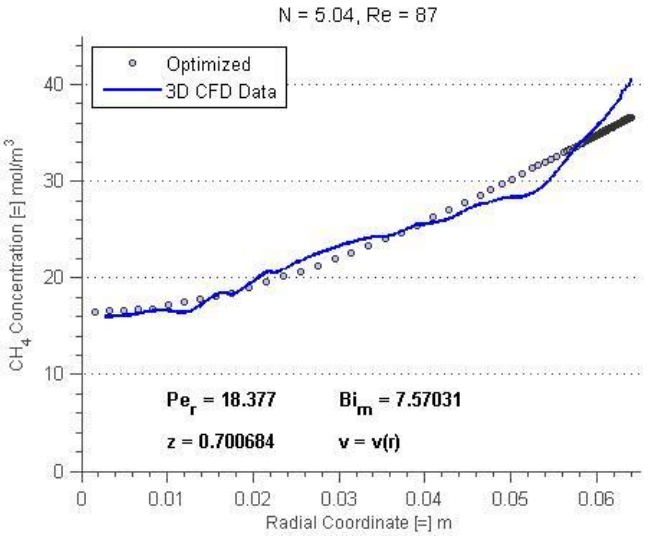

Figure 4.2.2. Fitted radial concentration profile for N = 5.04, Re = 87, bed depth 02.

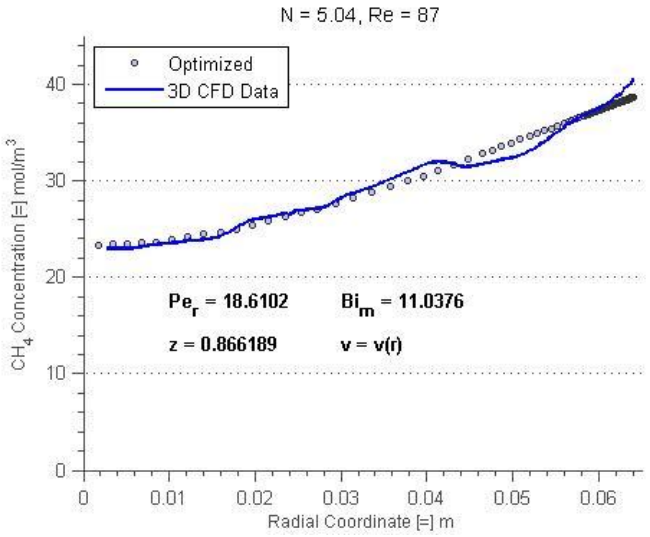

Figure 4.2.3. Fitted radial concentration profile for N = 5.04, Re = 87, bed depth 03.

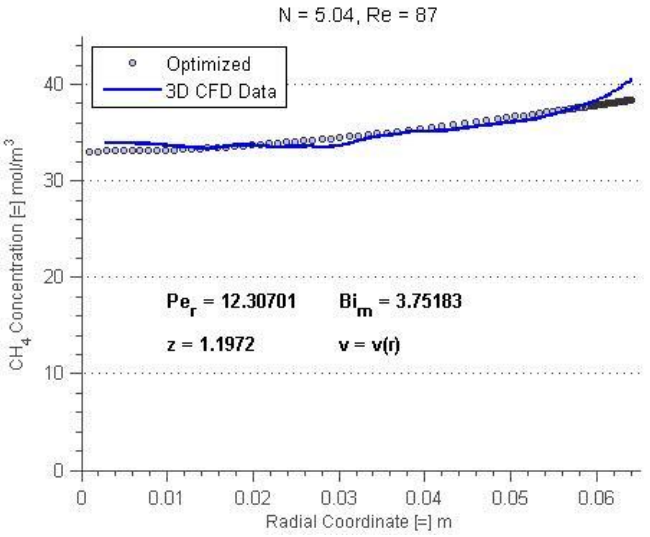

Figure 4.2.4. Fitted radial concentration profile for N = 5.04, Re = 87, bed depth 04.

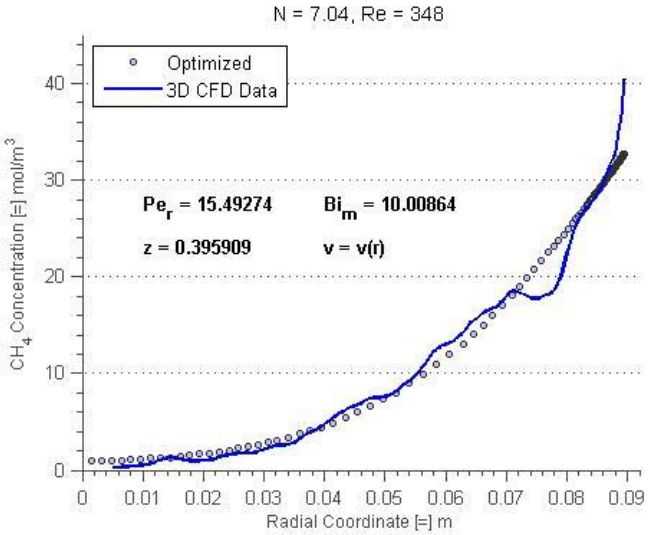

Figure 4.2.5. Fitted radial concentration profile for N = 7.04, Re = 348, bed depth 01.

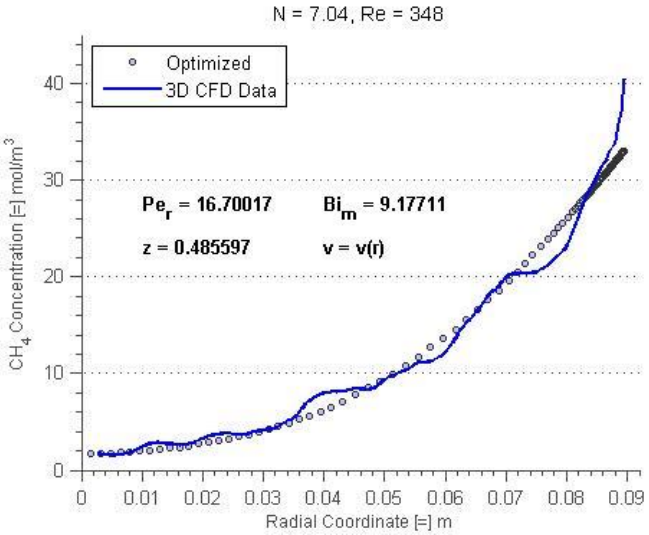

Figure 4.2.6. Fitted radial concentration profile for N = 7.04, Re = 348, bed depth 02.

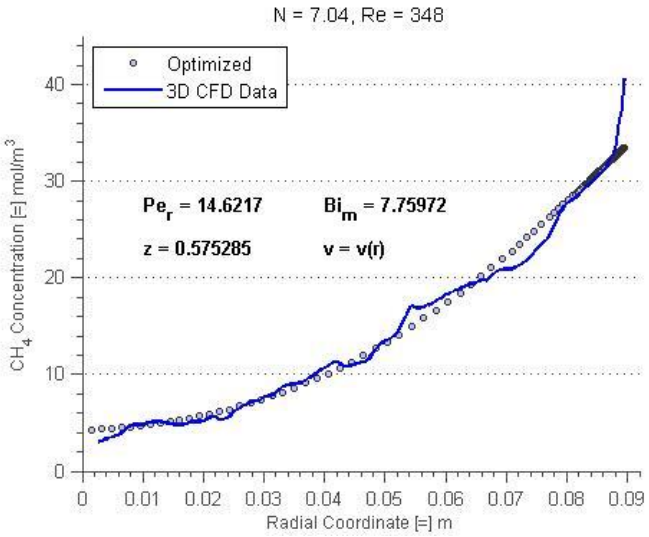

Figure 4.2.7. Fitted radial concentration profile for N = 7.04, Re = 348, bed depth 03.

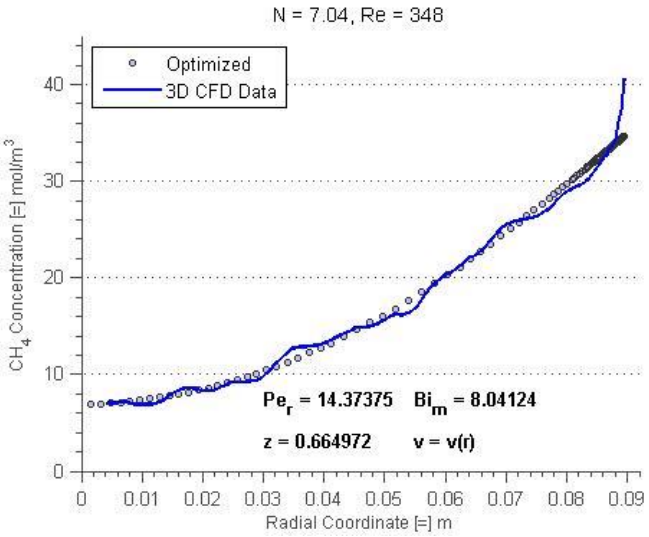

Figure 4.2.8. Fitted radial concentration profile for N = 7.04, Re = 348, bed depth 04.

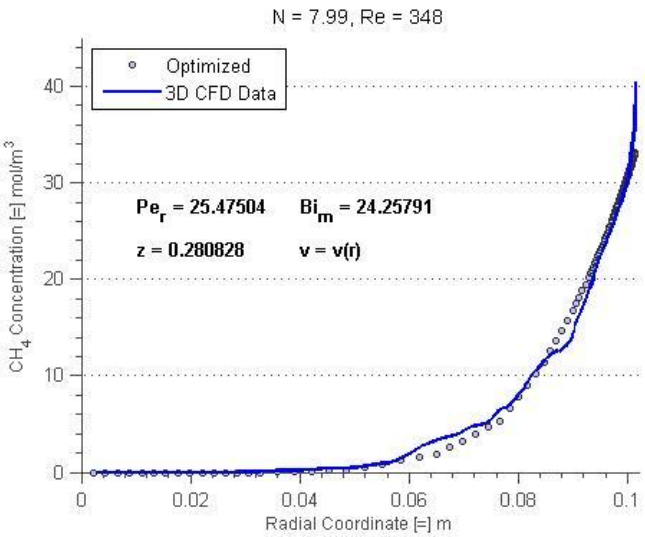

Figure 4.2.9. Fitted radial concentration profile for N = 7.99, Re = 348, bed depth 01.

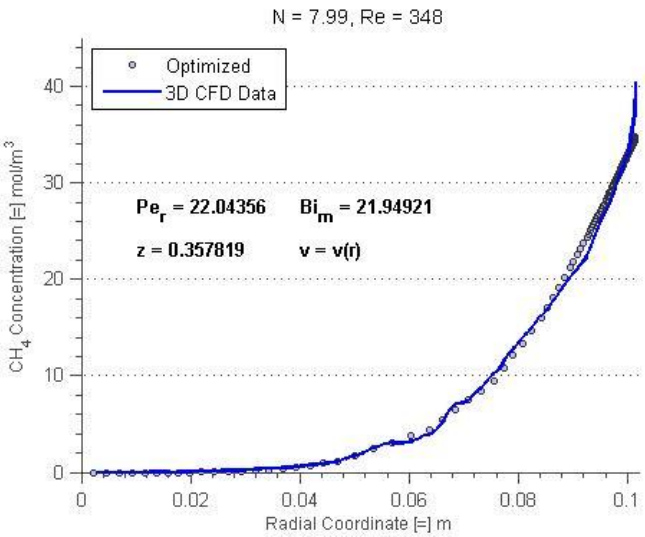

Figure 4.2.10. Fitted radial concentration profile for N = 7.99, Re = 348, bed depth 02.

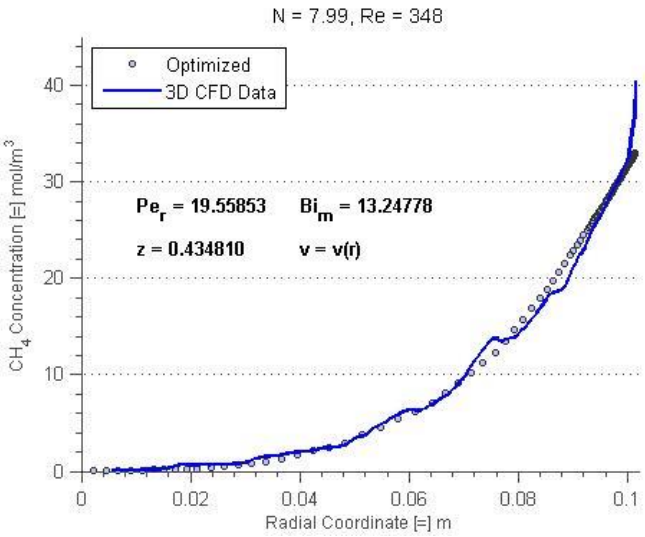

Figure 4.2.11. Fitted radial concentration profile for N = 7.99, Re = 348, bed depth 03.

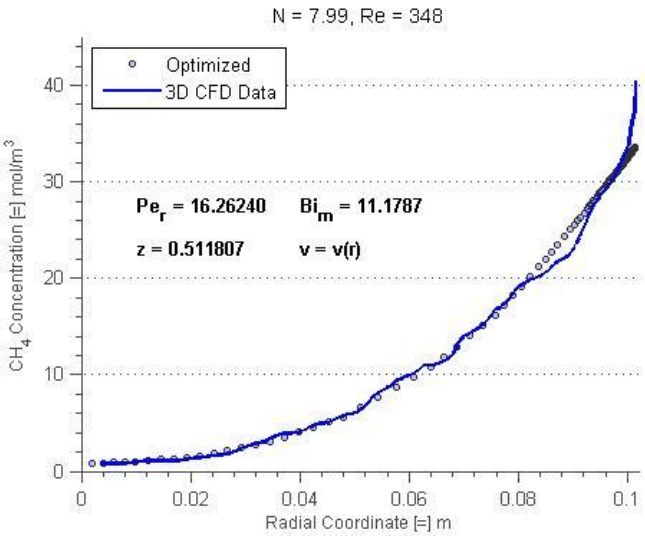

Figure 4.2.12. Fitted radial concentration profile for N = 7.99, Re = 348, bed depth 04.

The following post-processed images compare the COMSOL Multiphysics 2D representation (right) to the 3D CFD model from FLUENT (left). The images display methane concentration at a cutplane at the center of the bed. The study shown in Figure 4.2.13 is for N = 5.04, Re = 348, the following figure for N = 9.3, Re = 348.

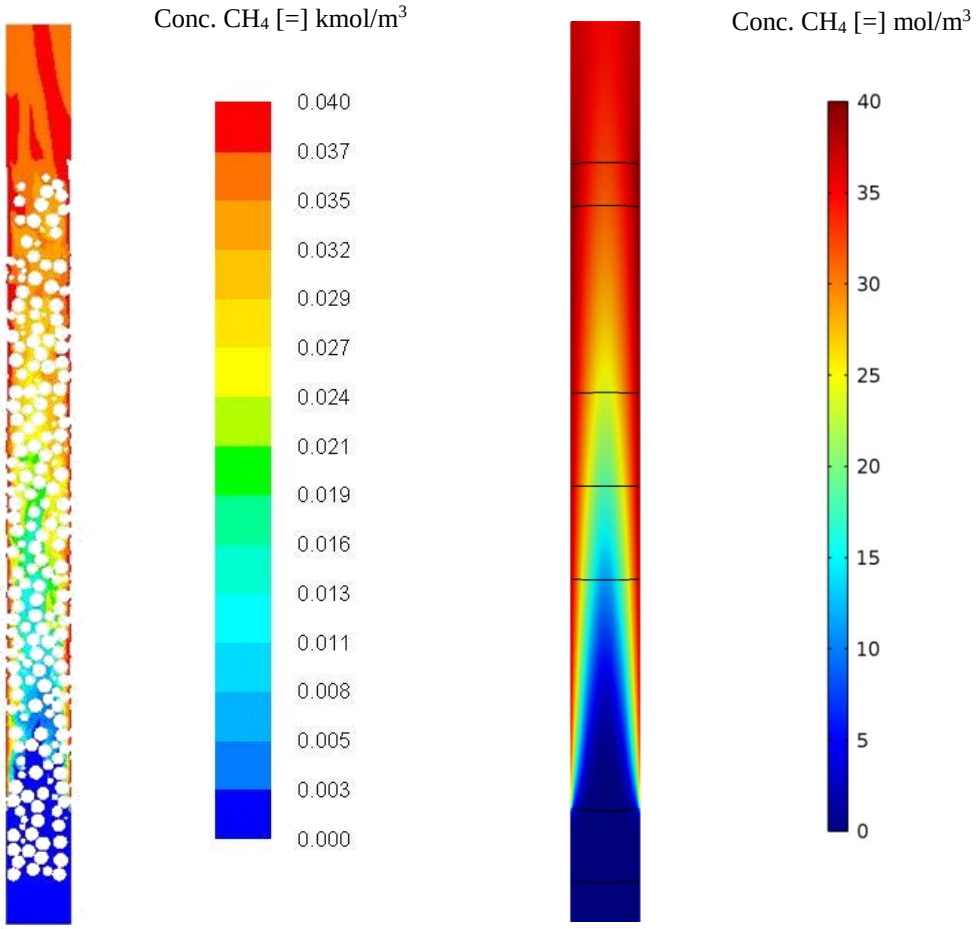

Figure 4.2.13. Methane concentration contour plot for N = 5.04, Re = 348. Three-dimensional CFD model is shown left, two-dimensional FEA model shown right.

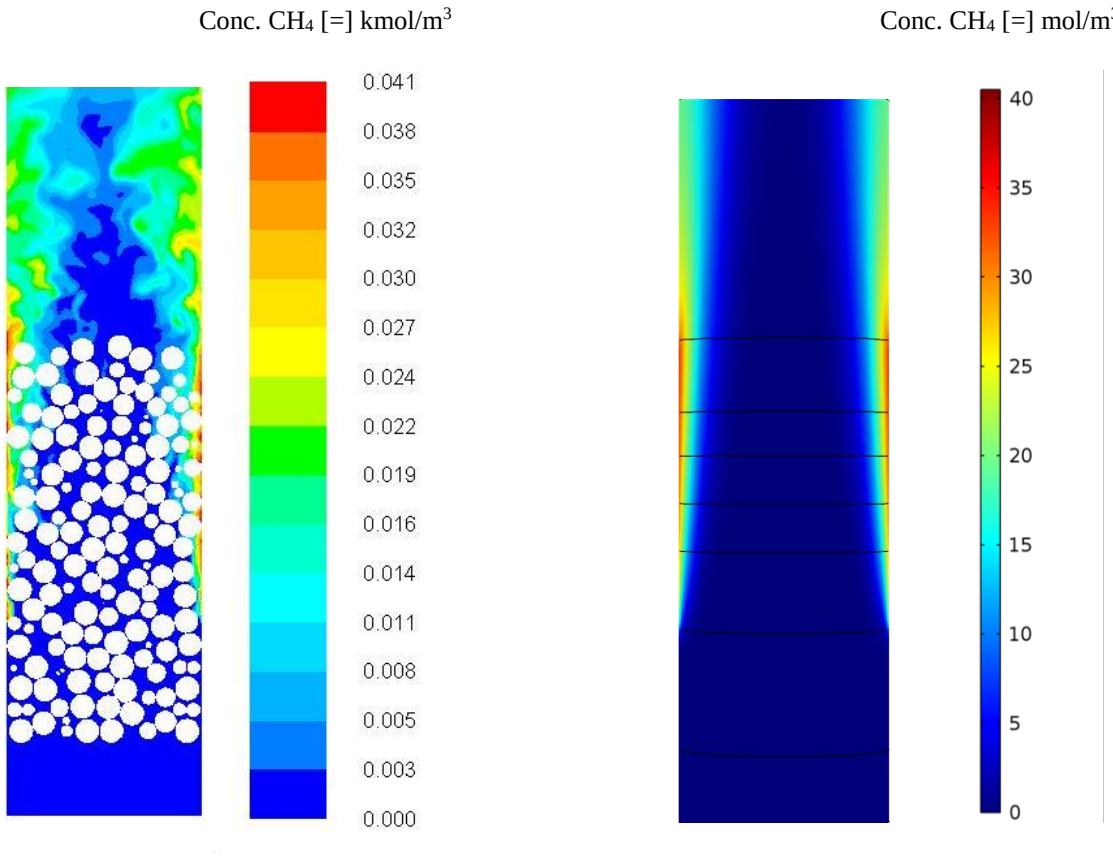

Figure 4.2.14. Methane concentration contour plot for N = 9.3, Re = 348. Three-dimensional CFD model is shown left, two-dimensional FEA model shown right.

The fitted two-dimensional model agrees well with the CFD-determined methane concentration up to the end of the packed length. Note the near wall methane concentration around the middle (axially) of the bed – the fitted model predicts methane concentration both with good qualitative and quantitative agreement. The discrepancy comes after the packed length to the bed exit where the boundary condition for methane switches from flux to no flux. The fitted model underpredicts the methane dispersion in the middle of the bed in this area for the N = 9.3 case, but overshoots the prediction for N = 5.04. It should also be noted that the axial symmetry condition imposed on the 2D models is not reflected exactly in the 3D models.

Below are plots comparing dispersion coefficients for all runs. Plots are divided between the four lower N and four higher N studied.

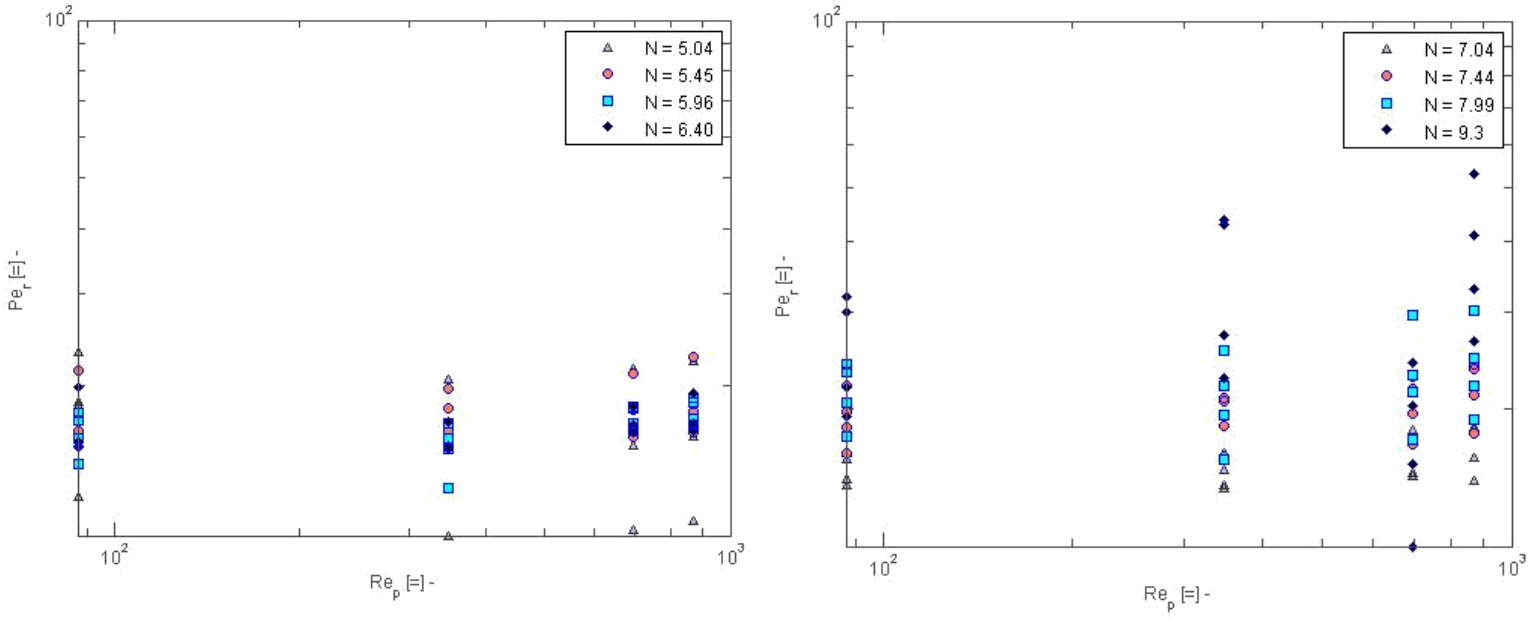

Figure 4.2.15. Radial Peclet number vs. Reynolds number for all N and bed depths.

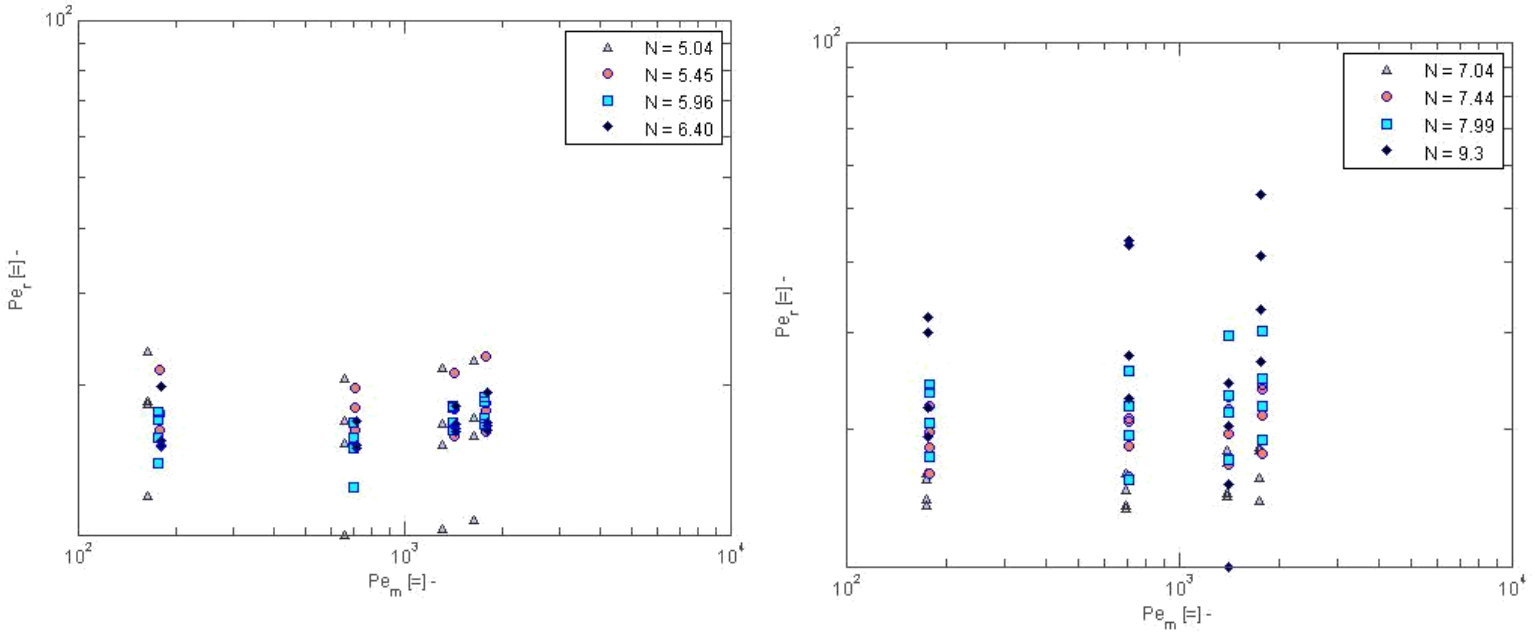

Figure 4.2.16. Radial Peclet number vs. Mass Peclet number for all N and bed depths.

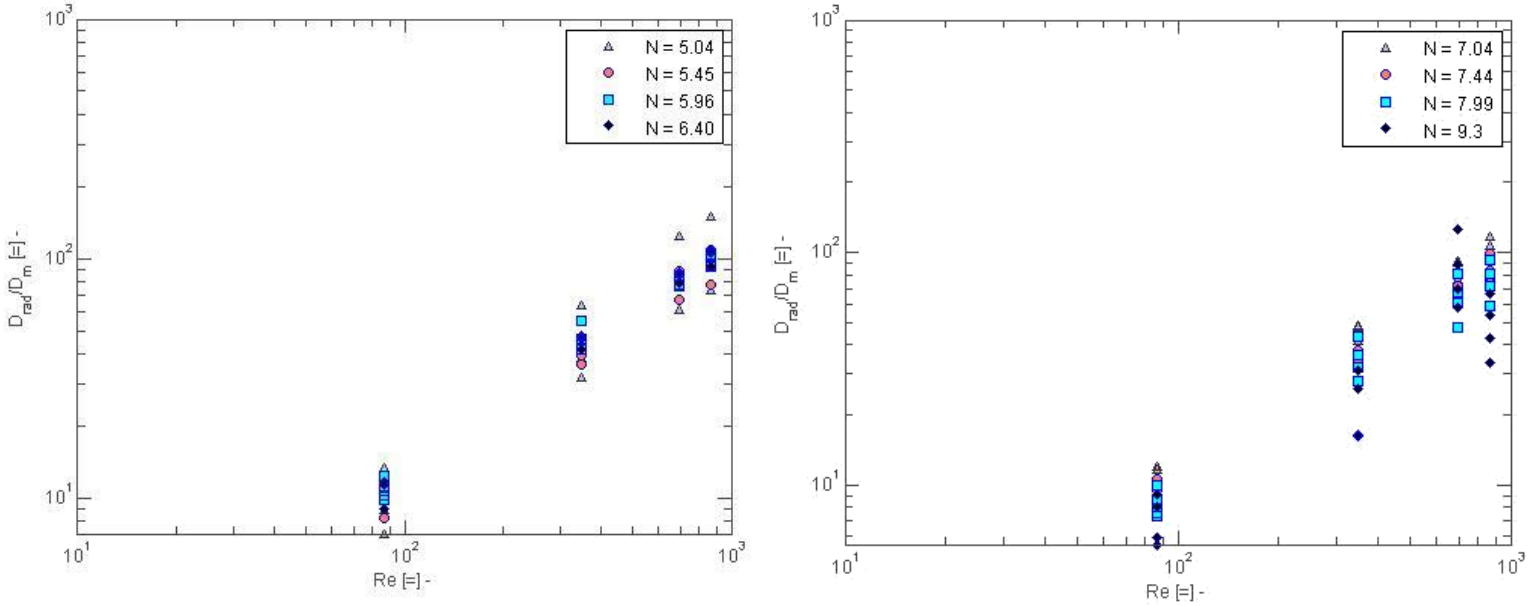

Figure 4.2.17. Radial dispersion coefficient vs. Reynolds number for all N and bed depths.

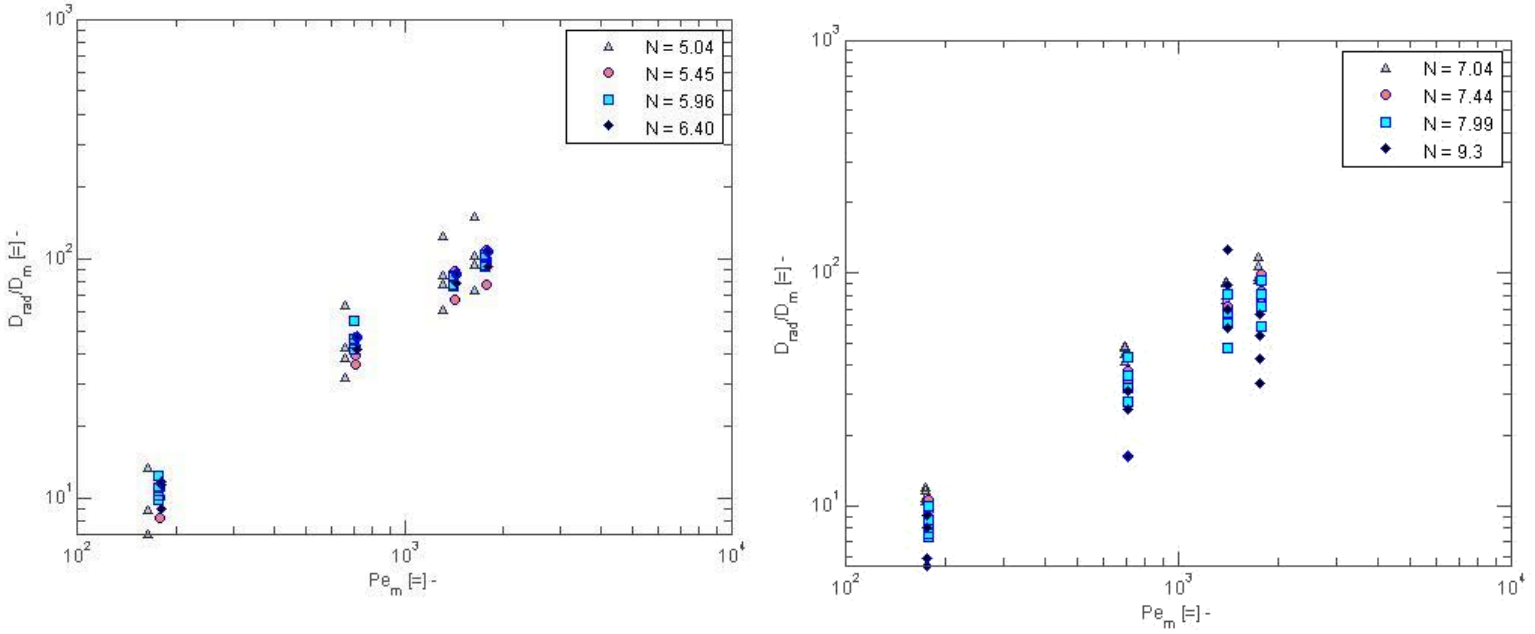

Figure 4.2.18. Radial dispersion coefficient vs. Mass Peclet number for all N and bed depths.

Wall concentration is better predicted at higher N, low Re, low bed depth combinations. In Figures 4.2.1 – 4.2.12, the computed wall concentration data from the optimization run is lower than what is shown in the CFD model. The use of the two parameter model with a flux condition at the wall predicts a constant rate

of dispersion from the tube center up to the wall, at which point a jump in concentration is predicted by the inclusion of the Biot mass transfer number. The mass transfer film coefficient used to calculate the Biot number is more poorly predicted at longer bed depths.

In beds of lower N and higher Re and depth cases (i.e., N = 5.04, Re = 870), small gradients in methane concentration characterize the radial concentration profiles. In these cases, enough methane has dispersed laterally from the wall and been transported axially up the bed that a small drop in concentration from the wall value is seen near the end of packing (the highest bed depth taken in each case). Fitting coefficients to these profiles with the convective-dispersion equation induces random error because of a small concentration gradient, and data points in these cases carry larger numerical uncertainty.

Radial concentration at bed depths near the reactor entrance are lower in dispersion than is expected. It appears the methane dispersion is controlled by slow diffusion through the wall boundary layer, and then dispersed at a reduced rate of convective-dispersion at the interface between the diffusive-dispersion and convective-dispersion layers. Previous literature has shown also that 2-D models predict higher dispersion coefficients to their 3-D counterparts due to higher intercellular fluid motion in the lateral direction (Jourak, 2014). These coupled effects serve as an explanation for the higher than expected dispersion coefficient values found in this research.

It appears that the mechanism of dispersion should be quantified by at least three types: slow, diffusive-dispersion in the tube wall boundary layer; then, an increasing rate of dispersion at the diffusive-dispersion and convective-dispersion interface and toward the tube center, and finally a fully convective dispersion at the tube center. The use of the two-parameter model shown here reduces this mechanism to two parts: that of constant radial dispersion from the tube center and up to the wall, at which point a jump in concentration is predicted by the Biot mass transfer number. This reduces the accuracy of the fitting model, and limits the physical realization of various dispersion mechanisms in the bed.

Radial dispersion coefficients appear to be somewhat length dependent, and this dependency is seen more in the low N range. Figure 4.2.19 displays each Peclet number from all runs and the bed length from which the optimization occurred:

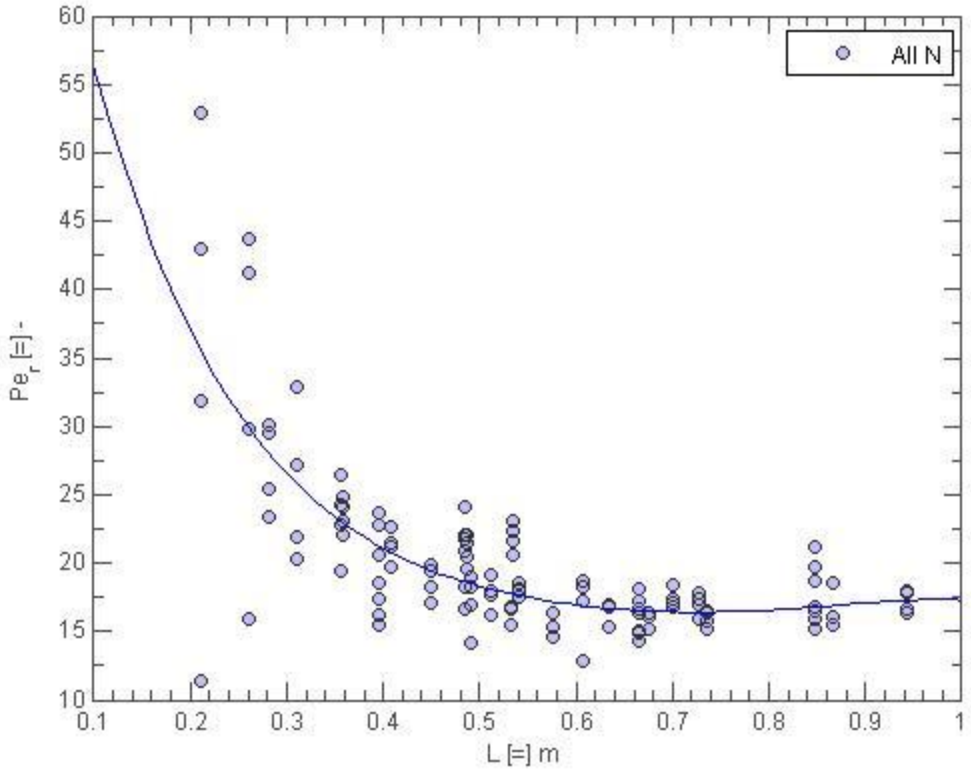

Figure 4.2.19. Radial Peclet Number vs. Bed Depth, All N.

It is clear that concentration profiles extracted from longer beds tend to lower Peclet numbers, particularly to the Pe = 12 limit. Literature studies of radial dispersion have noted that radial dispersion coefficients are independent of bed length at various Re. This statement is likely a result of pulling concentration samples at bed depths far enough from the bed entrance and tracer injection that the Peclet number has reached an asymptotic value relative to bed length, and not just at the limit of high Re. In this research, it appears that the dispersion coefficient has some length dependency, particularly in the developing sections of the bed.

4.3 Constant Velocity Effects on Dispersion Coefficients

The previous optimization results were obtained by implementing a velocity profile obtained by computing an area-weighted average of cell by cell axial velocity over the packed length (excluding $5d_p$ from the entrance and $3d_p$ from the exit of the bed, as previously mentioned.) The resulting profiles of this method were shown in figures 4.1.1 – 4.1.15. A separate study was conducted using N = 5.04, 6.40, and 9.3 in which the velocity profile remained constant as the inlet velocity assigned as the boundary condition at the

entrance of the bed. Meaning, the inlet velocity condition was equal to the axial velocity over the whole bed length. This simplifies the optimization, and leads to insight on the need for a velocity profile versus a uni-directional, constant velocity profile. A sample of the results of the optimization are shown below, with the remaining plots given in Appendix C:

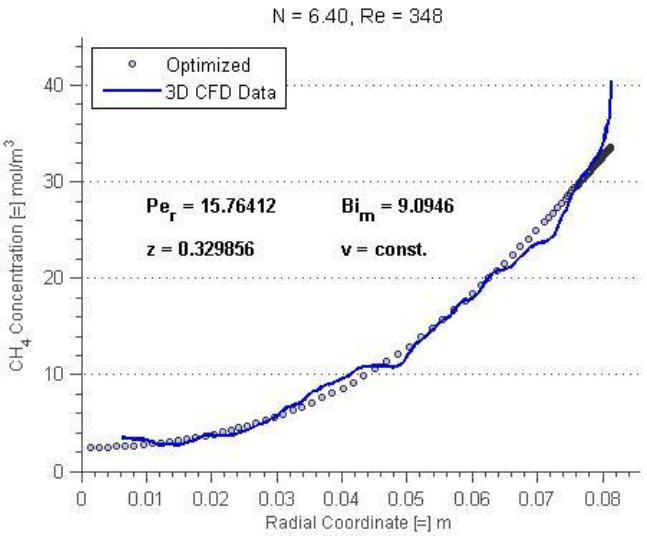

Figure 4.3.1. Fitted radial concentration profile for N = 6.40, Re = 348, bed depth 01.

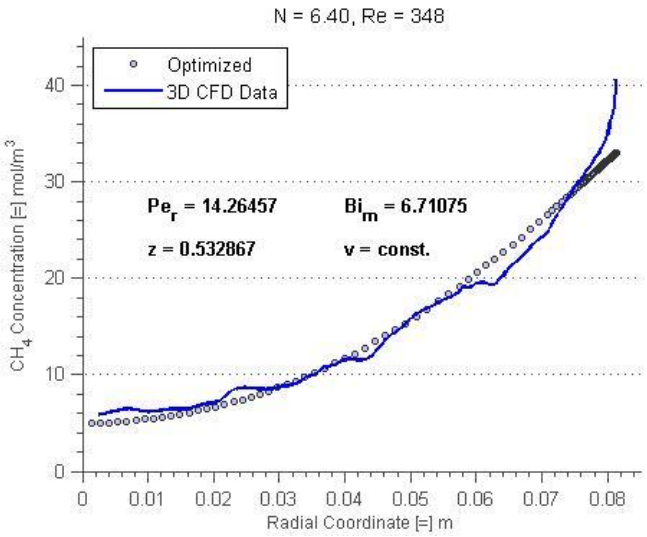

Figure 4.3.2. Fitted radial concentration profile for N = 6.40, Re = 348, bed depth 02.

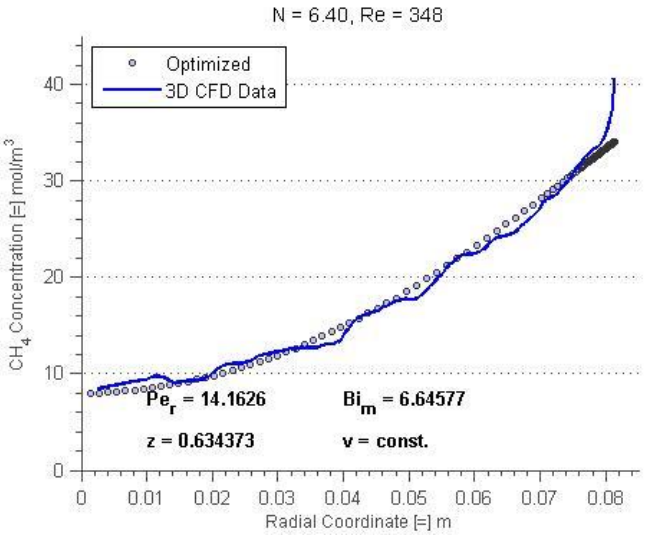

Figure 4.3.3. Fitted radial concentration profile for N = 6.40, Re = 348, bed depth 03.

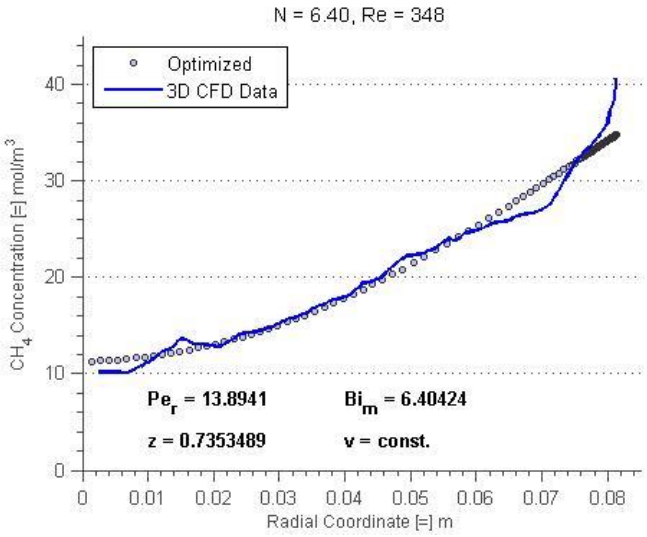

Figure 4.3.4. Fitted radial concentration profile for N = 6.40, Re = 348, bed depth 04.

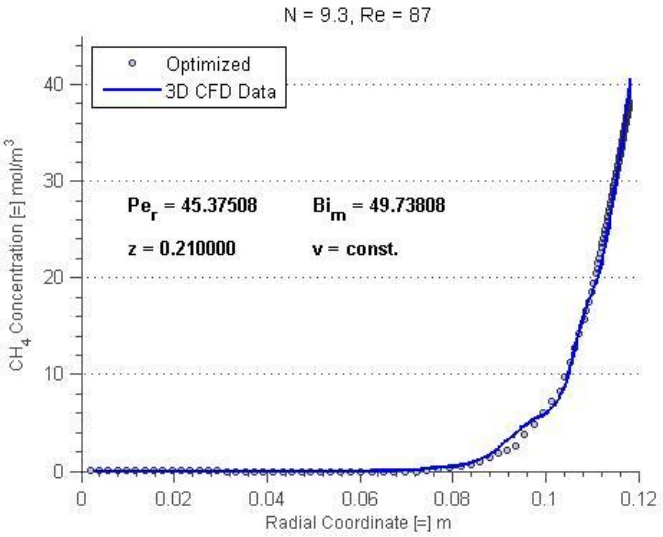

Figure 4.3.5. Fitted radial concentration profile for N = 9.3, Re = 348, bed depth 01.

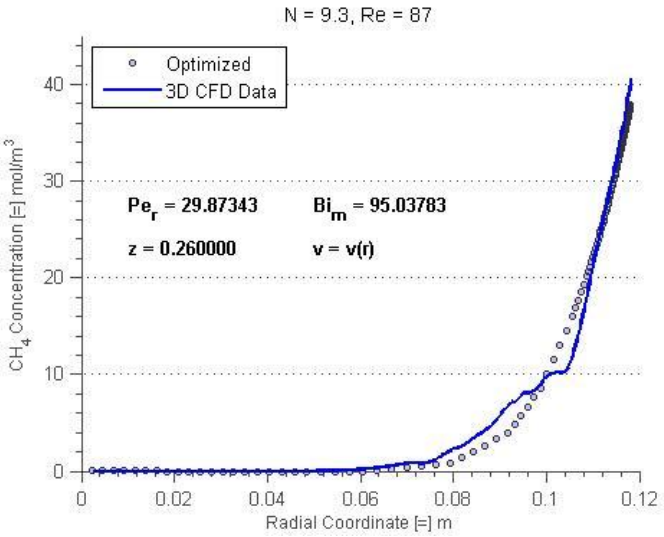

Figure 4.3.6. Fitted radial concentration profile for N = 6.40, Re = 9.3, bed depth 02.

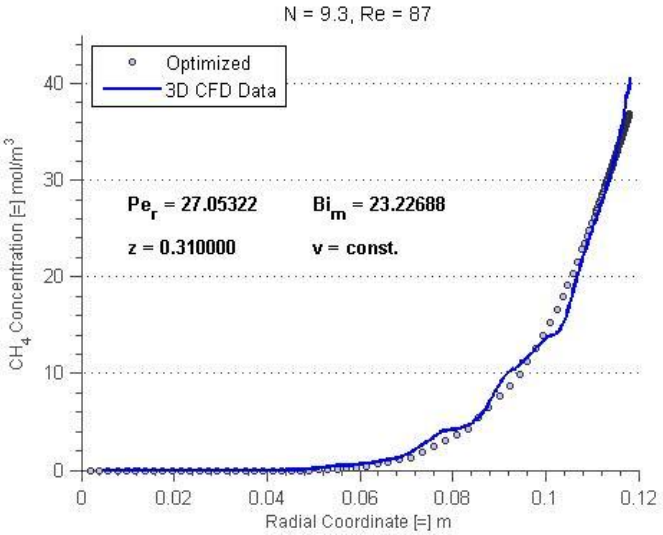

Figure 4.3.7. Fitted radial concentration profile for N = 9.3, Re = 348, bed depth 03.

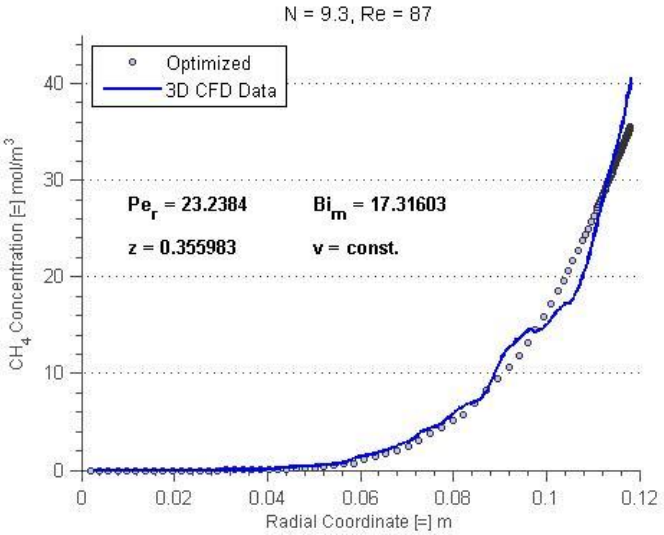

Figure 4.3.8. Fitted radial concentration profile for N = 9.3, Re = 348, bed depth 04.

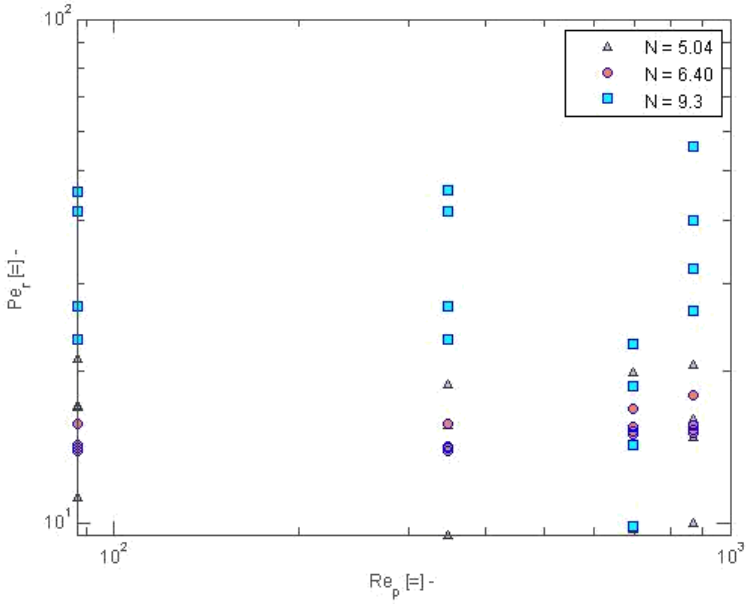

Figure 4.3.9. Radial Peclet Number vs. Reynolds number for three N at all bed depths.

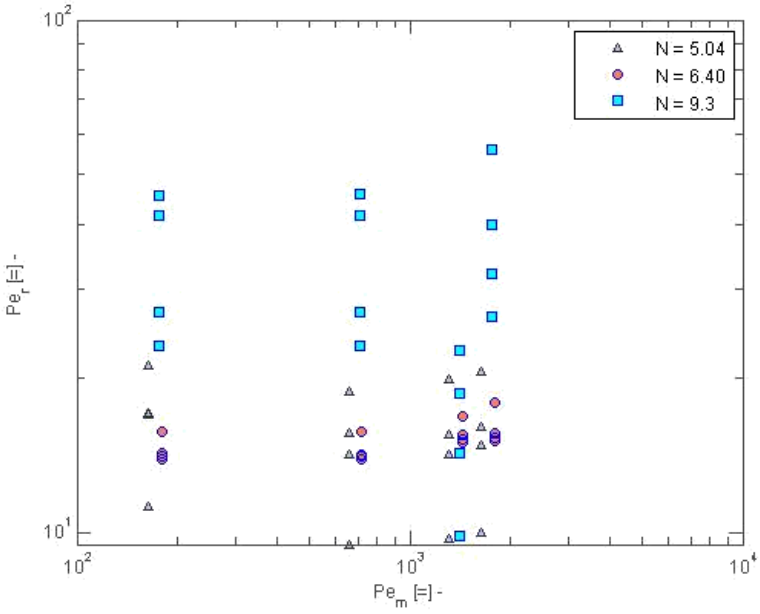

Figure 4.3.10. Radial Peclet number vs. Mass Peclet number for three N at all bed depths.

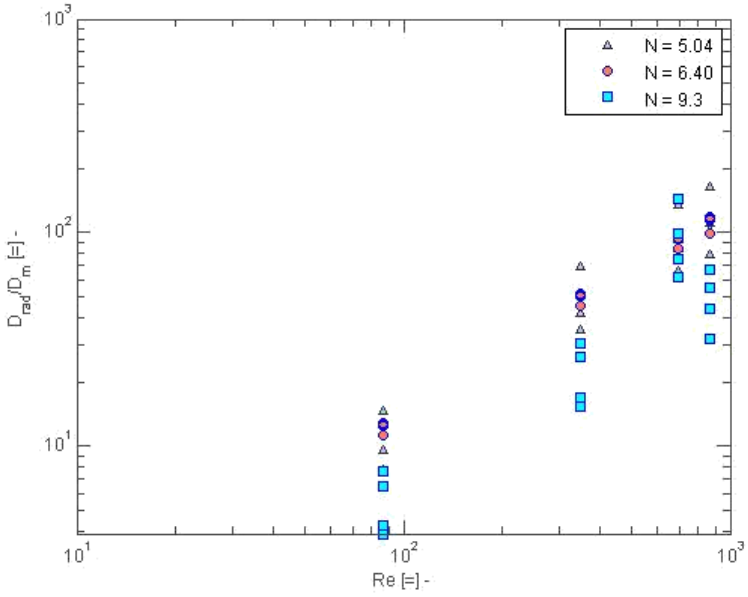

Figure 4.3.11. Radial dispersion coefficient vs. Reynolds number for three N at all bed depths.

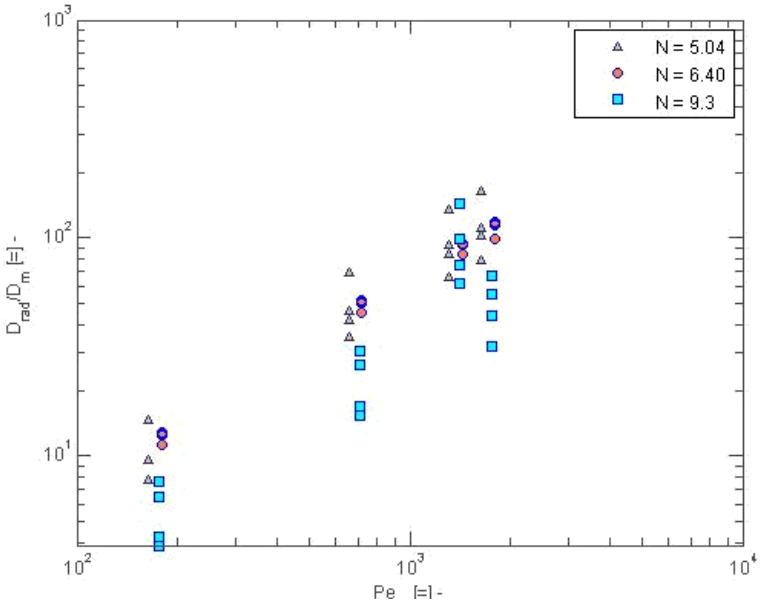

Figure 4.3.12. Radial dispersion coefficient vs. Mass Peclet number for three N at all bed depths.

Typical in all runs, the dispersion coefficients predicted with a constant velocity profile are higher than the previous studies, and with higher predicted Biot mass transfer numbers. The unidirectional, constant velocity profile includes a nonzero velocity at and before the wall, and so the mass transfer, diffusion-dominated boundary layer is no longer physically realized using this model. Bed depth effects on the fitted coefficients also appear in a similar manner as before, with a higher length dependency shown in beds of lower N. It is also noted that the exclusion of an axial velocity profile gave CPU clock times of the same magnitude as their previous counterparts, so no benefit was seen in computational savings. Numerically, the goodness of fit using the 2-D model was approximately the same between these constant velocity runs and those with a velocity profile.

4.4 Local Velocity Effects on Dispersion Coefficients

A sub-study was conducted in which velocity profiles were extracted instead from a 2 mm (axially) isosurface, as was concentration data from FLUENT. This gave essentially "local" velocity fluctuations at a particular bed height, along with concentration data pulled at the same bed height. This is shown pictorially below, in which the bed on the left shows a 2 mm isosurface (transparent blue) and the bed on the right (transparent gray) shows the length over which the velocity profile is usually area-averaged (i.e., most of the packed length). Example velocity profiles are displayed in the plot below:

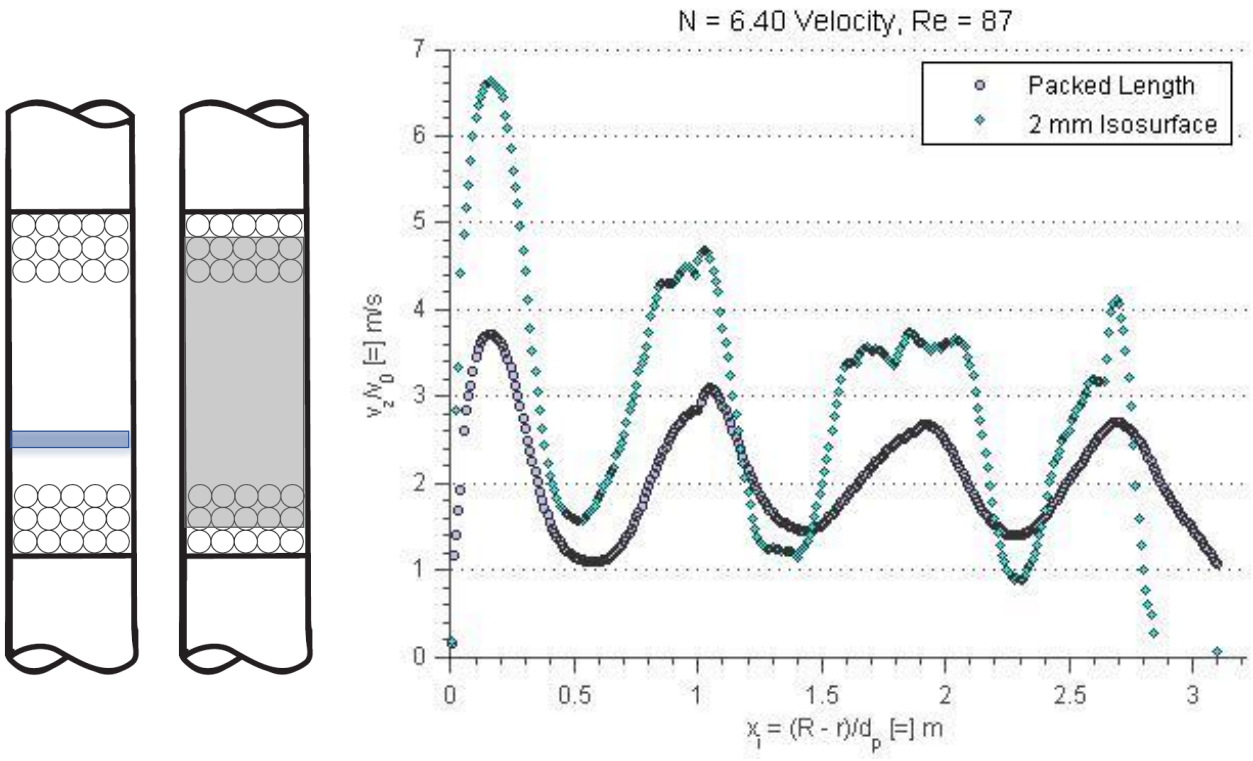

Figure 4.4.1. Local velocity and averaged velocity profiles vs. radial coordinate, N = 6.40, Re = 87.

The velocity profile shown in Figure 4.4.1 is averaged over a 2 mm isosurface, and so the axial velocity is a strong function of the local packed structure. Given the randomized placement of particles in the beds, this velocity profile may not be replicated as easily from case to case. Moreover, a comparison of local velocities at various bed depths of the same bed diameter are largely different, and these profiles are given in Appendix B. The intent of this study was to determine if local velocity fluctuations yielded significant effects on the dispersion characteristics in the bed. Optimization studies were re-run using these local velocity profiles for cases N = 5.04, 6.40, and 9.3 at four bed depths each and four Reynolds numbers. A selection of results are presented in the following pages, with the remainder given in Appendix C.

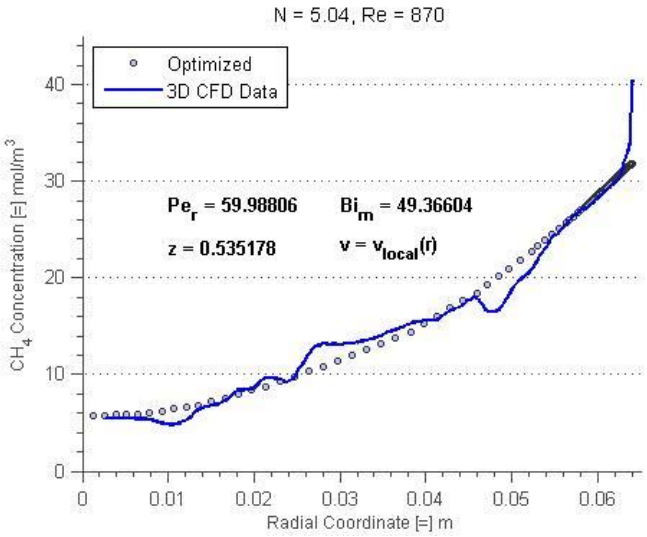

Figure 4.4.2. Fitted radial concentration profile for N = 5.04, Re = 870, bed depth 01.

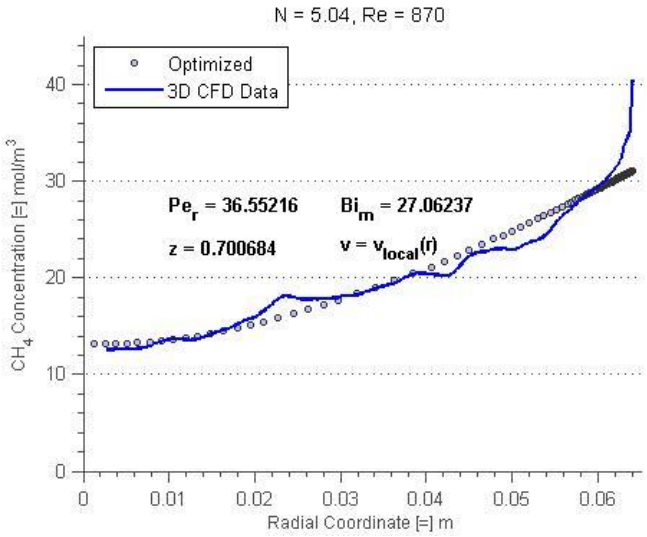

Figure 4.4.3. Fitted radial concentration profile for N = 5.04, Re = 870, bed depth 02.

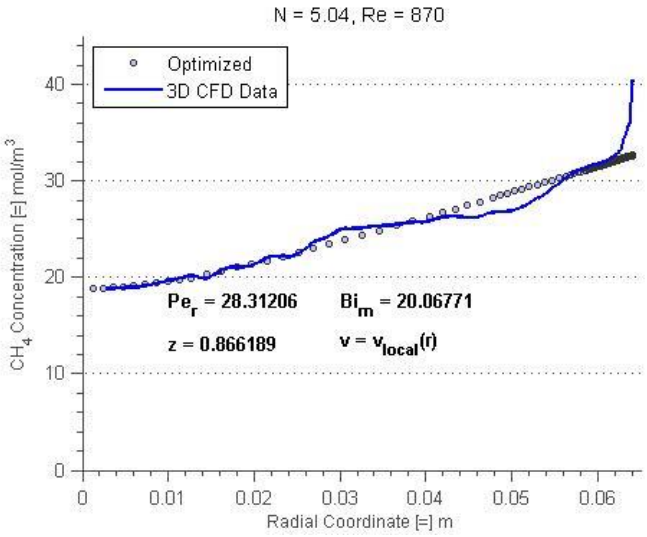

Figure 4.4.4. Fitted radial concentration profile for N = 5.04, Re = 870, bed depth 03.

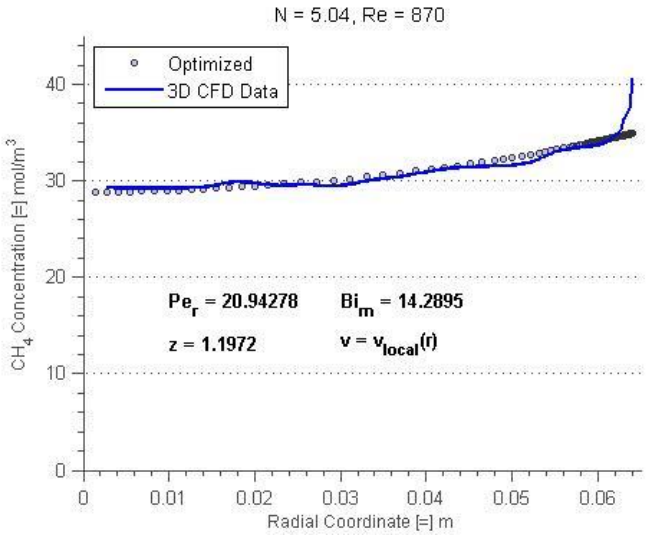

Figure 4.4.5. Fitted radial concentration profile for N = 5.04, Re = 870, bed depth 04.

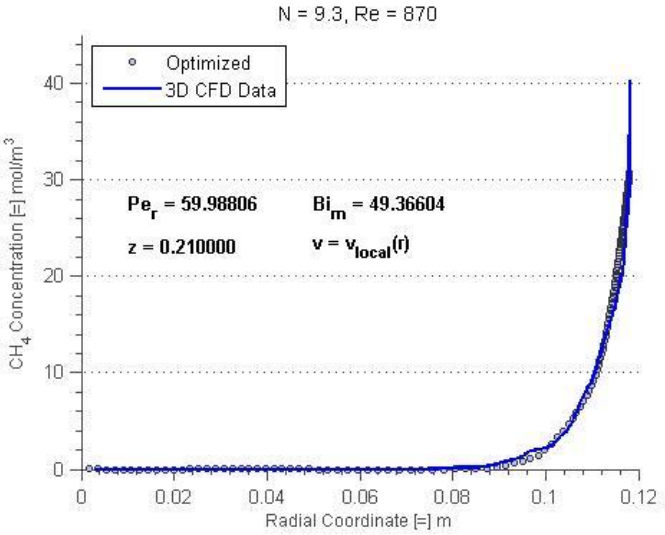

Figure 4.4.6. Fitted radial concentration profile for N = 9.3, Re = 870, bed depth 01.

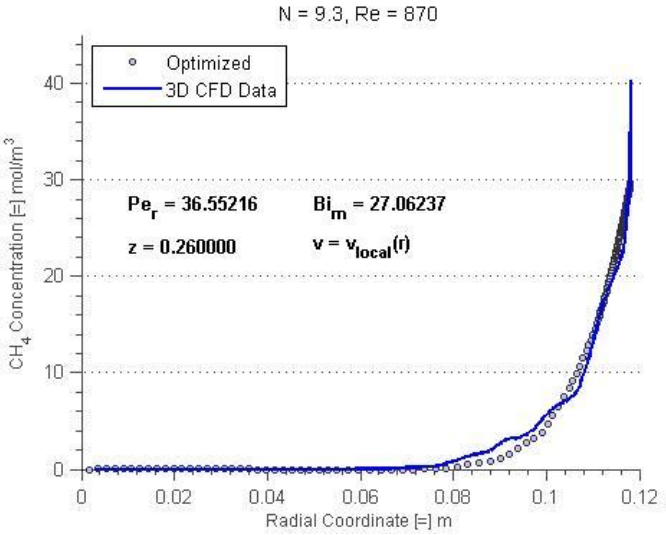

Figure 4.4.7. Fitted radial concentration profile for N = 9.3, Re = 870, bed depth 02.

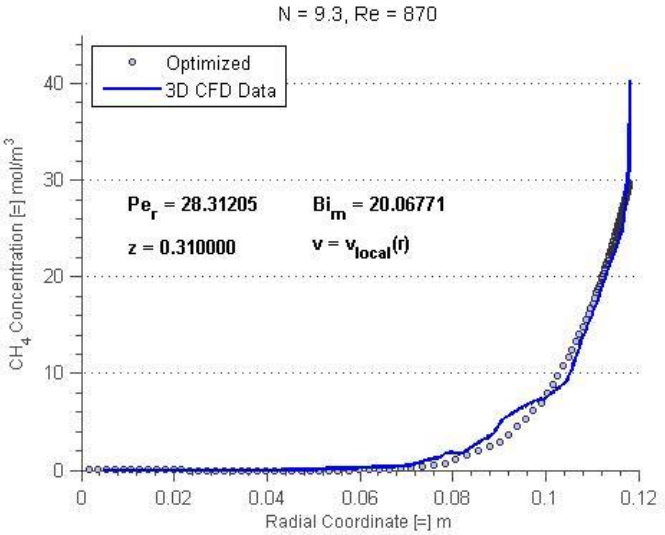

Figure 4.4.8. Fitted radial concentration profile for N = 9.3, Re = 870, bed depth 03.

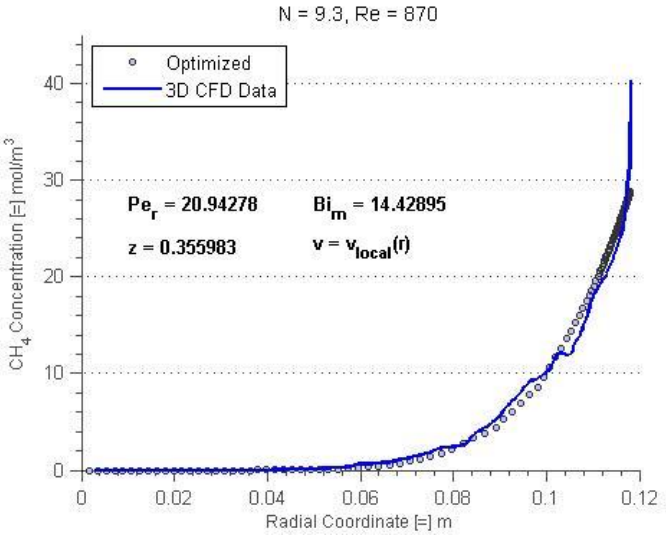

Figure 4.4.9. Fitted radial concentration profile for N = 9.3, Re = 870, bed depth 04.

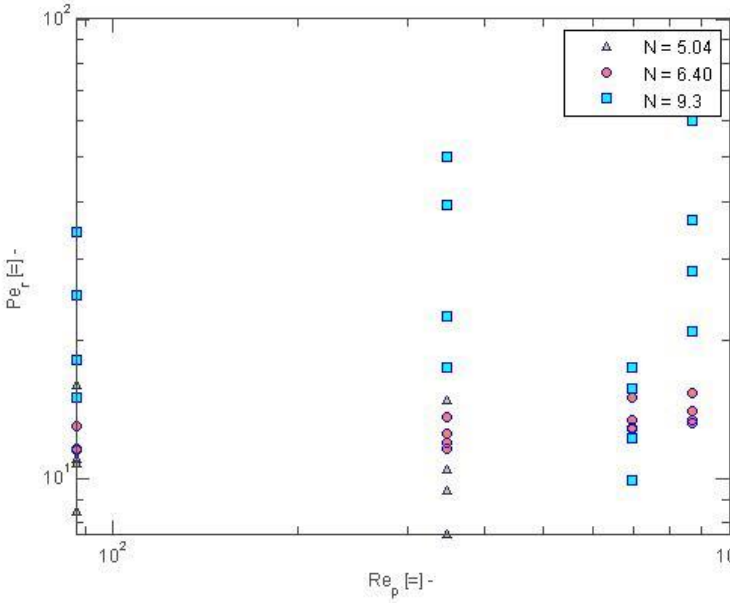

Figure 4.4.10. Radial Peclet Number vs. Reynolds number for three N at all bed depths.

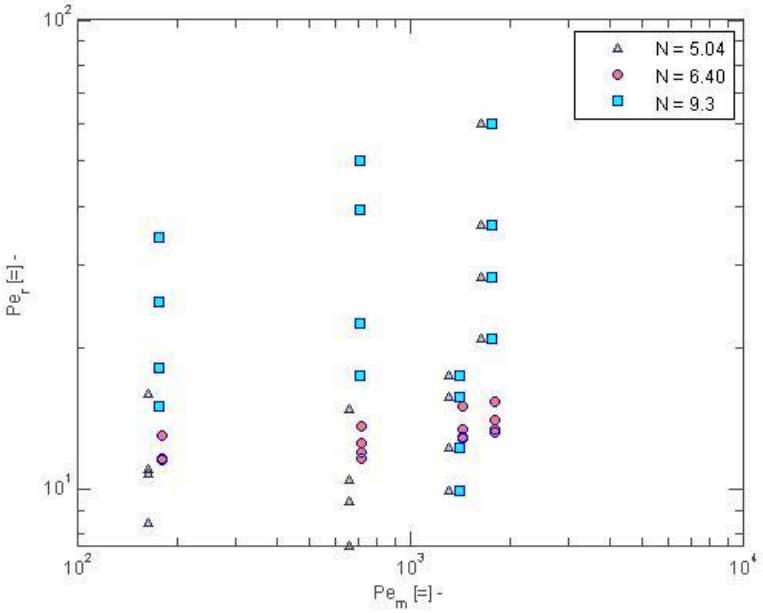

Figure 4.4.11. Radial Peclet number vs. Mass Peclet number for three N at all bed depths.

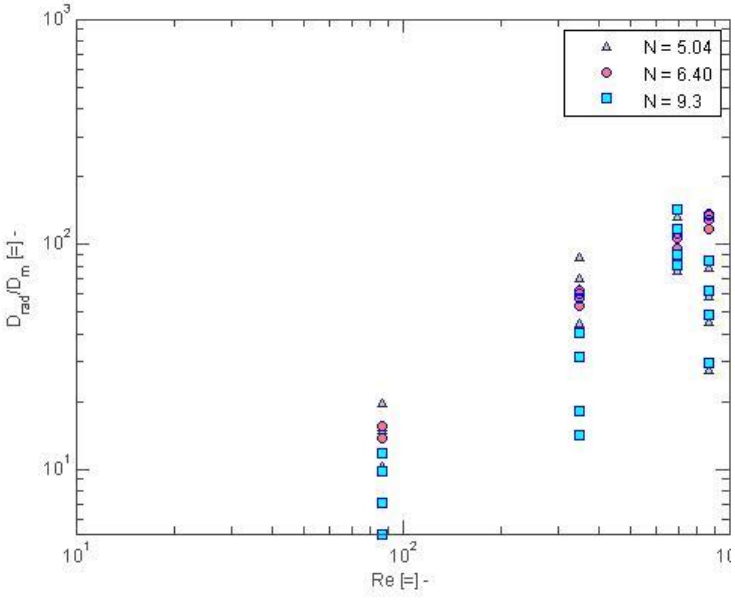

Figure 4.4.12. Radial dispersion coefficient vs. Reynolds number for three N at all bed depths.

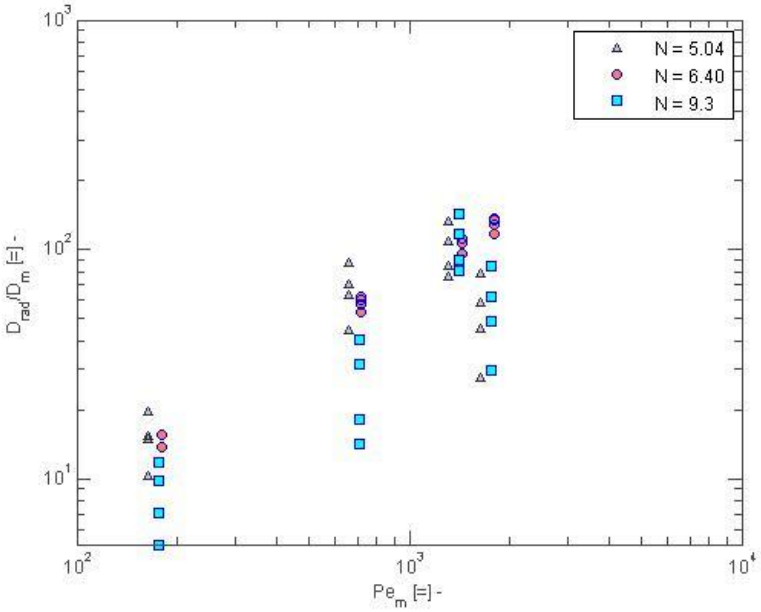

Figure 4.4.13. Radial dispersion coefficient vs. Mass Peclet number for three N at all bed depths.

A case could also be made that supplying these local velocities is incorrect and not indicative of actual bed velocities. The 2-D model allows a velocity profile only as a function of radial position, and the axial component is everywhere the same at a given radial position. Given that these local velocities vary widely at the same N, Re combination, a 3-D optimization model would more accurately accept the CFD-predicted velocities as an input.

Length dependency is shown in Figure 4.4.14, comparing the three overall cases studies: one with a constant velocity, those using local velocities, and runs using a velocity profile averaged over the packed length.

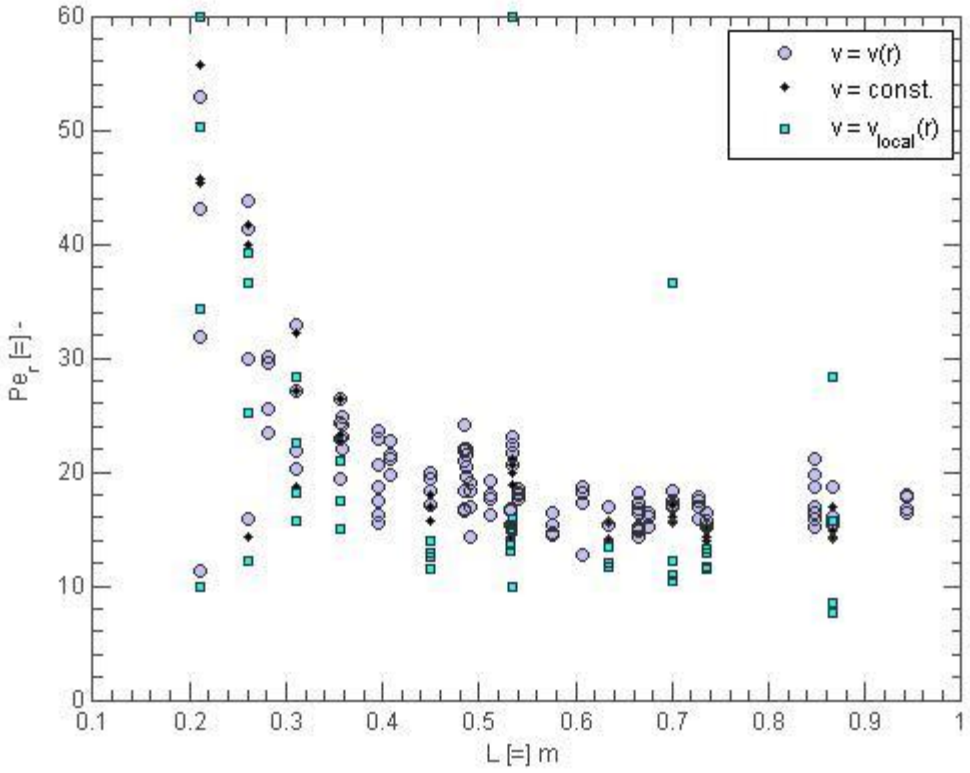

Figure 4.4.14. Radial Peclet number vs. Bed Depth, all cases.

A similar trend in length dependency resulted in the differing methods of supplying velocity profiles to the two-dimensional model. Figure 4.4.14 suggests that the length dependency is not a result of velocity in the bed interstices, but rather due to the steepness in concentration gradient in the bed.

4.5 Reconciling 2D and 3D Models

Modeling the three-dimensional beds using two-dimensional representations reduces the geometric complexities inherent in a packed bed and requires several simplifying assumptions. A discussion of these are given below, in an attempt to reconcile differences between the fitted parameters and the radial concentration profiles from the CFD simulations.

In the 2D model, axial symmetry is applied along the length of the rectangular geometry, which is only exactly true in the two empty sections of the bed. This assumption effectively ignores the complex, unstructured packing arrangement in the 3D beds.

Velocity in the optimization models is assigned uni-directionally, along the axial direction, with a zero radial velocity component. The overlay plot below compares the axial component of velocity to the velocity magnitude, and it is clear that the radial component is nonzero.

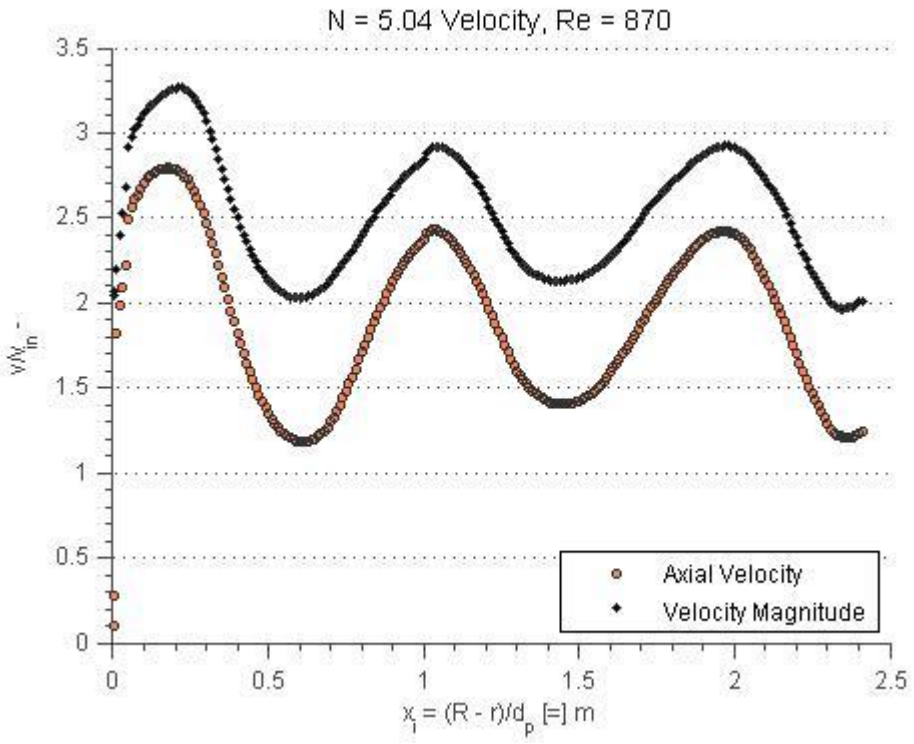

Figure 4.5.1. Comparison of axial velocity and magnitude of velocity, N = 5.04, Re = 870.

Velocity profiles supplied to these models is also taken as an area-weighted average over the packed length in the 3D models. In the 2D model, this profile is applied over the entire bed, including the calming and empty sections. In optimization studies that included local velocity profiles, this local velocity profile was again applied over the whole bed, making a more drastic assumption, given that these local profiles are from 2 mm isosurfaces.

In the CFD simulations, a methane mass fraction equal to unity is specified at the tube wall, whereas in the optimization studies, the Biot mass transfer number is used to predict the drop in methane concentration from the wall and radially outward. Figures 4.2.1 – 4.2.12 clearly demonstrate the inability of this wall parameter to predict the wall concentration value correctly. In general, the fitted radial concentration profiles under-predict the methane wall concentration.

In all optimization studies, the axial Peclet number $Pe_a = 2$ was assigned, through variability among different inlet velocities is expected. It was found that using $Pe_a = 2$ did not reliably predict methane concentration at low bed depths.

Although minor, but still relevant, is the differing methods of assigning concentration data. In the 3D models, concentration data is pulled using an area-weighted average over a 2 mm long (axially) isosurface. This data is supplied to the optimization model as a line (radial coordinate, axial coordinate, concentration data point).

5. Conclusions

Several simplifying assumptions were made in transforming the three-dimensional CFD models to a two-dimensional finite element model. The most important of these simplifications was the reduction of the dispersion mechanism as a whole into two parts: one represented by a constant rate of dispersion from the tube center and another by a jump at the wall using the Biot mass transfer number. The results suggest, instead, that the mechanism of dispersion is at least three-fold, with a diffusive-dispersion layer along the tube wall, a convective-dispersion region at the tube center, and intermediate, increasing rate of dispersion between the two. The results also seem to suggest some length-dependency in the radial dispersion coefficient, contradicting previous literature in which experimental studies found it to be constant as a function of bed depth. It was also found that a velocity profile supplied to the model as a constant function versus an axial velocity profile as a function of bed radius had little effect on the dispersion coefficient, but gave similar CPU clock times when performing the optimization procedure, showing that a more accurate picture of velocity is possible in a two-dimensional model, without added computational expense.

6. Recommendations for Future Study

6.1 Radial Dispersion

This study may be broadened to extend the 2-D model to fit the mechanisms of dispersion more accurately in the bed. It was shown that a two-parameter model, one that predicts a constant rate of dispersion up to the wall, and then a near-wall rate of dispersion, has various limitations. The inclusion of a third parameter, one that predicts in increasing rate of dispersion from the reactor wall boundary layer up to the bed center may provide higher accuracy and more physical meaning. Using a three-dimensional model is also possible, and it may serve to relieve some of the velocity profile limitations that were encountered in this research, mainly that the 2-D model accepted only velocity as a function of radial position, and this axial component was everywhere the same at a given radial coordinate.

This study should also be extended to include the optimization of radial dispersion coefficients within the turbulent flow regime. Given that packed bed reactors, such as those for alkane dehydrogenation and methane steam reforming are characterized both by laminar and turbulent flow, an additional study investigating radial dispersion under these conditions would be appropriate and necessary. It is also recommended that the same study be carried out using liquid phase fluids, as several studies in the literature have declared a sharp difference in radial dispersion between the two phases.

6.2 Axial Dispersion

A combined CFD and optimization study may also be done to fit axial dispersion coefficients, much in the same way as radial dispersion coefficients were determined here. Rather than extract concentration data as a function of radial position, averaged over a small axial length, concentration data at several bed depths would be needed to optimize axial dispersion coefficients with numerical confidence. This study could, as stated previously, be extended to include liquid and gas phase fluids, under both the laminar and turbulent flow regimes.

For both axial and radial dispersion studies, it is recommended that beds of lower diameter (i.e., N = 2, N = 3.96) be studied as well, in addition to heat and mass transfer, such as those offered by high wall temperature conditions. The same methodology of optimization modeling can also be applied to beds of

large enough N that wall-effects become negligible, assuming the computational resources are available to model such a large number of spheres.

7. Nomenclature

Computational Fluid Dynamics, **CFD**

Finite Element Analysis, **FEA**

Biot mass transfer number, $\mathbf{Bi_m}$

Concentration of species i (i = methane), $\mathbf{c_i}$

Catalyst particle diameter, $\mathbf{d_p}$

Axial, or longitudinal dispersion, coefficient, $\mathbf{D_a}$

Radial, or transverse dispersion, coefficient, $\mathbf{D_r}$

Molecular Diffusion Coefficient, $\mathbf{D_m}$

Total bed length, **L**

Length of packed section, $\mathbf{L_p}$

Tube to particle diameter ratio, **N**

Radial Peclet number, $\mathbf{Pe_r}$

Mass Peclet number, $\mathbf{Pe_m}$

Bed radius, **R**

Particle Reynolds Number, **Re**

Interstitial velocity, $\mathbf{v_0}$

Axial Interstitial Velocity, $\mathbf{v_{i,z}}$

Inlet superficial velocity, $\mathbf{v_{in}}$

Radial Coordinate, $\mathbf{x_i}$

Bed depth, $\mathbf{z_i}$

8. Literature Cited

Allain, F. (2011). *Evaluation of the Classical Reaction Engineering models in terms of mass transport and reaction rate distribution for low tube-to-particle diameter ratio beds* (Unpublished Master of Science thesis). Worcester Polytechnic Institute, Worcester, Massachusetts.

Augier, F., Idoux, F., & Delenne, J.Y. (2010). Numerical simulations of transfer and transport properties inside packed beds of spherical particles. *Chemical Engineering Science, 65,* 1055 – 1064.

Coelho, M.A.N., Guedes De carvalho, J.R.F. (1988). Transverse dispersion in granular beds. *Chemical Engineering Researcn and Design, 66,* 166 – 177.

Delgado, J.M.P.Q. (2006). A critical review of dispersion in packed beds. *Heat Mass Transfer, 42,* 279 – 310.

Delgado, J.M.P.Q. (2007). Longitudinal and transverse dispersion in porous media. *Chemical Engineering Research and Design, 85(A9),* 1245 – 1252.

Dixon, A.G., Nijemiesland, M., & Stitt, E.H. (2013). Systematic mesh development for 3D CFD simulation of fixed beds: Contact point study. *Computer and Chemical Engineering,* 48¸135-153.

Eppinger, T., Seidler, K., & Kraume, M. (2011). DEM-CFD simulations of fixed bed reactors with small tube to particle diameter ratios. *Chemical Engineering journal, 166,* 324 – 331.

Fahien, R.W., Smith, J.M. (1955). Mass transfer in packed beds. *AIChE Journal, 1,* 28 – 37.

Fluent UNS version 14.5 User's Guide (2011). ANSYS, Inc.

Freund, h., Zeiser, T., Huber, F., Klemm, E., Brenner, G., Durst, F., & Emig, G. (2003). Numerical simulations of single phase reacting flows in randomly packed fixed-bed reactors and experimental validation. *Chemical Engineering Science, 58,* 903 – 910.

Giese, M., Rottschafer, K. & Vortmeyer, D. (1998). Measured and modeled superficial flow profiles in packed beds with liquid flow. *AIChE Journal, 44,* 484 – 490.

Guardo, A., Coussirat, m., Larrayoz, M.A., Recasens, F., & Egusquiza, E., (2004). CFD flow and heat transfer in nonregular packings for fixed bed equipment design. *Industrial & Engineering Chemistry Research, 43,* 7049 – 7056.

Guedes de Carvalho, J.R.F., Delgado, J.M.P.Q. (2000). Lateral dispersion in liquid flow through packed beds at Pe_m > 1,400. *AIChE Journal, 46, (5)* 1089 – 1095.

Gunn, D.J. (1969). Theory of axial and radial dispersion in packed beds. *Transactions of the Institution of Chemical Engineers, 47,* 351 – 359.

Jourak, A., Gunnar Hellstrom, J., & Staffan Jundstrom, T. (2014). Numerical derivation of dispersion coefficients for flow through three-dimensional randomly packed beds of monodisperse spheres. *AIChE Journal, 60(2),* 749 – 759.

Langsch, R., Mueller, A., Haase, S., & Lange, R. (2013). Proceedings from AICHE 2013 Annual Meeting Catalyst and Reaction Engineering Division: *Process intensification of gas-liquid-solid reactions in the production of fine chemicals with milli packed bed reactors*. San Francisco, CA.

Logtenberg, S.A., Nijeisland, M., & Dixon, A.G. (1999). Computational fluid dynamics simulations of fluid flow and heat transfer at the wall-particle contact points in a fixed bed reactor. *Chemical Engineering Science, 54,* 2433 – 2439.

Magnico, P. (2003). Hydrodynamic and transport properties of packed beds in small tube-to-sphere diameter ratio; pore scale simulation using an Eurlerian and a Lagrangian approach. *Chemical Engineering Science, 58,* 5005 – 5024.

Nijemeisland, M., Dixon, A.G. (2001). Comparison of CFD simulations to experiment for convective heat transfer in a gas-solid fixed bed. *Chemical Engineering Journal, 82,* 231-246.

Ookawara, S., Kuroki, M., Street, D., & Ogawa, K. (2007). High-fidelity DEM-CFD modeling of packed bed reactors for process intensification. Paper no. 1005, ECCE-6 proceedings CD. *Europena Congress of Chemical Engineering, 6.* ISBN 978-87-91435-57-9.

Schnitzlein, K. (2001). Modelling radial dispersion in terms of the local structure of packed beds. *Chemical Engineering Science, 56,* 579-585.

9. Appendix A

Reactor Data Sheets

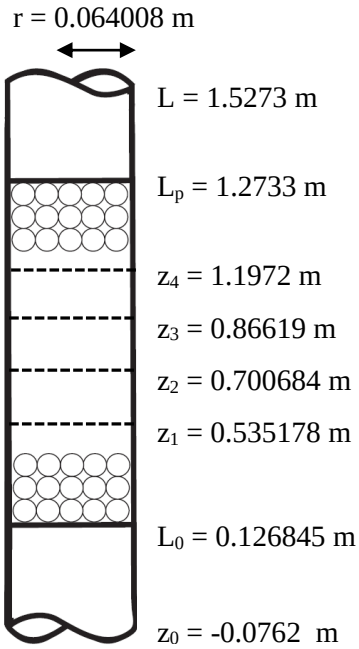

Figure A-01. N = 5.04 Reactor Data Sheet.

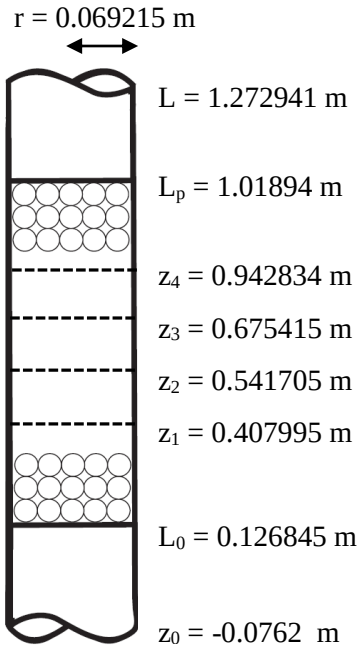

Figure A-02. N = 5.45 Reactor Data Sheet.

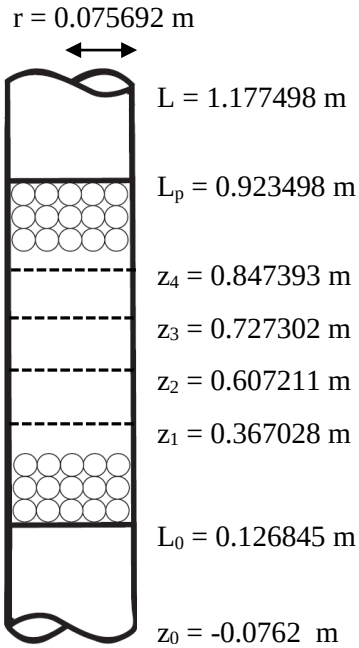

Figure A-03. N = 5.96 Reactor Data Sheet.

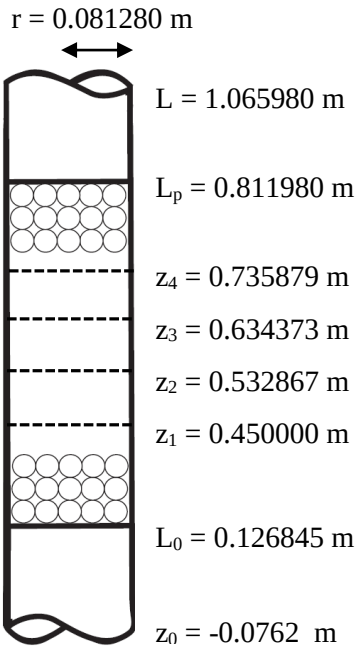

Figure A-04. N = 6.40 Reactor Data Sheet.

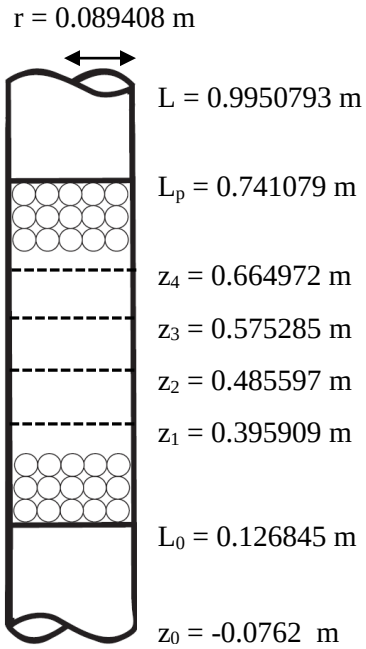

Figure A-05. N = 7.04 Reactor Data Sheet.

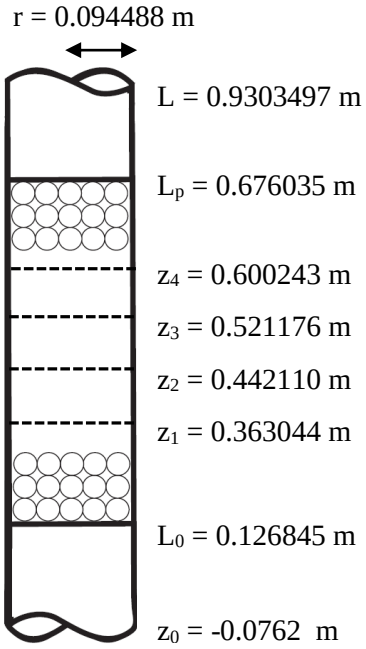

Figure A-06. N = 7.44 Reactor Data Sheet.

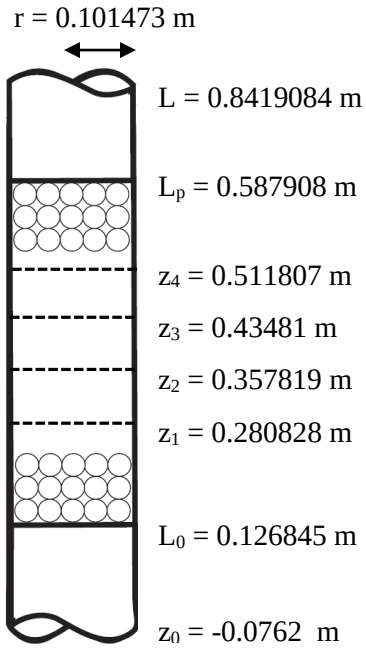

Figure A-07. N = 7.99 Reactor Data Sheet.

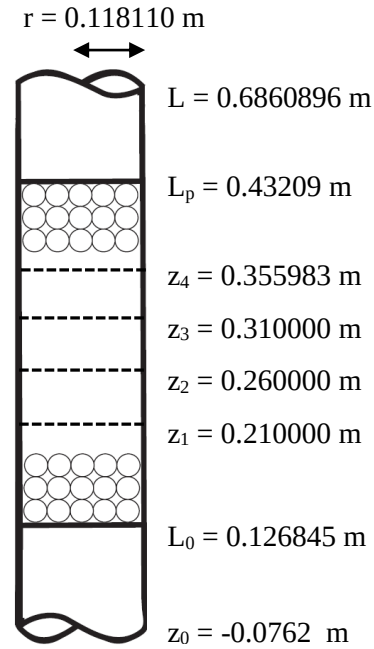

Figure A-08. N = 9.30 Reactor Data Sheet.

10. Appendix B

Local Velocity Profiles

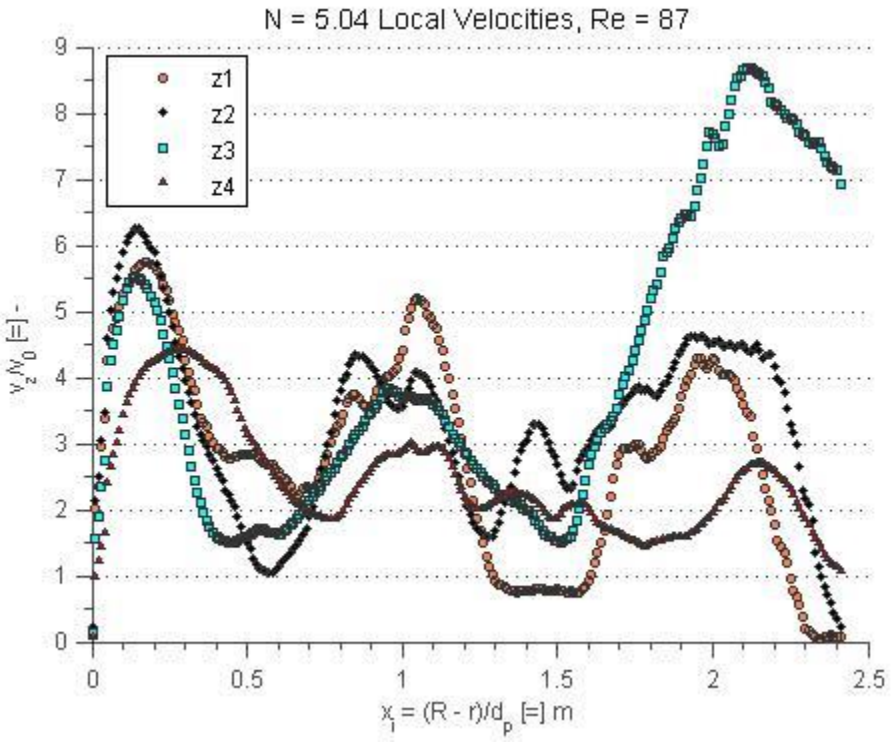

Figure B-01. Local Velocity vs. Radial Coordinate, N = 5.04, Re =87.

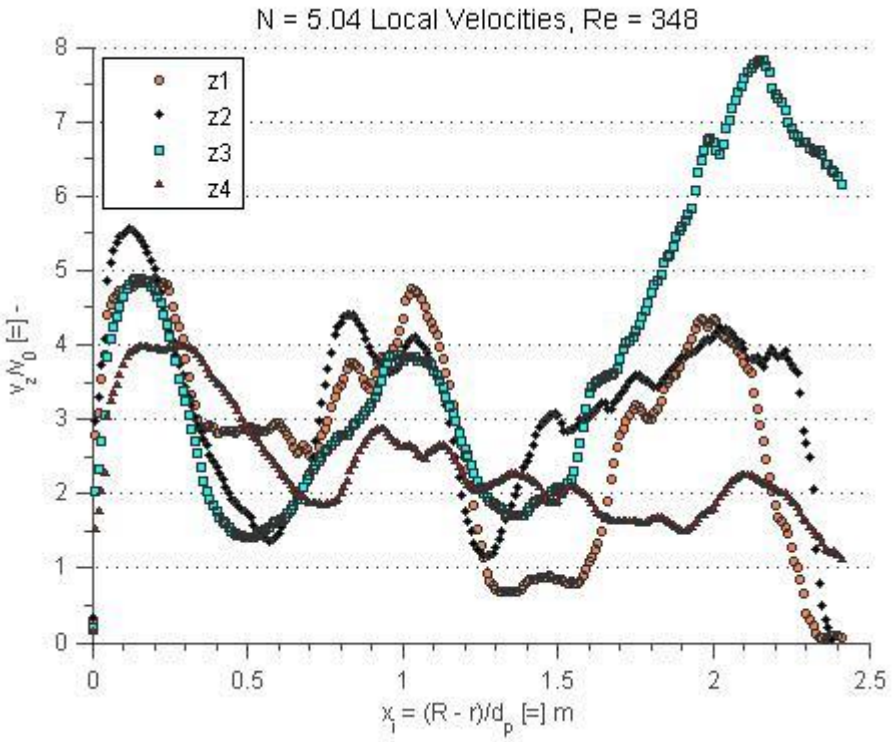

Figure B-02. Local Velocity vs. Radial Coordinate, N = 5.04, Re = 348.

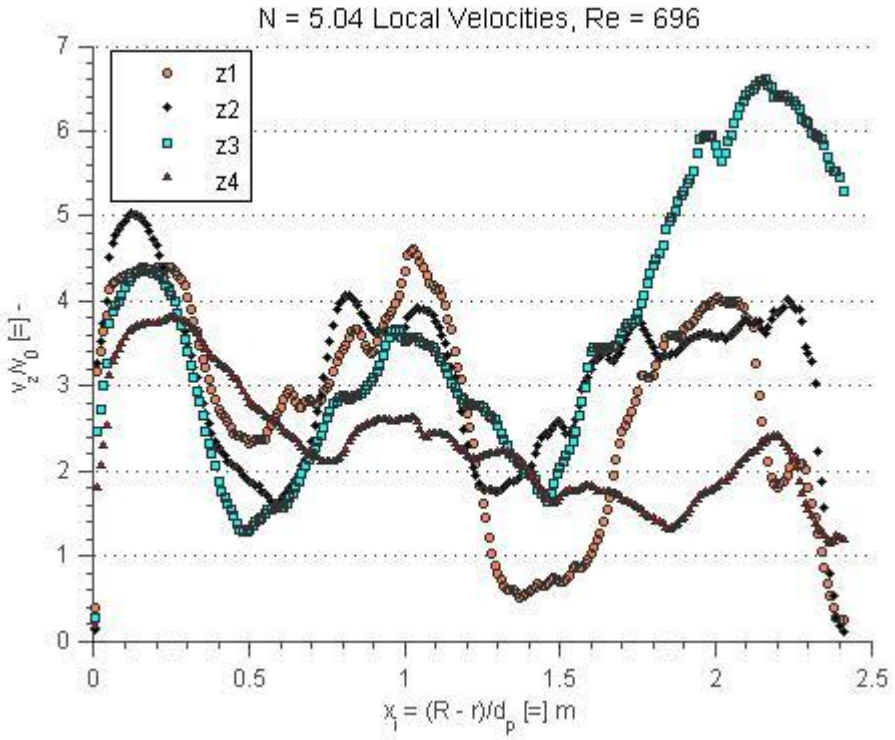

Figure B-03. Local Velocity vs. Radial Coordinate, N = 5.04, Re = 696.

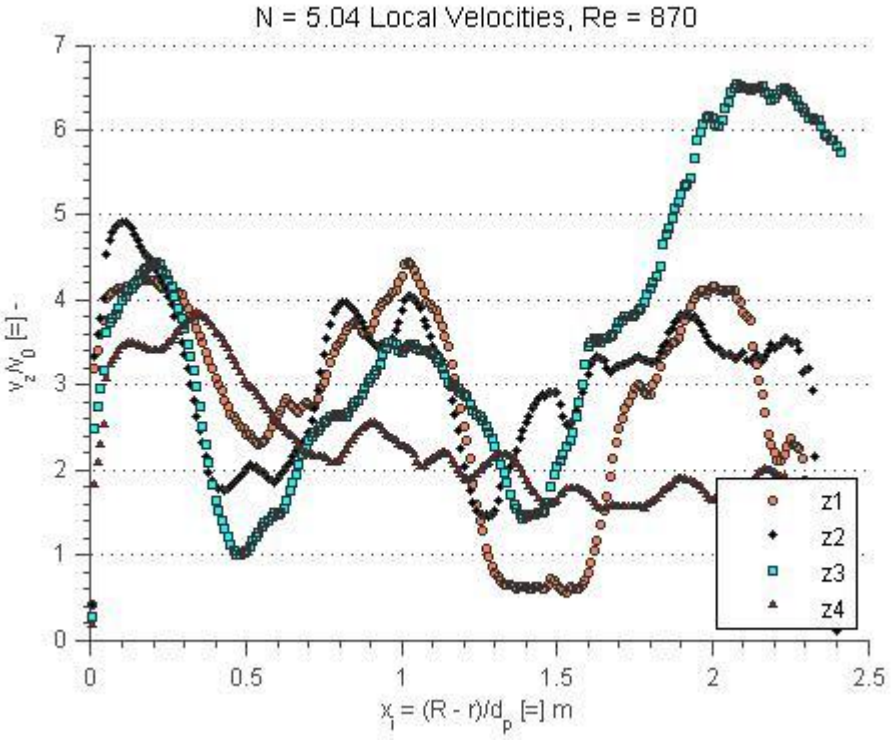

Figure B-04. Local Velocity vs. Radial Coordinate, N = 5.04, Re = 870.

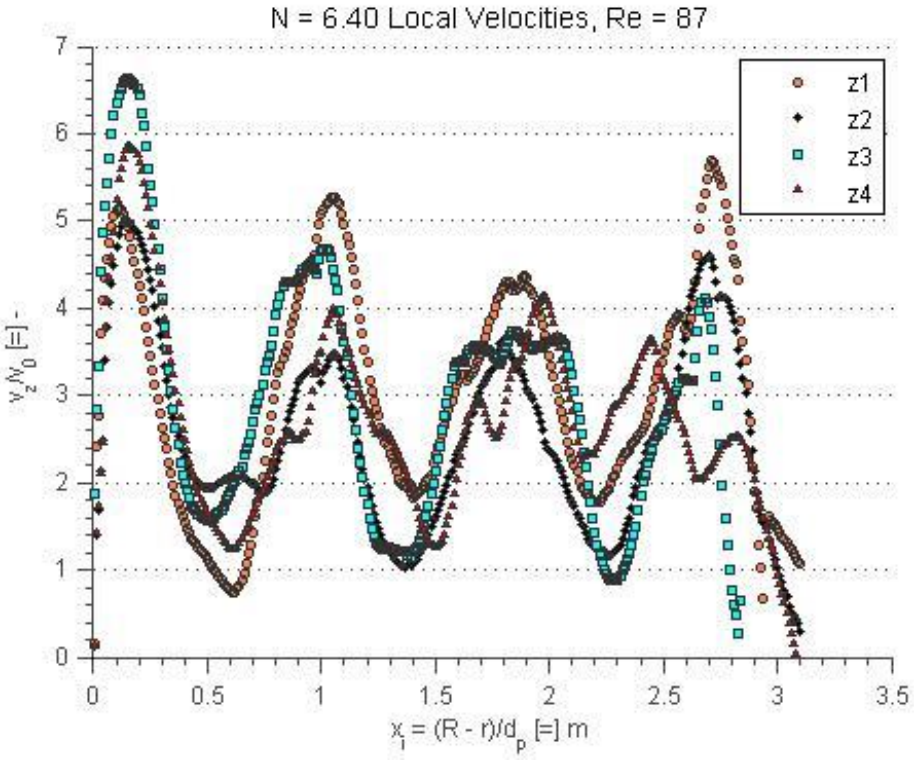

Figure B-05. Local Velocity vs. Radial Coordinate, N = 6.40, Re = 87.

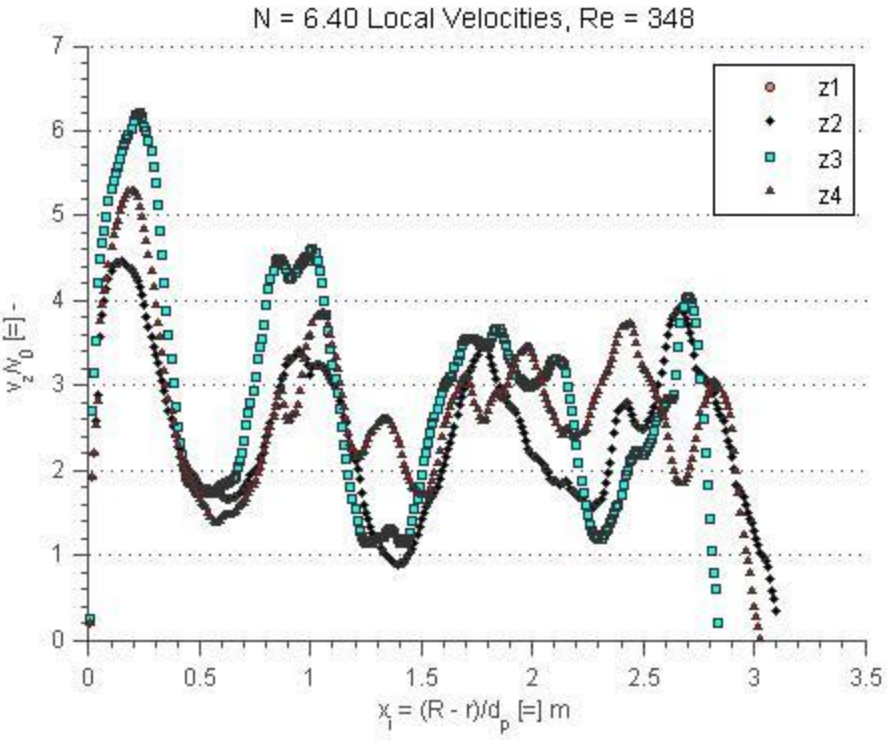

Figure B-06. Local Velocity vs. Radial Coordinate, N = 6.40, Re = 348.

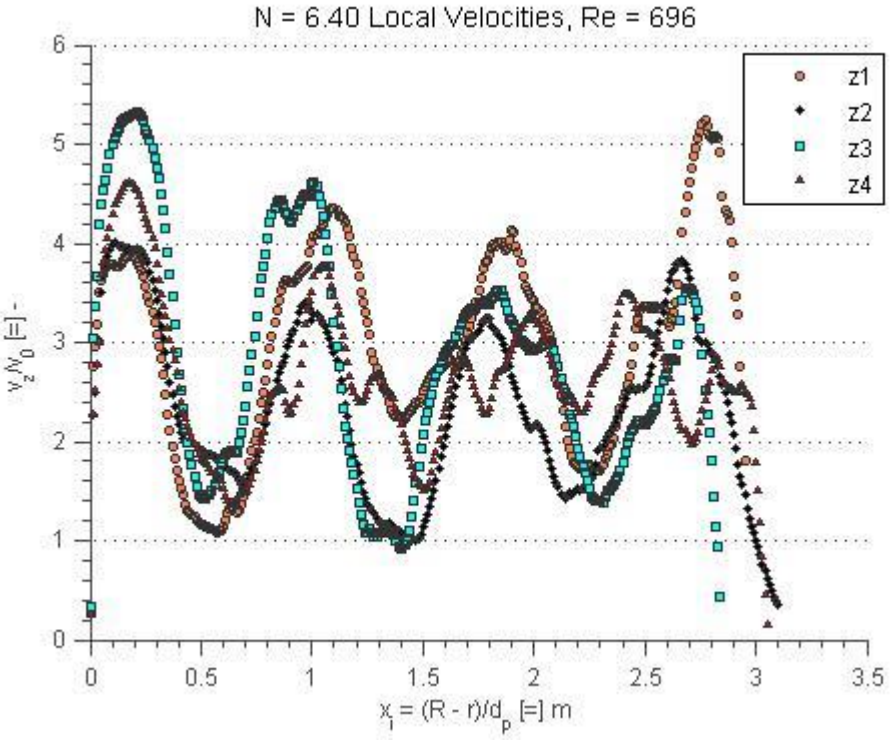

Figure B-07. Local Velocity vs. Radial Coordinate, N = 6.40, Re = 696.

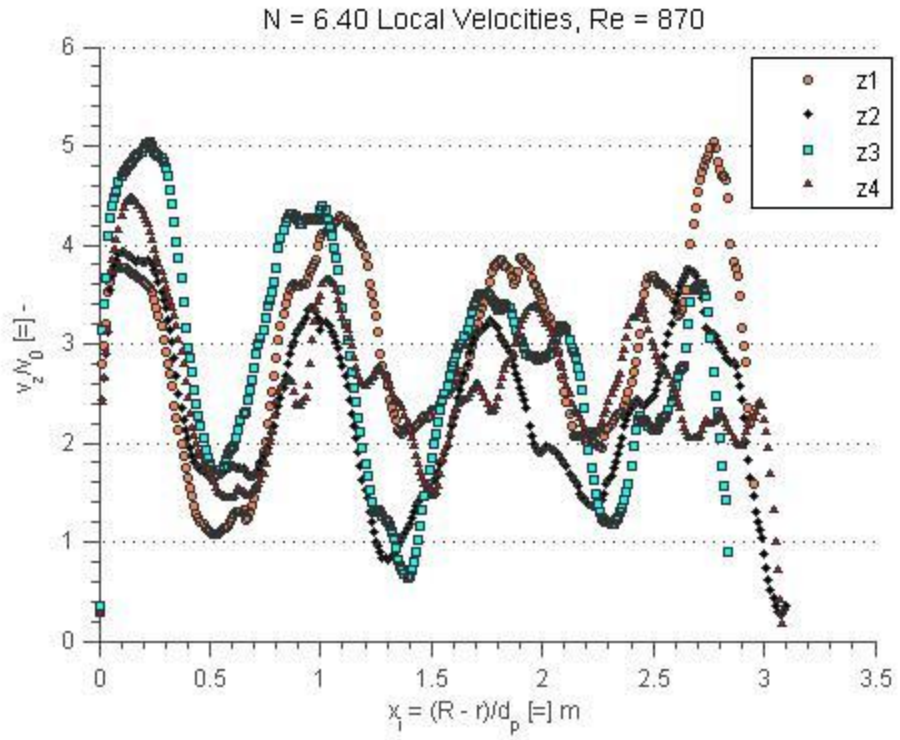

Figure B-08. Local Velocity vs. Radial Coordinate, N = 6.40, Re = 870.

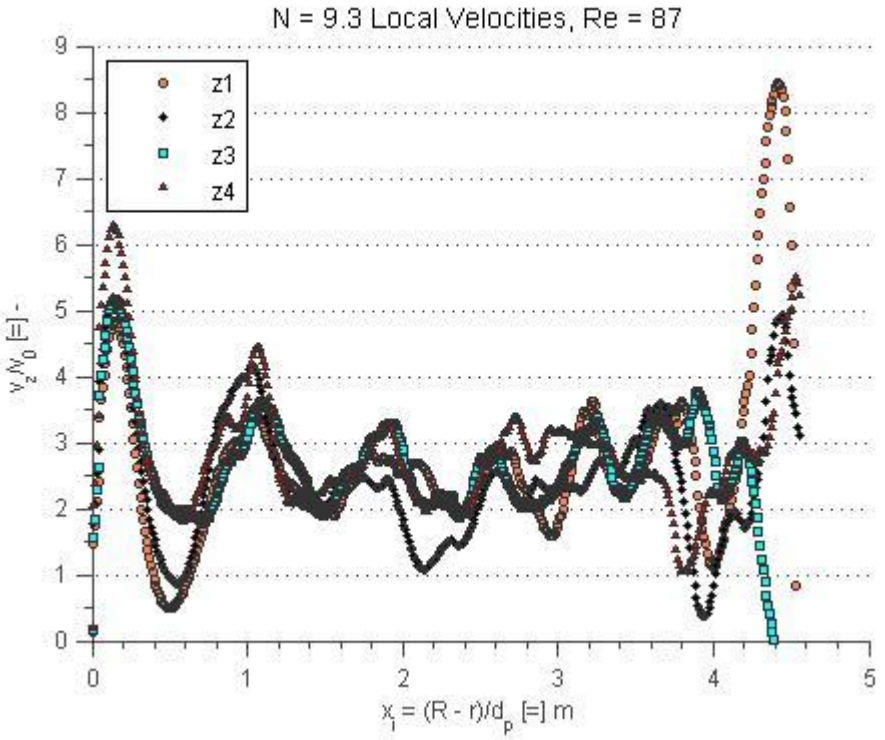

Figure B-09. Local Velocity vs. Radial Coordinate, N = 9.3, Re = 87.

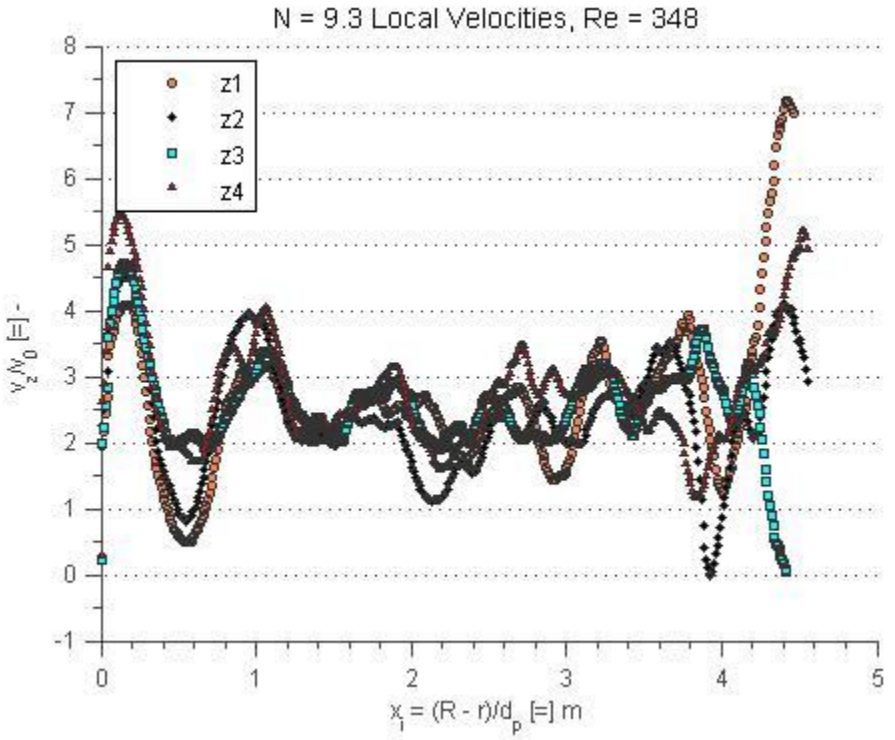

Figure B-10. Local Velocity vs. Radial Coordinate, N = 9.3, Re = 348.

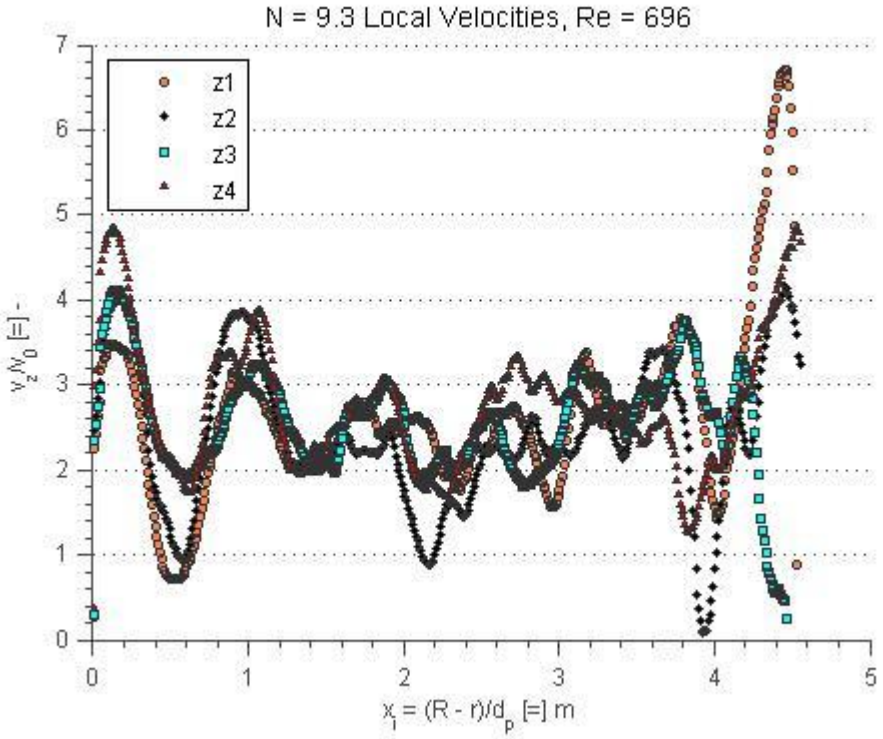

Figure B-11. Local Velocity vs. Radial Coordinate, N = 9.3, Re = 696.

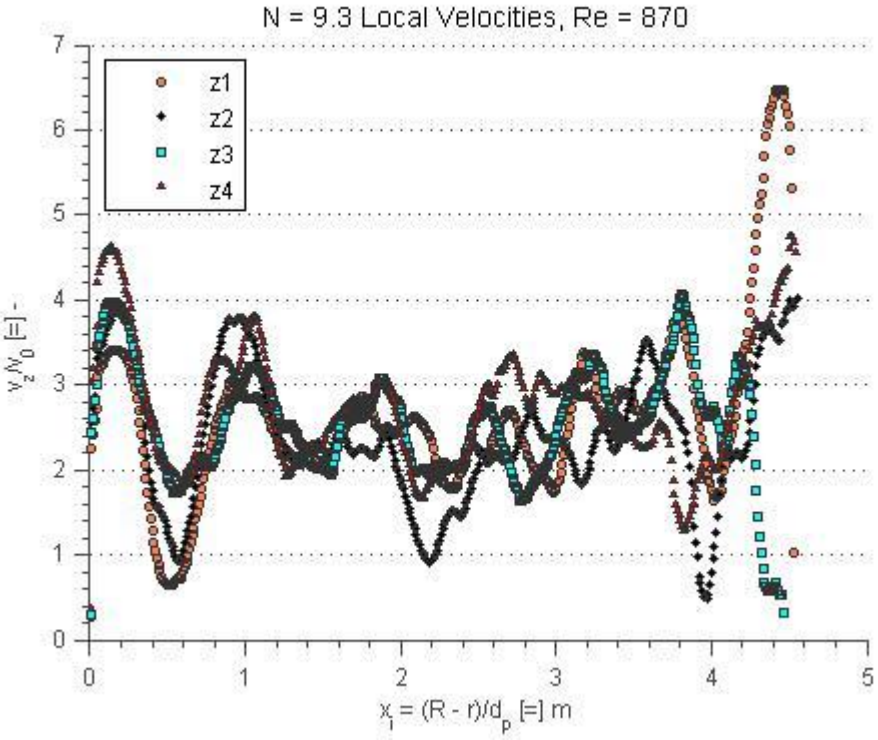

Figure B-12. Local Velocity vs. Radial Coordinate, N = 9.3, Re = 870.

11. Appendix C

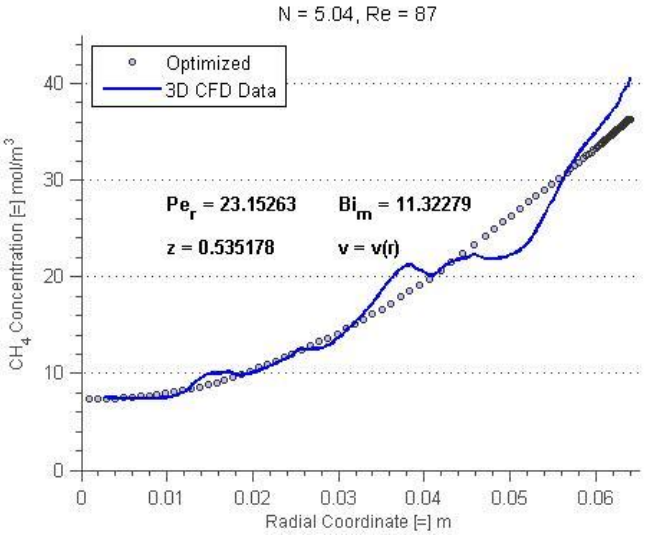

Figure C-001. Fitted radial concentration profile for N = 5.04, Re = 87, bed depth 01.

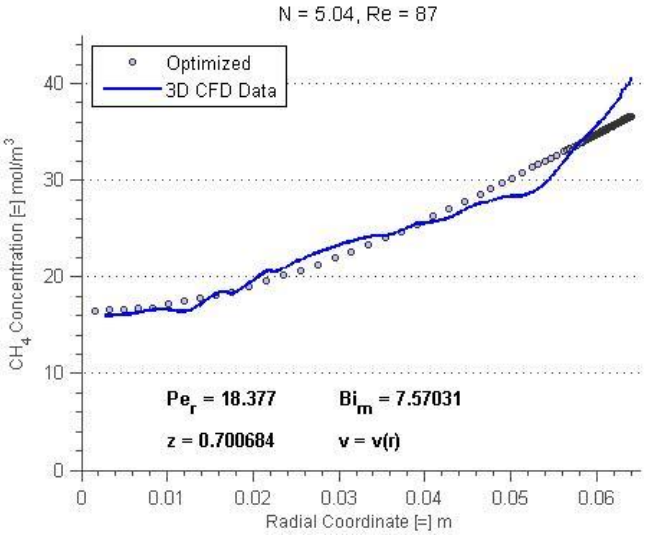

Figure C-002. Fitted radial concentration profile for N = 5.04, Re = 87, bed depth 02.

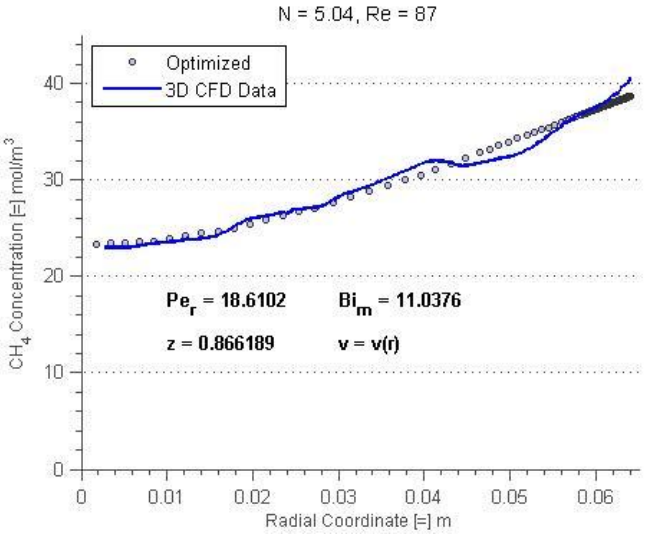

Figure C-003. Fitted radial concentration profile for N = 5.04, Re = 87, bed depth 03.

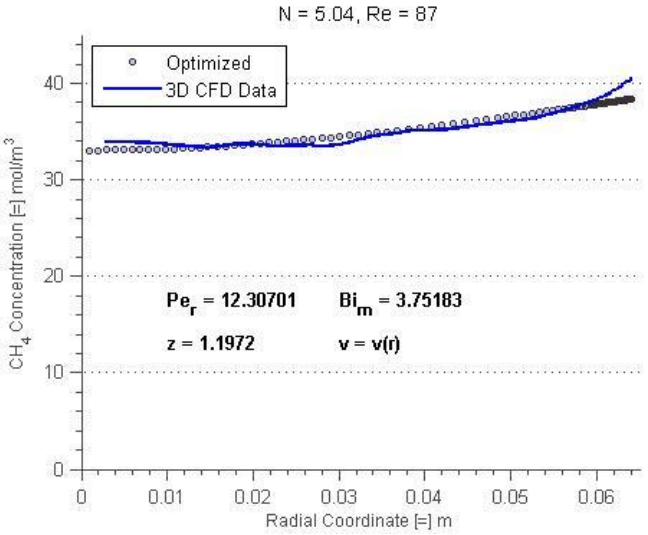

Figure C-004. Fitted radial concentration profile for N = 5.04, Re = 87, bed depth 04.

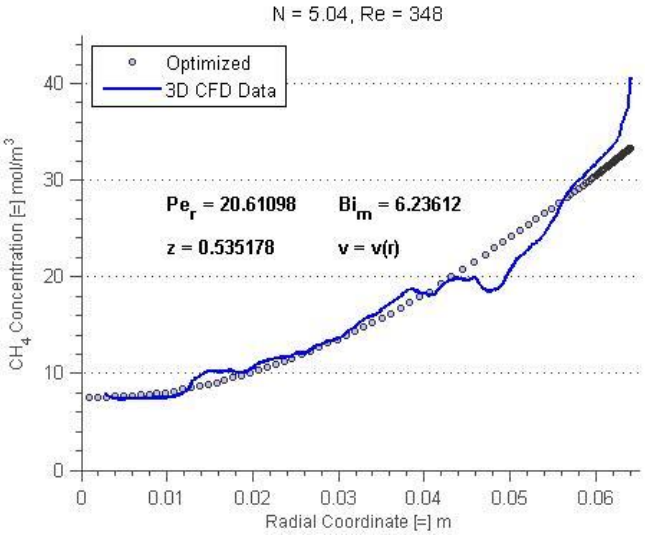

Figure C-005. Fitted radial concentration profile for N = 5.04, Re = 348, bed depth 01.

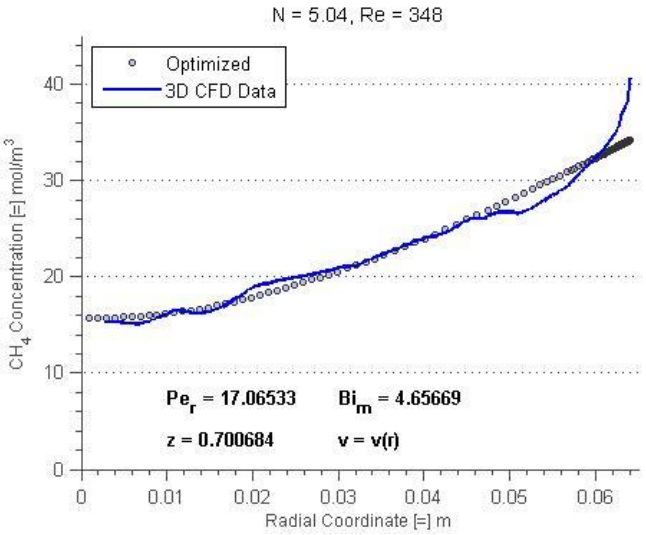

Figure C-006. Fitted radial concentration profile for N = 5.04, Re = 348, bed depth 02.

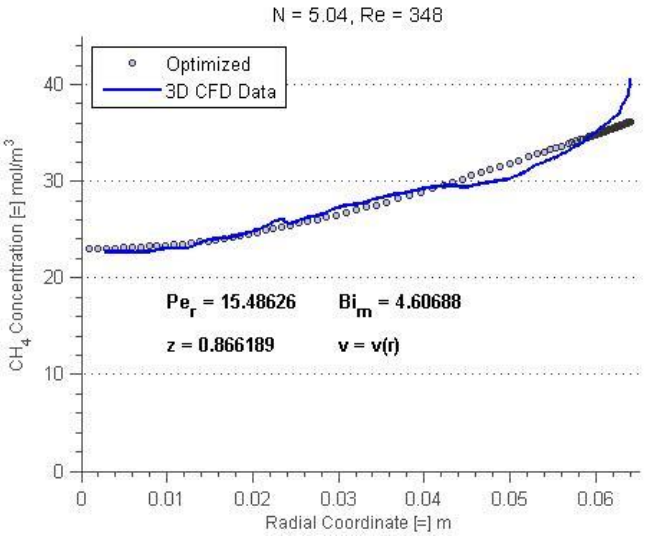

Figure C-007. Fitted radial concentration profile for N = 5.04, Re = 348, bed depth 03.

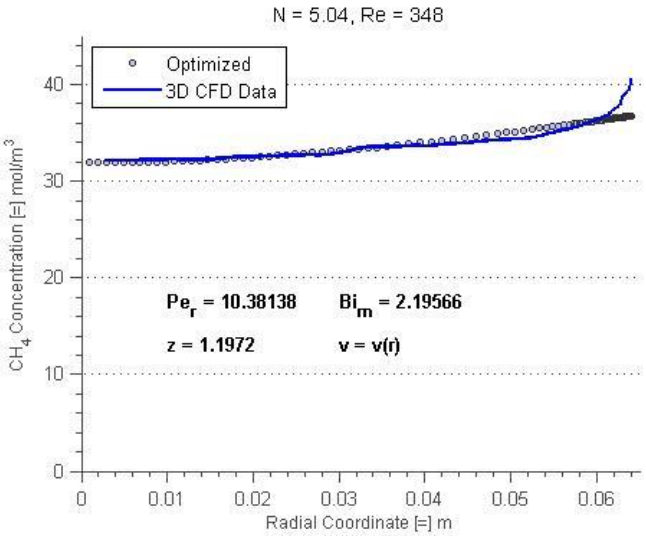

Figure C-008. Fitted radial concentration profile for N = 5.04, Re = 348, bed depth 04.

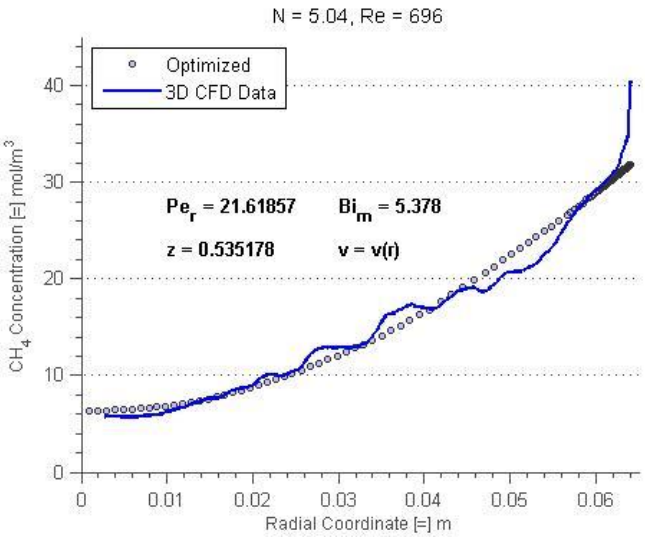

Figure C-009. Fitted radial concentration profile for N = 5.04, Re = 696, bed depth 01.

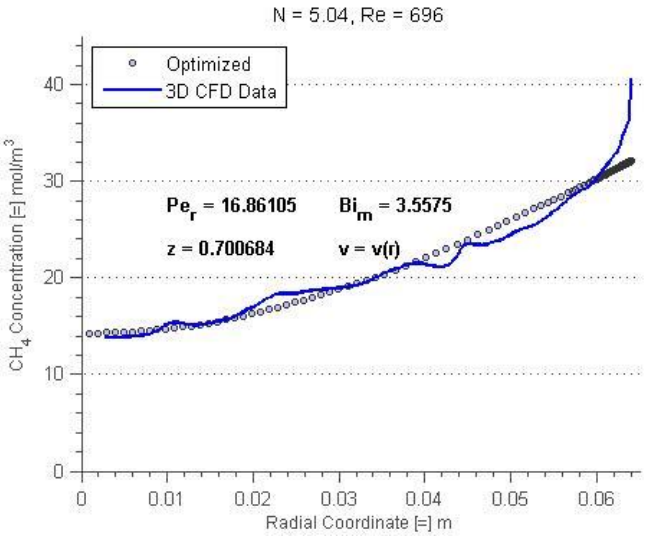

Figure C-010. Fitted radial concentration profile for N = 5.04, Re = 696, bed depth 02.

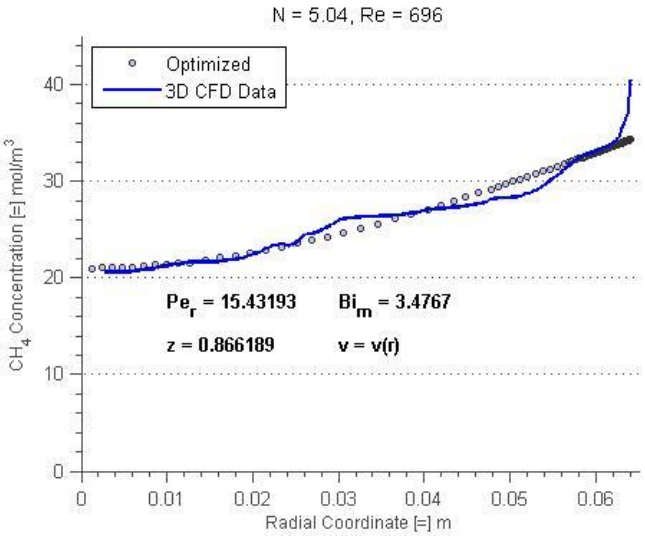

Figure C-011. Fitted radial concentration profile for N = 5.04, Re = 696, bed depth 03.

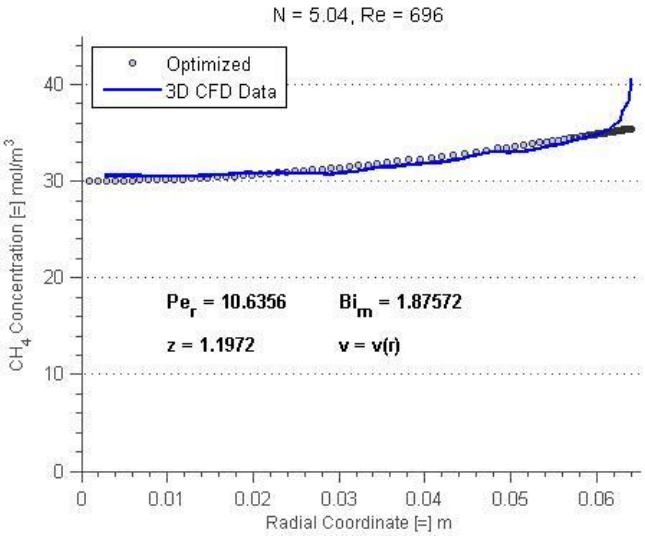

Figure C-012. Fitted radial concentration profile for N = 5.04, Re = 696, bed depth 04.

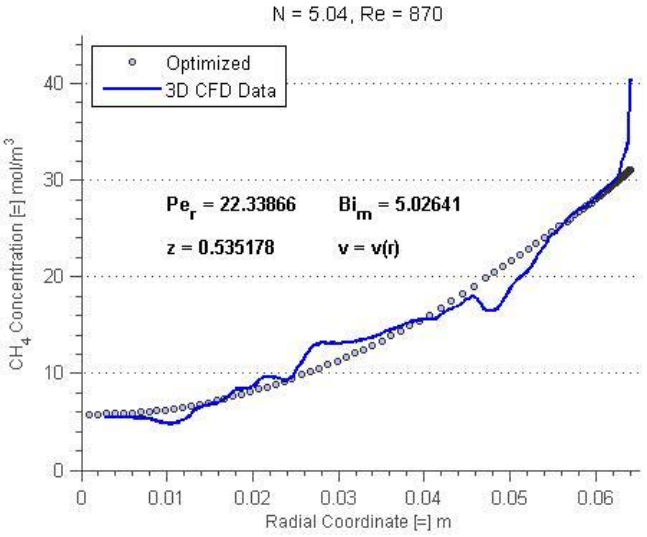

Figure C-013. Fitted radial concentration profile for N = 5.04, Re = 870, bed depth 01.

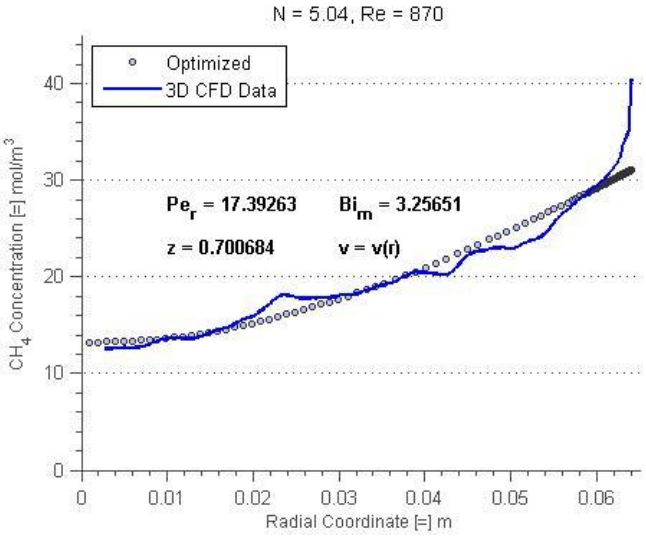

Figure C-014. Fitted radial concentration profile for N = 5.04, Re = 870, bed depth 02.

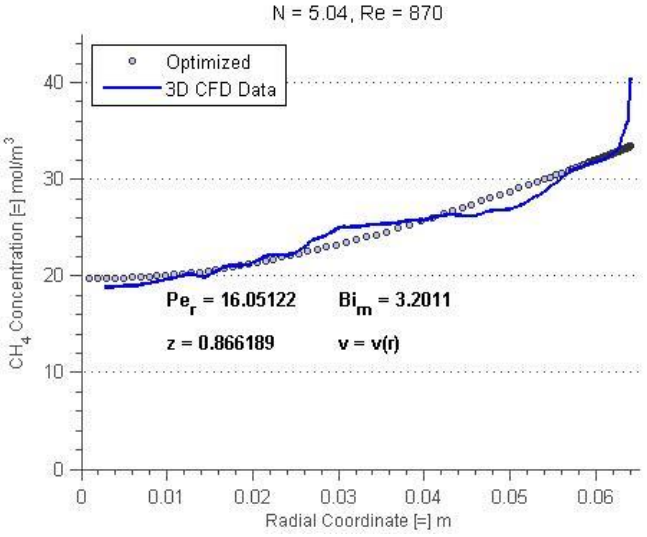

Figure C-015. Fitted radial concentration profile for N = 5.04, Re = 870, bed depth 03.

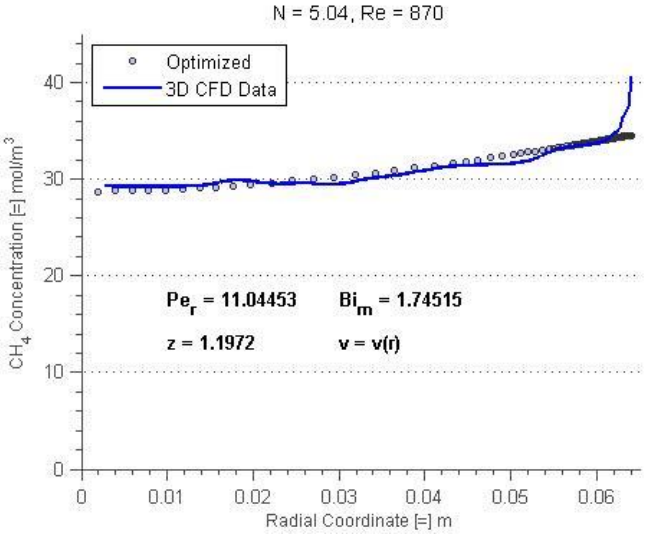

Figure C-016. Fitted radial concentration profile for N = 5.04, Re = 870, bed depth 04.

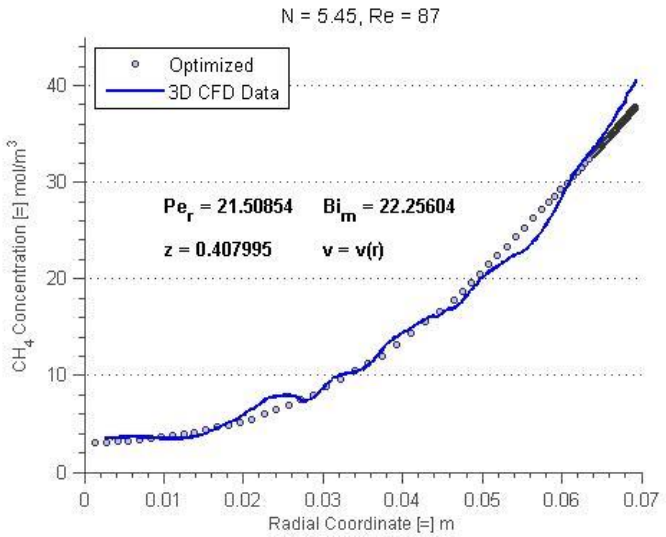

Figure C-017. Fitted radial concentration profile for N = 5.45, Re = 87, bed depth 01.

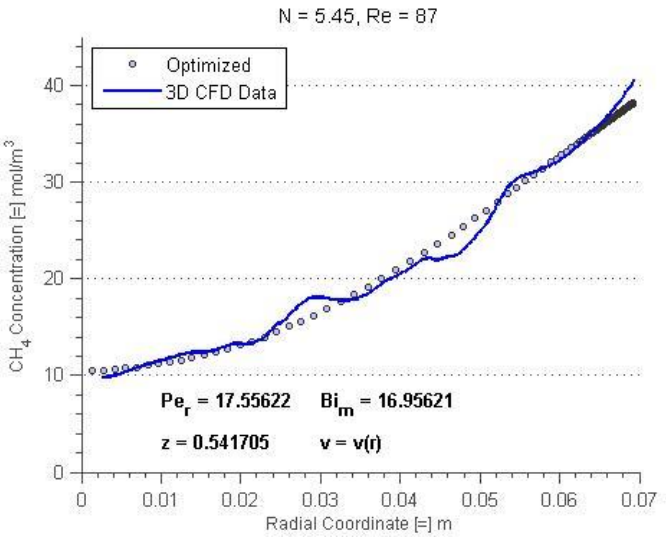

Figure C-018. Fitted radial concentration profile for N = 5.45, Re = 87, bed depth 02.

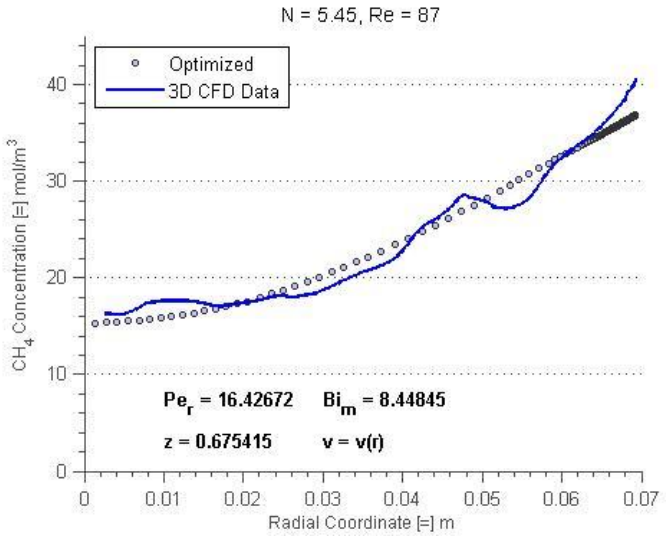

Figure C-019. Fitted radial concentration profile for N = 5.45, Re = 87, bed depth 03.

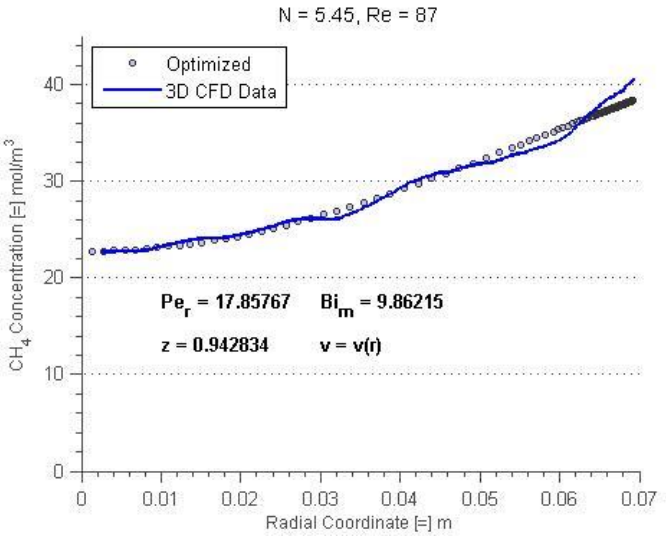

Figure C-020. Fitted radial concentration profile for N = 5.45, Re = 87, bed depth 04.

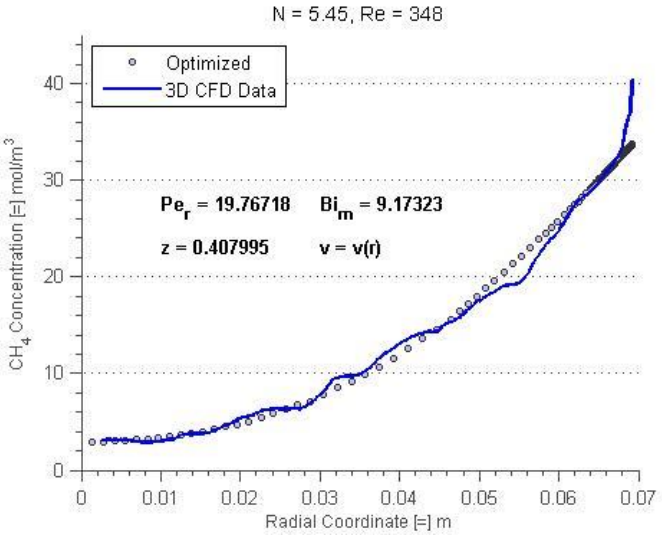

Figure C-021. Fitted radial concentration profile for N = 5.45, Re = 348, bed depth 01.

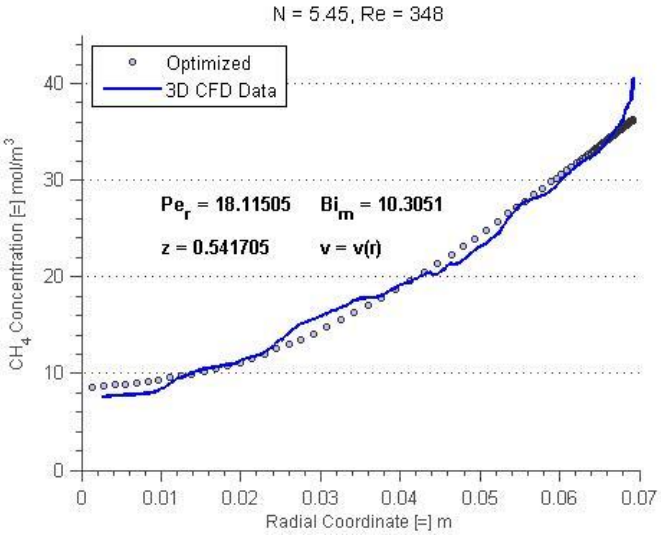

Figure C-022. Fitted radial concentration profile for N = 5.45, Re = 348, bed depth 02.

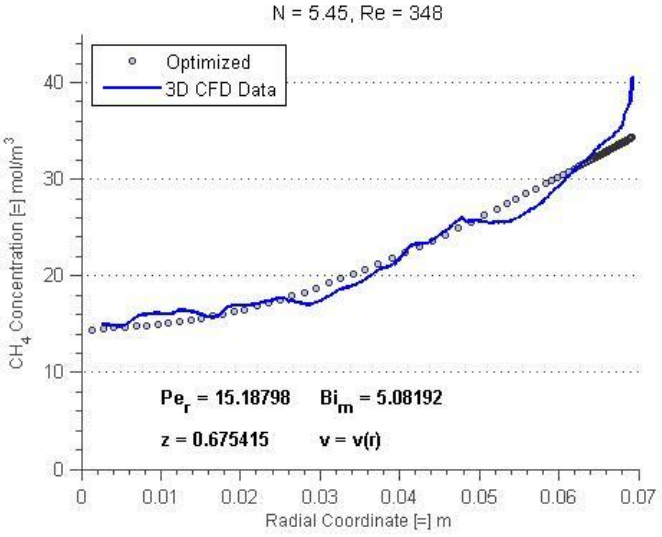

Figure C-023. Fitted radial concentration profile for N = 5.45, Re = 348, bed depth 03.

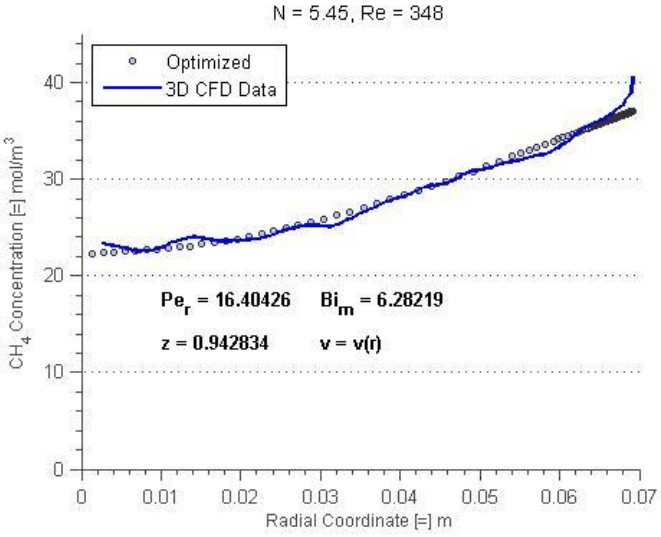

Figure C-024. Fitted radial concentration profile for N = 5.45, Re = 348, bed depth 04.

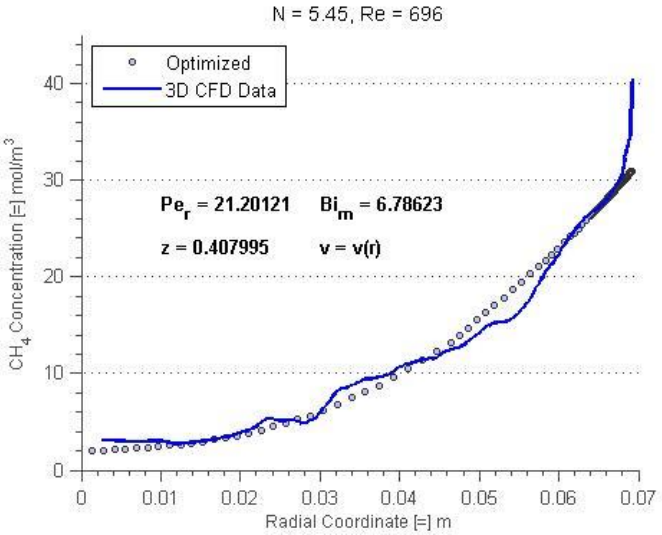

Figure C-025. Fitted radial concentration profile for N = 5.45, Re = 696, bed depth 01.

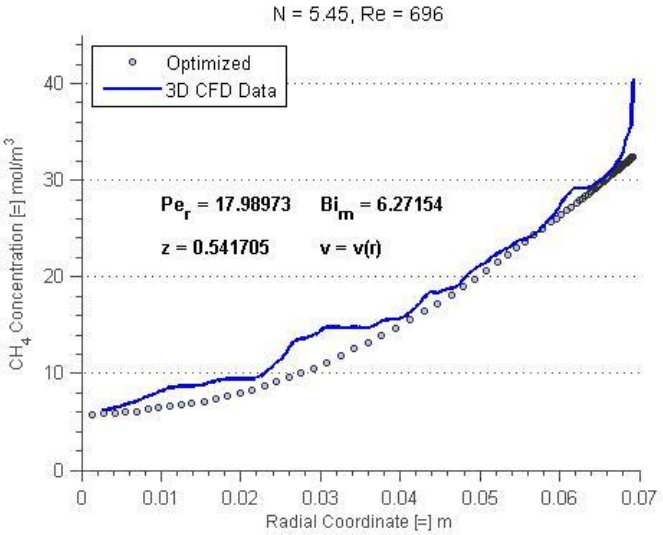

Figure C-026. Fitted radial concentration profile for N = 5.45, Re = 696, bed depth 02.

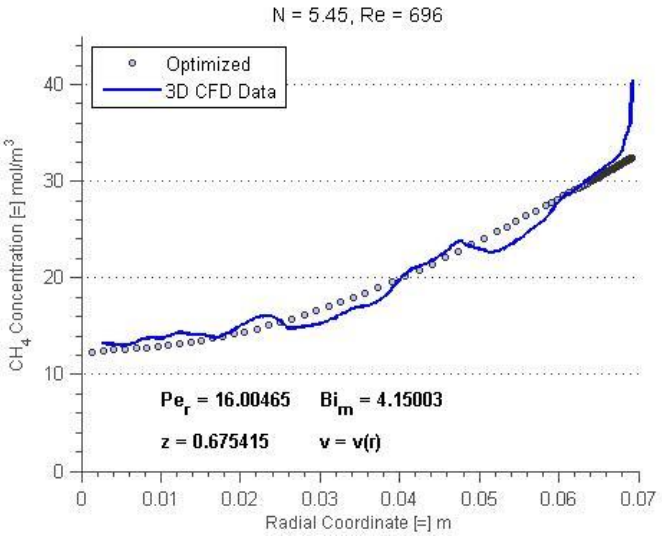

Figure C-027. Fitted radial concentration profile for N = 5.45, Re = 696, bed depth 03.

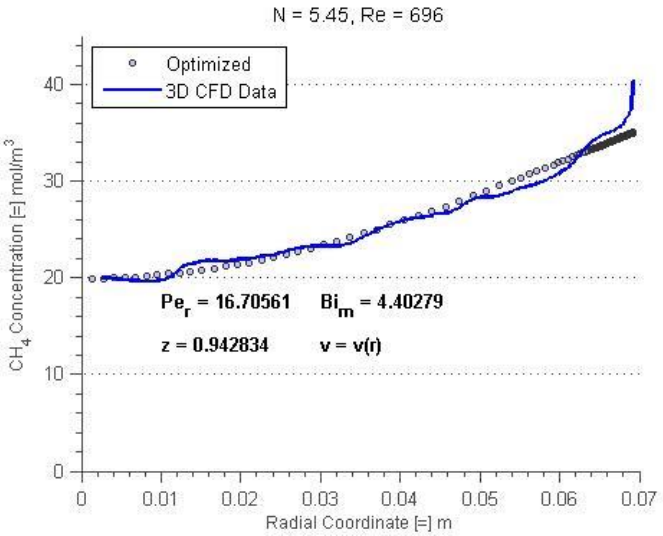

Figure C-028. Fitted radial concentration profile for N = 5.45, Re = 696, bed depth 04.

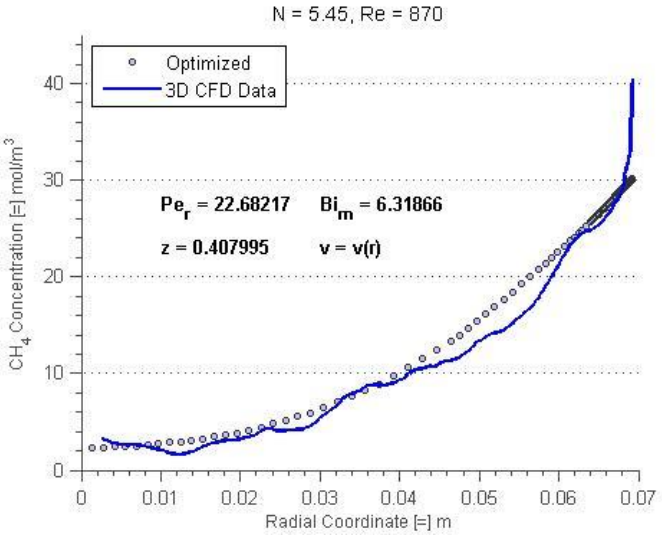

Figure C-029. Fitted radial concentration profile for N = 5.45, Re = 870, bed depth 01.

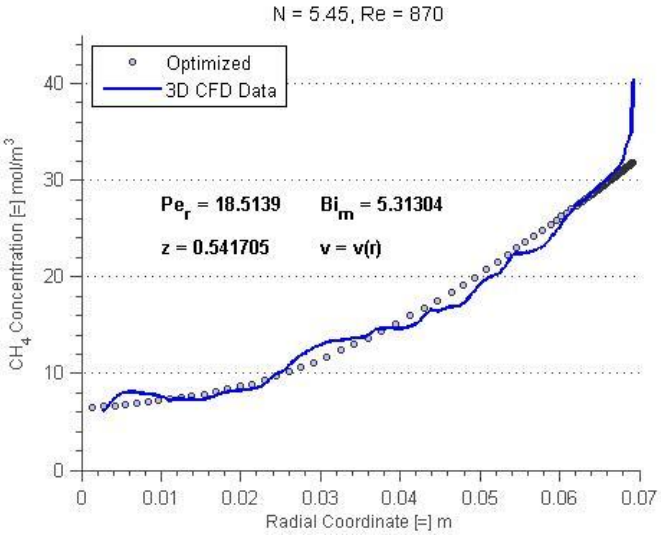

Figure C-030. Fitted radial concentration profile for N = 5.45, Re = 870, bed depth 02.

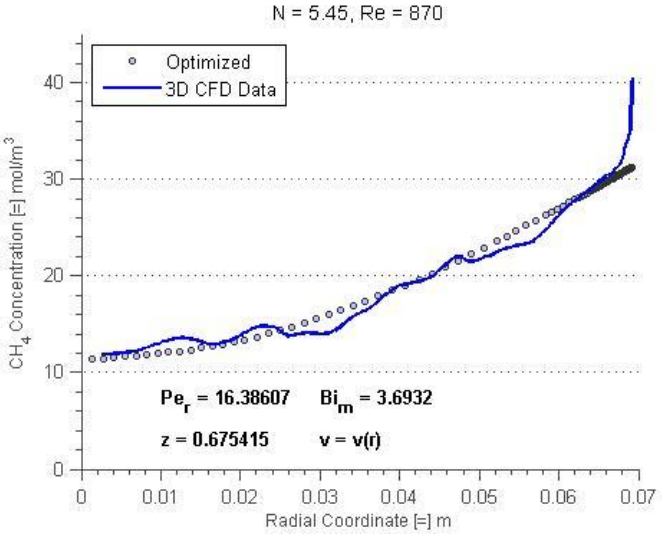

Figure C-031. Fitted radial concentration profile for N = 5.45, Re = 870, bed depth 03.

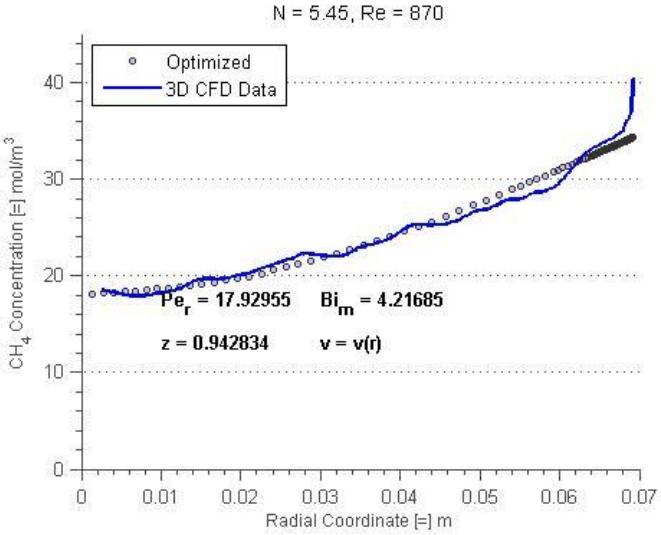

Figure C-032. Fitted radial concentration profile for N = 5.45, Re = 870, bed depth 04.

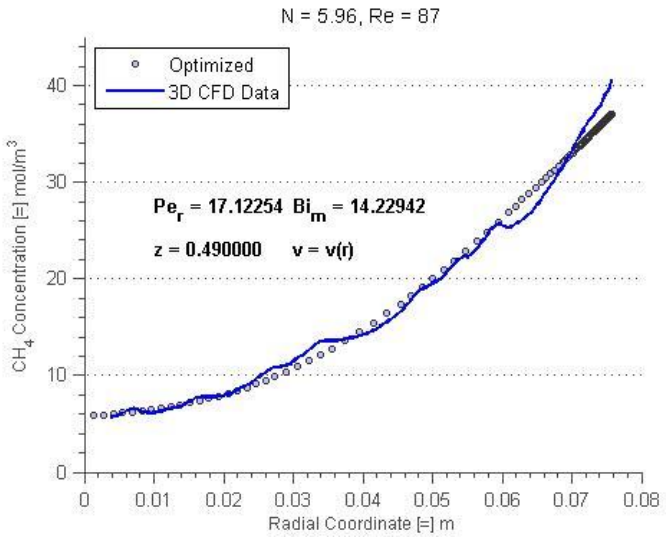

Figure C-033. Fitted radial concentration profile for N = 5.96, Re = 87, bed depth 01.

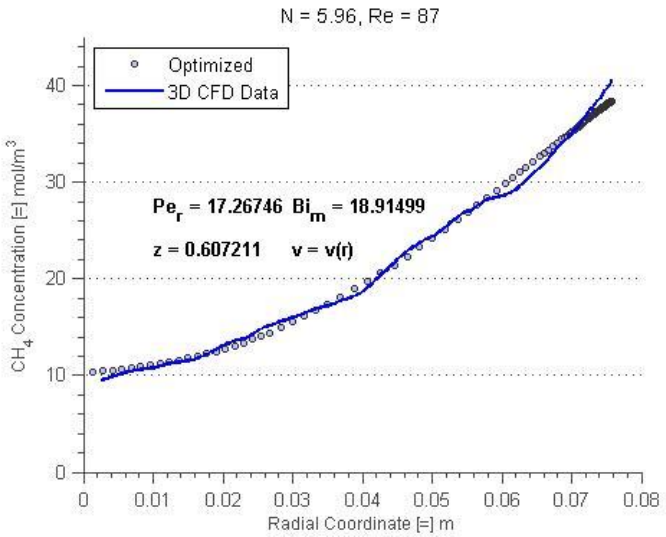

Figure C-034. Fitted radial concentration profile for N = 5.96, Re = 87, bed depth 02.

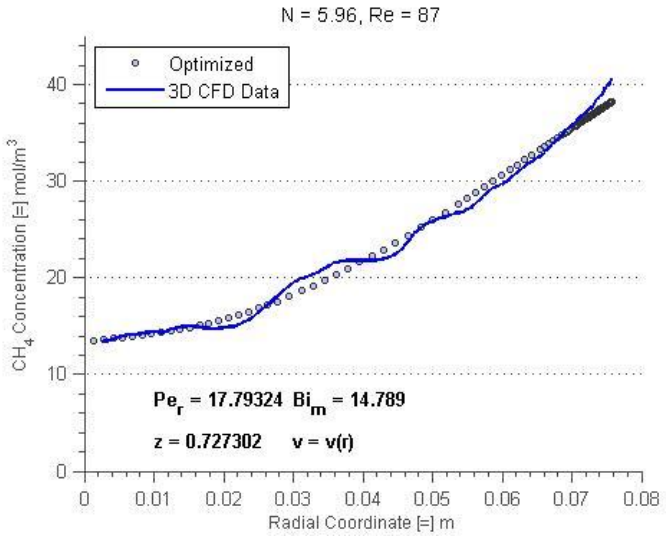

Figure C-035. Fitted radial concentration profile for N = 5.96, Re = 87, bed depth 03.

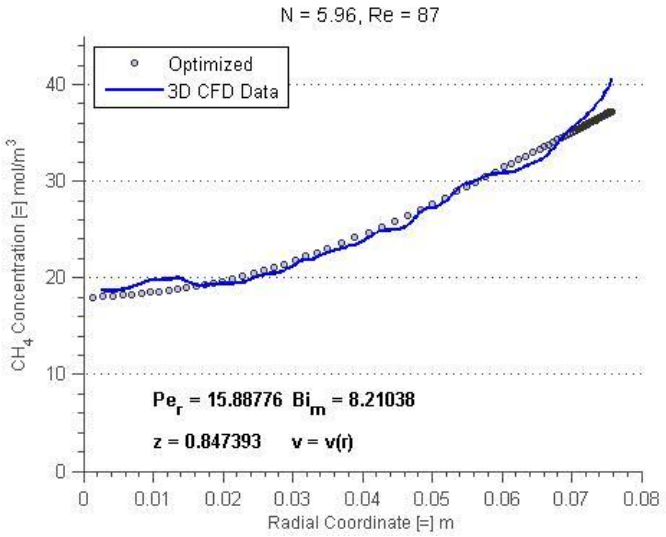

Figure C-036. Fitted radial concentration profile for N = 5.96, Re = 87, bed depth 04.

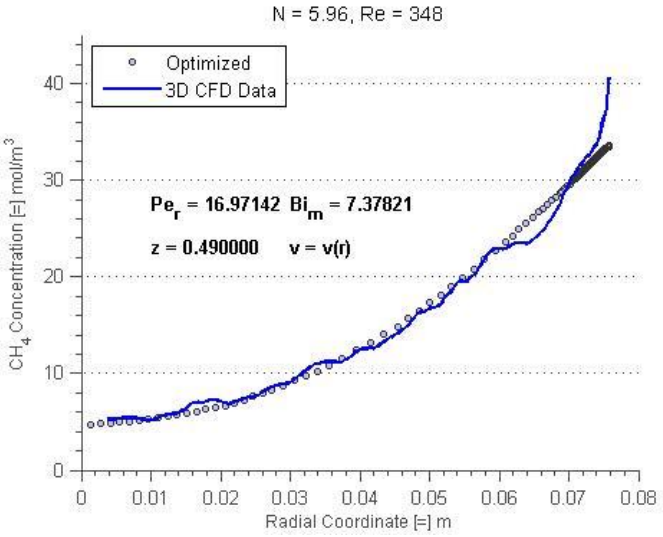

Figure C-037. Fitted radial concentration profile for N = 5.96, Re = 348, bed depth 01.

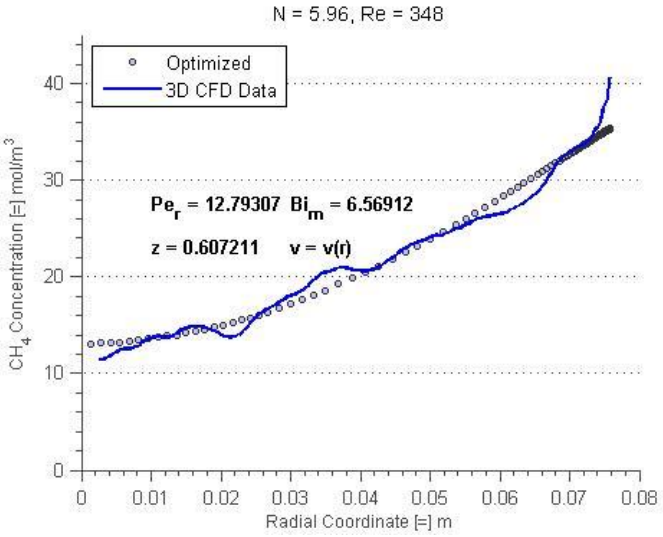

Figure C-038. Fitted radial concentration profile for N = 5.96, Re = 348, bed depth 02.

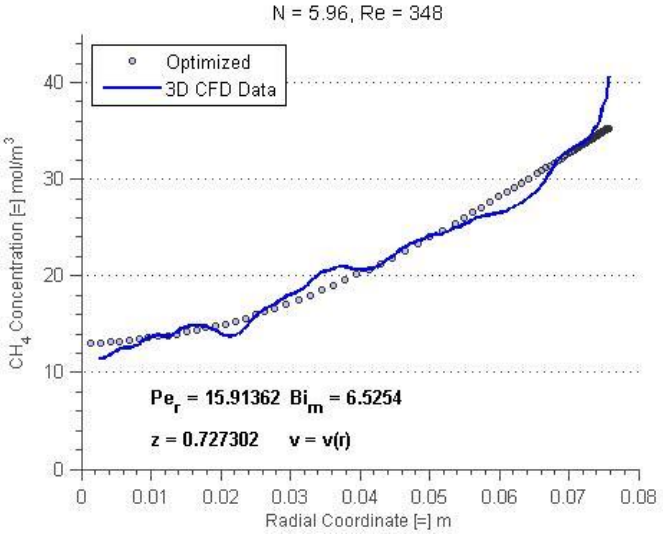

Figure C-039. Fitted radial concentration profile for N = 5.96, Re = 348, bed depth 03.

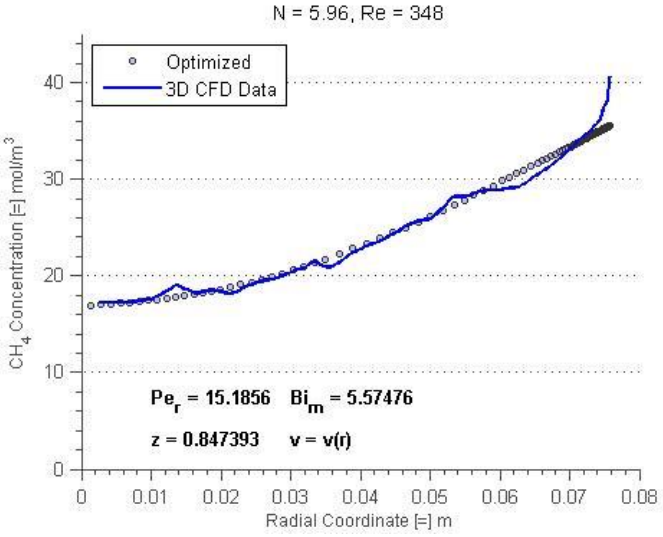

Figure C-040. Fitted radial concentration profile for N = 5.96, Re = 348, bed depth 04.

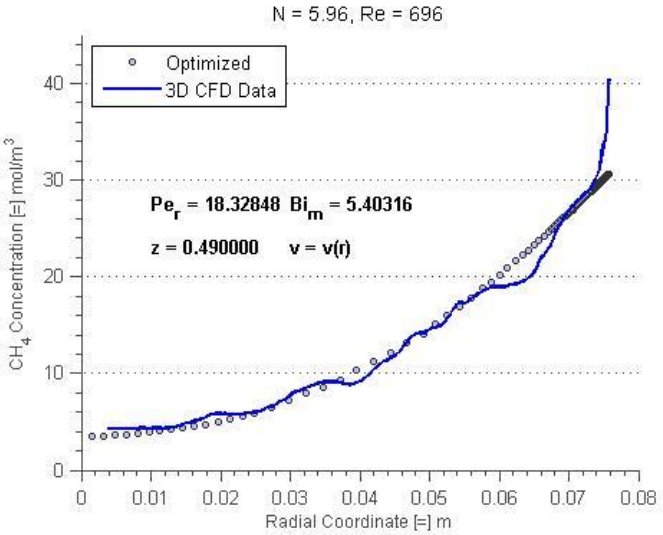

Figure C-041. Fitted radial concentration profile for N = 5.96, Re = 696, bed depth 01.

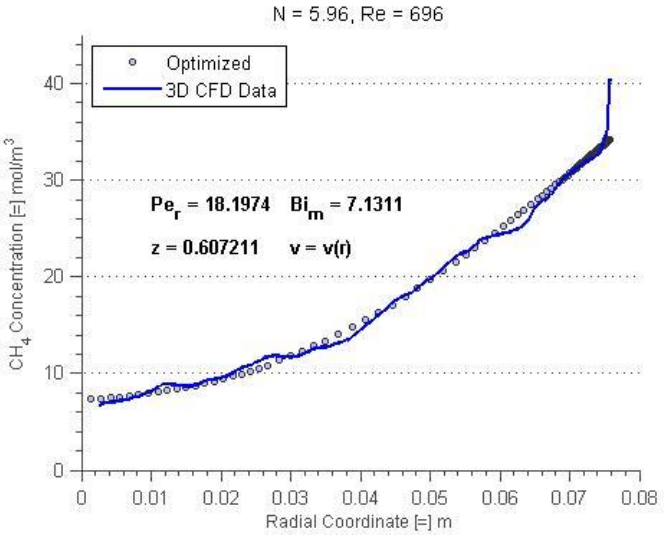

Figure C-042. Fitted radial concentration profile for N = 5.96, Re = 696, bed depth 02.

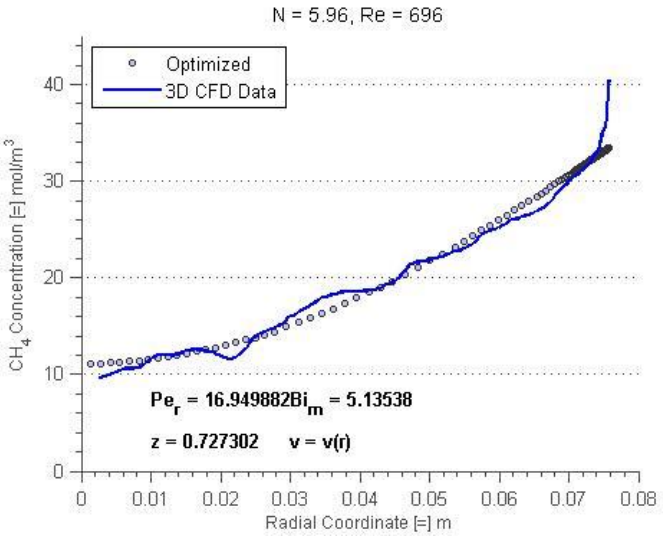

Figure C-043. Fitted radial concentration profile for N = 5.96, Re = 696, bed depth 03.

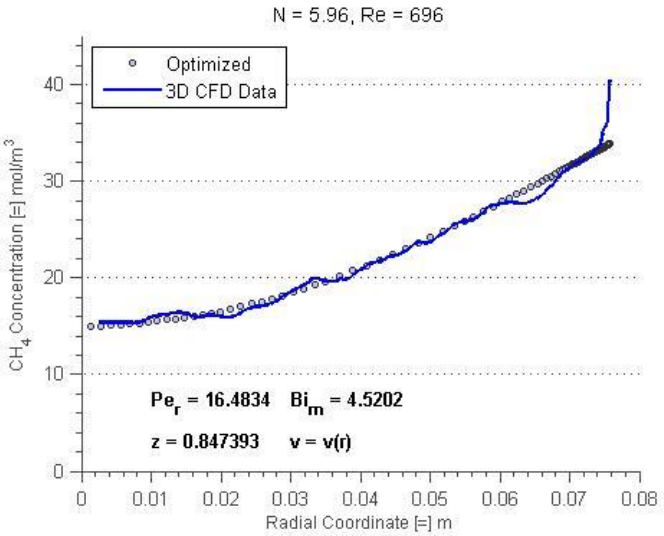

Figure C-044. Fitted radial concentration profile for N = 5.96, Re = 696, bed depth 04.

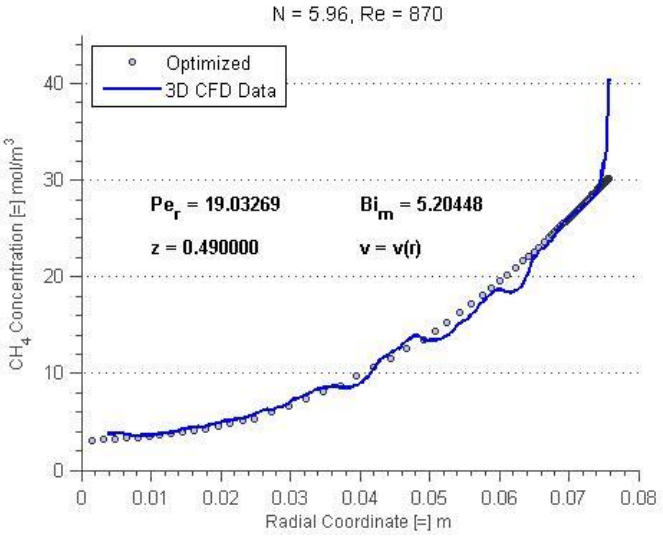

Figure C-045. Fitted radial concentration profile for N = 5.96, Re = 870, bed depth 01.

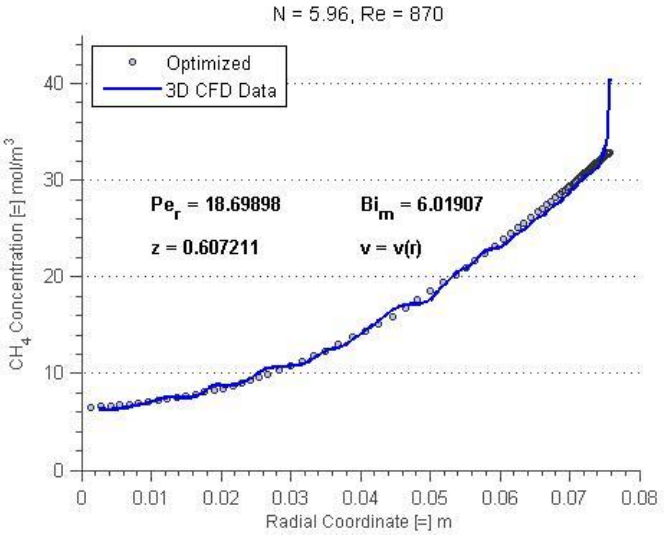

Figure C-046. Fitted radial concentration profile for N = 5.96, Re = 870, bed depth 02.

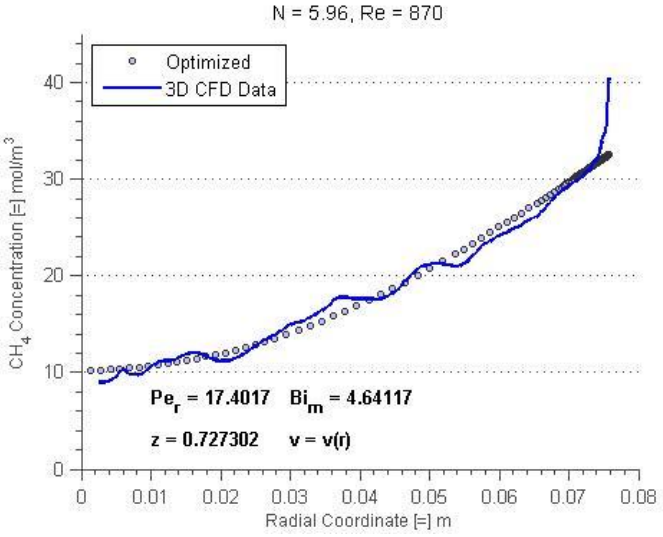

Figure C-047. Fitted radial concentration profile for N = 5.96, Re = 870, bed depth 03.

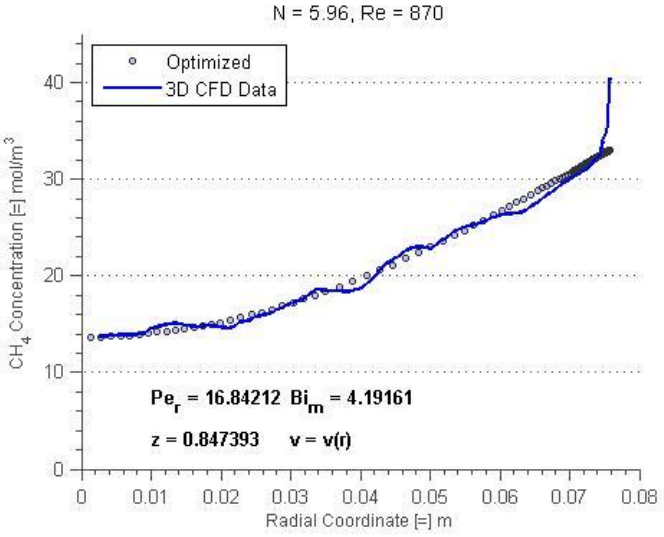

Figure C-048. Fitted radial concentration profile for N = 5.96, Re = 870, bed depth 04.

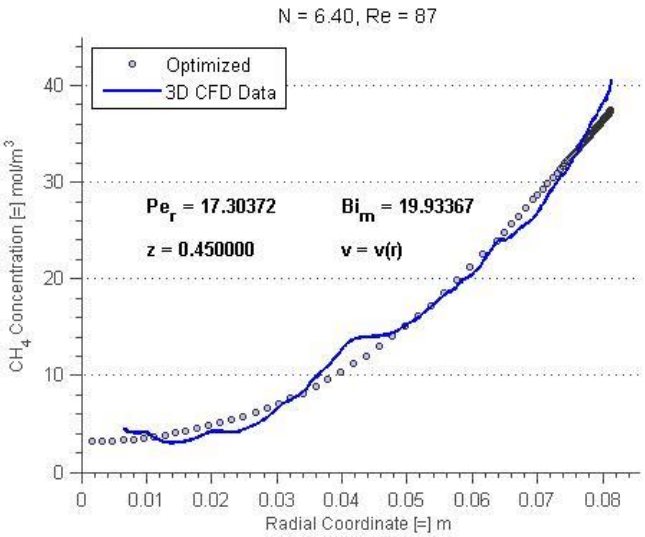

Figure C-049. Fitted radial concentration profile for N = 6.40, Re = 87, bed depth 01.

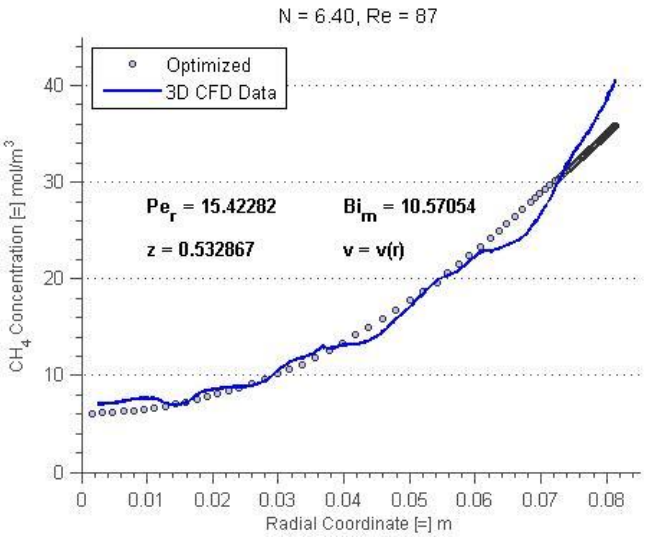

Figure C-050. Fitted radial concentration profile for N = 6.40, Re = 87, bed depth 02.

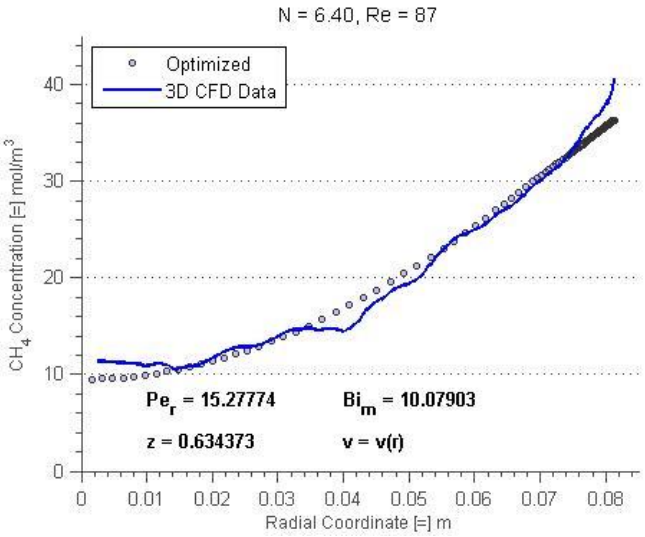

Figure C-051. Fitted radial concentration profile for N = 6.40, Re = 87, bed depth 03.

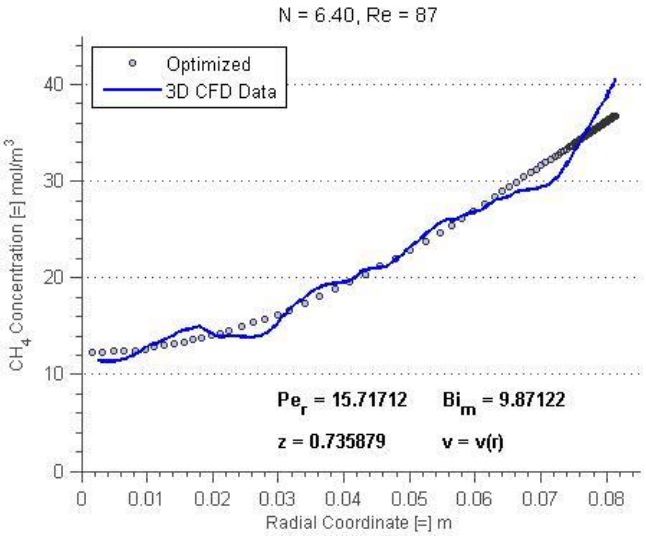

Figure C-052. Fitted radial concentration profile for N = 6.40, Re = 87, bed depth 04.

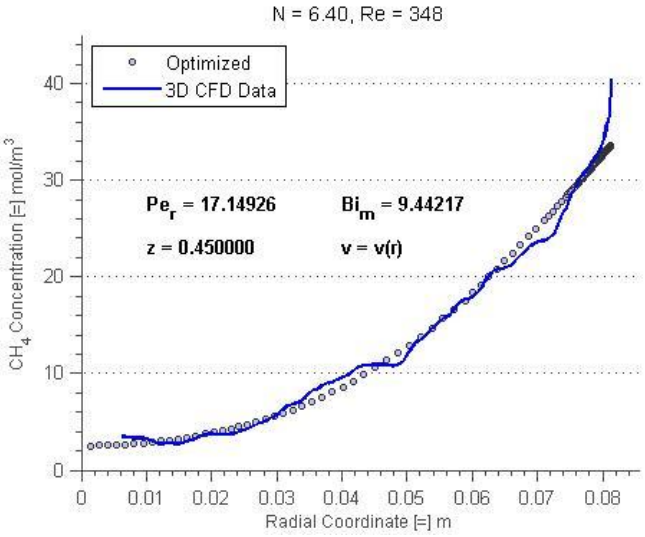

Figure C-053. Fitted radial concentration profile for N = 6.40, Re = 348, bed depth 01.

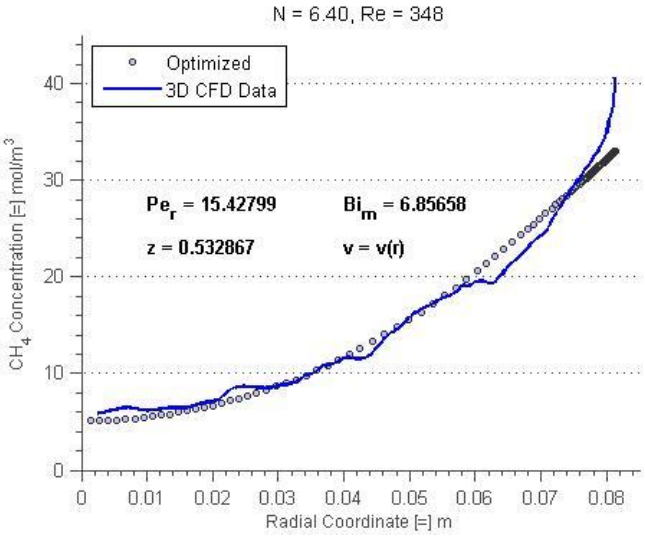

Figure C-054. Fitted radial concentration profile for N = 6.40, Re = 348, bed depth 02.

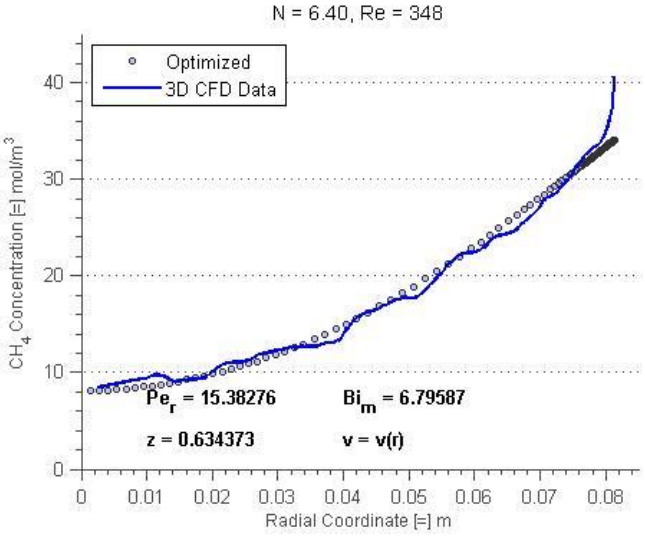

Figure C-055. Fitted radial concentration profile for N = 6.40, Re = 348, bed depth 03.

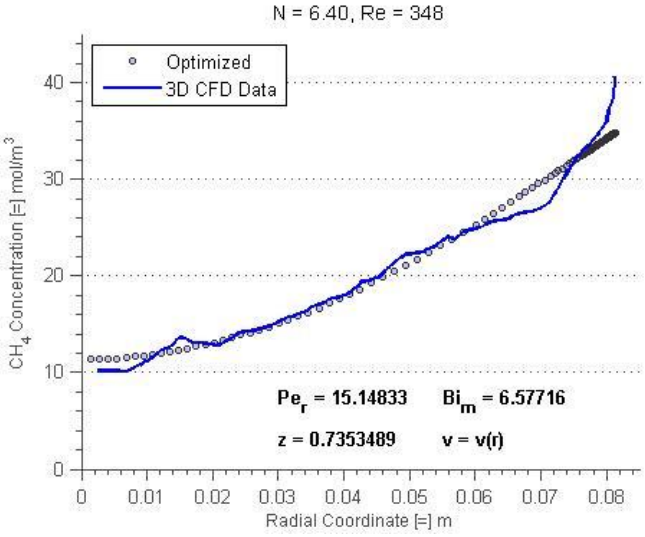

Figure C-056. Fitted radial concentration profile for N = 6.40, Re = 348, bed depth 04.

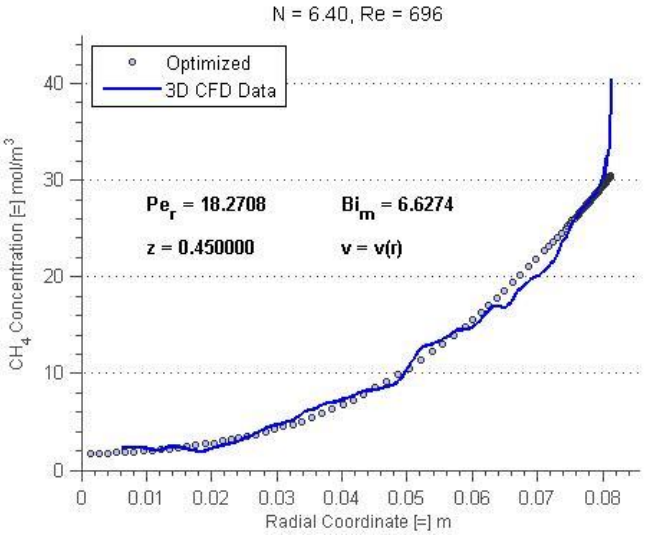

Figure C-057. Fitted radial concentration profile for N = 6.40, Re = 696, bed depth 01.

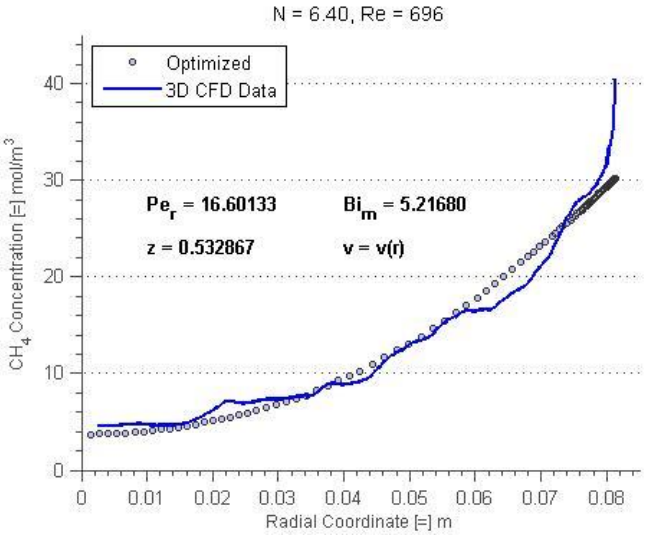

Figure C-058. Fitted radial concentration profile for N = 6.40, Re = 696, bed depth 02.

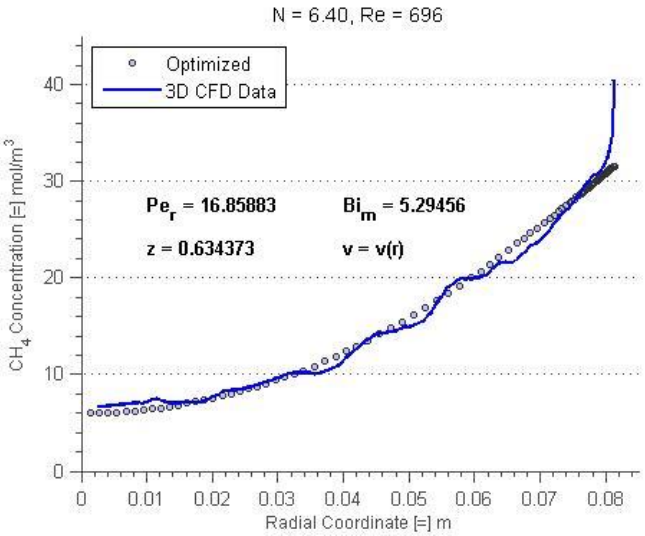

Figure C-059. Fitted radial concentration profile for N = 6.40, Re = 696, bed depth 03.

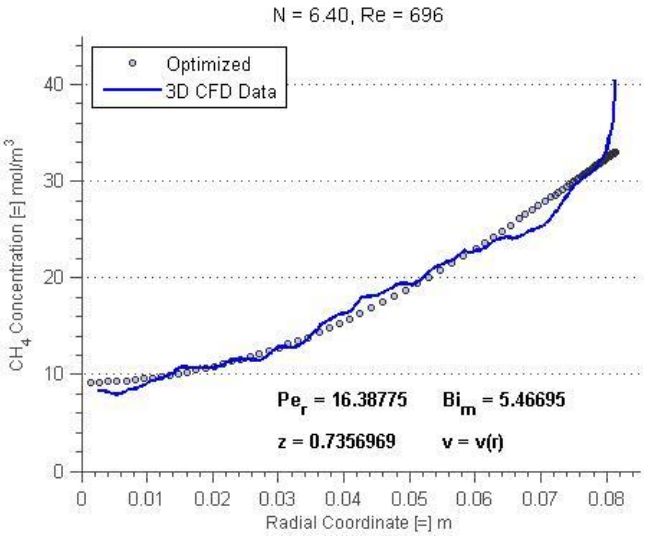

Figure C-060. Fitted radial concentration profile for N = 6.40, Re = 696, bed depth 04.

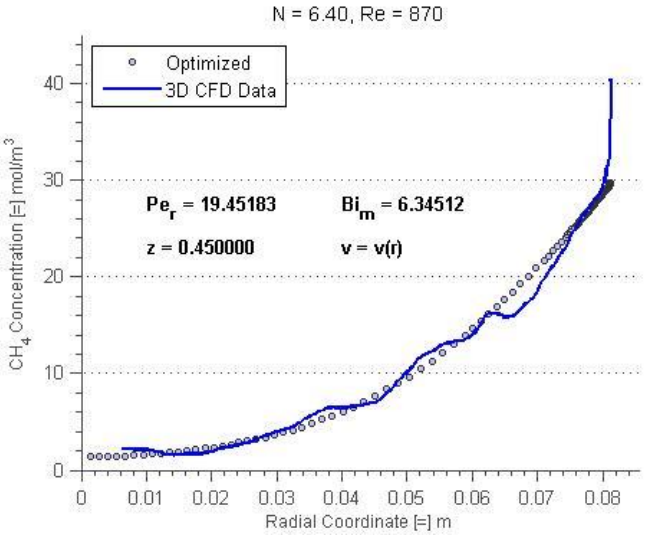

Figure C-061. Fitted radial concentration profile for N = 6.40, Re = 870, bed depth 01.

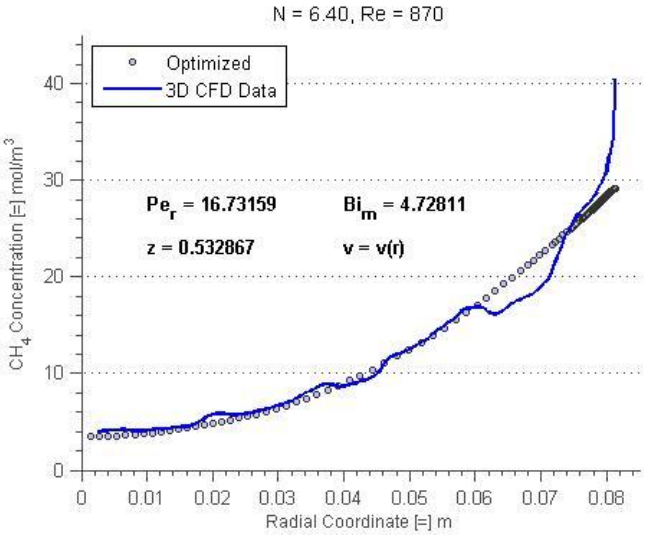

Figure C-062. Fitted radial concentration profile for N = 6.40, Re = 870, bed depth 02.

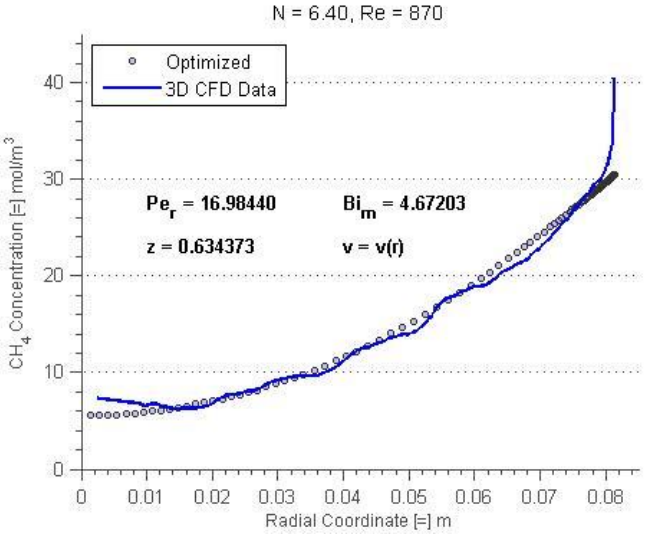

Figure C-063. Fitted radial concentration profile for N = 6.40, Re = 870, bed depth 03.

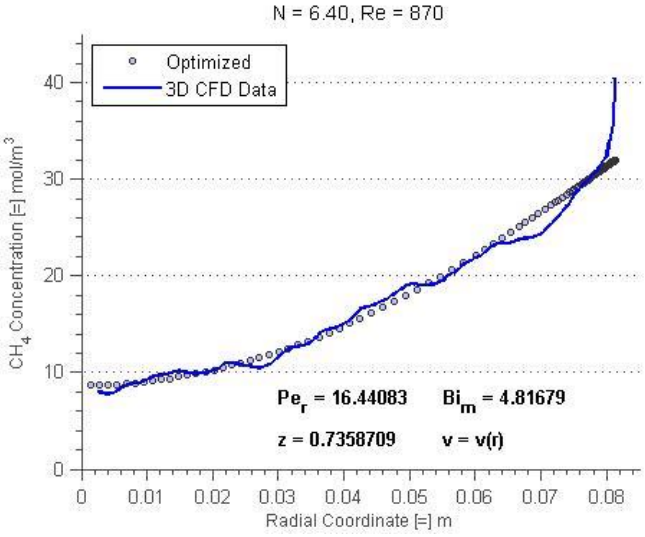

Figure C-064. Fitted radial concentration profile for N = 6.40, Re = 870, bed depth 04.

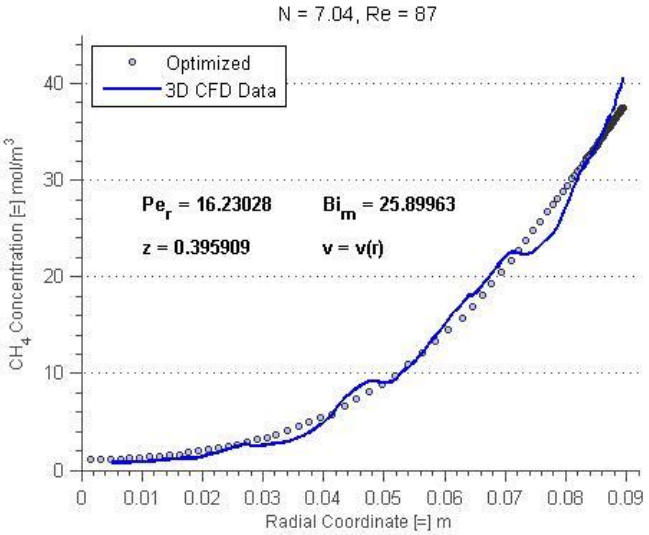

Figure C-065. Fitted radial concentration profile for N = 7.04, Re = 87, bed depth 01.

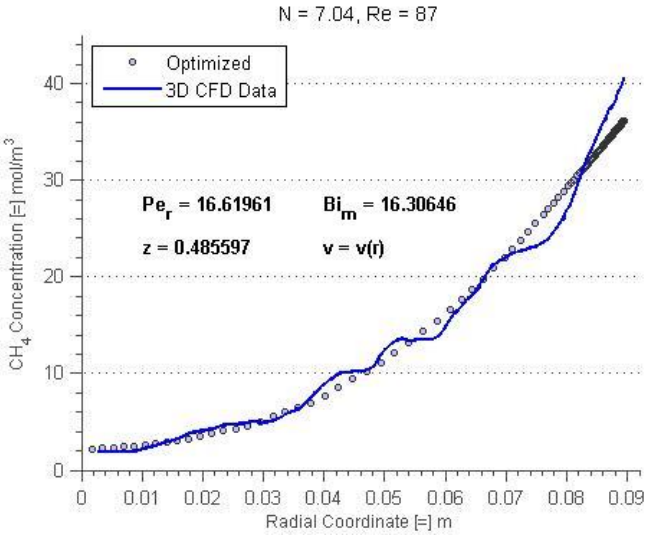

Figure C-066. Fitted radial concentration profile for N = 7.04, Re = 87, bed depth 02.

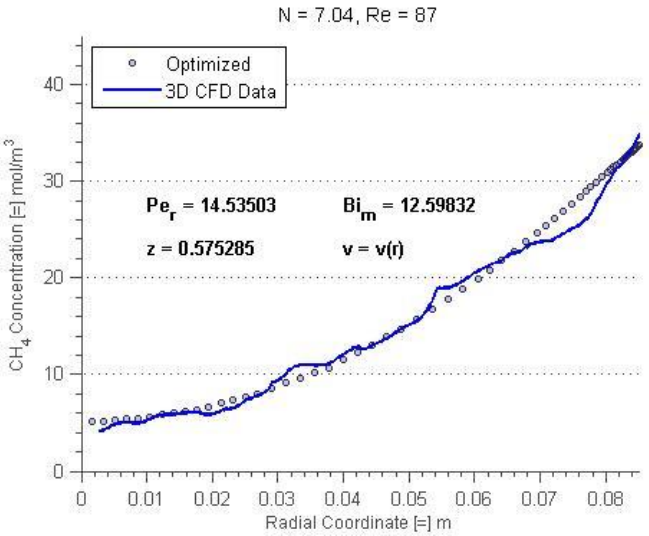

Figure C-067. Fitted radial concentration profile for N = 7.04, Re = 87, bed depth 03.

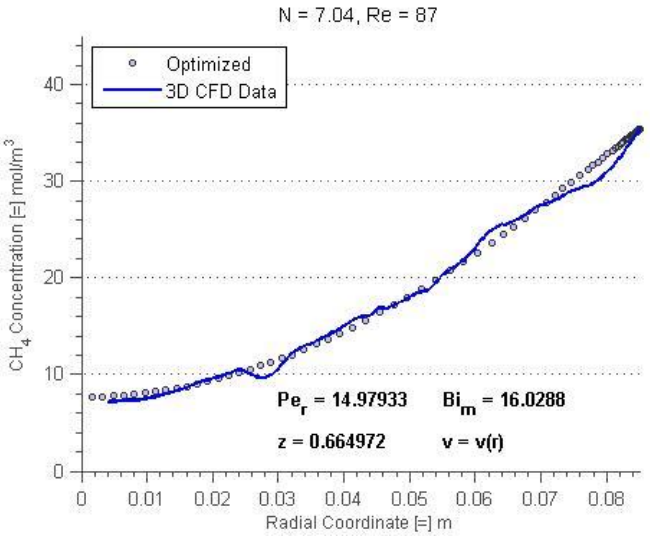

Figure C-068. Fitted radial concentration profile for N =7.04, Re = 87, bed depth 04.

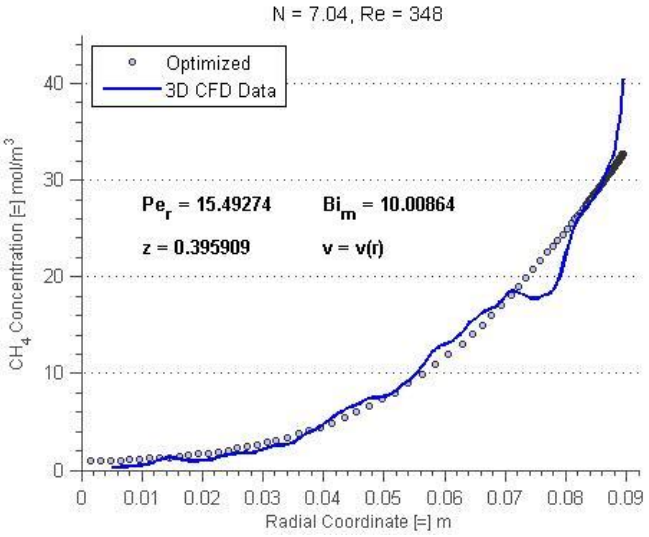

Figure C-069. Fitted radial concentration profile for N = 7.04, Re = 348, bed depth 01.

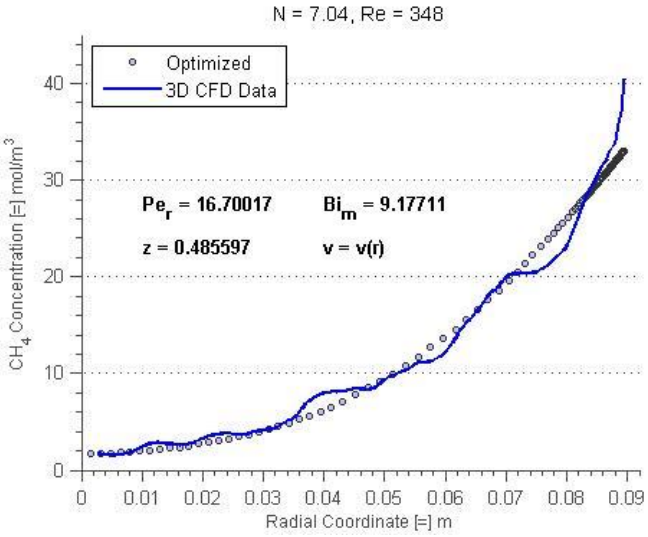

Figure C-070. Fitted radial concentration profile for N = 7.04, Re = 348, bed depth 02.

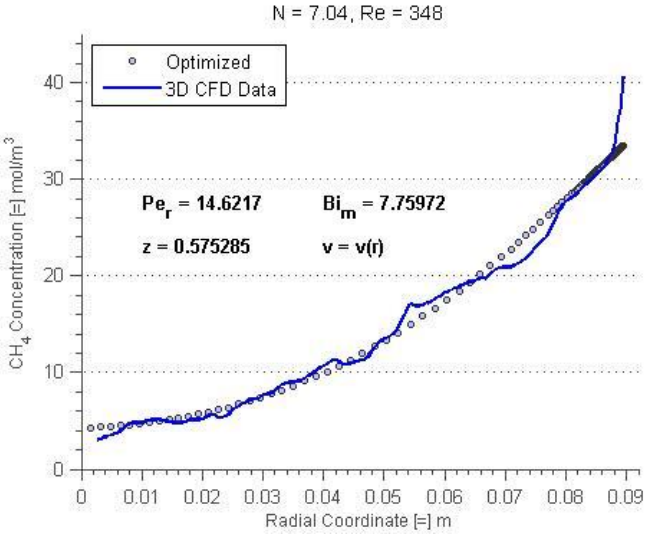

Figure C-071. Fitted radial concentration profile for N = 7.04, Re = 348, bed depth 03.

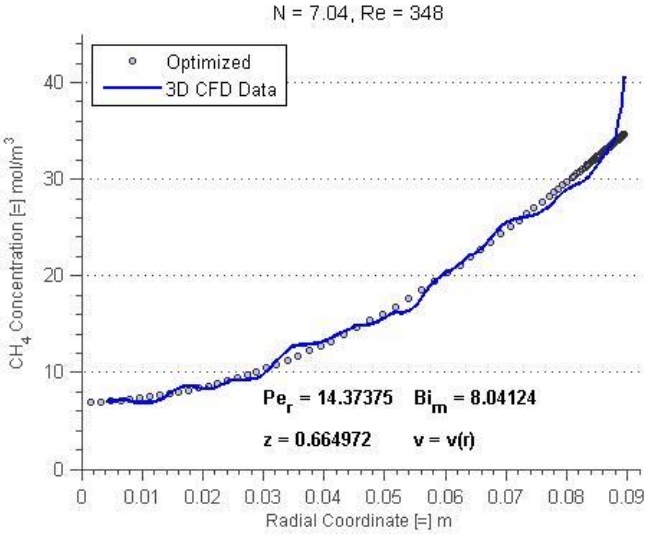

Figure C-072. Fitted radial concentration profile for N = 7.04, Re = 348, bed depth 04.

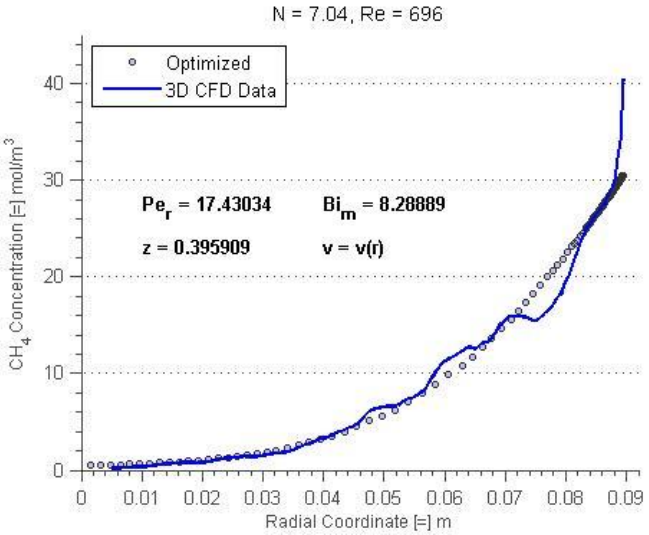

Figure C-073. Fitted radial concentration profile for N = 7.04, Re = 696, bed depth 01.

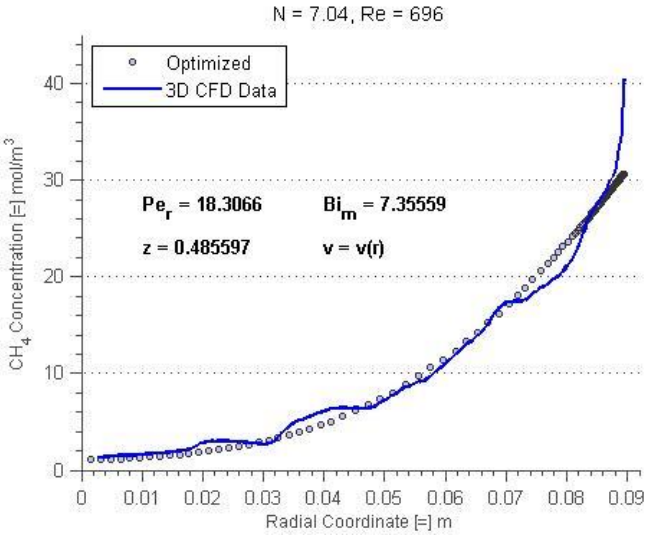

Figure C-074. Fitted radial concentration profile for N = 7.04, Re = 696, bed depth 02.

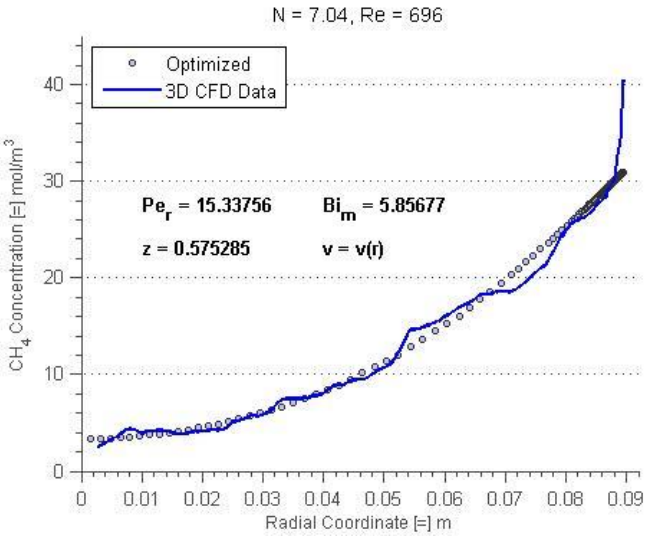

Figure C-075. Fitted radial concentration profile for N = 7.04, Re = 696, bed depth 03.

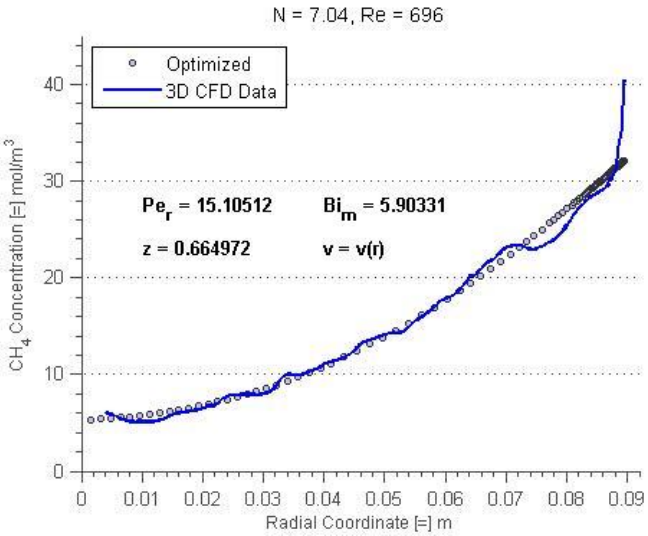

Figure C-076. Fitted radial concentration profile for N = 7.04, Re = 696, bed depth 04.

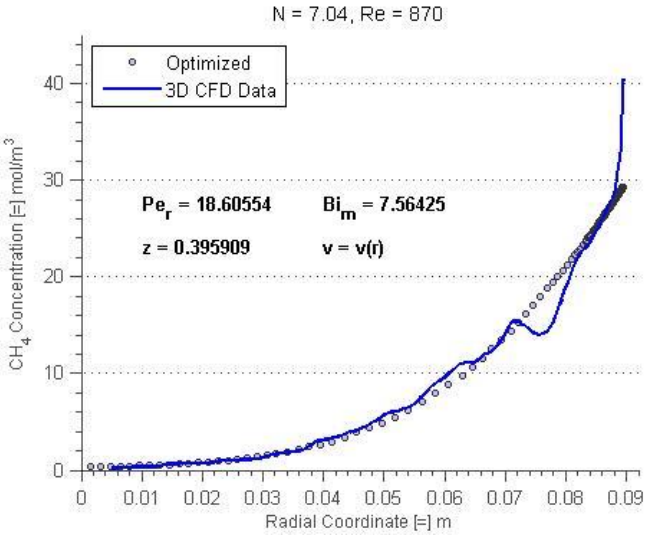

Figure C-077. Fitted radial concentration profile for N = 7.04, Re = 870, bed depth 01.

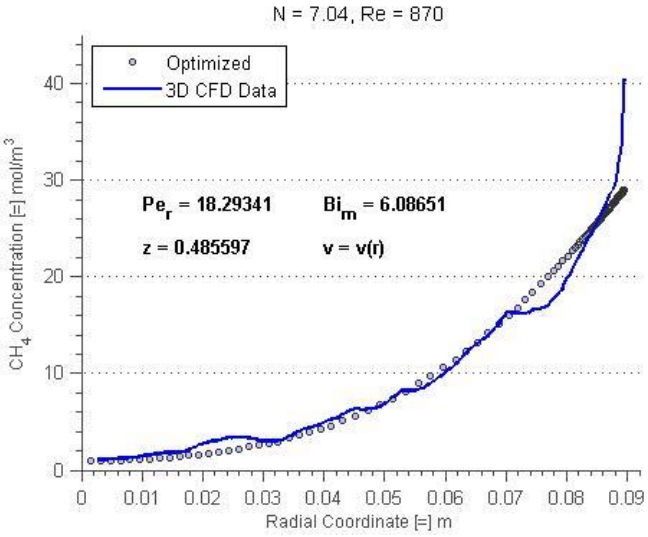

Figure C-078. Fitted radial concentration profile for N = 7.04, Re = 870, bed depth 02.

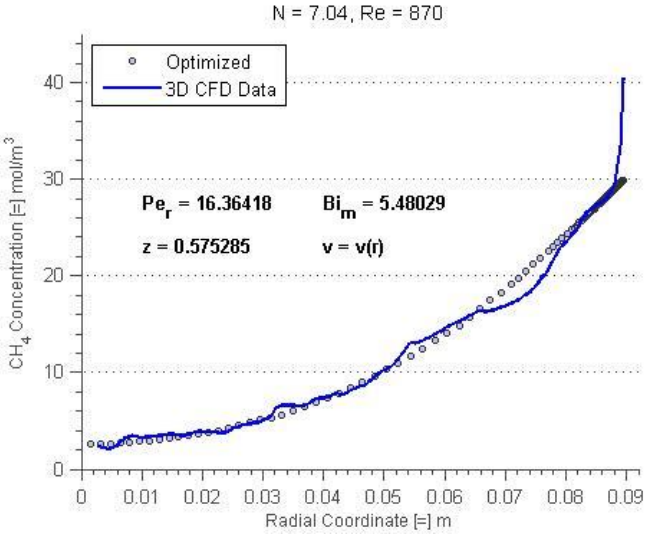

Figure C-079. Fitted radial concentration profile for N = 7.04, Re = 870, bed depth 03.

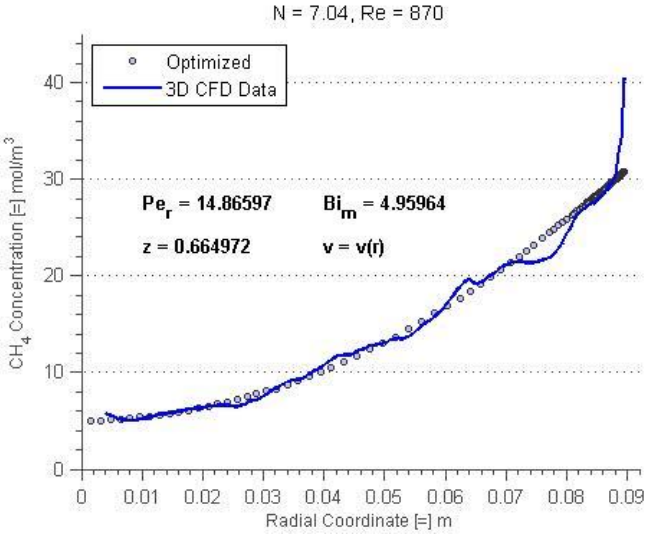

Figure C-080. Fitted radial concentration profile for N = 7.04, Re = 870, bed depth 04.

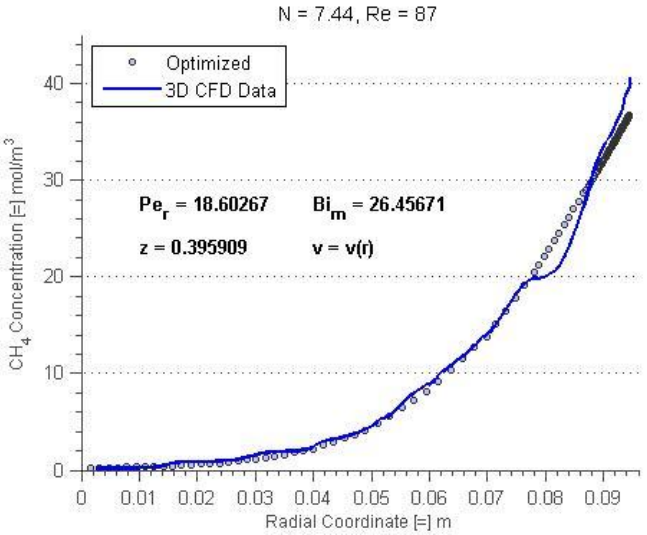

Figure C-081. Fitted radial concentration profile for N = 7.04, Re = 87, bed depth 01.

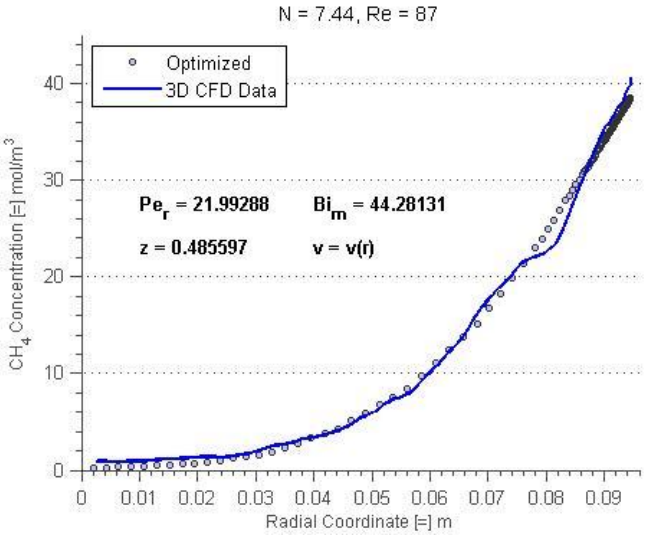

Figure C-082. Fitted radial concentration profile for N = 7.04, Re = 87, bed depth 02.

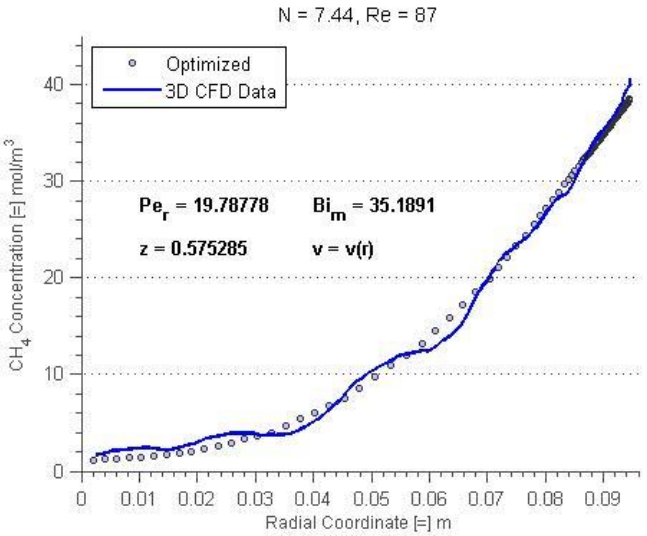

Figure C-083. Fitted radial concentration profile for N = 7.04, Re = 87, bed depth 03.

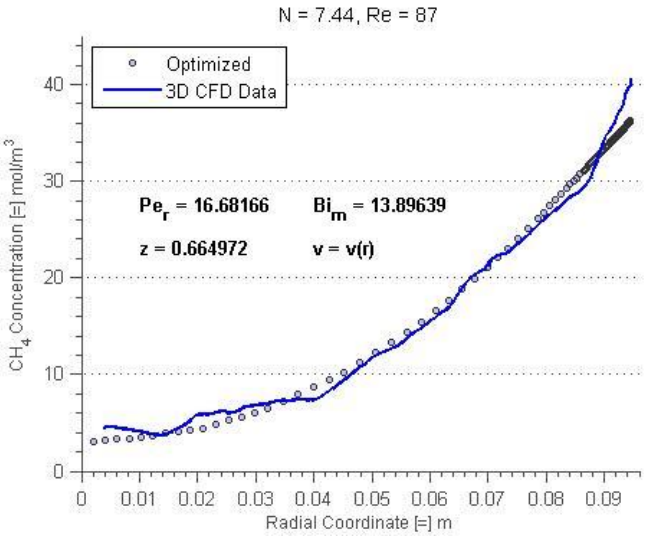

Figure C-084. Fitted radial concentration profile for N = 7.04, Re = 87, bed depth 04.

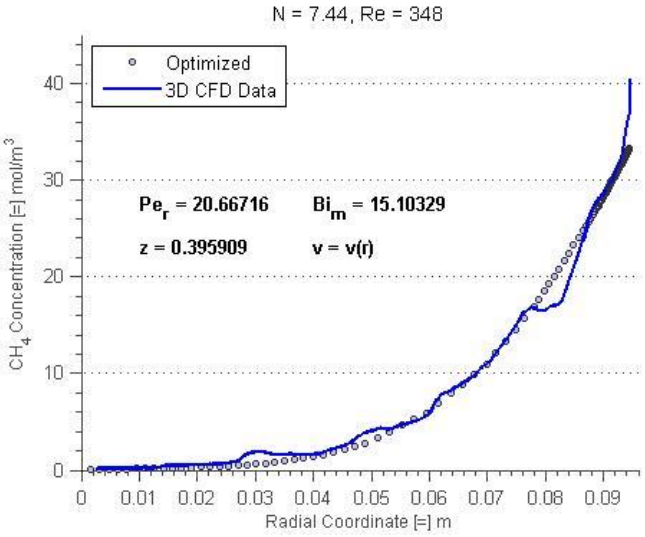

Figure C-085. Fitted radial concentration profile for N = 7.44, Re = 348, bed depth 01.

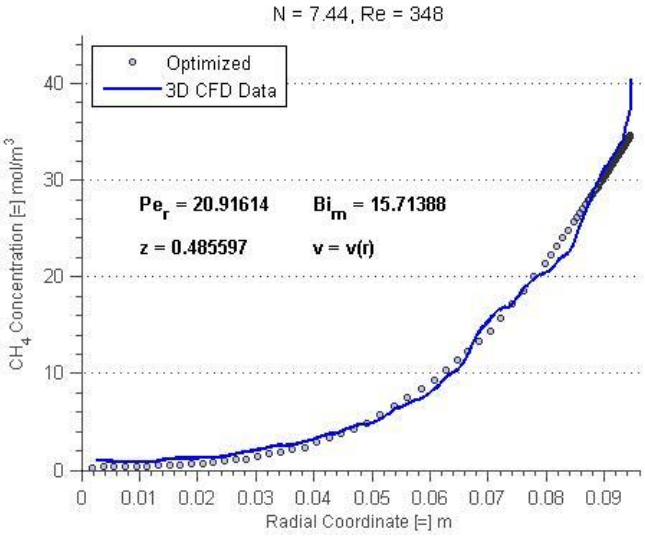

Figure C-086. Fitted radial concentration profile for N = 7.44, Re = 348, bed depth 02.

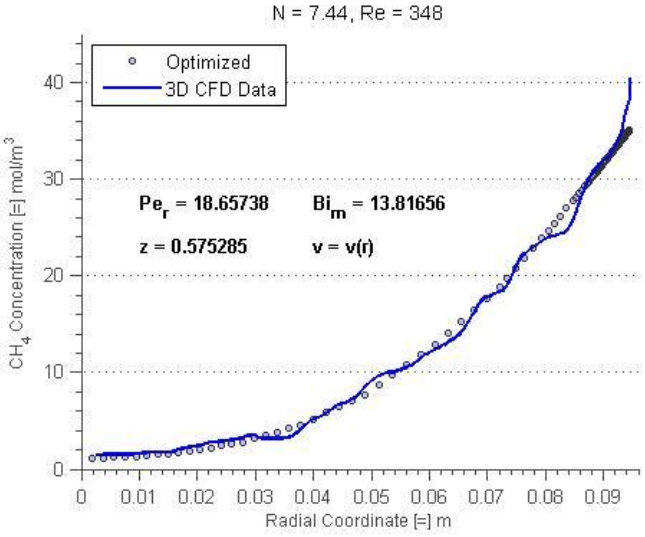

Figure C-087. Fitted radial concentration profile for N = 7.44, Re = 348, bed depth 03.

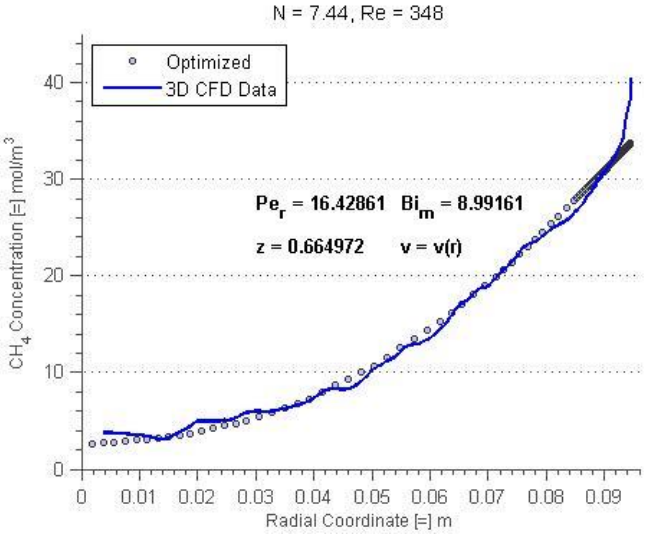

Figure C-088. Fitted radial concentration profile for N = 7.44, Re = 348, bed depth 04.

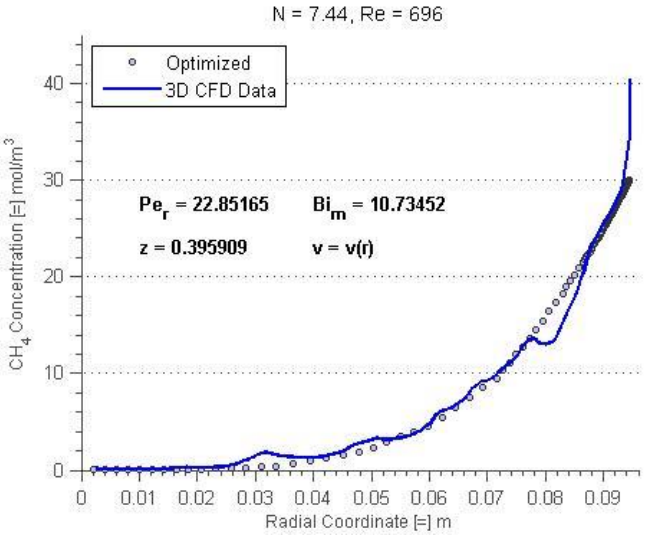

Figure C-089. Fitted radial concentration profile for N = 7.44, Re = 696, bed depth 01.

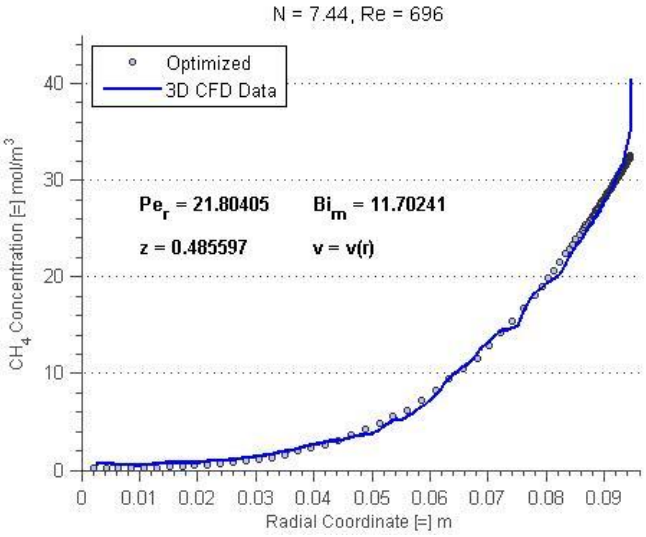

Figure C-090. Fitted radial concentration profile for N = 7.44, Re = 696, bed depth 02.

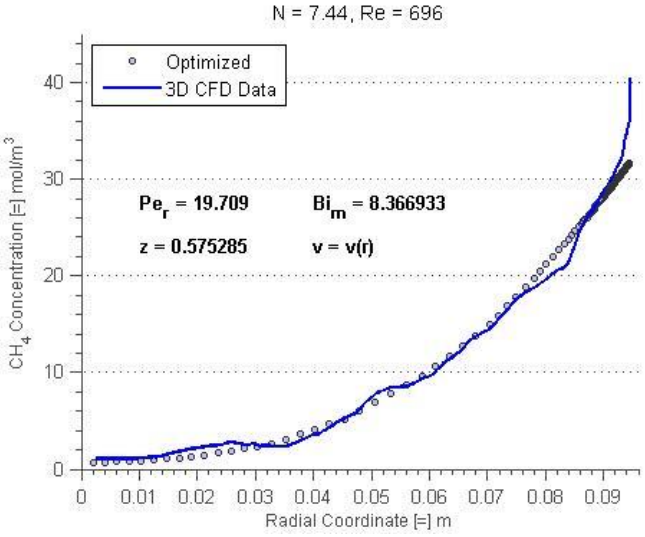

Figure C-091. Fitted radial concentration profile for N = 7.44, Re = 696, bed depth 03.

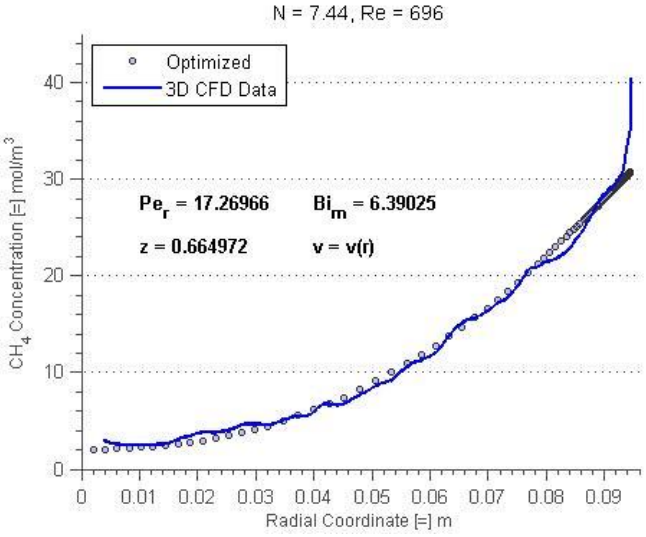

Figure C-092. Fitted radial concentration profile for N = 7.44, Re = 696, bed depth 04.

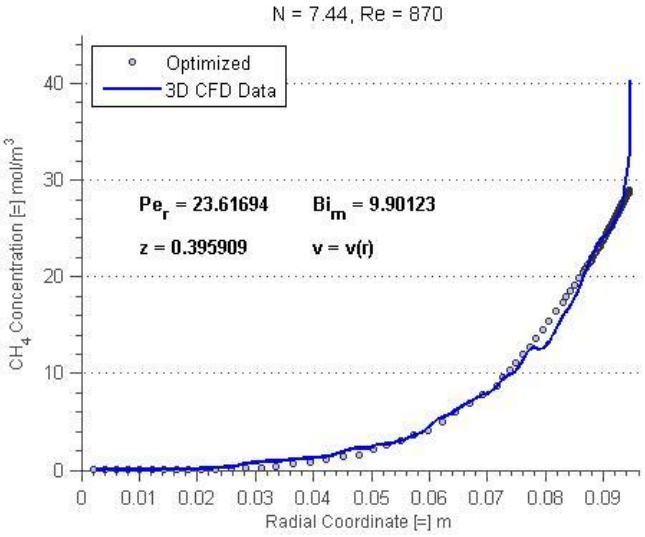

Figure C-093. Fitted radial concentration profile for N = 7.44, Re = 870, bed depth 01.

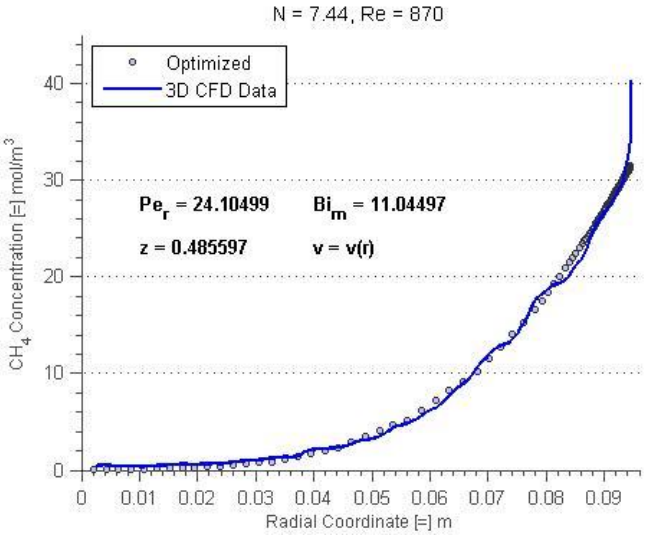

Figure C-094. Fitted radial concentration profile for N = 7.44, Re = 870, bed depth 02.

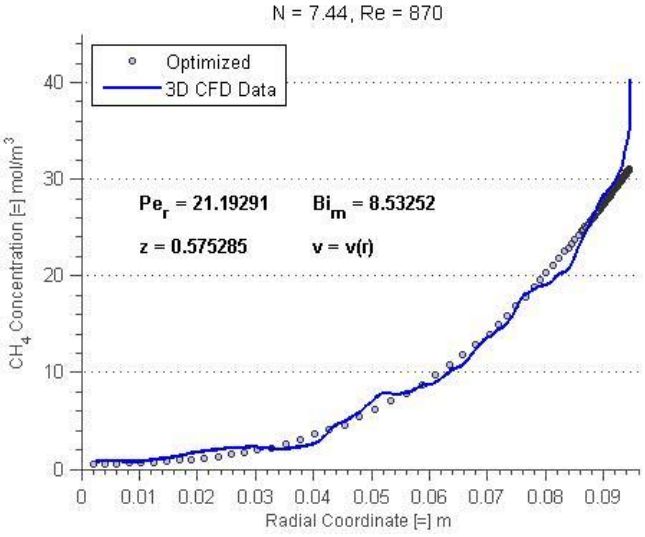

Figure C-095. Fitted radial concentration profile for N = 7.44, Re = 870, bed depth 03.

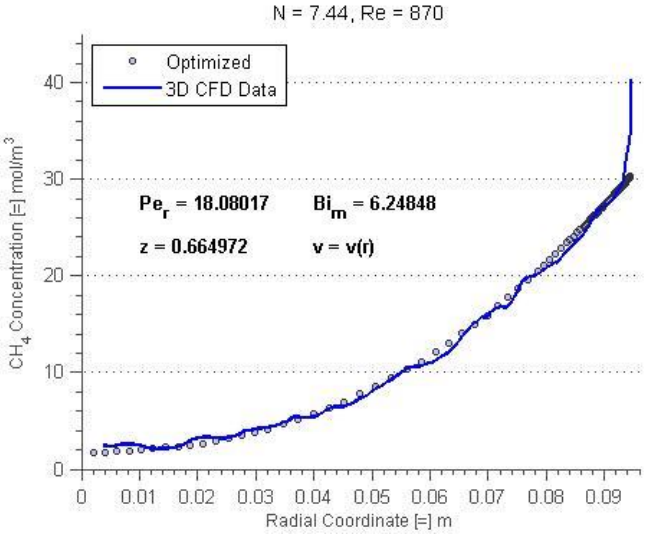

Figure C-096. Fitted radial concentration profile for N = 7.44, Re = 870, bed depth 04.

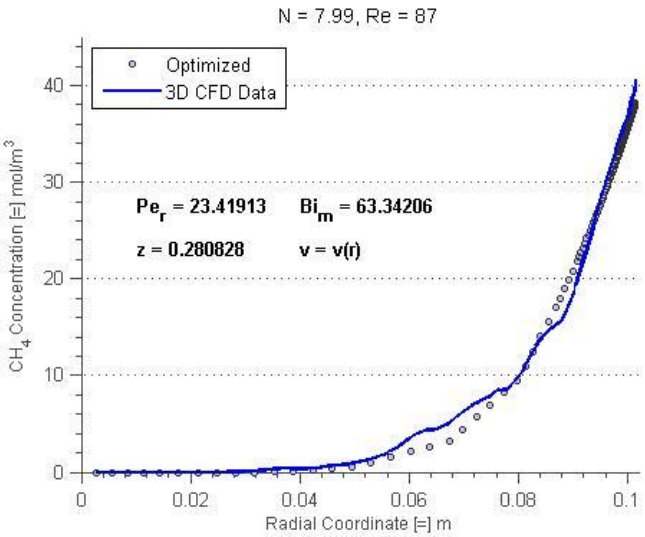

Figure C-097. Fitted radial concentration profile for N = 7.44, Re = 87, bed depth 01.

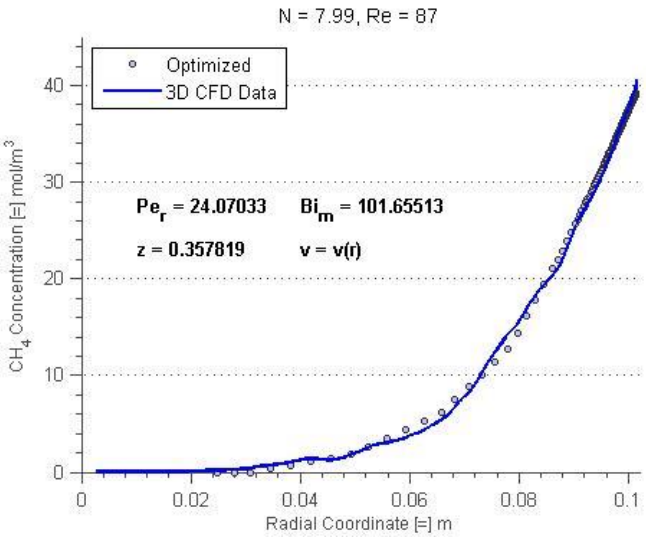

Figure C-098. Fitted radial concentration profile for N = 7.44, Re = 87, bed depth 02.

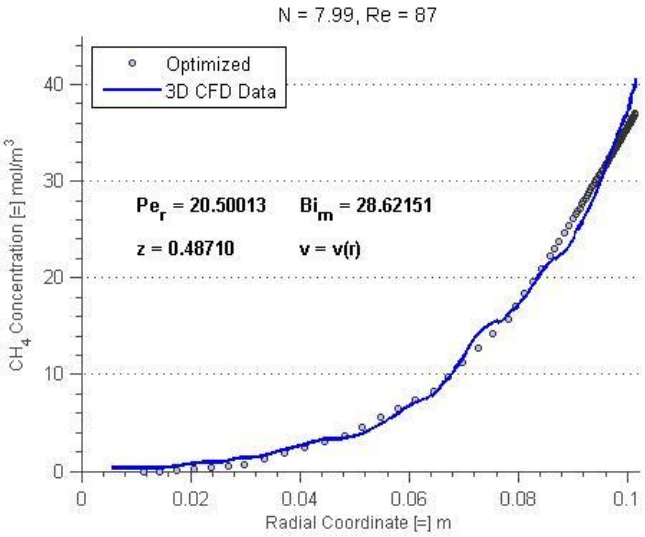

Figure C-99. Fitted radial concentration profile for N = 7.44, Re = 87, bed depth 03.

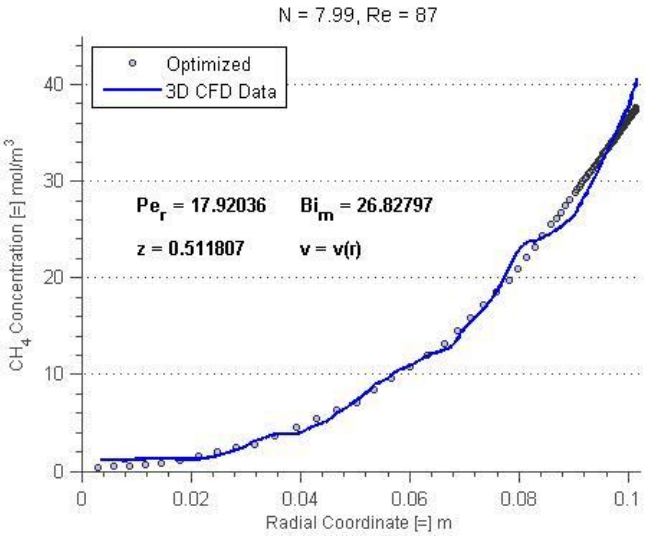

Figure C-100. Fitted radial concentration profile for N = 7.44, Re = 87, bed depth 04.

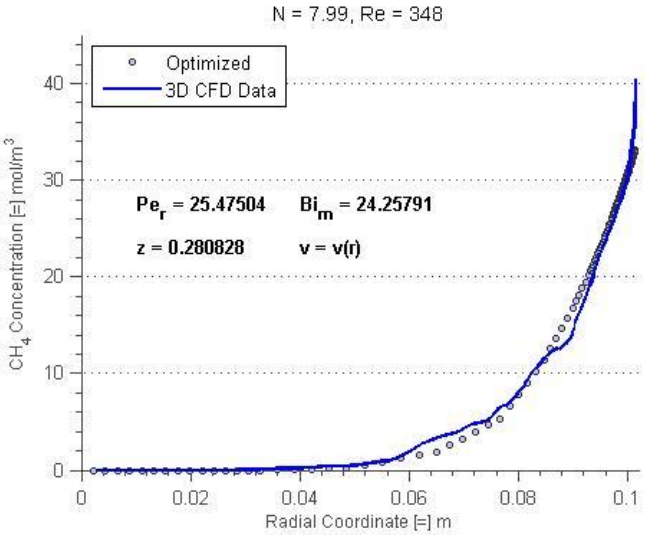

Figure C-101. Fitted radial concentration profile for N = 7.99, Re = 348, bed depth 01.

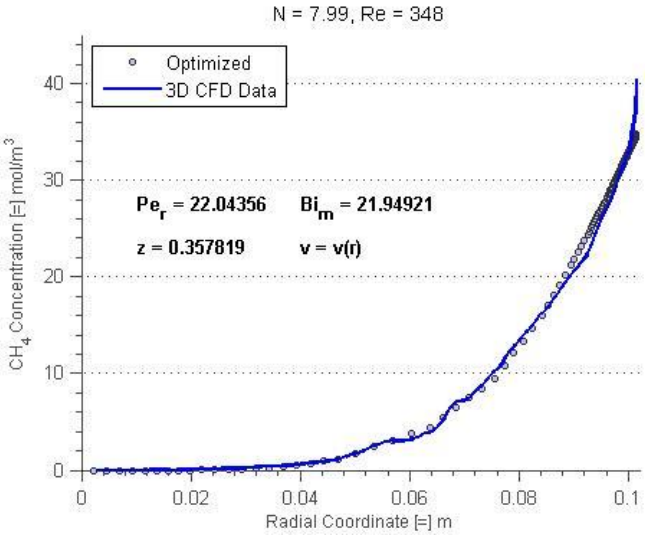

Figure C-102. Fitted radial concentration profile for N = 7.99, Re = 348, bed depth 02.

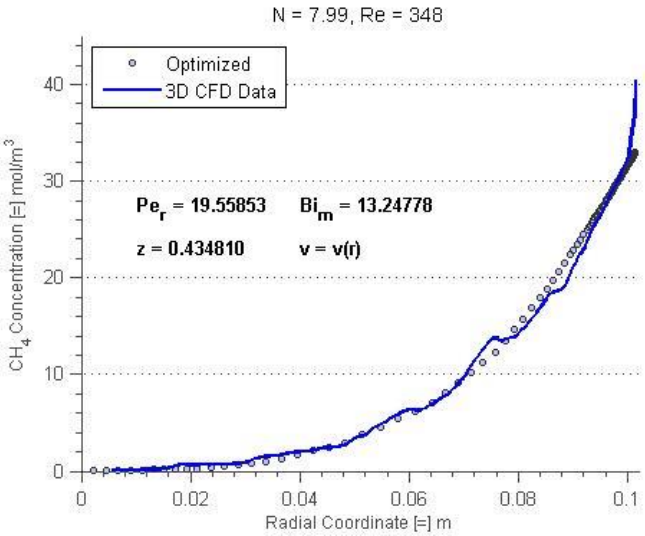

Figure C-103. Fitted radial concentration profile for N = 7.99, Re = 348, bed depth 03.

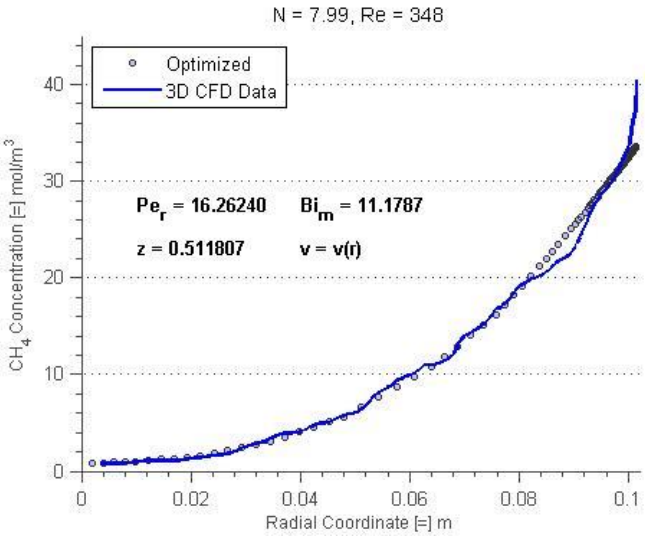

Figure C-104. Fitted radial concentration profile for N = 7.99, Re = 348, bed depth 04.

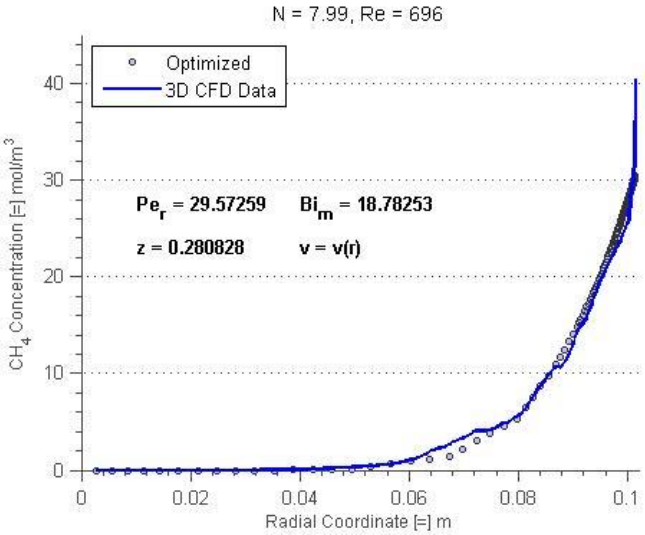

Figure C-105. Fitted radial concentration profile for N = 7.99, Re = 696, bed depth 01.

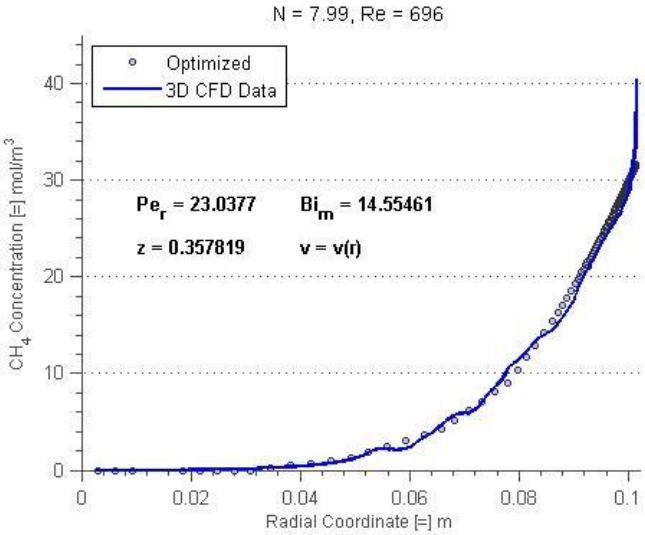

Figure C-106. Fitted radial concentration profile for N = 7.99, Re = 696, bed depth 02.

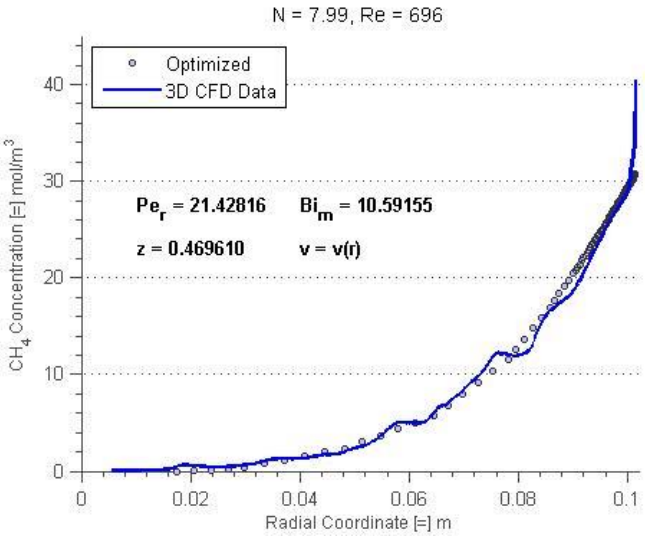

Figure C-107. Fitted radial concentration profile for N = 7.99, Re = 696, bed depth 03.

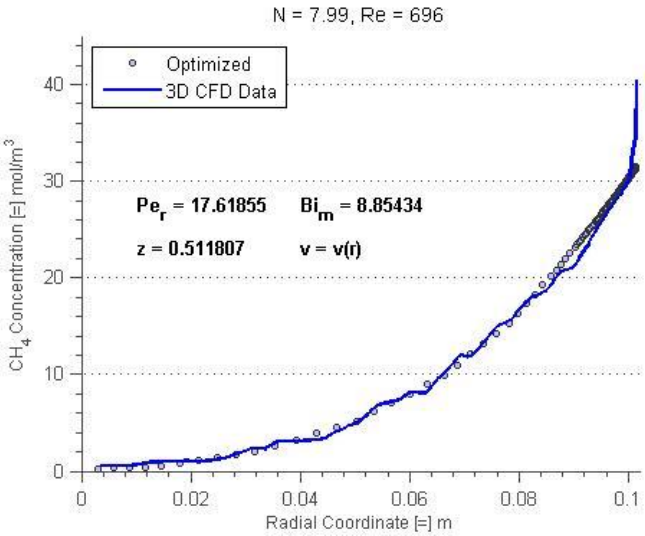

Figure C-108. Fitted radial concentration profile for N = 7.99, Re = 696, bed depth 04.

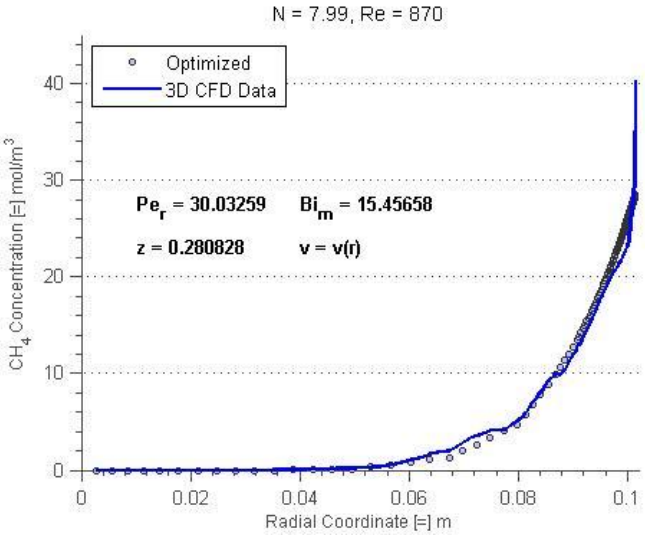

Figure C-109. Fitted radial concentration profile for N = 7.99, Re = 870, bed depth 01.

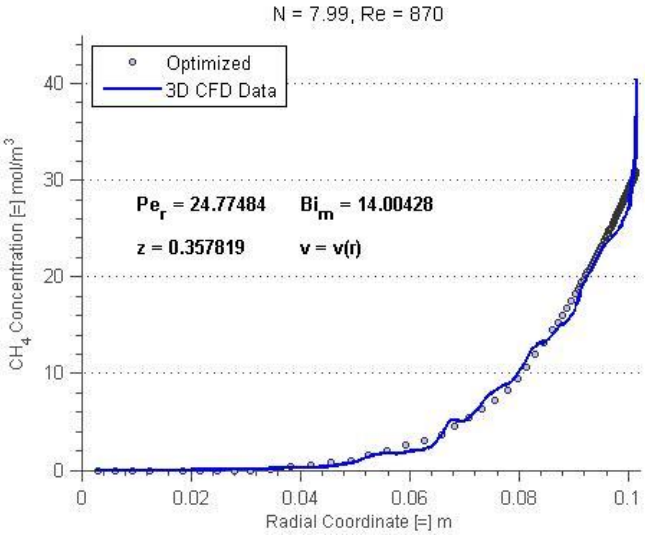

Figure C-110. Fitted radial concentration profile for N = 7.99, Re = 870, bed depth 02.

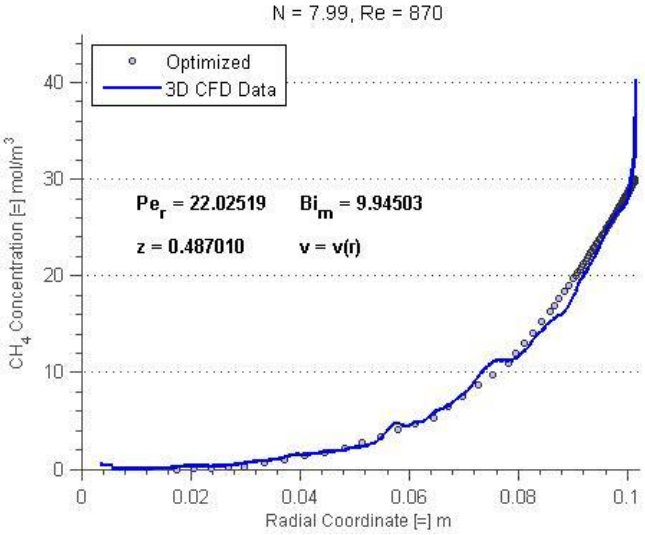

Figure C-111. Fitted radial concentration profile for N = 7.99, Re = 870, bed depth 03.

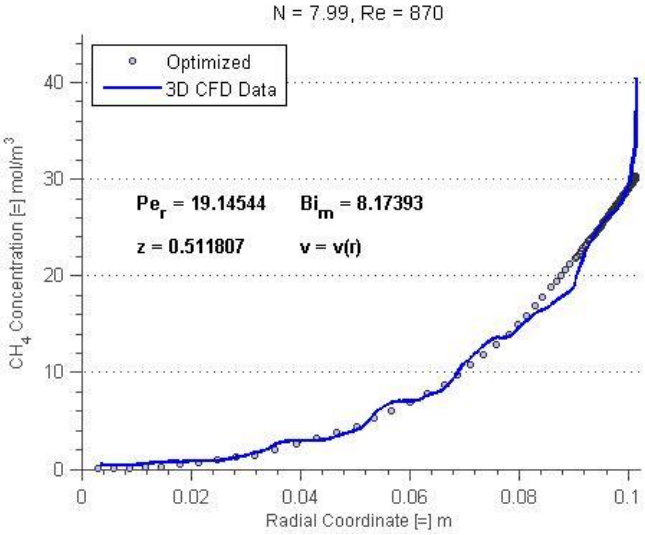

Figure C-112. Fitted radial concentration profile for N = 7.99, Re = 870, bed depth 04.

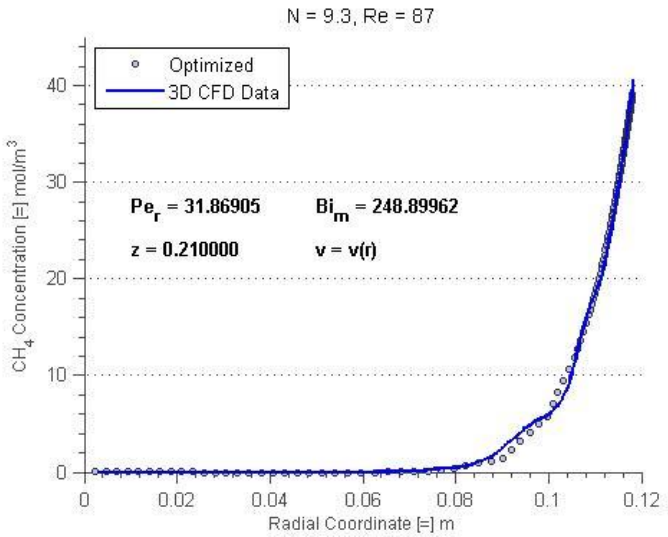

Figure C-113. Fitted radial concentration profile for N = 9.3, Re = 87, bed depth 01.

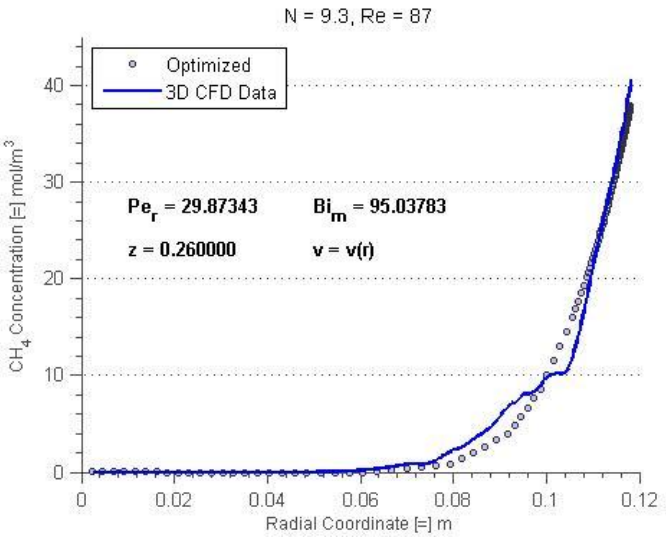

Figure C-114. Fitted radial concentration profile for N = 9.3, Re = 87, bed depth 02.

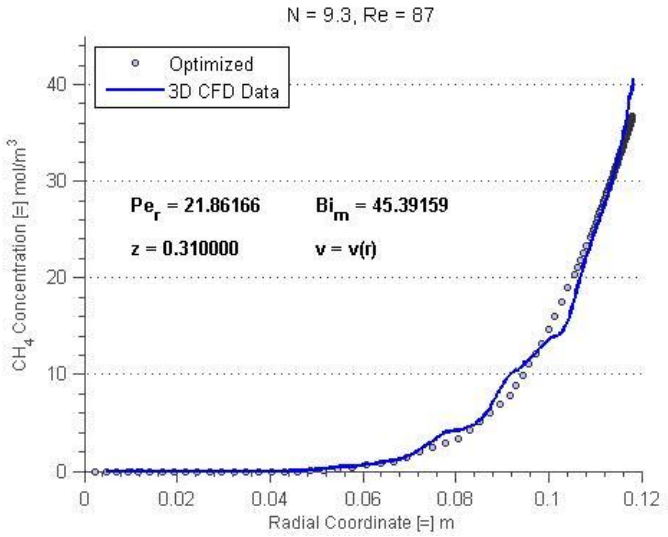

Figure C-115. Fitted radial concentration profile for N = 9.3, Re = 87, bed depth 03.

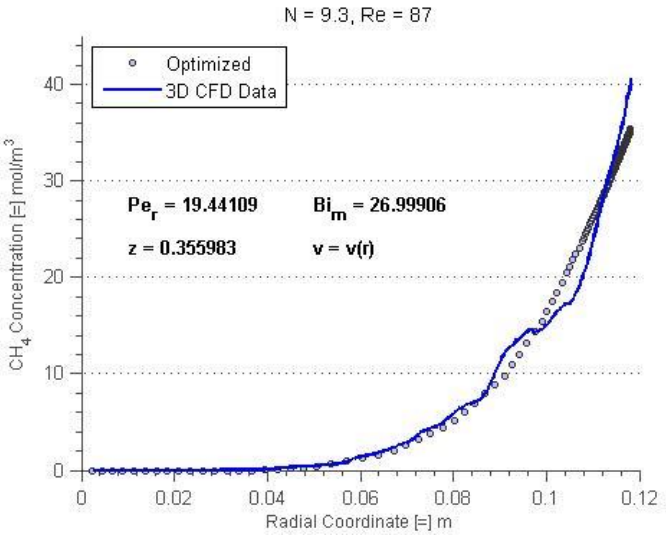

Figure C-116. Fitted radial concentration profile for N = 9.3, Re = 87, bed depth 04.

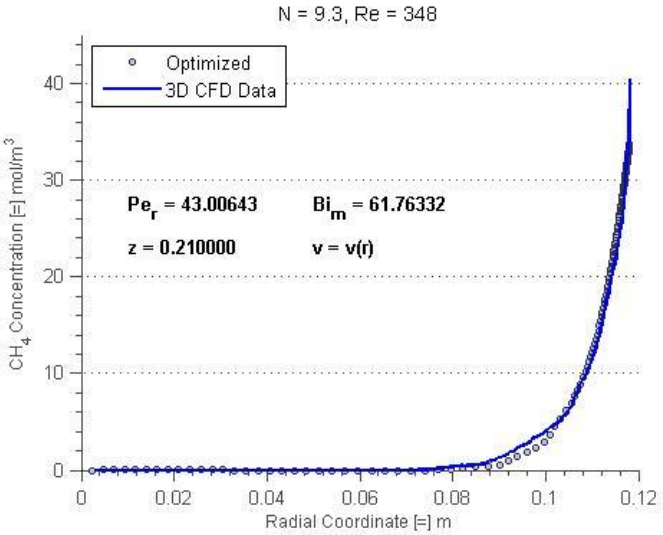

Figure C-117. Fitted radial concentration profile for N = 9.3, Re = 348, bed depth 01.

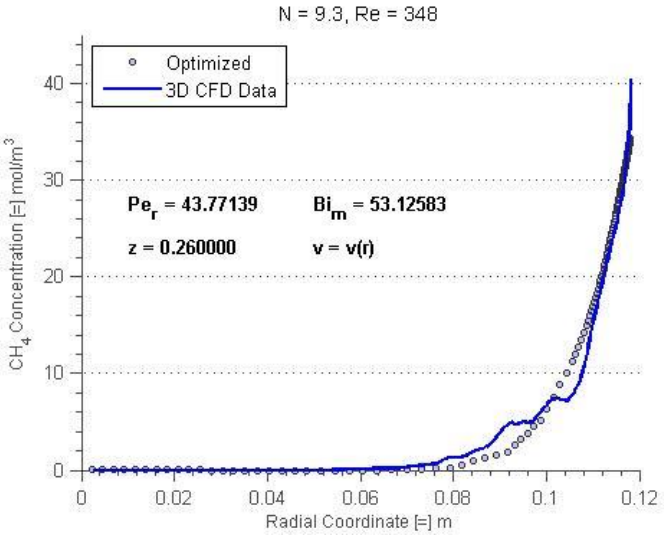

Figure C-118. Fitted radial concentration profile for N = 9.3, Re = 348, bed depth 02.

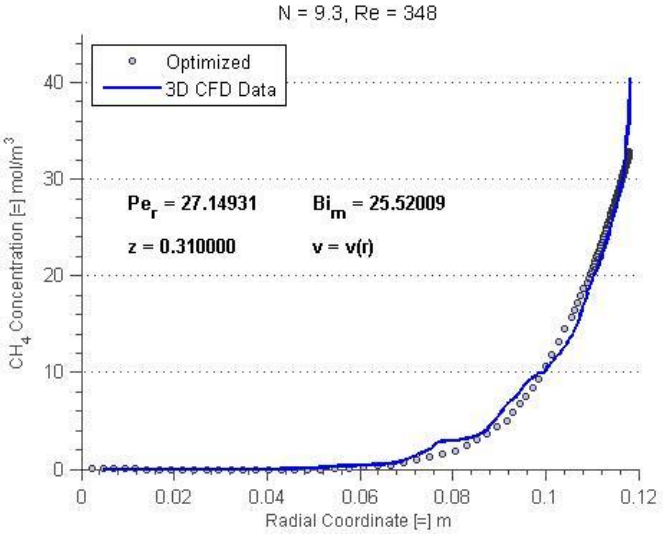

Figure C-119. Fitted radial concentration profile for N = 9.3, Re = 348, bed depth 03.

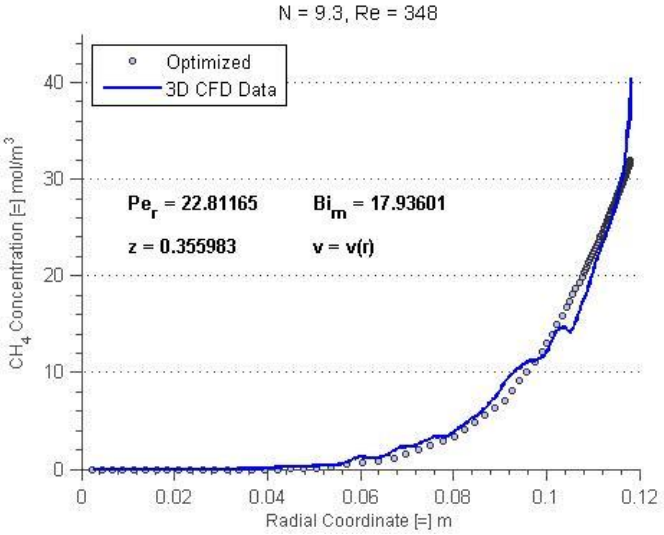

Figure C-120. Fitted radial concentration profile for N = 9.3, Re = 348, bed depth 04.

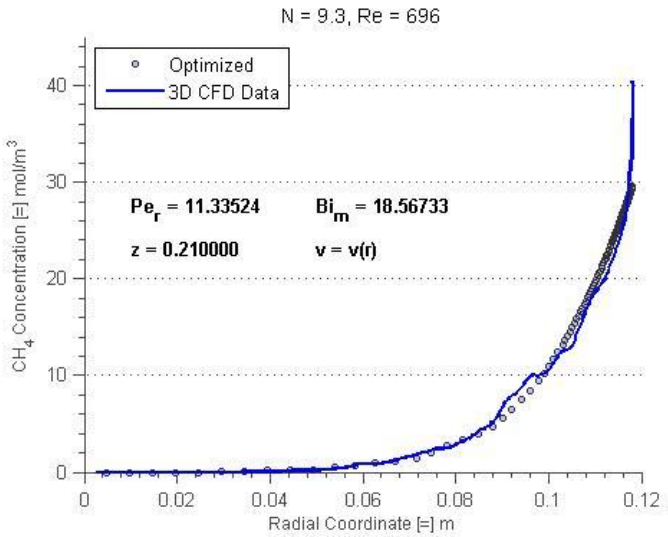

Figure C-121. Fitted radial concentration profile for N = 9.3, Re = 696, bed depth 01.

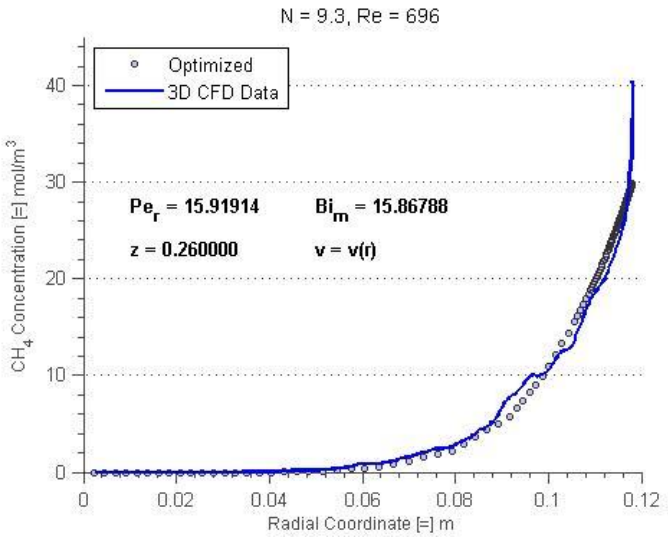

Figure C-122. Fitted radial concentration profile for N = 9.3, Re = 696, bed depth 02.

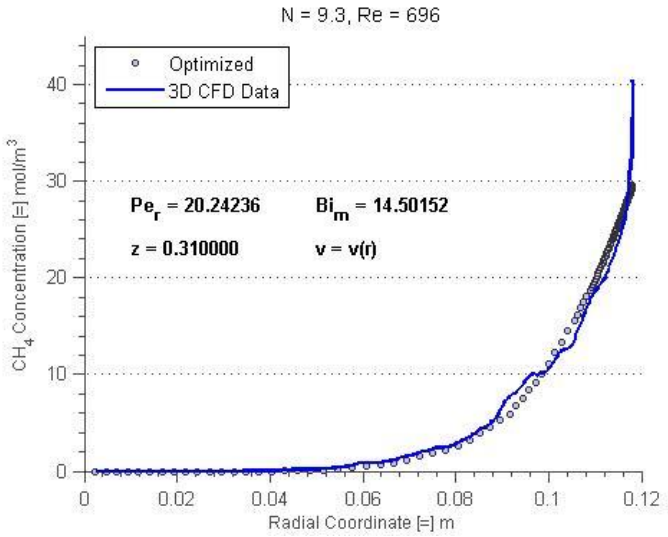

Figure C-123. Fitted radial concentration profile for N = 9.3, Re = 696, bed depth 03.

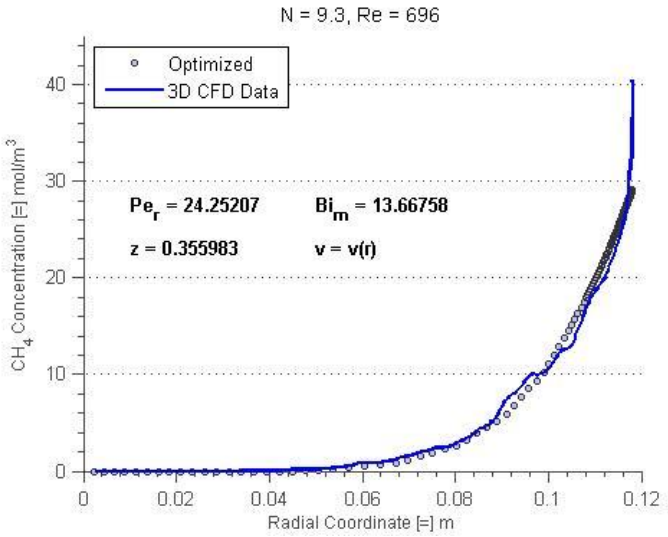

Figure C-124. Fitted radial concentration profile for N = 9.3, Re = 696, bed depth 04.

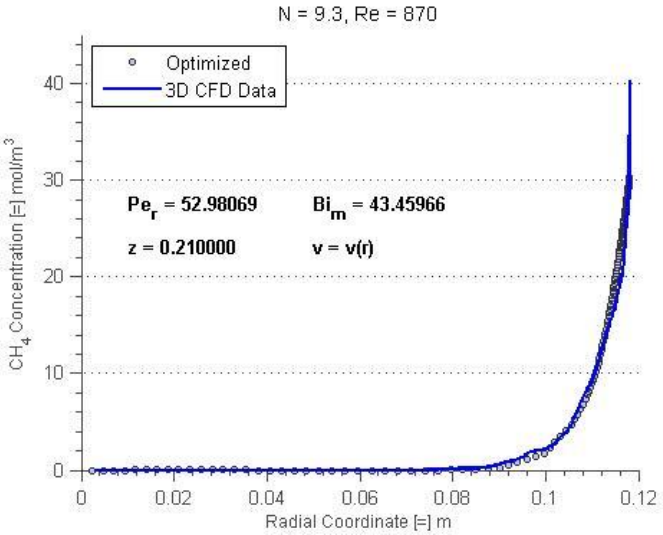

Figure C-125. Fitted radial concentration profile for N = 9.3, Re = 870, bed depth 01.

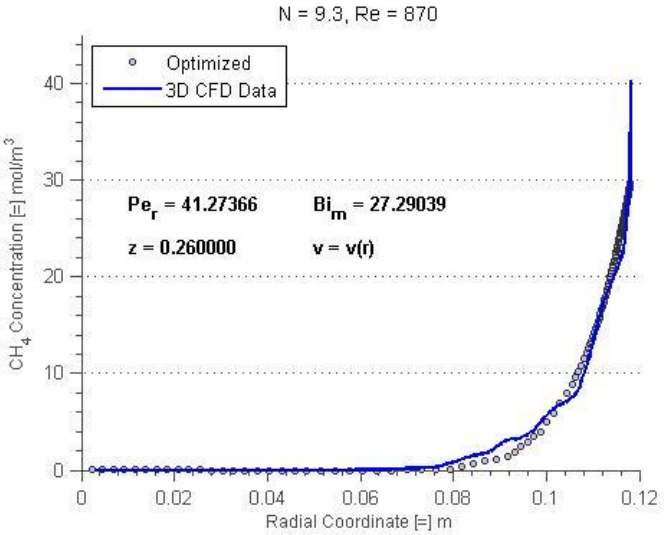

Figure C-126. Fitted radial concentration profile for N = 9.3, Re = 870, bed depth 02.

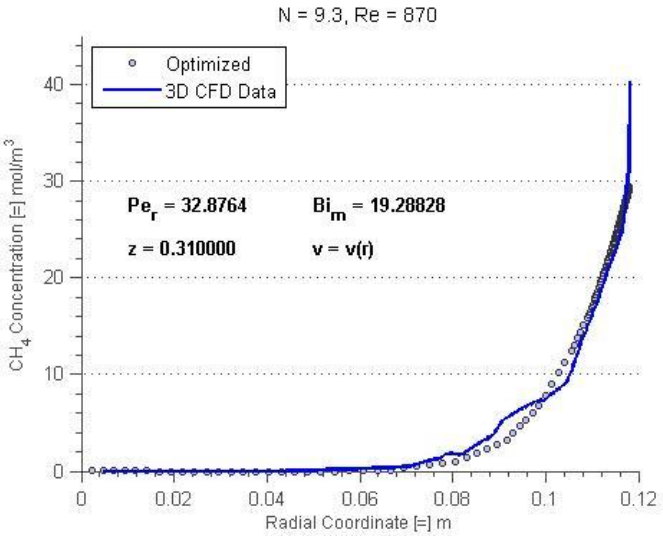

Figure C-127. Fitted radial concentration profile for N = 9.3, Re = 870, bed depth 03.

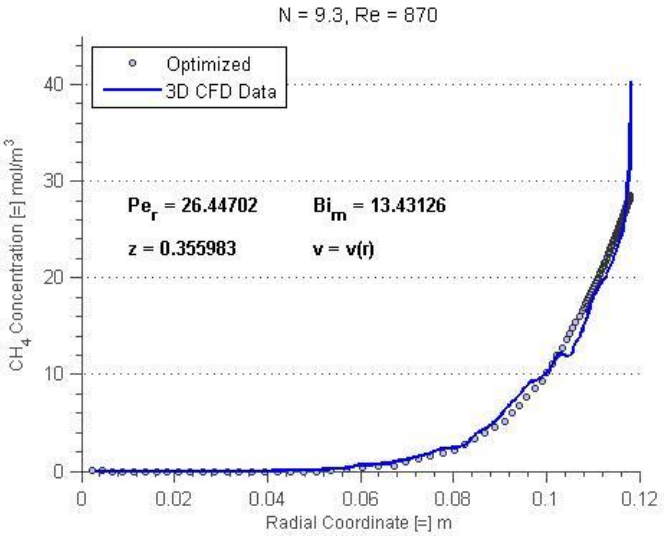

Figure C-128. Fitted radial concentration profile for N = 9.3, Re = 870, bed depth 04.

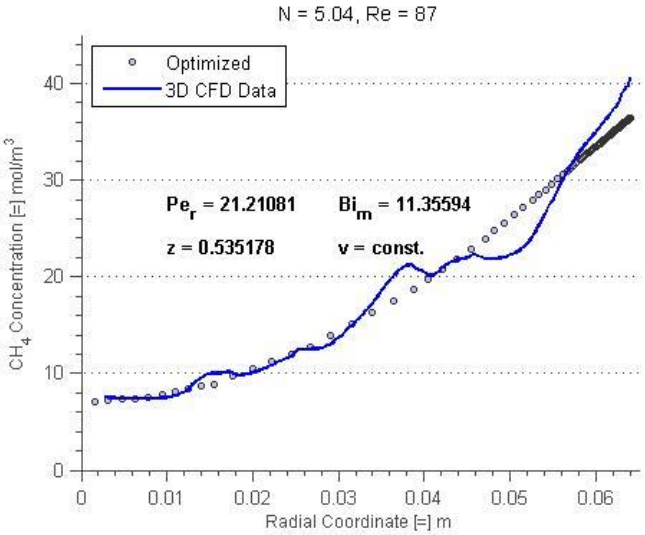

Figure C-129. Fitted radial concentration profile for N = 5.04, Re = 87, bed depth 01.

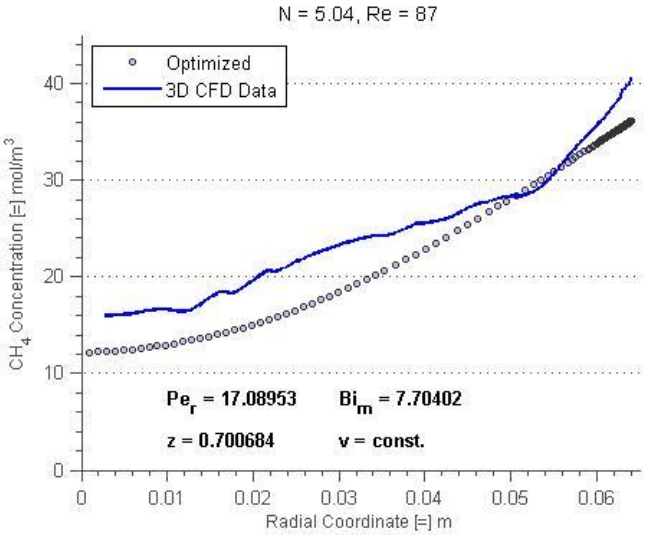

Figure C-130. Fitted radial concentration profile for N = 5.04, Re = 87, bed depth 02.

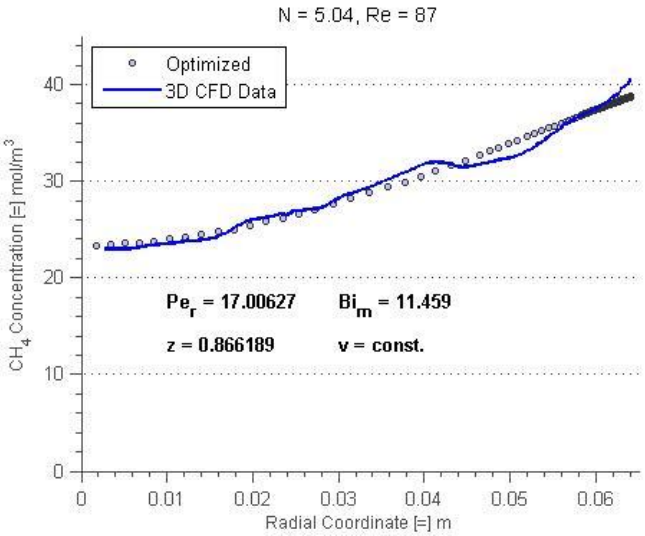

Figure C-131. Fitted radial concentration profile for N = 5.04, Re = 87, bed depth 03.

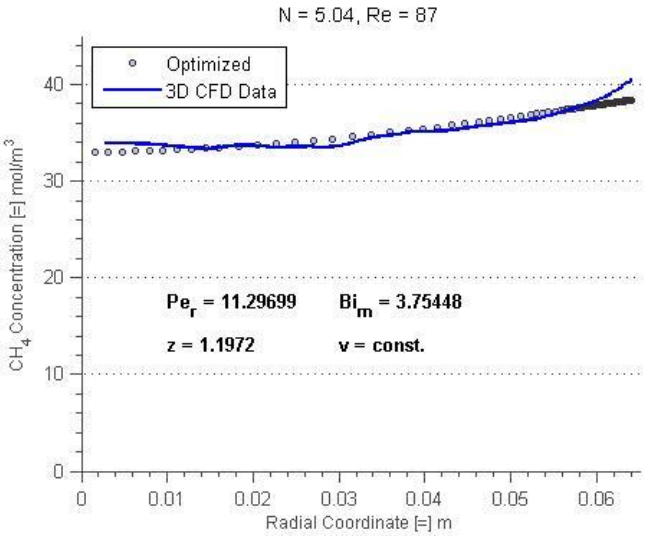

Figure C-132. Fitted radial concentration profile for N = 5.04, Re = 87, bed depth 04.

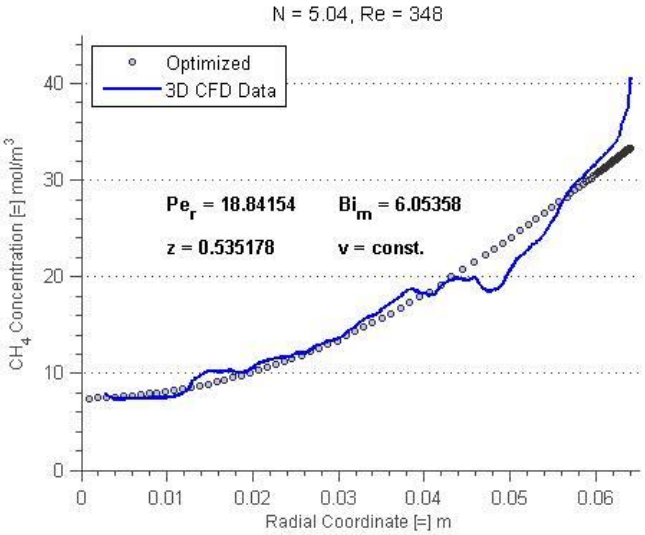

Figure C-133. Fitted radial concentration profile for N = 5.04, Re = 348, bed depth 01.

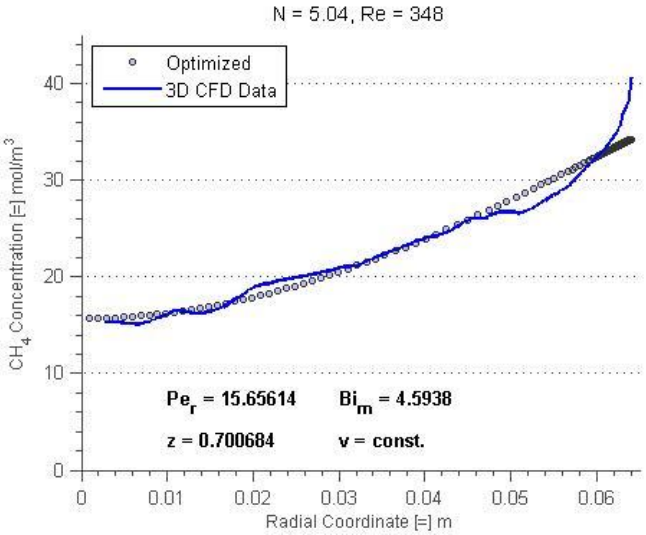

Figure C-134. Fitted radial concentration profile for N = 5.04, Re = 348, bed depth 02.

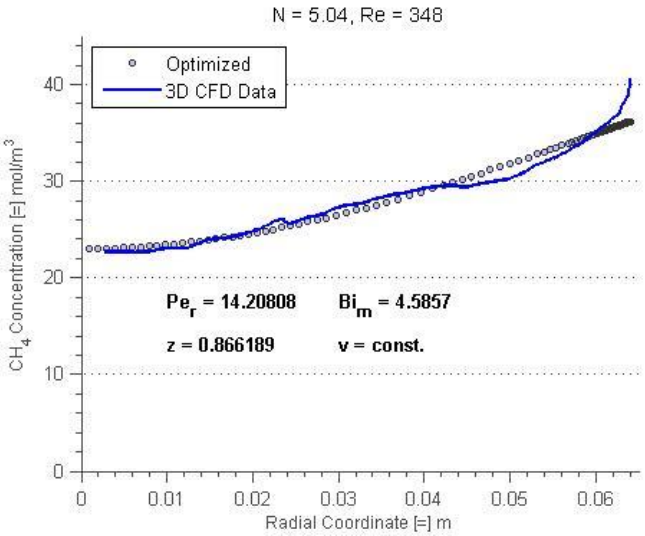

Figure C-135. Fitted radial concentration profile for N = 5.04, Re = 348, bed depth 03.

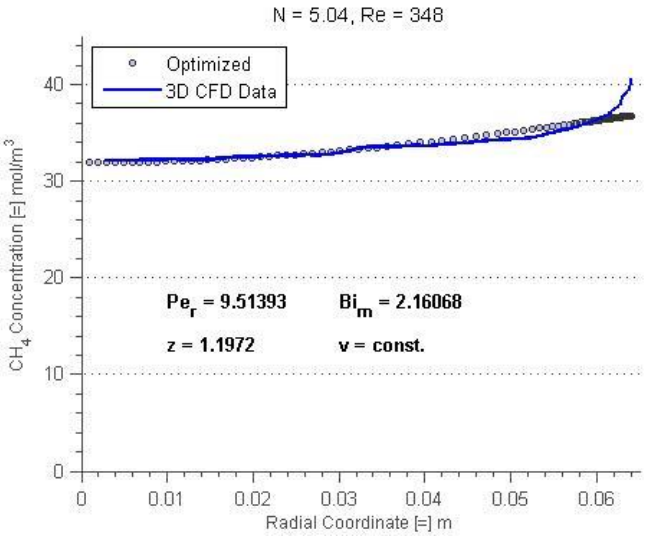

Figure C-136. Fitted radial concentration profile for N = 5.04, Re = 348, bed depth 04.

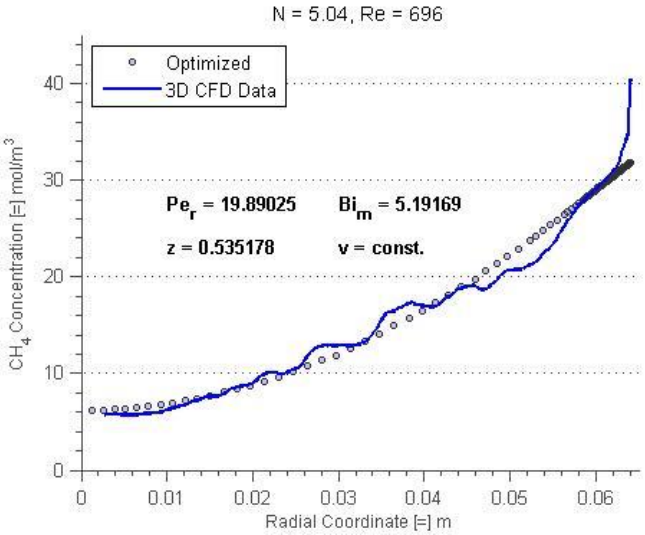

Figure C-137. Fitted radial concentration profile for N = 5.04, Re = 696, bed depth 01.

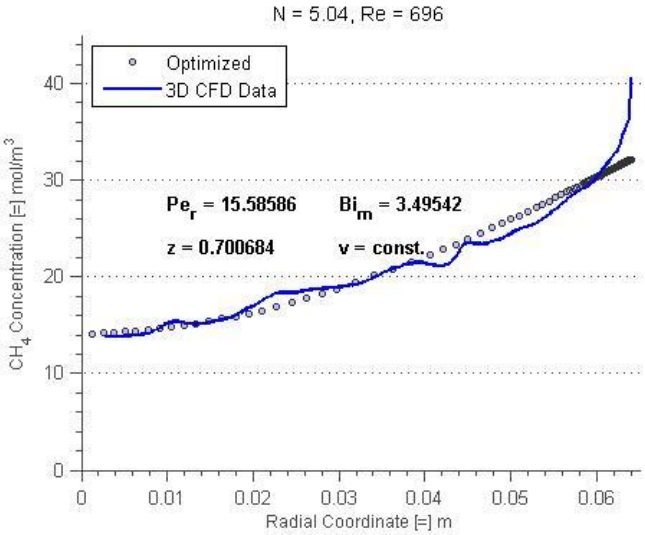

Figure C-138. Fitted radial concentration profile for N = 5.04, Re = 696, bed depth 02.

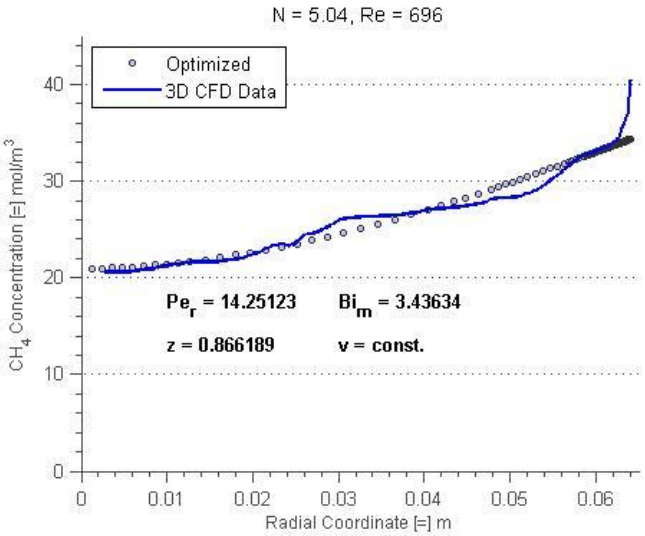

Figure C-139. Fitted radial concentration profile for N = 5.04, Re = 696, bed depth 03.

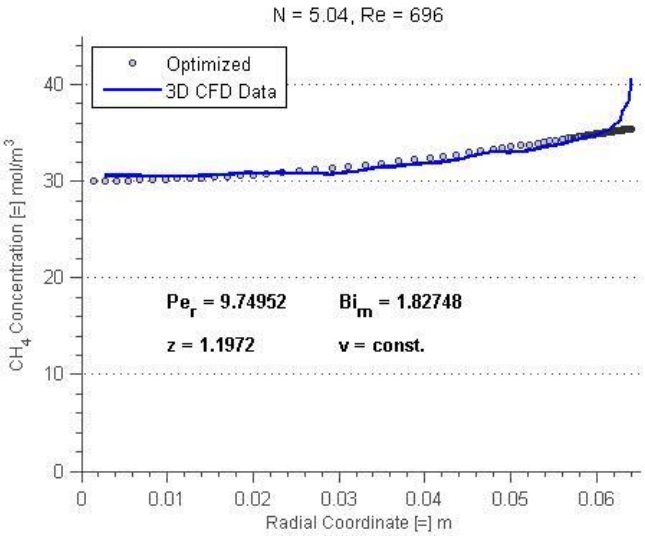

Figure C-140. Fitted radial concentration profile for N = 5.04, Re = 696, bed depth 04.

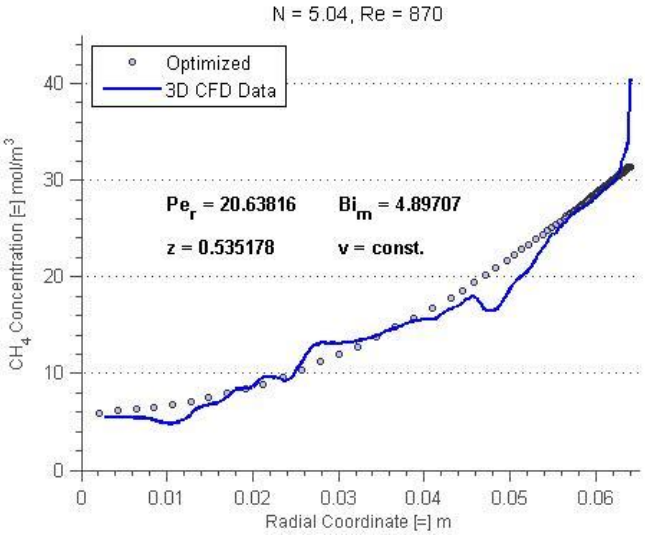

Figure C-141. Fitted radial concentration profile for N = 5.04, Re = 870, bed depth 01.

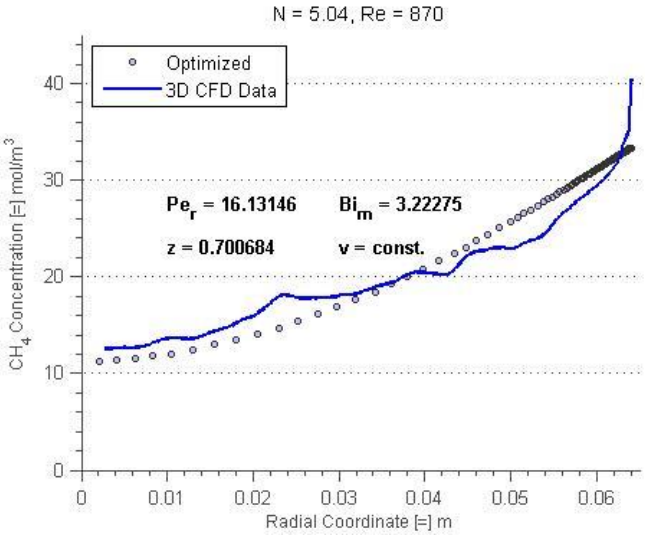

Figure C-142. Fitted radial concentration profile for N = 5.04, Re = 870, bed depth 02.

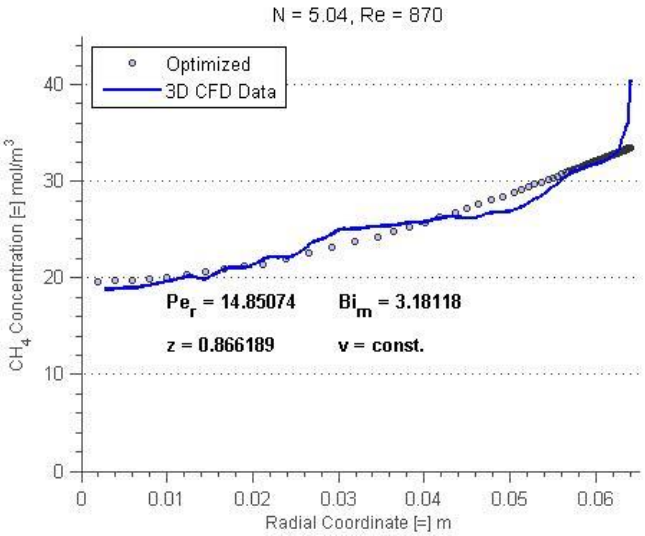

Figure C-143. Fitted radial concentration profile for N = 5.04, Re = 870, bed depth 03.

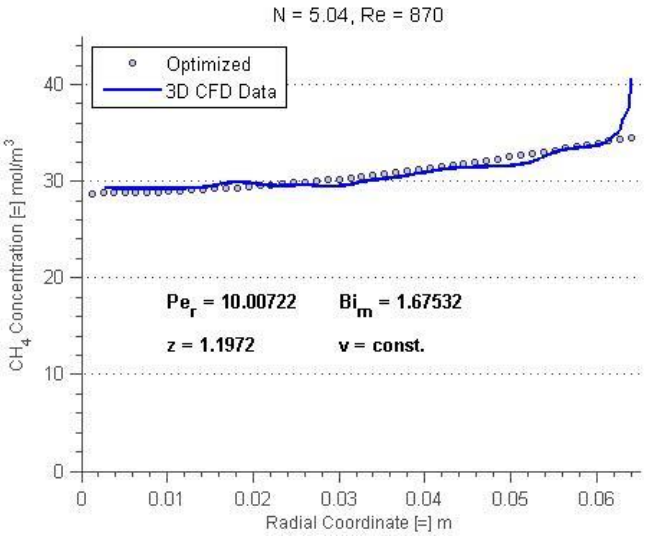

Figure C-144. Fitted radial concentration profile for N = 5.04, Re = 870, bed depth 04.

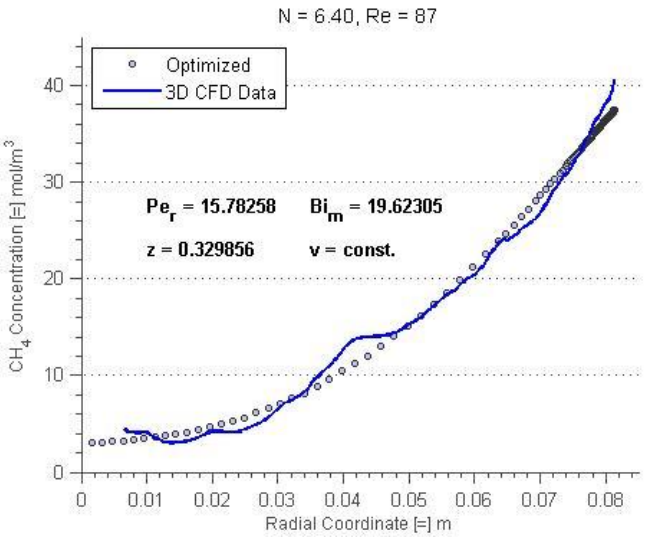

Figure C-145. Fitted radial concentration profile for N = 6.40, Re = 87, bed depth 01.

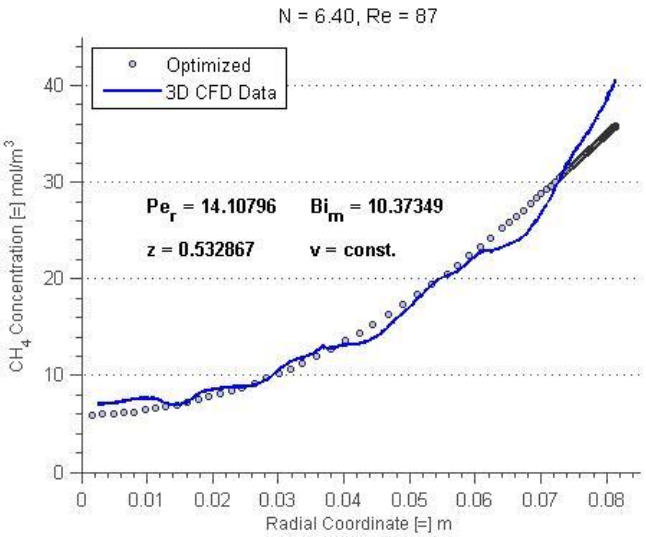

Figure C-146. Fitted radial concentration profile for N = 6.40, Re = 87, bed depth 02.

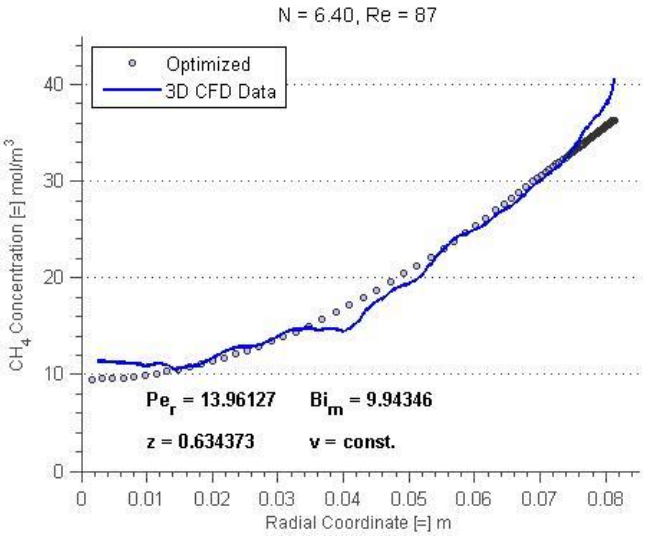

Figure C-147. Fitted radial concentration profile for N = 6.40, Re = 87, bed depth 03.

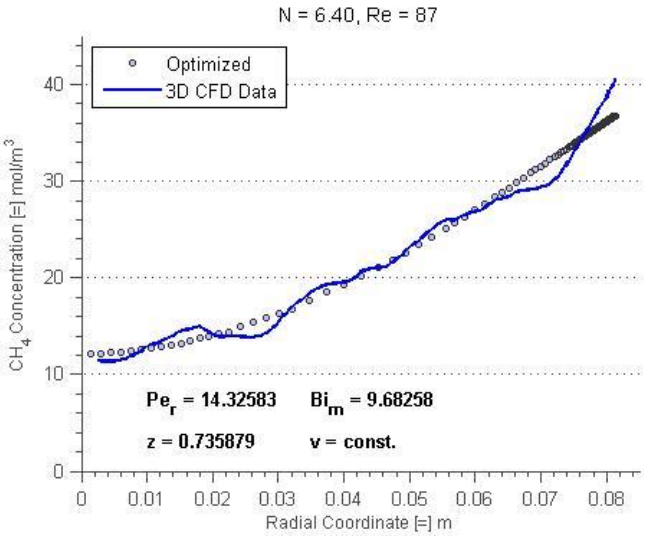

Figure C-148. Fitted radial concentration profile for N = 6.40, Re = 87, bed depth 04.

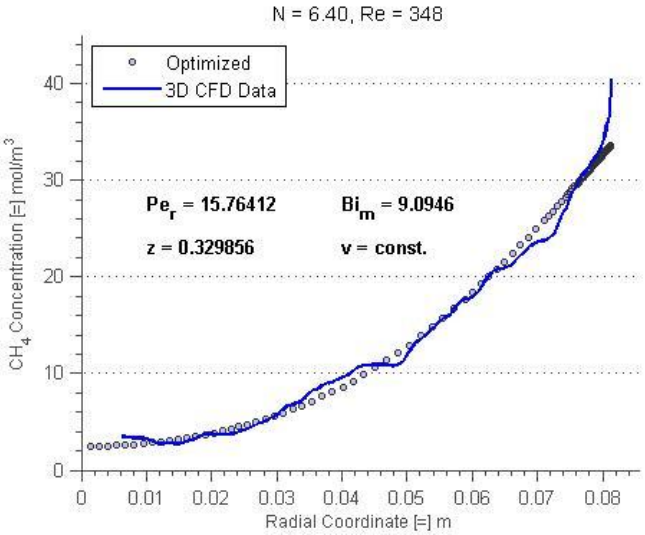

Figure C-149. Fitted radial concentration profile for N = 6.40, Re = 348, bed depth 01.

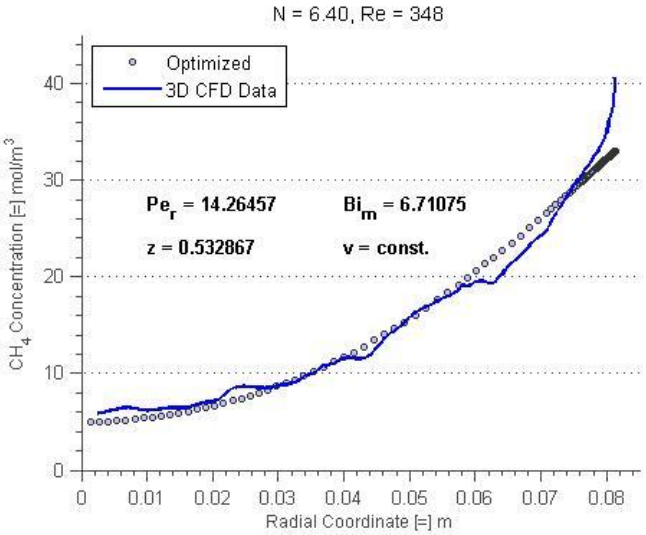

Figure C-150. Fitted radial concentration profile for N = 6.40, Re = 348, bed depth 02.

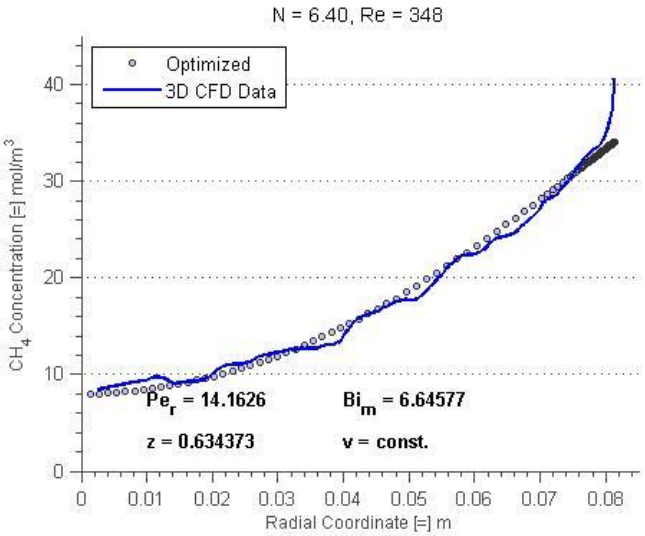

Figure C-151. Fitted radial concentration profile for N = 6.40, Re = 348, bed depth 03.

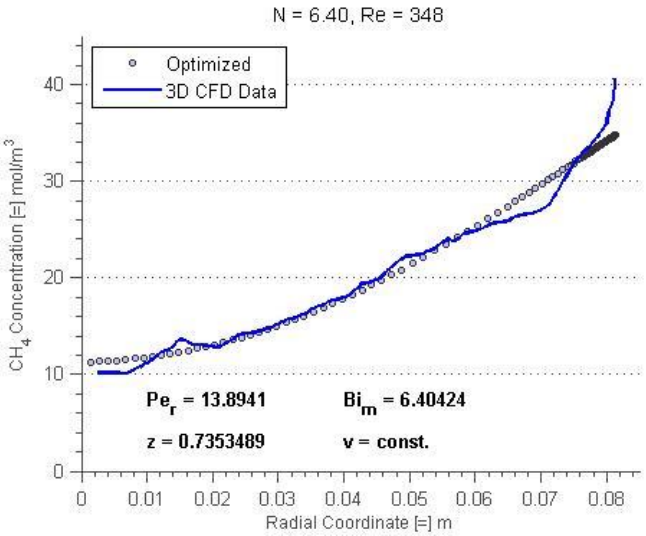

Figure C-152. Fitted radial concentration profile for N = 6.40, Re = 348, bed depth 04.

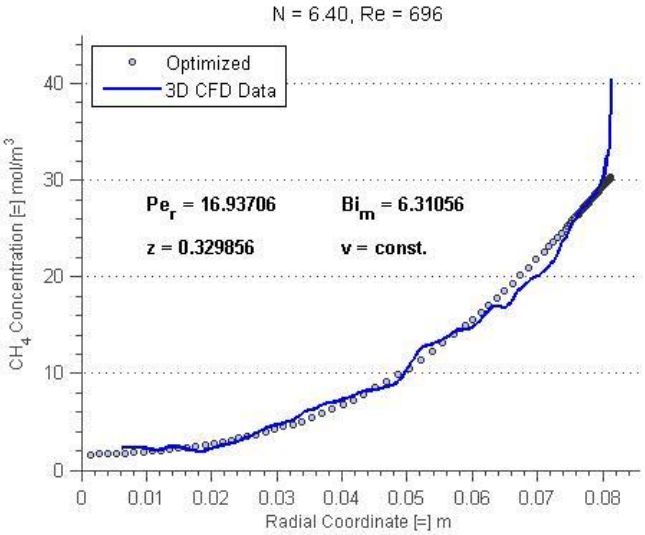

Figure C-153. Fitted radial concentration profile for N = 6.40, Re = 696, bed depth 01.

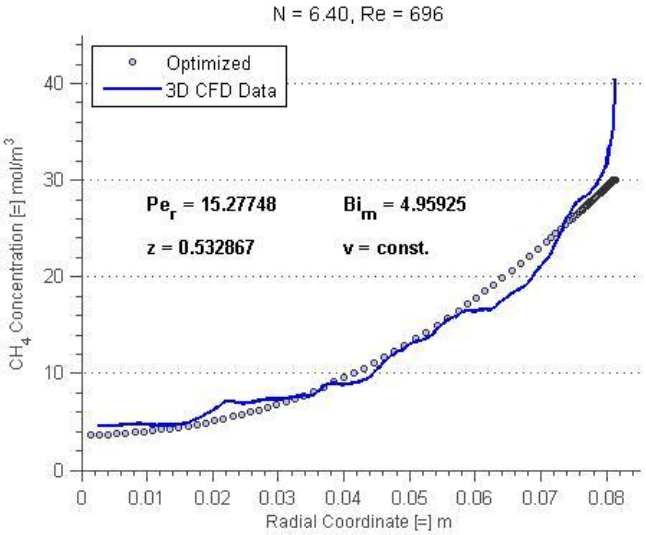

Figure C-154. Fitted radial concentration profile for N = 6.40, Re = 696, bed depth 02.

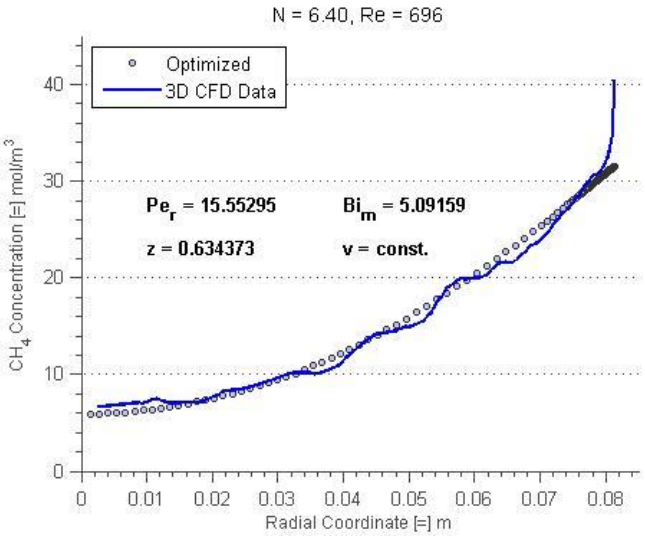

Figure C-155. Fitted radial concentration profile for N = 6.40, Re = 696, bed depth 03.

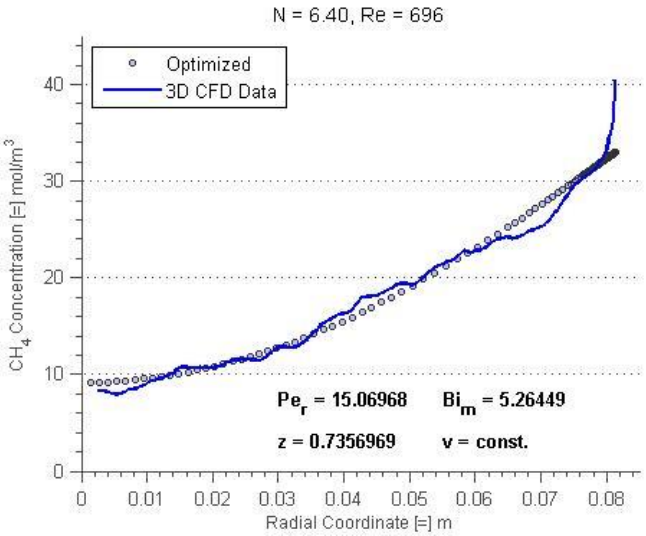

Figure C-156. Fitted radial concentration profile for N = 6.40, Re = 696, bed depth 04.

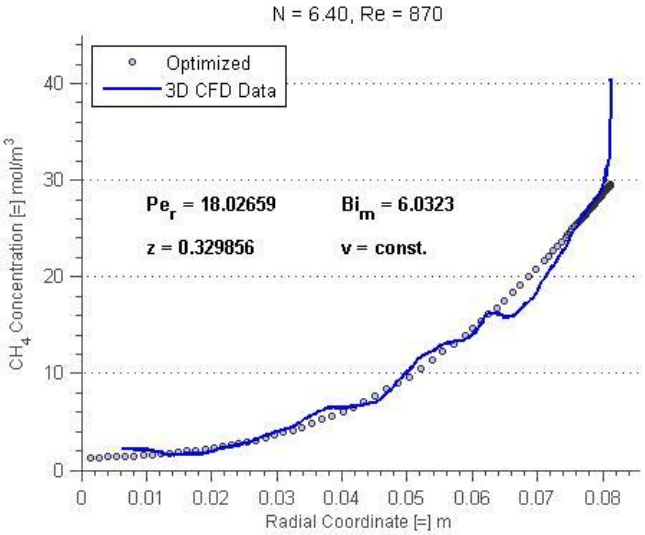

Figure C-157. Fitted radial concentration profile for N = 6.40, Re = 870, bed depth 01.

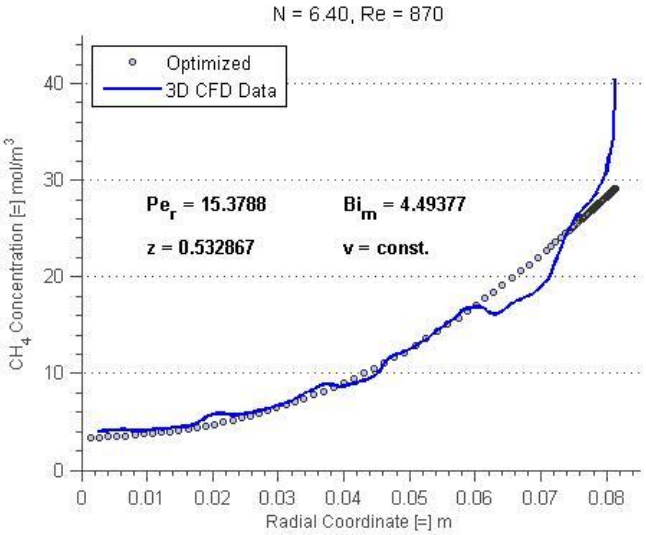

Figure C-158. Fitted radial concentration profile for N = 6.40, Re = 870, bed depth 02.

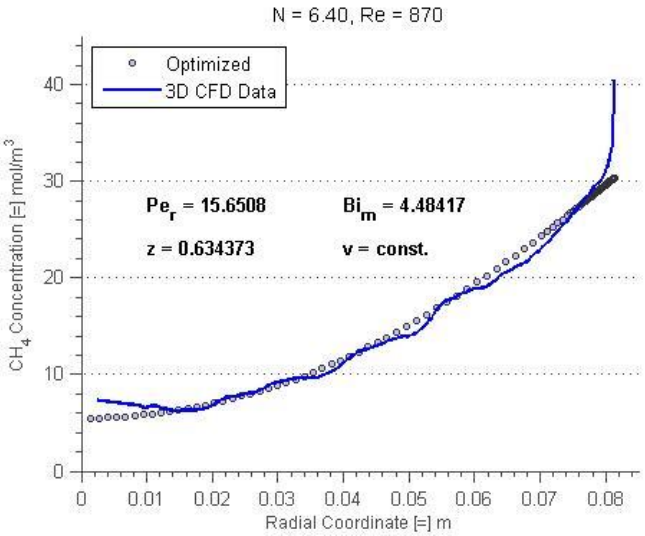

Figure C-159. Fitted radial concentration profile for N = 6.40, Re = 870, bed depth 03.

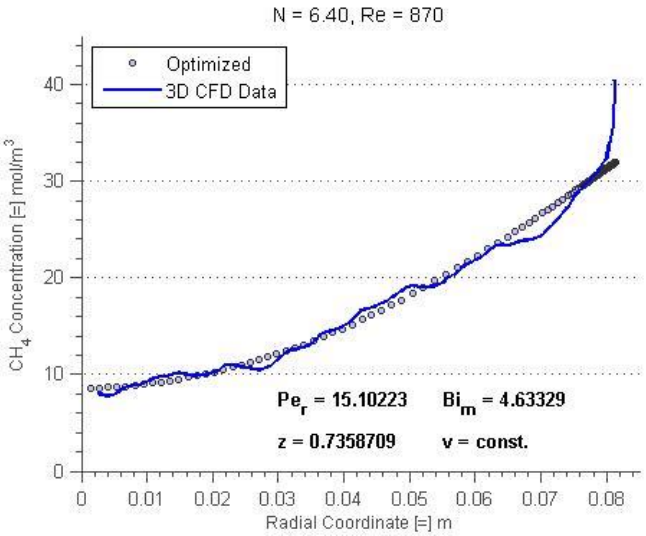

Figure C-160. Fitted radial concentration profile for N = 6.40, Re = 870, bed depth 04.

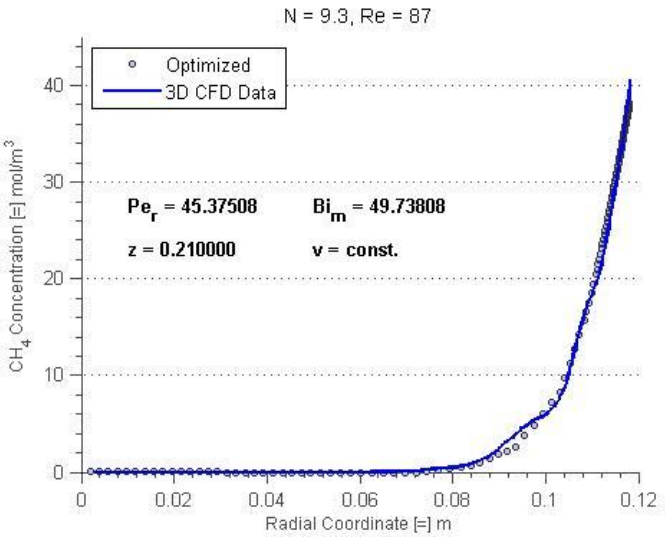

Figure C-161. Fitted radial concentration profile for N = 9.3, Re = 87, bed depth 01.

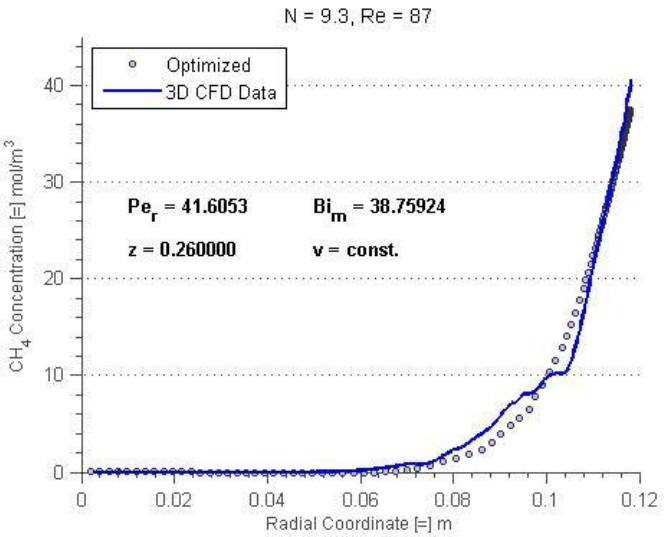

Figure C-162. Fitted radial concentration profile for N = 9.3, Re = 87, bed depth 02.

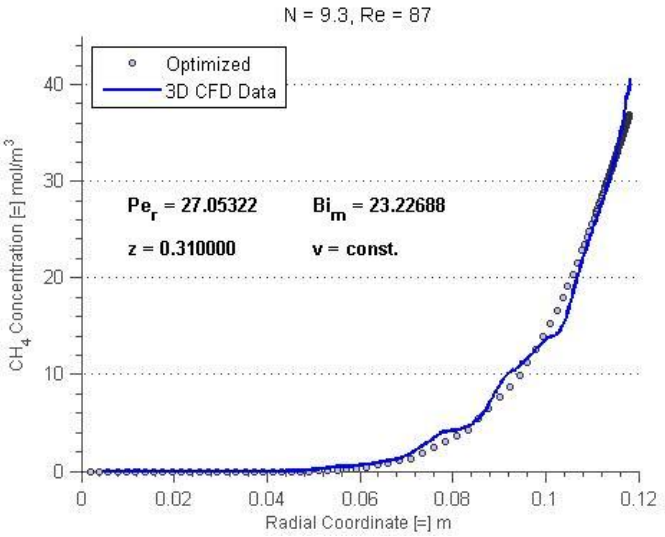

Figure C-163. Fitted radial concentration profile for N = 9.3, Re = 87, bed depth 03.

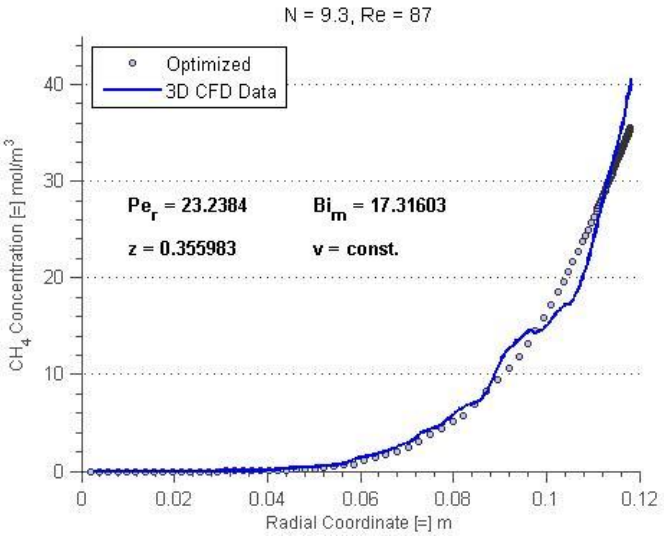

Figure C-164. Fitted radial concentration profile for N = 9.3, Re = 87, bed depth 04.

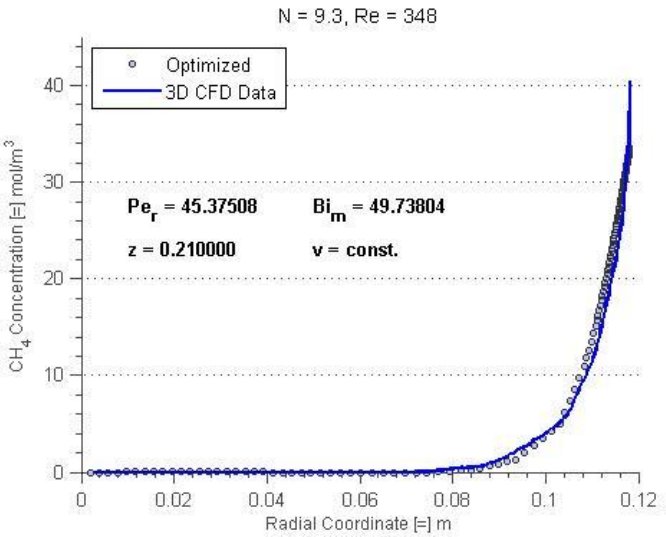

Figure C-165. Fitted radial concentration profile for N = 9.3, Re = 348, bed depth 01.

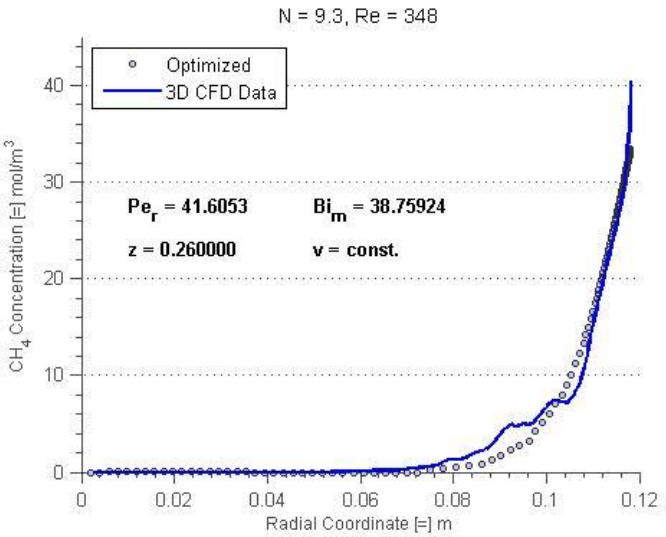

Figure C-166. Fitted radial concentration profile for N = 9.3, Re = 348, bed depth 02.

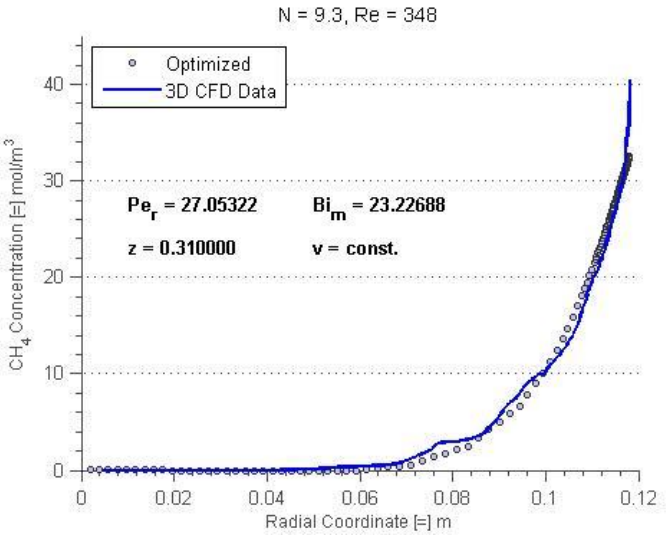

Figure C-167. Fitted radial concentration profile for N = 9.3, Re = 348, bed depth 03.

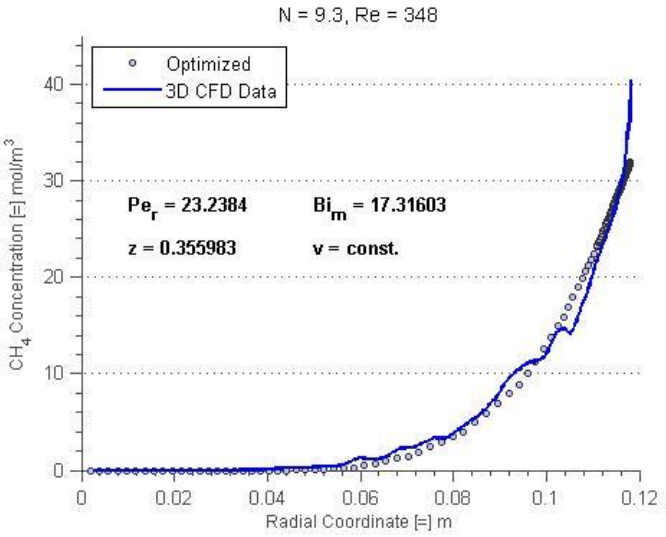

Figure C-168. Fitted radial concentration profile for N = 9.3, Re = 348, bed depth 04.

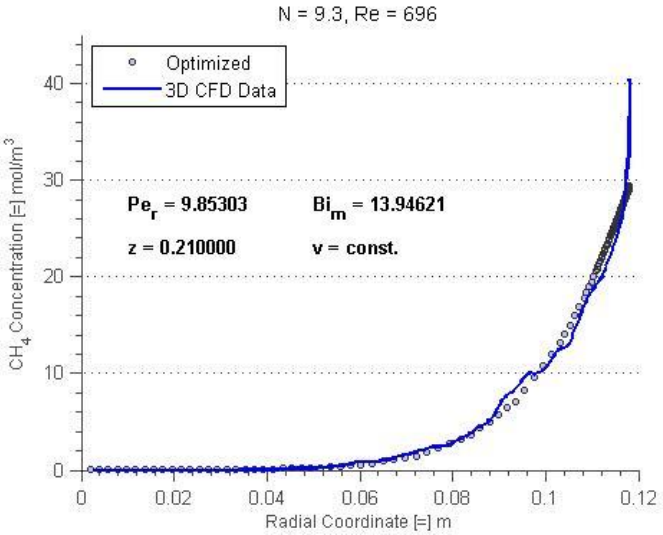

Figure C-169. Fitted radial concentration profile for N = 9.3, Re = 696, bed depth 01.

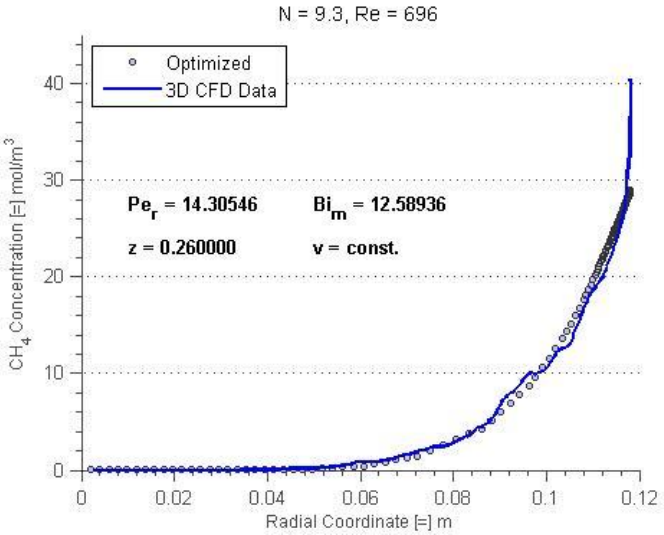

Figure C-170. Fitted radial concentration profile for N = 9.3, Re = 696, bed depth 02.

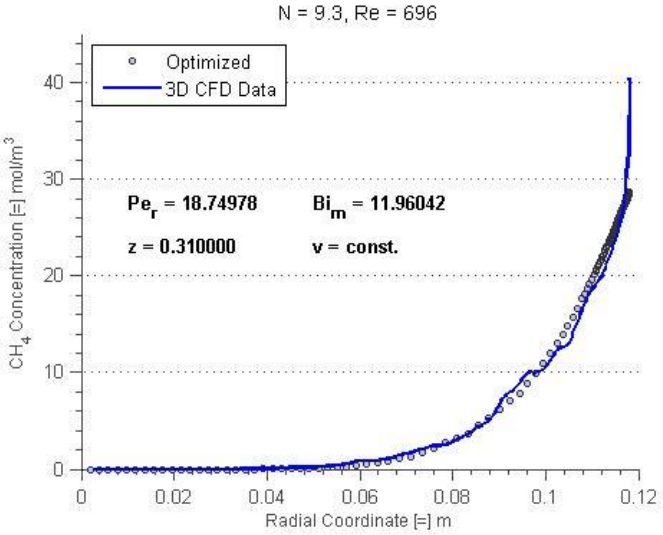

Figure C-171. Fitted radial concentration profile for N = 9.3, Re = 696, bed depth 03.

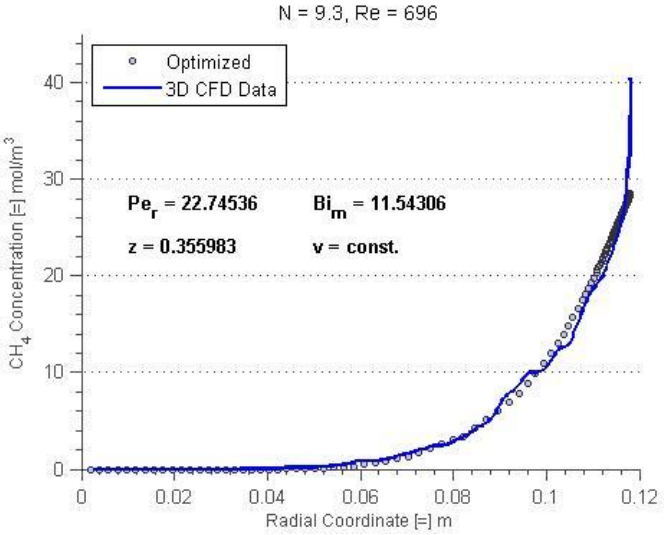

Figure C-172. Fitted radial concentration profile for N = 9.3, Re = 696, bed depth 04.

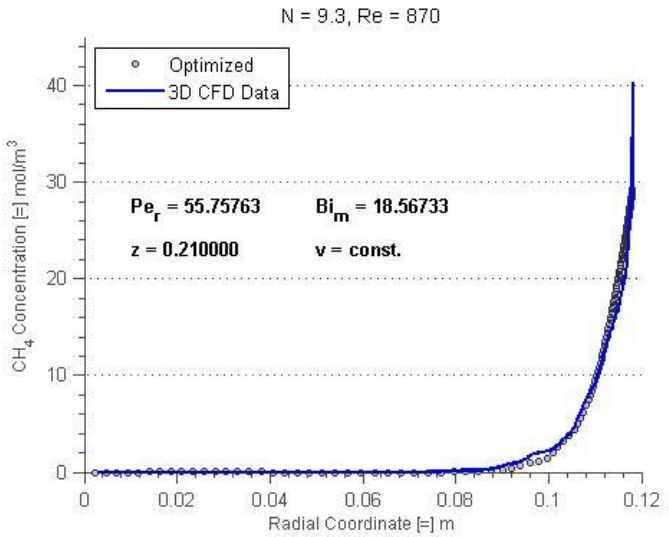

Figure C-173. Fitted radial concentration profile for N = 9.3, Re = 870, bed depth 01.

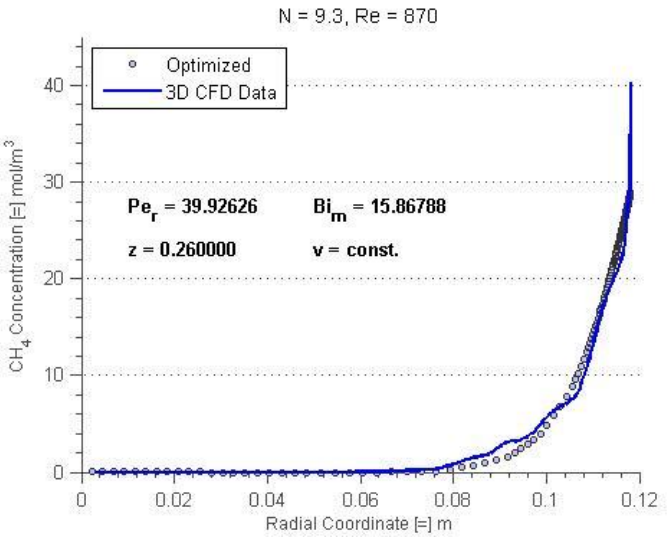

Figure C-174. Fitted radial concentration profile for N = 9.3, Re = 870, bed depth 02.

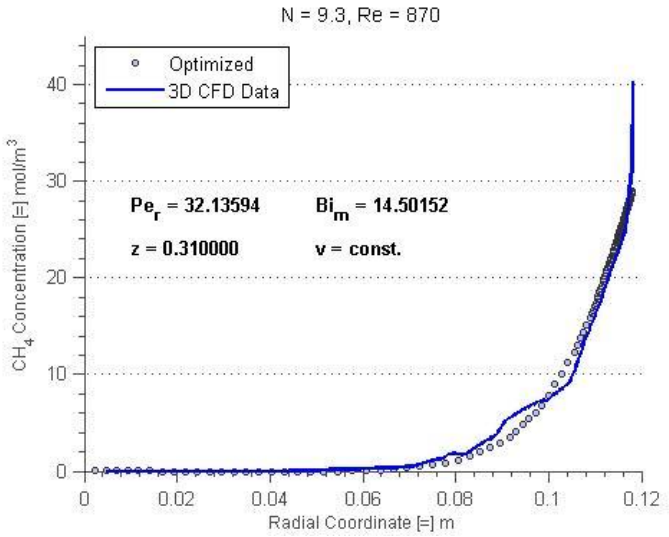

Figure C-175. Fitted radial concentration profile for N = 9.3, Re = 870, bed depth 03.

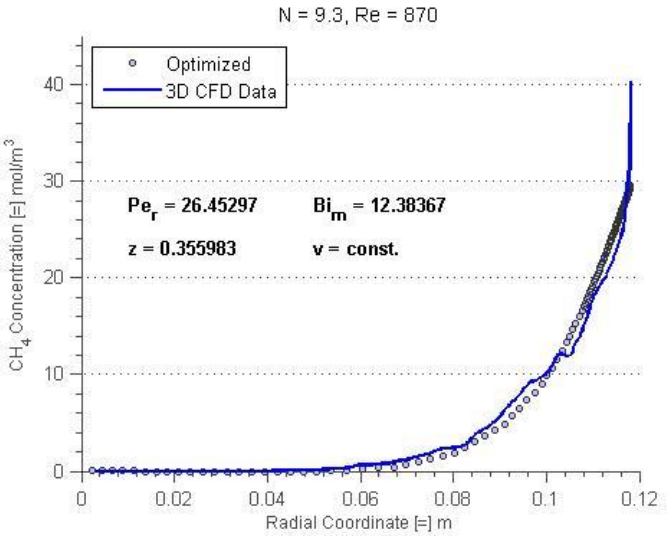

Figure C-176. Fitted radial concentration profile for N = 9.3, Re = 870, bed depth 04.

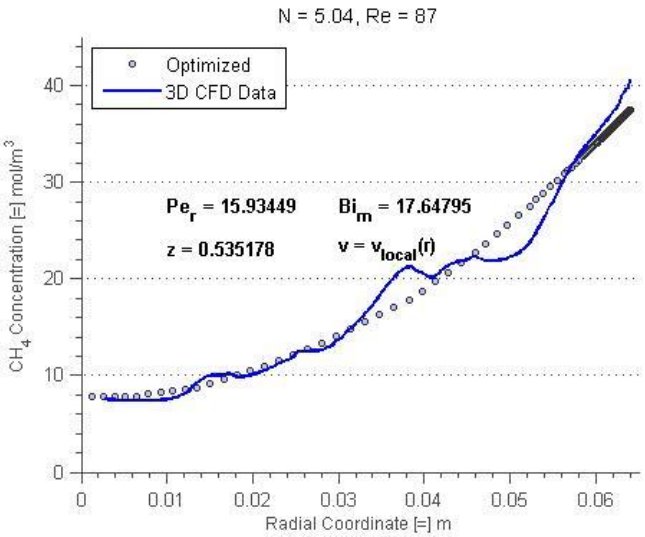

Figure C-177. Fitted radial concentration profile for N = 5.04, Re = 87, bed depth 01.

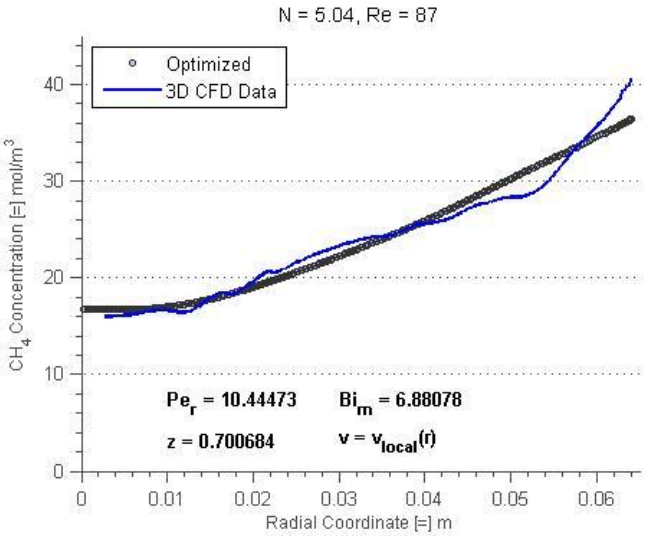

Figure C-178. Fitted radial concentration profile for N = 5.04, Re = 87, bed depth 02.

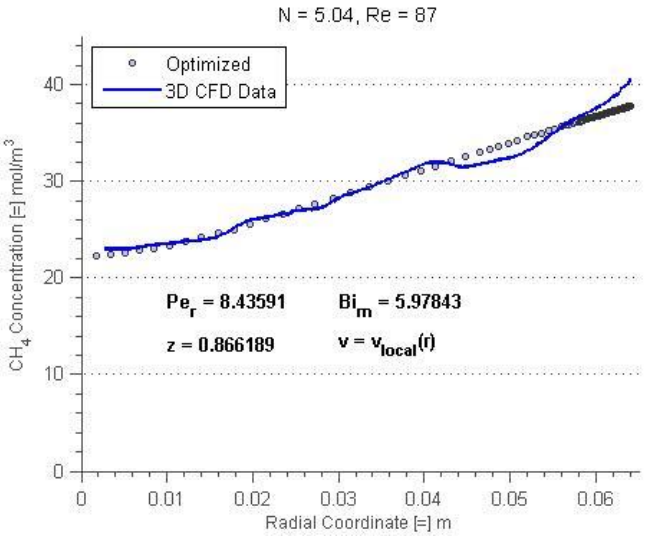

Figure C-179. Fitted radial concentration profile for N = 5.04, Re = 87, bed depth 03.

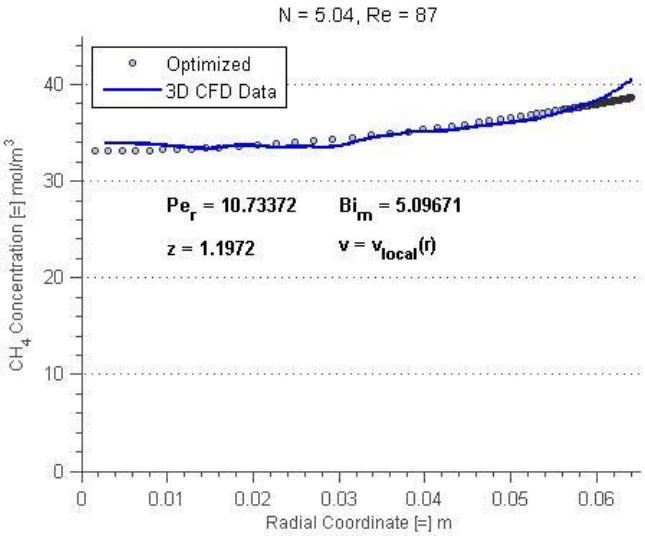

Figure C-180. Fitted radial concentration profile for N = 5.04, Re = 87, bed depth 04.

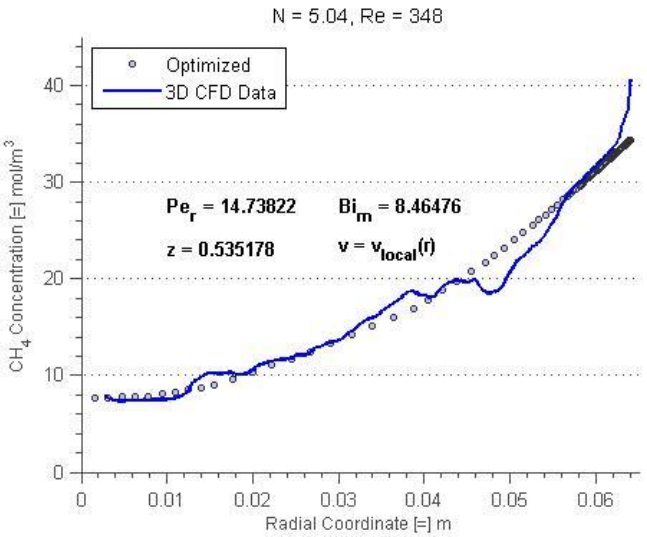

Figure C-181. Fitted radial concentration profile for N = 5.04, Re = 348, bed depth 01.

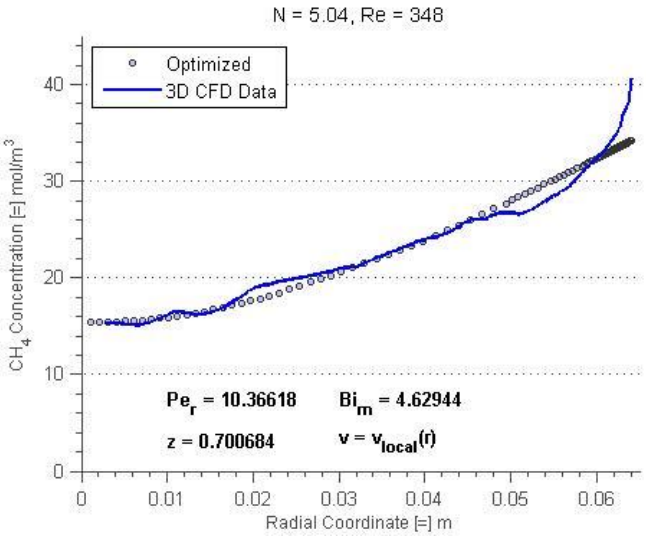

Figure C-182. Fitted radial concentration profile for N = 5.04, Re = 348, bed depth 02.

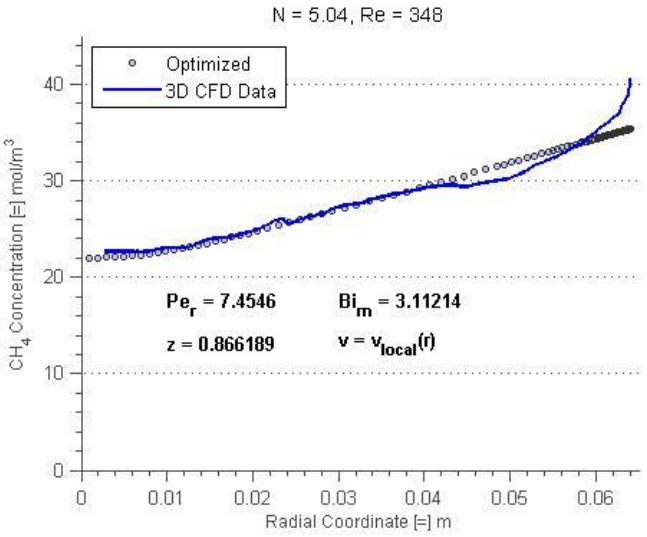

Figure C-183. Fitted radial concentration profile for N = 5.04, Re = 348, bed depth 03.

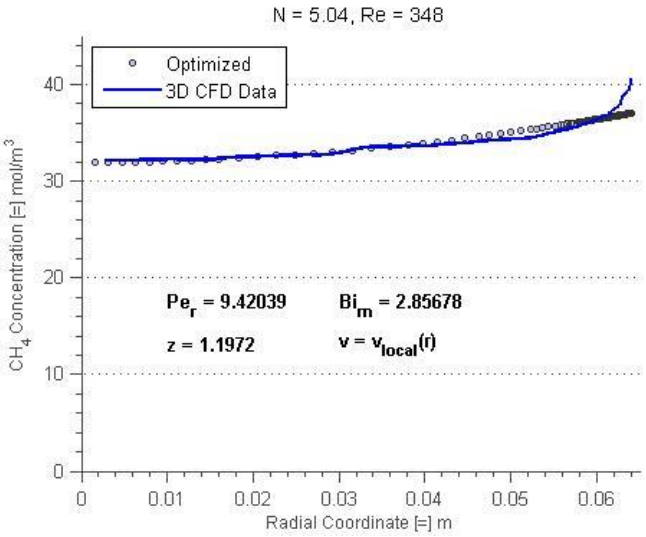

Figure C-184. Fitted radial concentration profile for N = 5.04, Re = 348, bed depth 04.

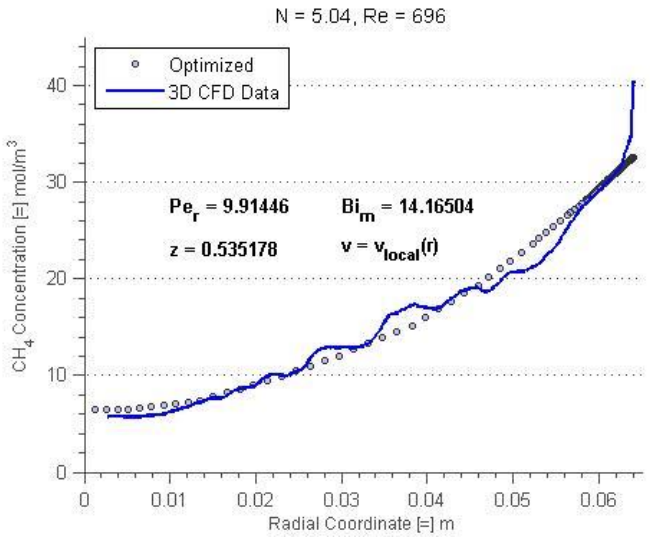

Figure C-185. Fitted radial concentration profile for N = 5.04, Re = 696, bed depth 01.

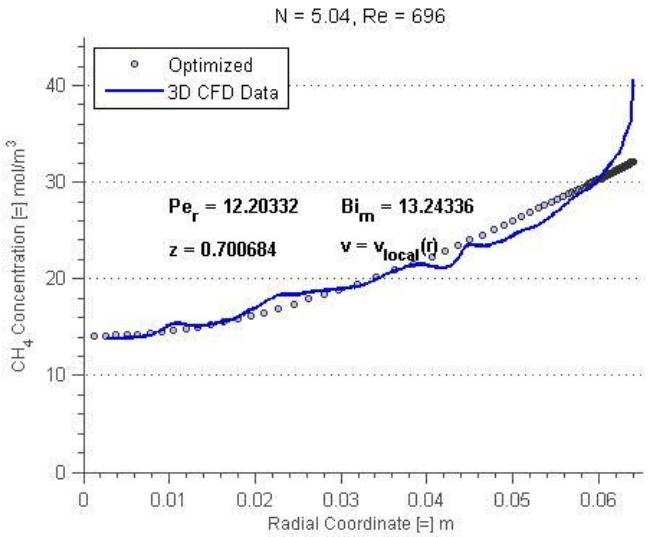

Figure C-186. Fitted radial concentration profile for N = 5.04, Re = 696, bed depth 02.

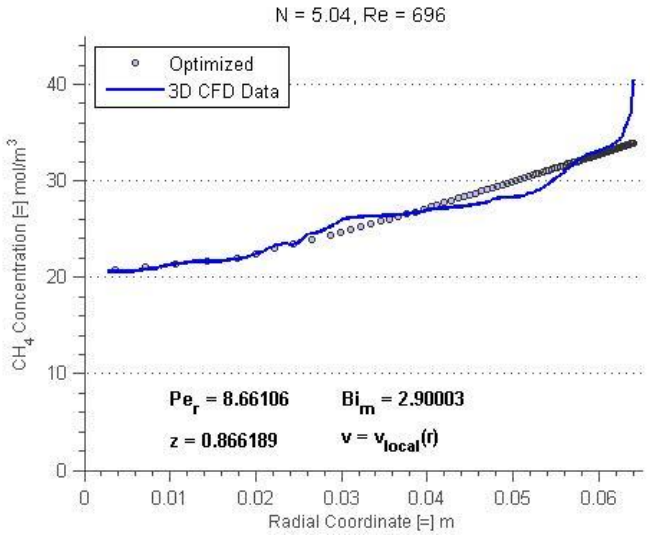

Figure C-187. Fitted radial concentration profile for N = 5.04, Re = 696, bed depth 03.

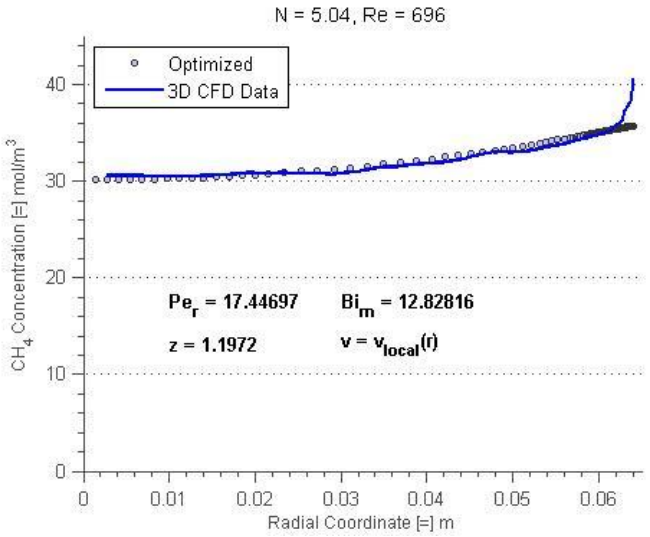

Figure C-188. Fitted radial concentration profile for N = 5.04, Re = 696, bed depth 04.

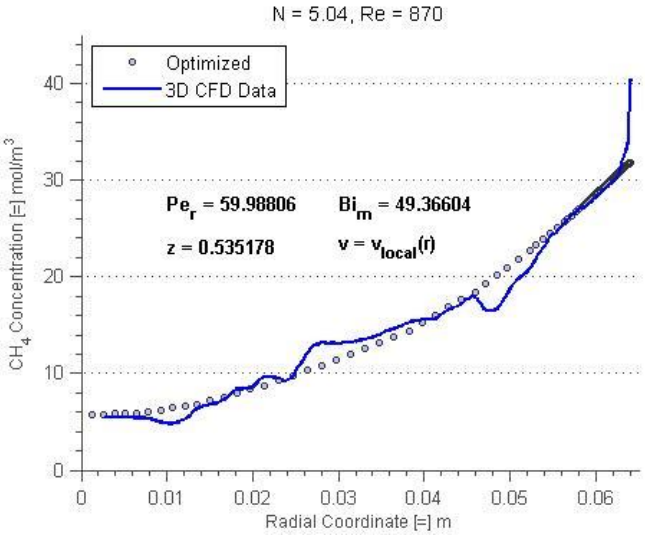

Figure C-189. Fitted radial concentration profile for N = 5.04, Re = 870, bed depth 01.

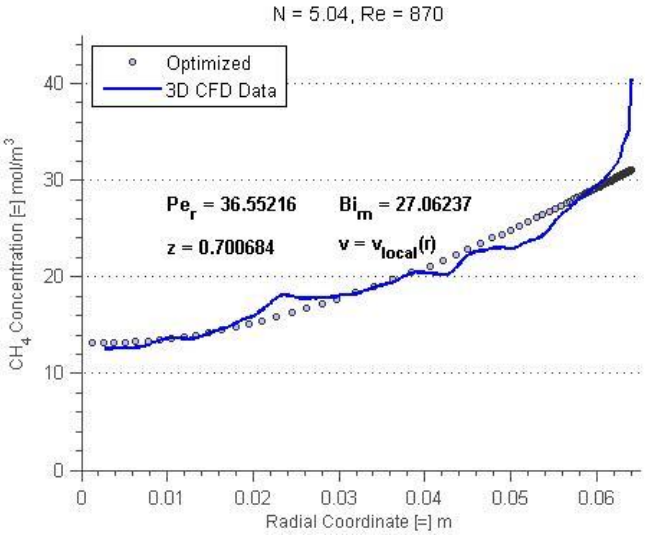

Figure C-190. Fitted radial concentration profile for N = 5.04, Re = 870, bed depth 02.

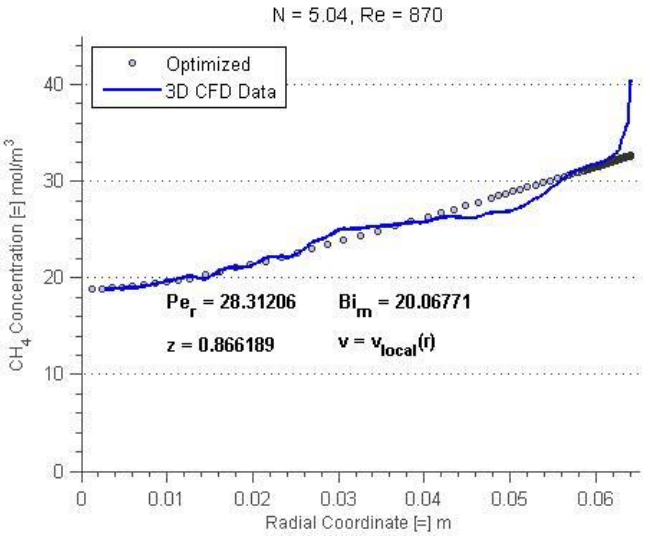

Figure C-191. Fitted radial concentration profile for N = 5.04, Re = 870, bed depth 03.

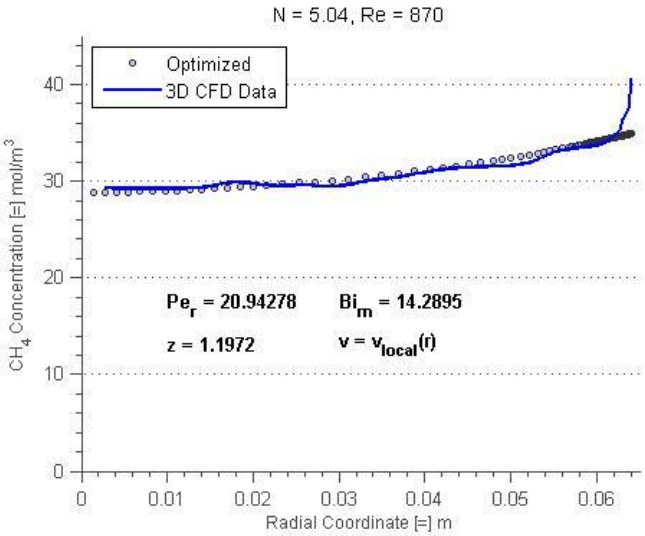

Figure C-192. Fitted radial concentration profile for N = 5.04, Re = 870, bed depth 04.

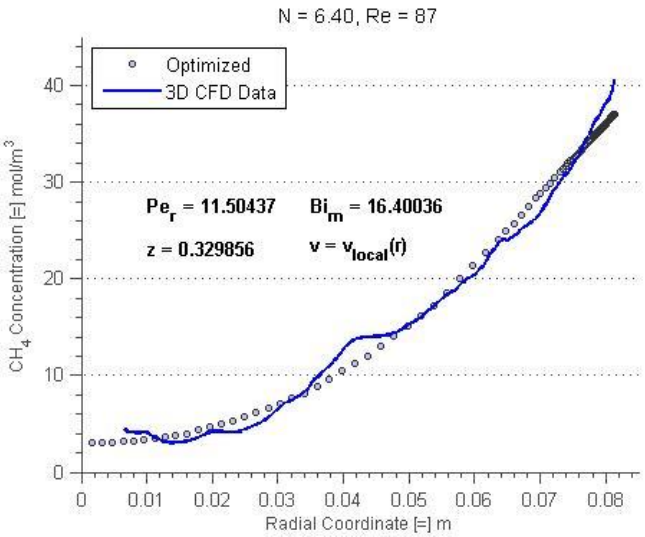

Figure C-193. Fitted radial concentration profile for N = 6.40, Re = 87, bed depth 01.

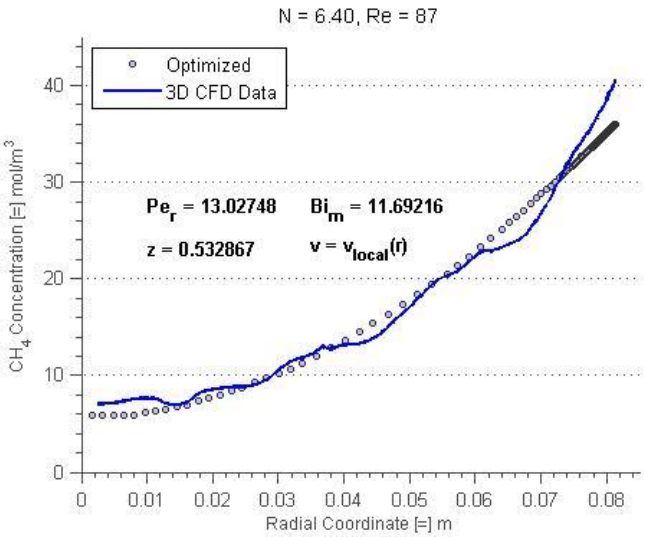

Figure C-194. Fitted radial concentration profile for N = 6.40, Re = 87, bed depth 02.

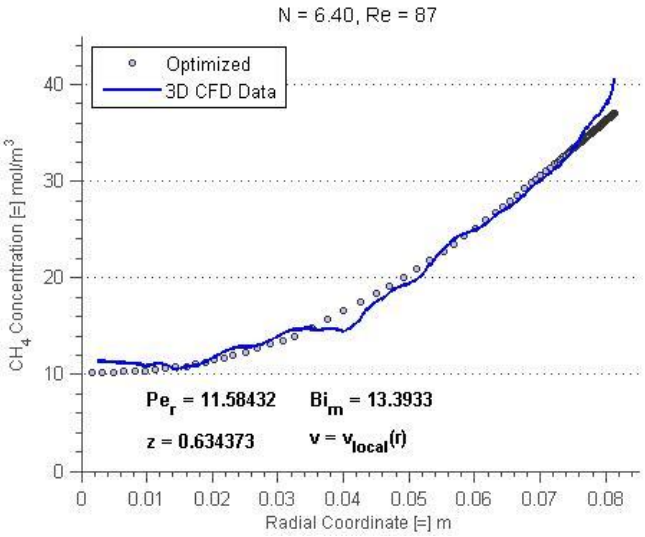

Figure C-195. Fitted radial concentration profile for N = 6.40, Re = 87, bed depth 03.

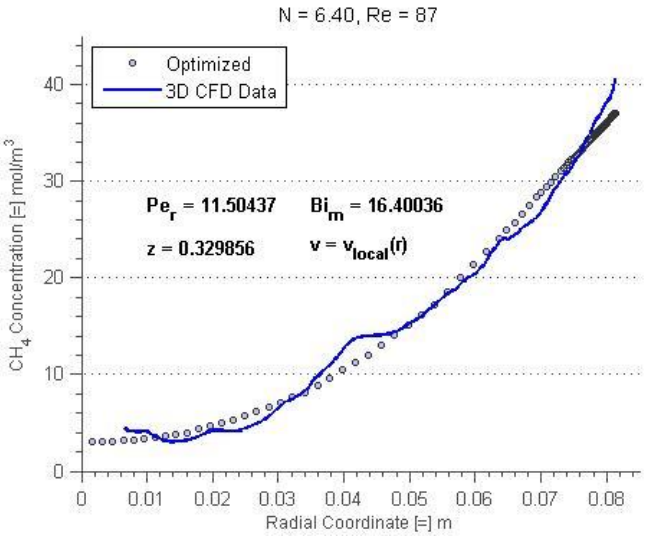

Figure C-196. Fitted radial concentration profile for N = 6.40, Re = 87, bed depth 04.

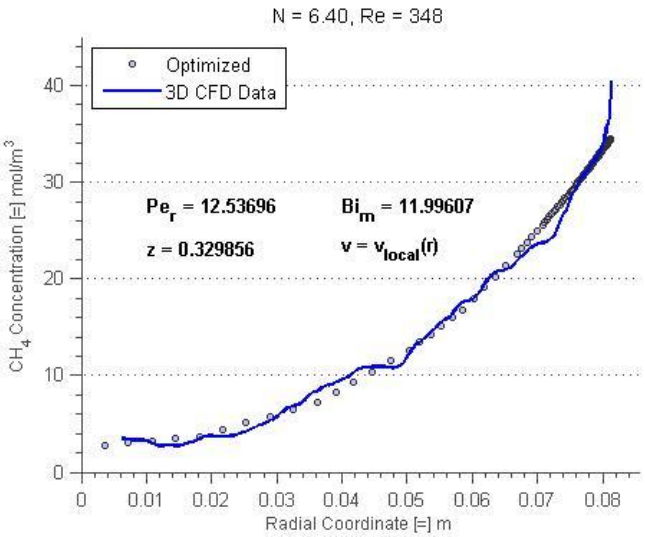

Figure C-197. Fitted radial concentration profile for N = 6.40, Re = 348, bed depth 01.

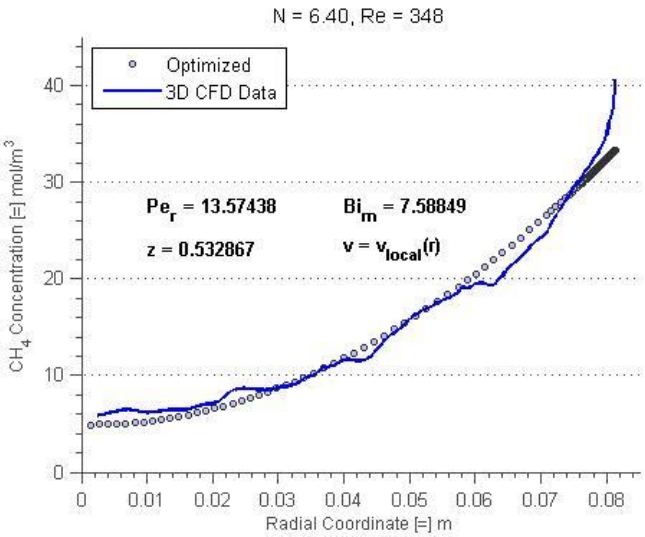

Figure C-198. Fitted radial concentration profile for N = 6.40, Re = 348, bed depth 02.

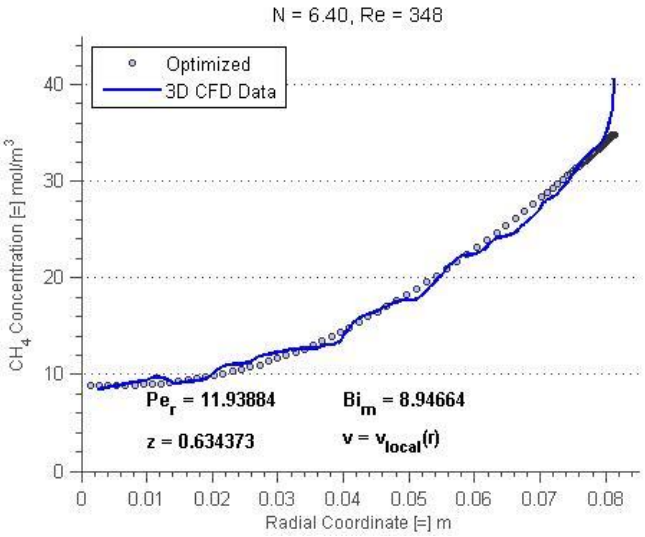

Figure C-199. Fitted radial concentration profile for N = 6.40, Re = 348, bed depth 03.

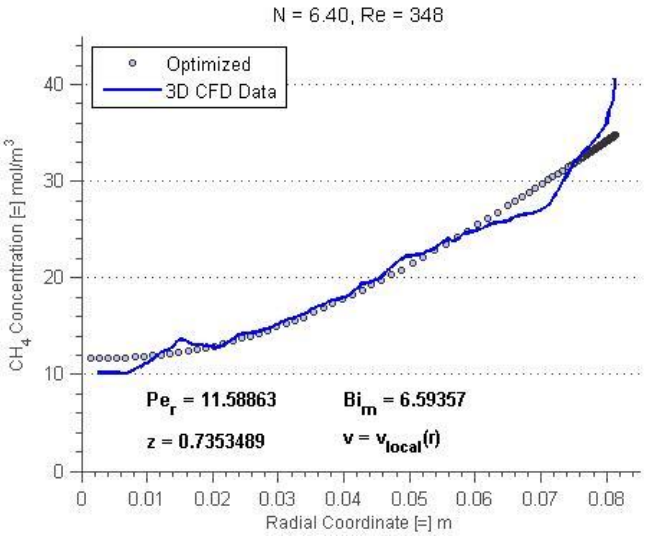

Figure C-200. Fitted radial concentration profile for N = 6.40, Re = 348, bed depth 04.

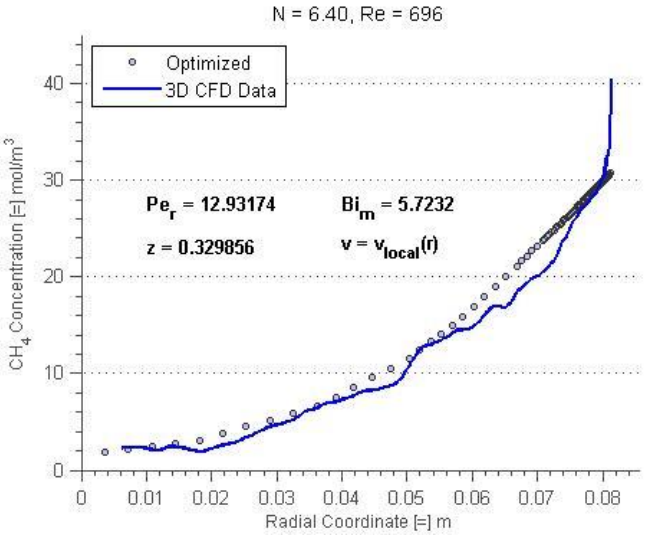

Figure C-201. Fitted radial concentration profile for N = 6.40, Re = 696, bed depth 01.

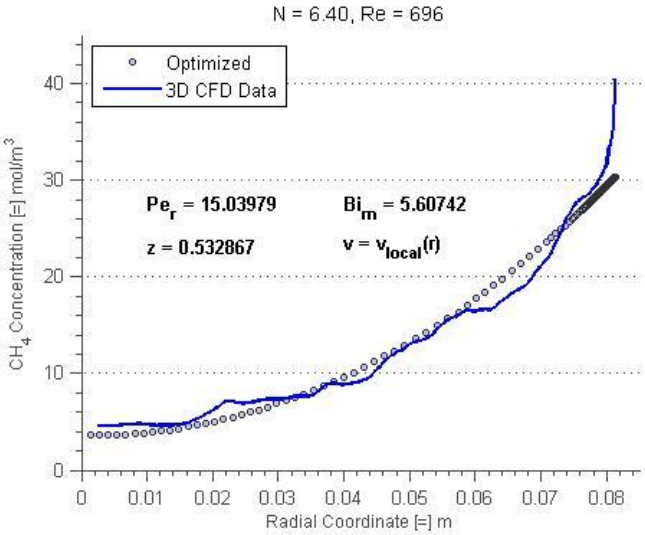

Figure C-202. Fitted radial concentration profile for N = 6.40, Re = 696, bed depth 02.

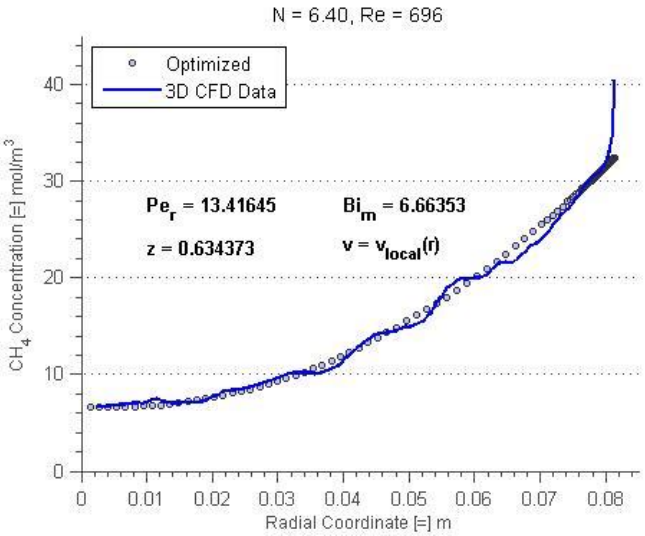

Figure C-203. Fitted radial concentration profile for N = 6.40, Re = 696, bed depth 03.

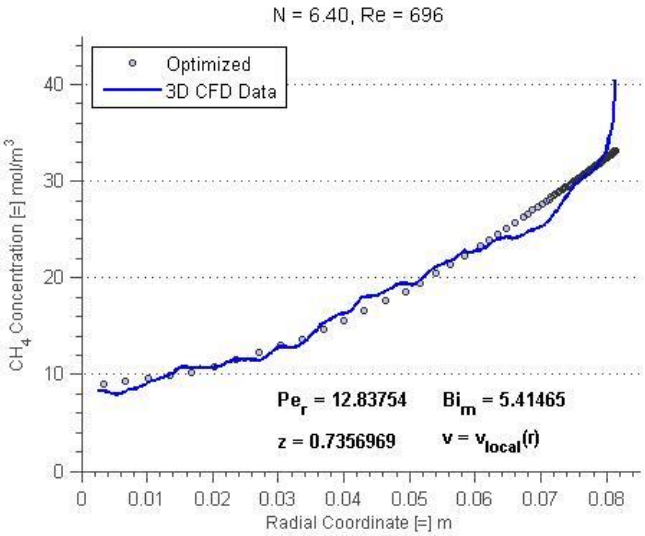

Figure C-204. Fitted radial concentration profile for N = 6.40, Re = 696, bed depth 04.

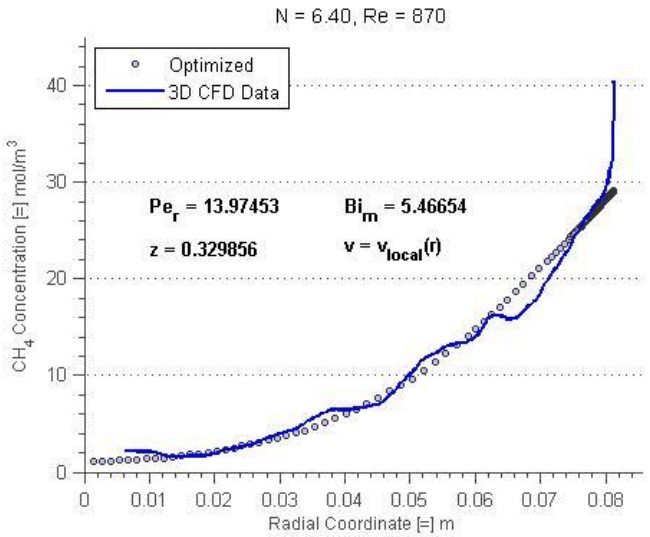

Figure C-205. Fitted radial concentration profile for N = 6.40, Re = 870, bed depth 01.

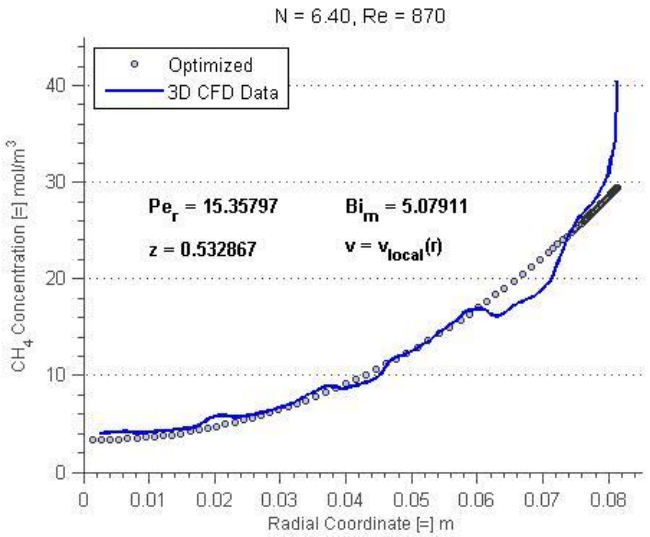

Figure C-206. Fitted radial concentration profile for N = 6.40, Re = 870, bed depth 02.

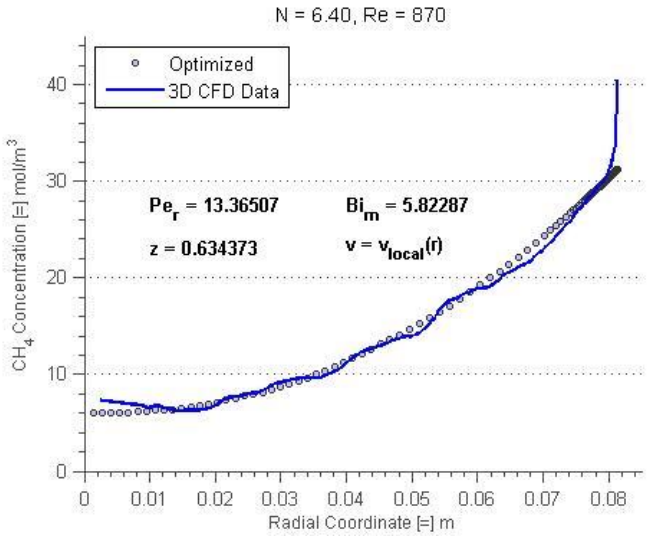

Figure C-207. Fitted radial concentration profile for N = 6.40, Re = 870, bed depth 03.

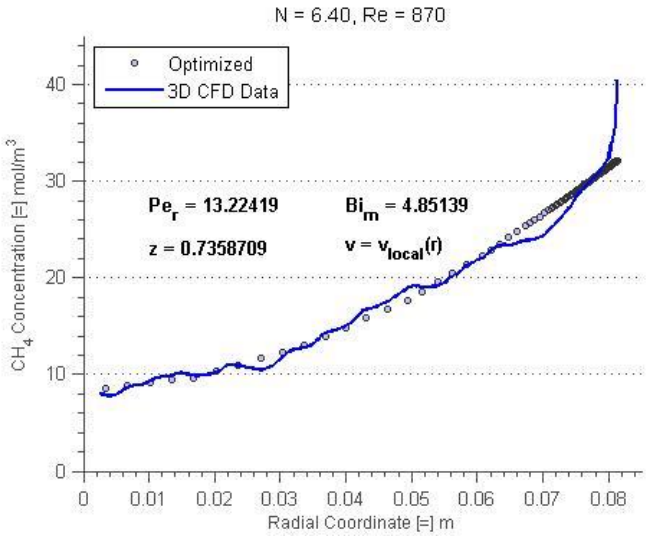

Figure C-208. Fitted radial concentration profile for N = 6.40, Re = 870, bed depth 04.

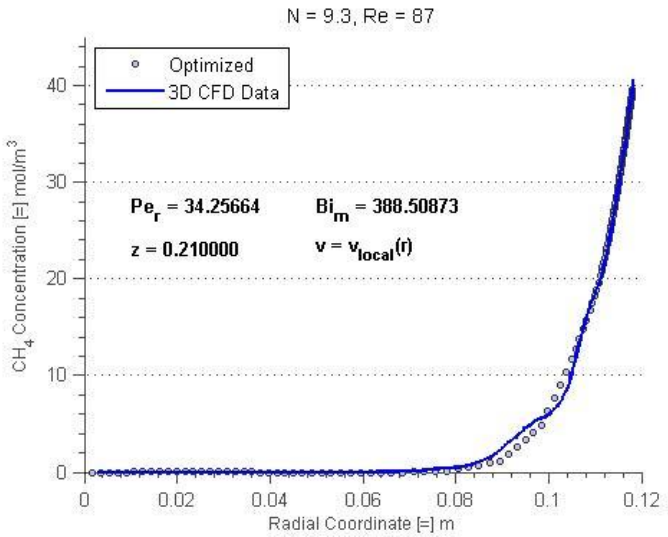

Figure C-209. Fitted radial concentration profile for N = 9.3, Re = 87, bed depth 01.

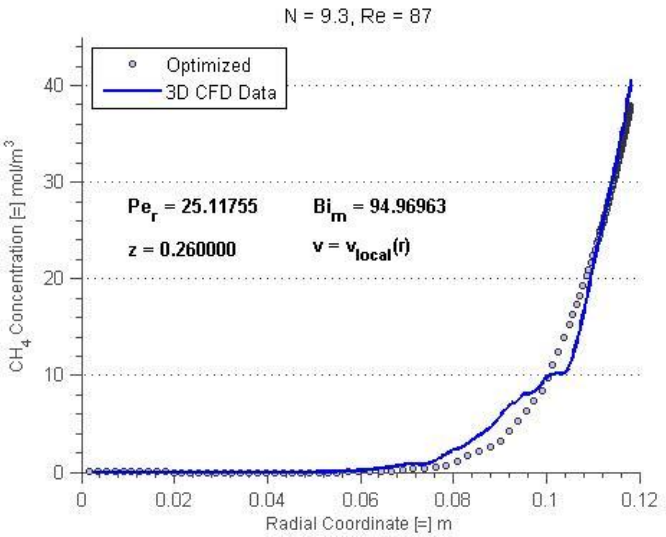

Figure C-210. Fitted radial concentration profile for N = 9.3, Re = 87, bed depth 02.

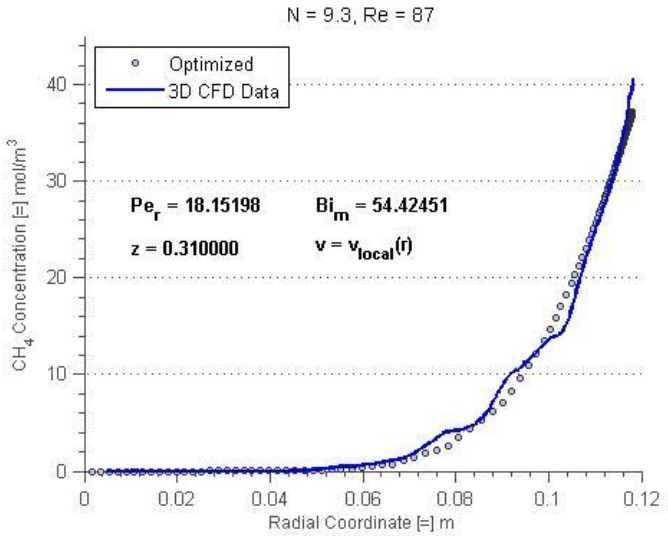

Figure C-211. Fitted radial concentration profile for N = 9.3, Re = 87, bed depth 03.

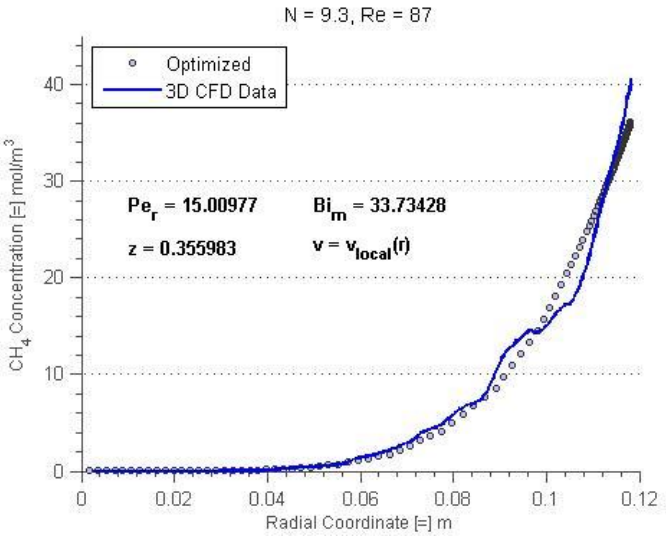

Figure C-212. Fitted radial concentration profile for N = 9.3, Re = 87, bed depth 04.

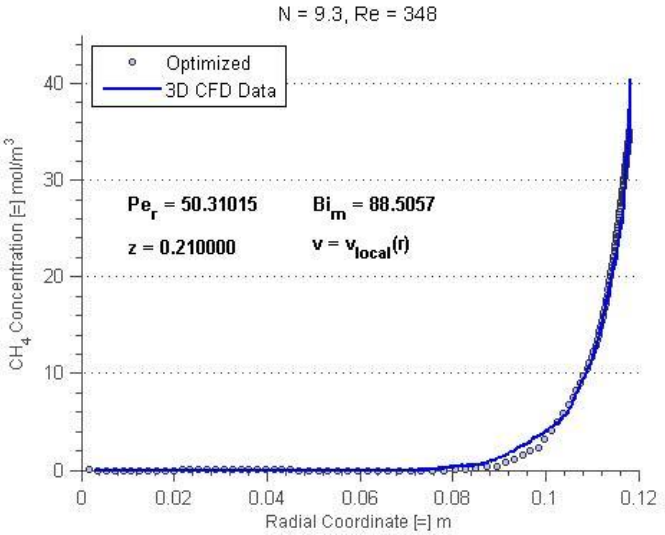

Figure C-213. Fitted radial concentration profile for N = 9.3, Re = 348, bed depth 01.

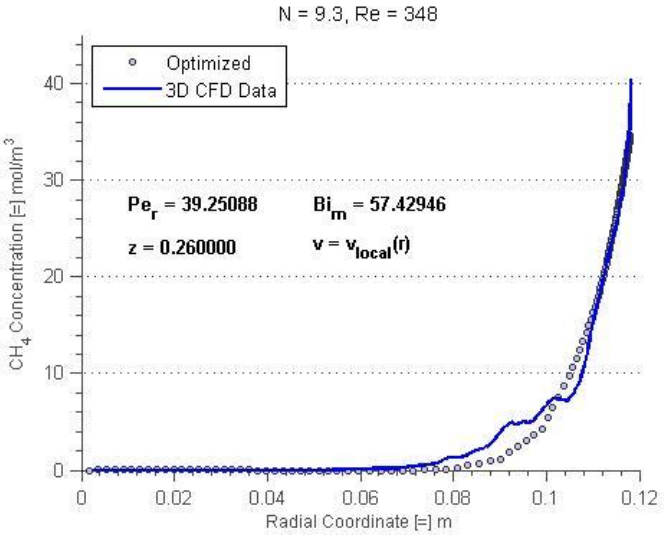

Figure C-214. Fitted radial concentration profile for N = 9.3, Re = 348, bed depth 02.

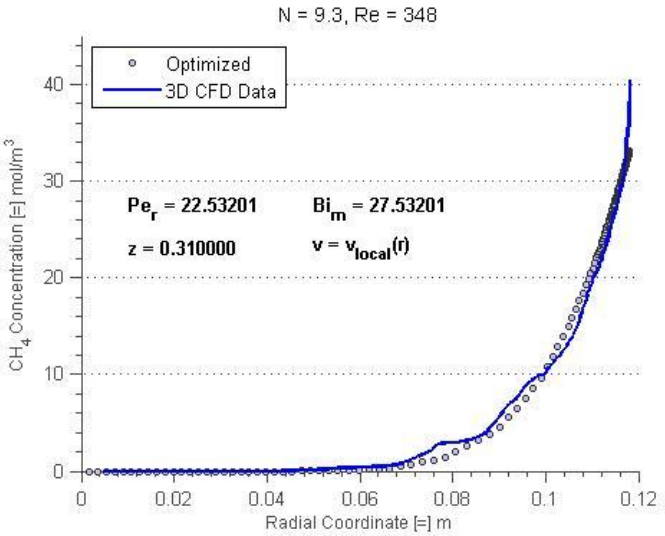

Figure C-215. Fitted radial concentration profile for N = 9.3, Re = 348, bed depth 03.

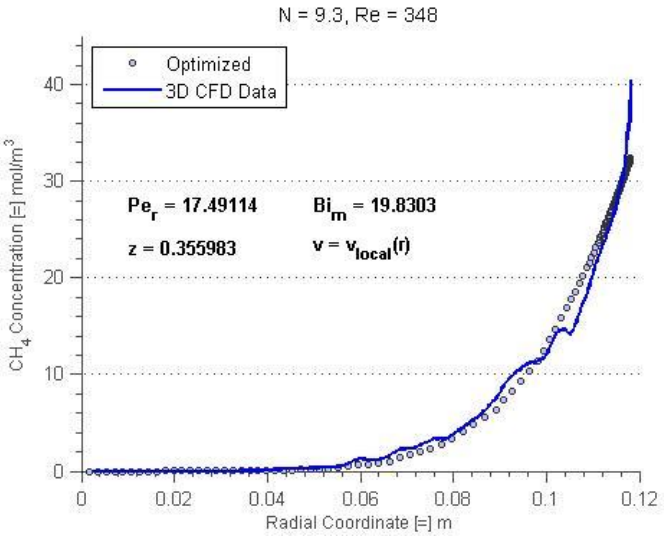

Figure C-216. Fitted radial concentration profile for N = 9.3, Re = 348, bed depth 04.

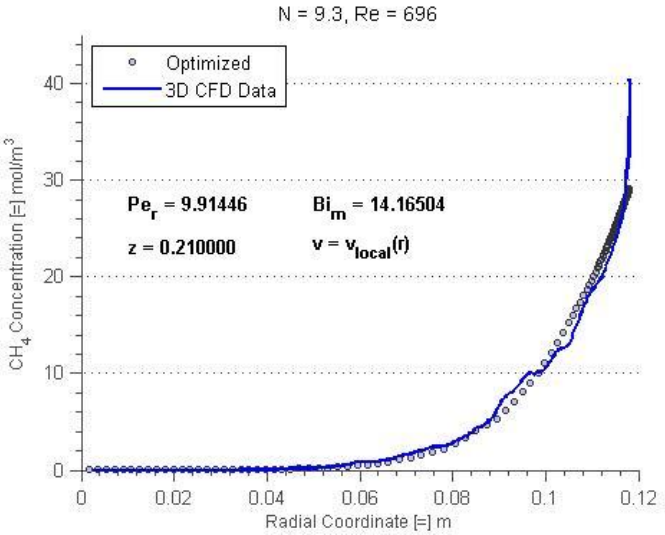

Figure C-217. Fitted radial concentration profile for N = 9.3, Re = 696, bed depth 01.

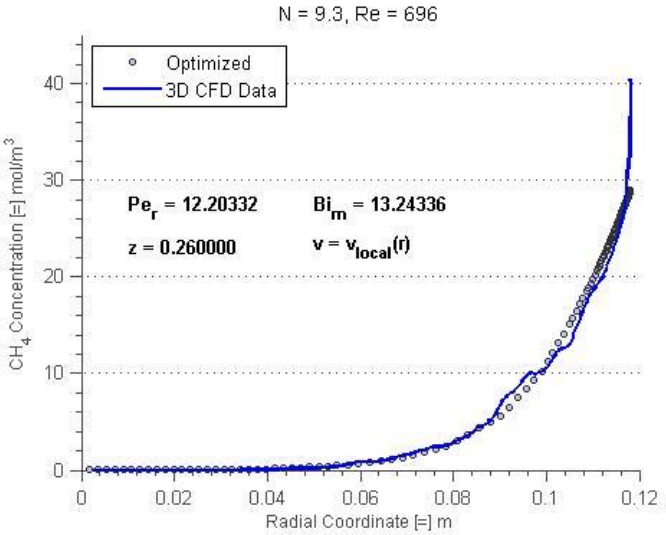

Figure C-218. Fitted radial concentration profile for N = 9.3, Re = 696, bed depth 02.

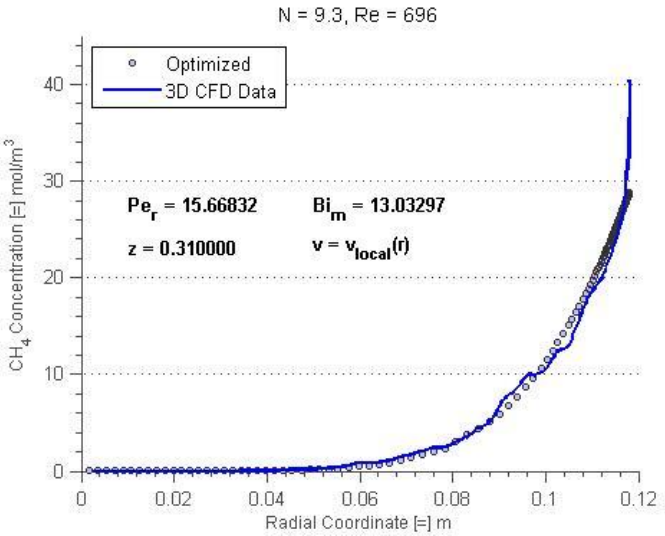

Figure C-219. Fitted radial concentration profile for N = 9.3, Re = 696, bed depth 03.

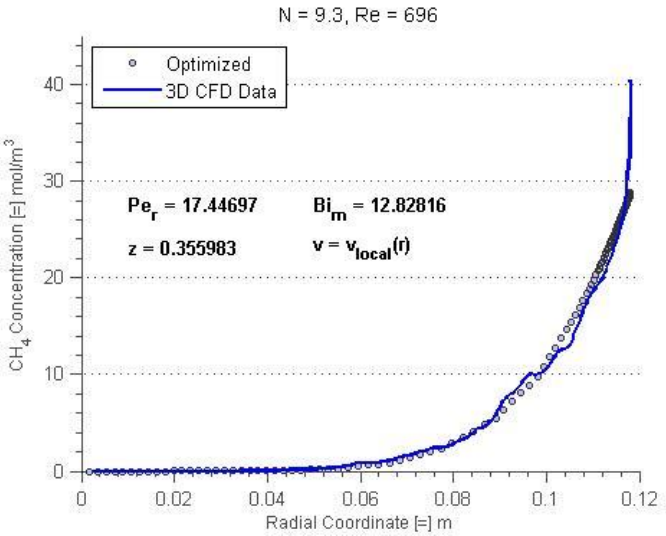

Figure C-220. Fitted radial concentration profile for N = 9.3, Re = 696, bed depth 04.

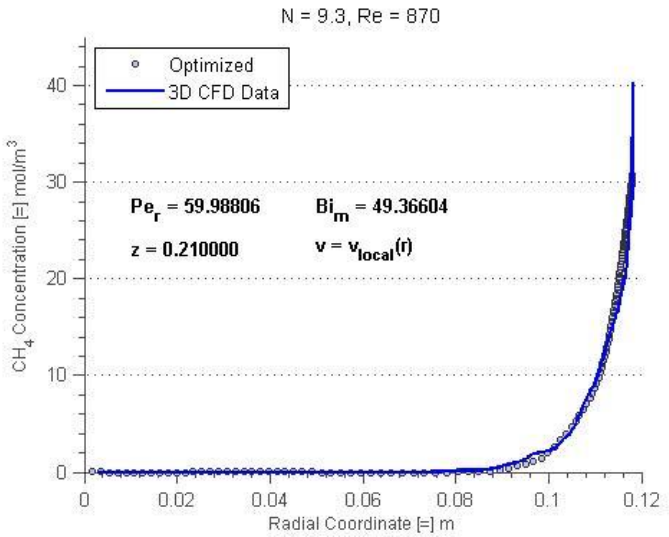

Figure C-221. Fitted radial concentration profile for N = 9.3, Re = 870, bed depth 01.

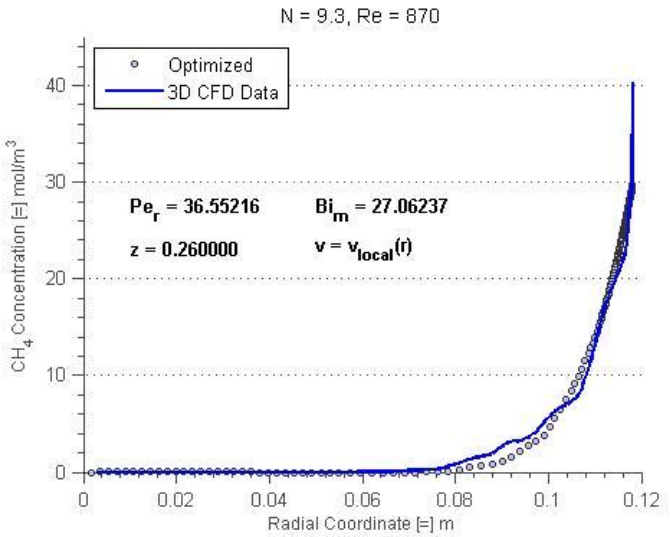

Figure C-222. Fitted radial concentration profile for N = 9.3, Re = 870, bed depth 02.

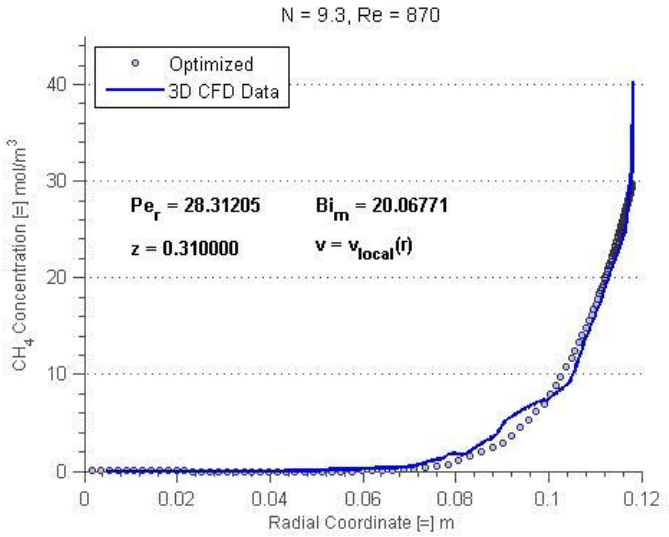

Figure C-223. Fitted radial concentration profile for N = 9.3, Re = 870, bed depth 03.

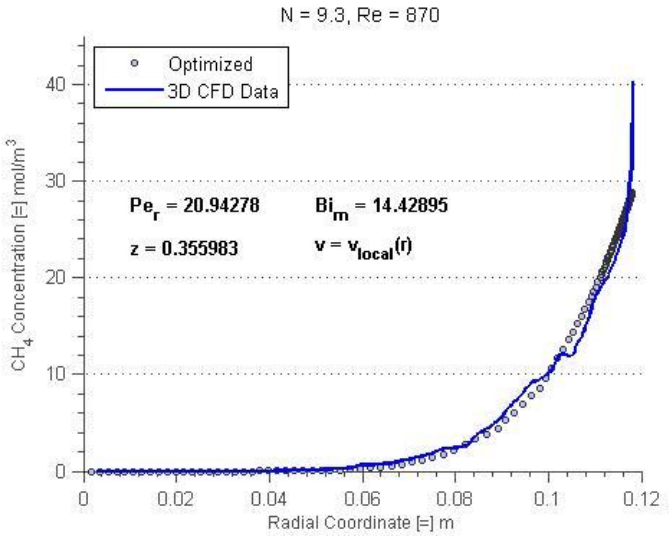

Figure C-224. Fitted radial concentration profile for N = 9.3, Re = 870, bed depth 04.